INVESTIGATING THE INFLUENCE OF FUTURE CLIMATE ON SLOPE STABILITY

A case study in Eidsvoll, SE Norway

Silje Merete Kristiansen Falkeid

Thesis submitted for the degree of Master of Science in Geosciences:
Geohazards and Geomechanics
60 credits

Department of Geosciences
Faculty of Mathematics and Natural Sciences

UNIVERSITY OF OSLO

April 2023

INVESTIGATING THE INFLUENCE OF FUTURE CLIMATE ON SLOPE STABILITY

A case study in Eidsvoll, SE Norway

Silje M.K. Falkeid

Photo:
Silje Falkeid, Eidsvoll study site 3rd November 2022

Investigating the influence of future climate on slope stability; A case study in Eidsvoll, SE Norway

http://www.duo.uio.no/

Printed: Reprosentralen, University of Oslo

Preface

This master's thesis was submitted to the Department of Geoscience at the University of Oslo, as the final product of a two-year Master's Degree in Geohazards and Geomechanics. The submitted work represents 60 ECTS credit points. The study is proposed by the Norwegian Geotechnical Institute (NGI) as a part of the Klima2050 and NordicLink pilot project at Eidsvoll. The work with the thesis is conducted under supervision by Project Engineer; Luca Piciullo (NGI), Technical Expert; Anders Solheim (NGI), Prof. Karen Mair (UiO) and Prof. Francois Renard (UiO).

Abstract

Understanding the influence of future climate on slope stability is becoming increasingly urgent as global warming is expected to shift precipitation patterns and the frequency of extreme rainfall events, which will entail an increased hazard of rainfall-triggered landslides in, i.e., the Nordic region. However, significant uncertainties remain linked with global warming and its impact on our globe since quantifying the effects of climate change is challenging and complex. This thesis is a component of the Klima2050 (https://www.klima2050.no/) collaboration and is linked to the pilot project "Railway Corridors" for the InterCity (IC) Venjar-Eidsvoll train section. The aim is to establish connections between future hydrological climate drivers obtained from climate projections and how slope stability changes over time in response to a changing climate, based on a detailed study of a location in Eidsvoll, south-east Norway.

The study site is a steep natural unsaturated soil slope adjacent to a railway track in Eastern Norway. The slope is instrumented at several depths with soil water content sensors, piezometers for pore-water pressure measurements, and tensiometers for suction estimation. The pore pressure regime influences the slope stability, i.e., the water supply from precipitation and/or snowmelt. An excess of pore water pressure can lead to a reduced effective shear strength of the soil and, thereby, reduced slope stability.

The commercial software GeoStudio is used for analyzing how future climate influences slope stability by combining the SEEP/W and SLOPE/W modules. The future climate's snowmelt, precipitation, and temperature series are introduced in an existing hydrological model, which simulates the development of daily volumetric water content (VWC) and pore water pressure (PWP) over time. In addition, other climate drivers (i.e., relative humidity, wind speed, albedo, solar radiation) and vegetation parameters from the literature have been included to make the hydrological model as realistic as possible. The SLOPE/W module uses the limit equilibrium method for calculating the Factor of Safety based on soil characteristics obtained from previous field investigations and laboratory tests, including pressure plate and triaxial tests. Furthermore, a sensitivity analysis was conducted to determine hydraulic conductivity and anisotropy ratio based on the relationship between the in-situ measured and

the hydrological model's predicted values. The sensitivity analysis contributed to better defining the input data and improving the best-fit model result.

Future hydrological variables are based on climate projections obtained from downscaled climate models. Due to the Norwegian topography, only the finest grid resolution (EUR-11) is used to derive local-scale climate change information. Climate changes towards the end of the century 2046–2100 compared to a reference period 1971–2000 was estimated at the slope's location and compared to corresponding changes from pre-existing estimates for Akershus County for validation purposes. Then, future hydrological input values for two future intervals are determined based on locally measured data and estimated changes. Furthermore, a specific climate model that best reflects the expected future climate for different years within each of these intervals is selected.

Numerical stress tests identified slope stability thresholds by systematically increasing water supply and temperatures. The stress tests were performed using the hydrological model with and without vegetation cover. This way, the analyses could identify triggering factors leading to slope failure and define the slope's water supply and temperature thresholds.

The simulations with the vegetated model yielded a satisfactory geotechnical Factor of Safety (FS) above 1.4, which is the limit set by the railroad authorities. Despite increased water supplies and temperatures until 2100, the modeled change in the Factor of Safety is relatively small. During the stress tests, results show that increasing temperatures increase slope stability, whereas increasing water supply is the most influential factor and may cause instability. No slope failure (FS<1) is identified until the water supply is increased by 300%, which is highly unrealistic. When using the hydrological model without vegetation cover, the Factor of Safety is below 1.4 before any increase is applied. During the stress tests, the Factor of Safety reduces faster than during simulations with vegetation cover, indicating that the slope's stability is more susceptible if vegetation is removed.

Although the analysis shows a stable slope despite the effect of climate change, the uncertainties associated with climate projections and the study's limitations may not accurately reflect the actual outcome. In particular, intense hourly precipitation is the leading cause of triggering rainfall-induced landslides, which was beyond the scope of this thesis but should be included in future evaluations of the effect of climate change on slope stability at this site.

Acknowledgments

First, I would like to thank my supervisor Anders Solheim at the Norwegian Geotechnical Institute (NGI). I am truly grateful for all his invaluable support, guidance, encouragement, and genuine interest in my development throughout this thesis. A supervisor that went above and beyond by offering so much of his time and knowledge, for all his feedback, and for always being there to answer all my questions. I will be forever grateful for all the support from Anders throughout this thesis, it would not have been possible without him.

I am also deeply grateful to my other supervisors, Luca Piciullo at the Norwegian Geotechnical Institute (NGI), Prof. Karen Mair, and Prof. Francois Renard at the University of Oslo, for offering their time and sharing their knowledge. I especially want to thank them for all their valuable feedback and advice in the writing progress and Luca for guiding me through the modelling part. I am thankful to have such a wonderful supervising team, and I highly appreciate you all.

I also want to express my gratitude to Kjersti Gisnås at NGI for her time and kindness in sharing her python script with me and, by so, helping me to manage a large dataset of climate projections in an acceptable amount of time.

Finally, I would like to thank my family and friends for being supportive and understanding during this project. And a special thanks to my partner Enrique for being patient with me throughout this process.

Table of Contents

Preface IV
Abstract V
Acknowledgments VII

1 Introduction 1
1.1 Klima 2050 1
1.2 The pilot project "Railway corridors" 2
1.2.1 The railway project (InterCity) 3
1.2.2 Eidsvoll case study 3
1.3 Motivation 3
1.3.1 Aims and objectives 5
1.4 Previous research 7
1.5 Structure of the master thesis 10

2 Theoretical Background 11
2.1 Factors influencing slope stability 11
2.1.1 Water flow and hydraulic conductivity 11
2.1.2 Effects on infiltration 11
2.1.3 Porewater pressure 12
2.1.4 Volumetric water content and suction (SWRC) 13
2.2 Stresses in soil 14
2.2.1 Principle of effective stress 15
2.2.2 Shear failure in soil 16
2.2.3 Cohesion and friction angle 16
2.2.4 The extended Mohr-Coulomb failure criterion 18
2.2.5 Influence of seepage in partially saturated soils 19
2.3 Failure mechanisms 19
2.3.1 Types of slope failures 20

3 The numerical software GeoStudio 22
3.1 SEEP/W module 22
3.2 SLOPE/W module 22
3.2.1 Factor of Safety 23

4 Study Area 25
4.1 Bedrock and Quaternary deposits in Eidsvoll 26
4.1.1 Characteristics and properties of fluvial and marine deposits 29
4.2 Landslide activity at Eidsvoll 30
4.2.1 Documented landslides along Dovrebanen (Eidsvoll-Langset) 31
4.3 The slope under investigation 33
4.3.1 Instrumentation and a IoT-based monitoring system 35
4.3.2 Slope vegetation 37
4.3.3 Mitigation work against slope failure in soils 37
4.4 Future climate based on climate models 39
4.4.1 Future climate predictions for Oslo and Akershus County 39

5 Eidsvoll slope model set-up and data inputs 44
5.1 Ground conditions and soil properties 44
5.2 Evaporation flux 45
5.3 The hydrological model 46
5.3.1 Calibration and validation of the hydrological model 47

6 Method 48
6.1 Sensitivity analysis for VWC and PWP 48
6.2 Historical observation data 49
6.3 Climate data as input to SEEP/W 50
6.4 Extracting hydrological variables from projected climate models 52
6.5 Validation of projected climate data for SEEP/W model input 53
6.5.1 Assessing the credibility of the projected hydrological variables 55
6.5.2 Eidsvoll climate change estimation and Oslo/Akershus climate profile 57
6.5.3 Estimated future climate values based on measured data 58
6.5.4 Selecting a climate model based on estimated changes 60

6.6 Other climate drivers as input 61
6.6.1 Estimated solar radiation flux 61
6.7 Simulations combining SEEP/W and SLOPE/W modules 62
6.7.1 Slope stability at Eidsvoll based on future climate until 2100 63
6.7.2 Slope stability based on numerical stress-tests of artificial data 64

7 Results 65
7.1 Sensitivity analysis on the hydraulic conductivity and anisotropy ratio 65
7.1.1 Changing the saturated hydraulic conductivity 66
7.1.2 Parametric analysis of the anisotropy ratio 68
7.1.3 The best accuracy of PWP and VWC 69
7.1.4 Varying the hydraulic conductivity and anisotropy ratio of layer 3 71
7.2 Eidsvoll and Oslo/Akershus precipitation and temperature changes 72
7.2.1 Eidsvoll RR, SWE and TM changes 2046-2100 74
7.3 Future precipitation, snowmelt, and temperature values at Eidsvoll 77
7.3.1 Predicted water supply and temperature values from climate models 80
7.4 Slope stability analysis based on estimated and predicted values 86
7.5 Defining thresholds through numerical stress-testing 90
7.5.1 Increasing the daily water supply 90
7.5.2 Increasing the daily temperatures 93
7.5.3 Combining water supply and temperature increase with/without vegetation 94

8 Discussion 98
8.1 Calibration of the hydrological model 98
8.2 Constrains on the examination of ground conditions and soil properties for modelling purposes 99
8.3 Sensitivity analysis of the hydraulic properties 100
8.3.1 Future changes in anisotropy ratio and hydraulic conductivity 102
8.4 Vegetation properties and additional atmospheric variables as input to SEEP/W 103
8.4.1 Vegetation's influence on slope stability 103
8.4.2 Hydrological model settings for future vegetation characteristics 104
8.4.3 Future solar radiation and albedo as input to the hydrological model 105
8.4.4 Future wind speed as input to the hydrological model 106

8.4.5 Future relative humidity as input to the hydrological model 107
8.5 The use of climate model projections 107
8.5.1 Advantages and disadvantages using climate projections in slope stability modelling..... 108
8.5.2 Obtaining future water supply and temperature values for model input..... 109
8.5.3 Future water supply and temperature values..... 111
8.6 Future slope stability..... 111
8.7 Slope stability using artificial temperature and water supply data..... 114
8.8 The influence of rainfall intensity on slope stability at Eidsvoll..... 116
8.9 Summary of the main modelling uncertainties and limitations..... 118

9 Conclusion..... 119
9.1 Suggestions for future work..... 121

Bibliography 122

Appendix A 139
A.I. Landslides 139
A.II. Soil properties and water flow..... 141
A.III. Types of slope failure in soil..... 144

Appendix B..... 147
B.I. The finite element method (FEM)..... 147
B.II. Material model..... 149
B.III. Boundary Conditions for Land-Climate Interactions..... 151

Appendix C 153
C.I. The limit equilibrium method (LEM) 153
C.II. The influence of interslice forces on failure surfaces..... 155
C.III. General Limit Equilibrium Formulation..... 156

Appendix D 158
D.I. Climate models 158

D.II. Emission scenarios..... 159

Appendix E..... 160

1 Introduction

This thesis is a component of the Klima2050 (https://www.klima2050.no/) collaboration and is linked to the pilot project "Railway Corridors" for the InterCity (IC) Venjar-Eidsvoll train section. The study area is an instrumented slope east of Eidsvoll church. The pilot project initiated by the Norwegian Railroad Directorate is part of WP3, with the Norwegian Geotechnical Institute (NGI) as the principal research partner.

1.1 Klima 2050

Klima 2050 is a Centre for Research-based Innovation (SFI) funded by the Research Council of Norway (RCN) and consortium partners. Their close collaboration across research partners increases Norway's ability to adapt to climate change and reduces the social risks associated with the built environment. The SFI is engaged in addressing both extreme weather and gradual climate change, emphasizing the development of moisture-resilient buildings, stormwater management, blue-green solutions, reduction of risk posed by water-triggered landslides, socio-economic incentives, and decision-making processes. Klima 2050 will serve as the foundation for improvements to laws, regulations, and standards pertinent to the design, building, management, operation, and maintenance of structures and infrastructure. The SFI concentrates on four major research areas, expressed as work packages (WP1-4).

- *WP1:* Climate exposure and moisture-resilient buildings
- *WP2:* Stormwater management in small catchments
- *WP3:* Landslides triggered by hydro-metrological processes
- *WP4:* Decision-making processes and impact

Pilots are the main arena for SFI's product development and testing of research results. Klima 2050 utilizes pilots as key development areas for the Consortium, where a pilot project is defined as follows:

"A pilot in the Research Centre, Klima 2050, may comprise a complete or delimited section of a building or facility or may be linked to a process or framework. Pilots must link to the development of new systems or processes. The objective is that a pilot shall act as a model and example of how we can demonstrate mitigation of risk to society employing measures designed to adapt to the impact of climate change."

1.2 The pilot project "Railway corridors"

The main aim of the pilot project is to develop a local early warning system (EWS) for landslides based on webcasting of in situ monitoring data (Figure 1-1). The EWS will help issue warnings for the railway authorities. These warning systems are being evaluated at two sites:

1. Bodø station
2. The section IC Venjar-Eidsvoll

The site at Bodø station is recently established and not yet fully developed. This thesis therefore focuses on the site at Eidsvoll. Automated stability measures may be derived by combining instrumented data and physical modelling of the stability conditions (Figure 1-1). A warning system of this type may help reduce the risk to human life and property loss due to hazardous events. Additionally, this approach can lead to a deeper comprehension of the slope's mechanics and a more accurate assessment of the real landslide-risks in critical areas (BaneNor, 2016).

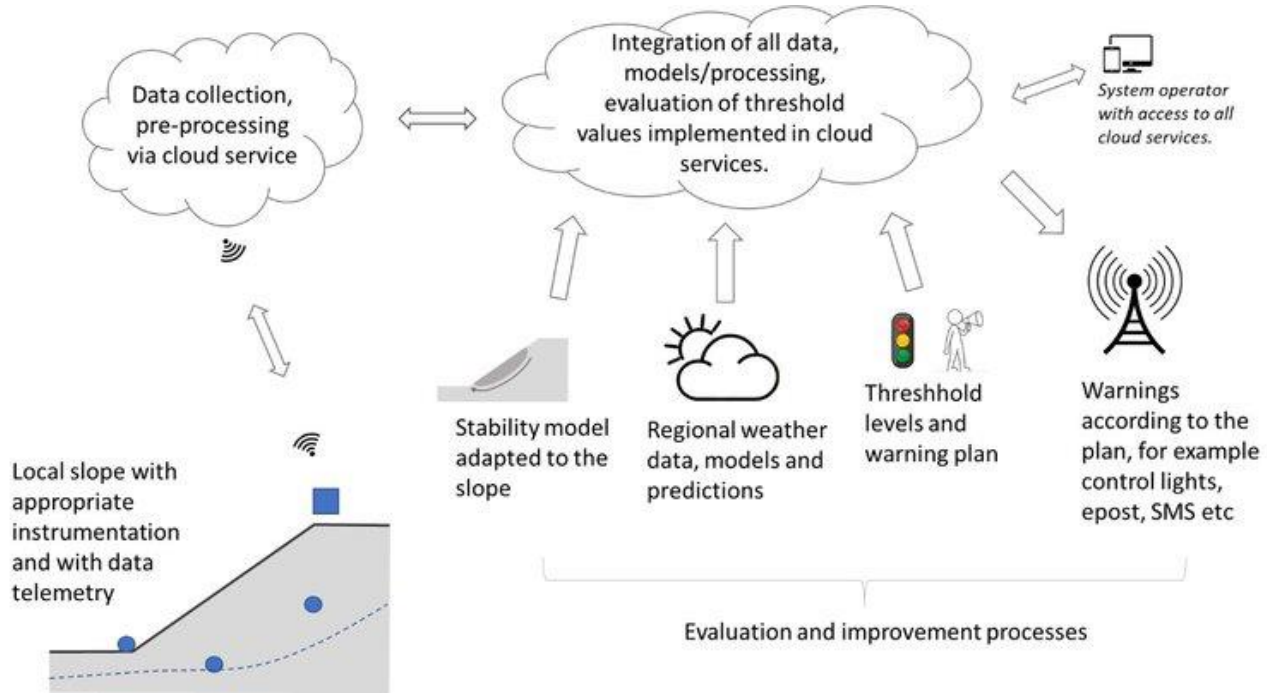

Figure 1-1. *A conceptual representation of a local landslide early warning system (Lo-LEWS) based on webcasting of in-situ data and automated stability computation (BaneNor, 2016).*

1.2.1 The railway project (InterCity)

Since the opening of Norway's oldest railway line ("Hovedbanen") from Oslo to Eidsvoll in 1854, Eidsvoll has been a popular transportation hub. Today, Eidsvoll station serves as the final stop for the local trains passing through Gardermoen-Oslo-Kongsberg and is part of the heavy traffic routes on Dovrebanen and Gardermobanen (Askheim, 2022). In 1998, the Gardermoen line was opened with a double track to Venjar. A new railway with a double track for Dovrebanen and Gardermobanen from Venjar to Eidsvoll was completed autumn 2022. The double-track project (InterCity) towards Eidsvoll will provide shorter travel times, better punctuality, and space for more trains as demands increase (Jernbaneverket, 2016). The railway project is facing several challenges, such as unstable conditions on slopes along the line (e.g., Eidsvoll case study). According to BaneNor's project descriptions, the geotechnical Factor of Safety (FS) along the new track must be at least 1.4 in areas where landslides may conflict with the railway (Jernbaneverket, 2016). Increased occurrences of landslides along roads and railways, anticipated to occur more frequently in the future, have elevated the importance of geotechnical stability.

1.2.2 Eidsvoll case study

A real-time early warning system will assist in limiting the damage that a potential landslide event may inflict by monitoring, modelling, forecasting, and issuing warnings (Jernbaneverket, 2016; Heyerdahl et al., 2018; Piciullo et al., 2022b). The case study at Eidsvoll is an initiative to provide a functional real-time warning system to optimize and secure the operation of the new railway (Ch. 1.2.1). The affected area is the steep slope between the new double-track line and Eidsvoll Church (Figure 4-1). Today, physical mitigation measures like drainage, terrain relief at the top of the slope, or slope support at the toe (Ch. 4.3.3) can improve the Factor of Safety. However, as the cultural heritage site (Eidsvoll church and cemetery) to the west of the slope is protected, physical slope stabilizing measures must be avoided. An IoT-based local landslide early warning system (Lo-LEWS) is under evaluation in this context.

1.3 Motivation

Landslides and/or snow avalanches are triggered virtually every day and together account for the highest number of fatalities among natural hazards in Norway (Olje- og Energi departementet, 2012). According to Norway's national landslide database, over 50,000

landslides and avalanches have been registered throughout historical times, where more than 4,000 people have lost their lives (Furseth, 2006). Aside from the numerous lives lost, these events have resulted in significant damages and severe economic consequences. According to Norsk Naturskadepool (2022), 14,548 damages related to mass movements were reported to insurance companies in Norway between 1980 and 2022. As a result of these incidents, compensation of more than NOK 2.3 billion has been issued. In Akershus County, which includes Eidsvoll municipality, at least 1,798 instances have been documented, resulting in compensation costs reaching more than NOK 854 million.

Landslides in soils are the most destructive and are mainly triggered by intense and prolonged rainfall, often in combination with snowmelt. Water-induced landslides cause yearly significant damage to buildings, infrastructure, roads, and railways (Krøgli et al., 2018). Transport systems, such as roads and railways, are particularly vulnerable to these landslides considering that it is challenging to avoid roads and railways passing through landslide-prone areas in Norway. In 1973, the Norwegian Public Roads Administration (NPRA) began compiling information about landslide incidents that affected roads (Lied, 1993). Over 24.500 slide events of various types are included in this database, which is currently the most extensive single collection of Norwegian landslide events (Jaedicke et al., 2009). Norway's national road database (NVDB) registers 1500 to more than 3000 mass movements affecting the roads yearly (NVDB, 2019). About 200 landslides hit the road sector, and 30 landslides hit railways (Hisdal et al., 2017). According to NGI (2013), at least 27% of roads and 31% of railway sections in Norway are at risk of landslide incidents. Furthermore, the report claims that closed roads alone cost society at least 100 million NOK annually.

In Norway, the climatic conditions and topography make it impossible to protect infrastructure from natural hazards fully. Forecasts and warnings have become a crucial mitigation strategy to reduce risk (Krøgli et al., 2018). Today's warning system is based on empirical data where the warning level is determined by experience-based threshold values for the ground condition and expected water supply. This method may be satisfactory for the regional warning but inaccurate for local slopes (Bane NOR, 2016). The drawbacks of this regional warning system include the inability to report landslides caused by local torrential rain, processes with a short response time (quick clay landslides, debris flows, and rock falls), or landslides triggered by human activity (Engen, 2016). Heavy rainfall, particularly in the summer, can occur very locally and be challenging to predict while also being critical for

slope stability (Walberg et al., 2014). According to Colleuille et al. (2017), the service's accuracy, precision, and usefulness should be improved in the current warning systems. Several factors contribute to the increased risk of landslides, such as weather types, the intensity of precipitation and snowmelt, terrain, and geological and hydrogeological ground conditions. Based on the results of the IPCC's fifth assessment report, future climate projections for emission scenario RCP 8.5 ('business as usual') indicates that temperatures will rise by 4.5 °C by 2100, with the most significant increases in the inner and northern regions (CICERO, 2018). Furthermore, an annual increase of precipitation by 18% is anticipated. Increased precipitation of this dimension will cause heavy rainfall events to become more intense and occur more frequently. Also, with increasing temperatures, a significant proportion of future precipitation is estimated to fall as rain instead of snow. Increased precipitation will also entail an increased hazard of landslides and floods. Changes in precipitation patterns in large parts of Norway are also expected. Climate change will thus affect weather-triggered landslides, which may lead to an increased frequency of landslides associated with heavy rainfall in areas previously not considered at risk (CICERO, 2018; Gariano and Guzzetti, 2016; Hanssen-Bauer et al., 2017).

Although landslide warning has improved our understanding of landslide processes, we must continue to improve, particularly given the country's changing climate and growing population. Climate change will generate more extreme weather and increase the frequency of landslides, where the exposure of infrastructure and constructed facilities is a growing concern in society, both economically and environmentally (Kalsnes et al., 2016). Additionally, risk interpretation becomes more uncertain, complex, and ambiguous as technology advances and globalization expands (Aven, 2017), highlighting the importance of a high-precision warning system.

1.3.1 Aims and objectives

This thesis aims to identify the influence of future climate on slope stability at Eidsvoll. A key goal is to determine the Factor of Safety based on the slope's characteristics with predicted precipitation, snowmelt, and temperatures towards the year 2100. The slope stability analysis will also assist in identifying triggering factors influencing the soil water content and pore-water pressures leading to slope failure, thereby determining the slope's

thresholds. An extensive analysis of future scenarios and a wide range of parameter inputs will be tested in addition to those currently measured by the instruments.

Specific objectives include:

- Estimates of future precipitation, temperature, and snowmelt at Eidsvoll derived from a combination of ten global and regional climate models.

- Use of projected climate variables to compute slope stability for the two time periods 2046-2075 and 2076-2100.

- Evaluate the potential effects of climate change on slope stability concerning extreme events and determine thresholds through numerical stress testing of artificial water supply and temperature data.

1.4 Previous research

Extreme precipitation can initiate different landslides, leading to the closure of transport lines and disturbances in local communities' telecommunications, power, and water supply. Hence estimates of extreme precipitation are frequently used in slope stability analysis and are decisive for the planning and designing of critical infrastructure (Klose et al., 2016). The relationship between extreme precipitation and landslides has been studied in several papers (e.g., Chatra et al., 2019; CICERO, 2018; Hansen-Bauer et al., 2017; Hisdal, 2017; Khan et al., 2021; NGI, 2013; Sandersen et al., 1996). Intense rainfall or prolonged precipitation over several consecutive days and snowmelt during spring significantly contributes to increasing the soil's volumetric water content through infiltration, which can reduce the suction and the shear strength of the soil mass. However, snowmelt is often a neglected component of hydrological slope stability analysis (Guthrie et al., 2010). Harr (1981) showed that snowmelt infiltration during rainfall was responsible for 85% of all slope failures in western Oregon, USA, between 1958 and 1977, and highlighted the importance of considering snowmelt's contribution in research where water infiltration is crucial.

The slope stability at Eidsvoll is influenced by the pore pressure regime, i.e., infiltration of precipitation and/or snowmelt (Heyerdahl et al., 2018; Piciullo et al., 2022a). Heyerdahl et al. (2018) evaluated the impact of soil suction and infiltration in the unsaturated soil at the Eidsvoll study site and found that the Factor of Safety drops at the end of a period of persistent rainfall. The rate of water infiltration into soils are mainly depending on the soil's hydraulic properties (Hou et al., 2021; Ashok et al., 2020; Reid et al., 1988), which are primarily influenced by various inherent soil properties such as the porosity and the permeability of soil profile (Greco et al., 2017; Haghnazari et al., 2015; Johnson, 1963). Water infiltration effect on slope stability can be assessed through numerical modelling by coupling a transient seepage and a stability analysis which provides the variation of the Factor of Safety with time. Godt et al. (2009) monitored how pore water pressure and soil suction responded to rainfall and illustrated the predictability of using measured soil suction and water content to calculate the Factor of Safety in time. Water infiltration effect on the Factor of Safety over time has also been studied for the monitored slope at Eidsvoll (Heyerdahl et al., 2018; Piciullo et al., 2022a), for residual soils in Croatia (Peranić et al., 2019), Singapore (Gasmo et al., 2000), a road embankment slope (Liu et al., 2017) and other soil slopes (Huang et al., 2018; Jeong et al., 2017).

Another process affecting water infiltration is the evaporation of water from the ground surface, a component often neglected to avoid unpredictability in the transient seepage analysis (Ng et al., 2008; Li et al., 2005; Fredlund et al., 2012). Additionally, neglecting vegetation can lead to incorrect estimation of the pore-water pressure regime over long periods (Rianna et al., 2014; Pagano et al., 2014) as roots help to increase the shear strength of the ground and extract moisture from the soil, thereby reducing the pore pressure (Liu et al., 2014). Removal of vegetation can impact the probability of slope failure by more than six times (Meehan, 1991) since the water supply can infiltrate more easily. Johnson et al. (2007) discovered that the same amount of water saturation in the soil was obtained after just 39% of the rainfall compared to the conditions before vegetation clearing. Mirus et al. (2017) examine the hydrological effects of landslide disturbance by comparing a slope with dense forest to a slope with limited root reinforcement and found that reduced root reinforcement and wetter soil promoted slope instability. Piciullo et al. (2022a) calibrated and validated a hydrogeological model for the Eidsvoll slope and concluded that the best representation of the slope conditions is by a hydrological model including both evapotranspiration and vegetation.

Due to the greenhouse effect, global warming is expected to cause a higher frequency of extreme rainfall events and changes in precipitation patterns, which will entail an increased hazard of rainfall-triggered landslides (CICERO, 2018; Gariano and Guzzetti, 2016; Hanssen-Bauer et al., 2017). The relationship between predicted rainfall and temperature variations under climate change and its impact on slope stability has been studied all over the world; some examples are; South-East France (Buma and Dehn, 1998), Italy (Dehn et al., 2000; Oggero et al., 2021), Eastern China (Pei et al., 2023), Croatia (Miklin et al., 2022), Northern Thailand (Chaithong, 2017) Slovenia (Bracko et al., 2022), Japan (Zhu et al., 2021) and Indonesia (Suryo et al., 2013). Few studies have examined how climate change may affect slope stability in Norway. However, one example can be found in Central Norway (Melchiorre and Frattini, 2012).

Several methods for predicting the impact of climate change on slope stability have been studied by linking slope models to climate scenarios obtained through downscaling General Circulation Models (GCM). In previous analyses of the impact of climate change on landslides, Dikau and Schrott (1999) established through their eight different study sites in Europe from 1850-2000 the difficulty of establishing a unique method to analyse the relationship between landslides and climate change in Europe. Buma and Dehn were the first

to exploit future rainfall records from a coupled ocean-atmosphere GCM to investigate the future stability of slopes (Buma and Dehn, 1998; Buma and Dehn, 2000; Dehn and Buma, 1999; Buma, 2000). They analysed the recurrence intervals of a shallow landslide in France from 1928 to 1970, investigated using a stability model coupled with a hydrological model, and recorded rainfall in the same period. Other examples are; expanded downscaling for a mudslide in Italy (Dehn et al., 2000) by combining statistical methods and monthly rainfall forecasts (Suryo et al., 2013) and by using a reconstructed landslide inventory and a set of downscaled meteorological data (Pei et al., 2023).

Coe and Godt (2012) analysed different approaches to assessing the impact of climate change on landslides and stated that attempts to predict landslide activity using air temperature and annual/seasonal rainfall exhibit a lower uncertainty. Sidle and Ochiai (2006) found that increasing temperatures and changes in precipitation were the most relevant climate variations affecting slope stability. Crozier (2010) investigated numerous factors linking landslides to climate change and assessed the impact of predicted climate changes on slope stability, discovering that increased air temperatures result in higher evapotranspiration rates and more abundant vegetation, causing a higher hydraulic conductivity which may have positive effects on slope stability.

So far, no deformations have been recorded at the Eidsvoll slope location (Heyerdahl et al., 2018). However, since landslides are expected to become more frequent as climate change progresses (Gariano and Guzzetti, 2016), and the Nordic region's future climate is predicted to be wetter and more erratic (Hanssen-Bauer et al., 2017), it is becoming increasingly important to understand how slope stability may be impacted by the future climate in order to ensure that current slopes and their design standards can accommodate changes in environmental factors like precipitation and temperature (Wong et al., 2022).

1.5 Structure of the master thesis

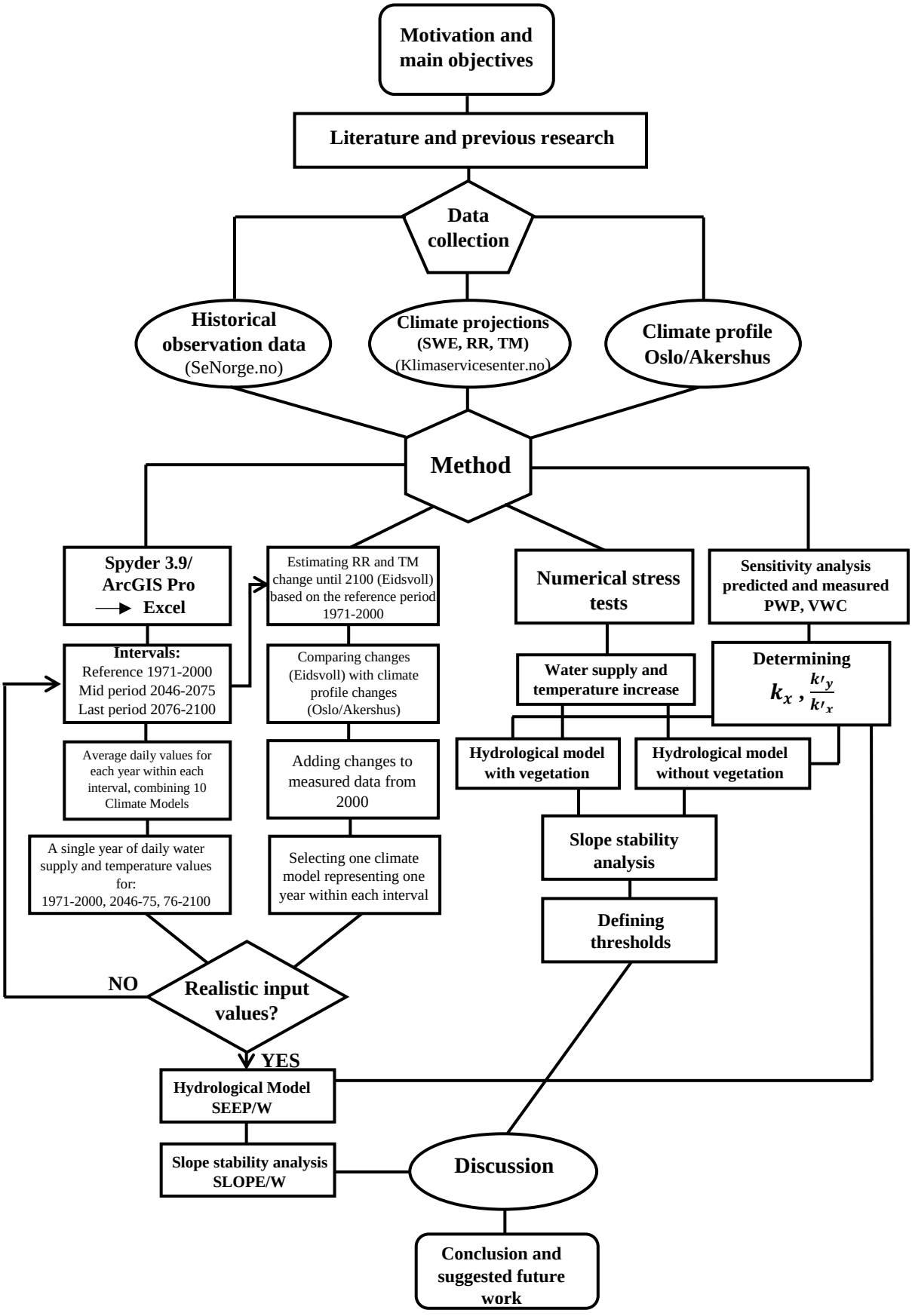

Figure 1-2. *Flowchart showing the steps involved in the scope of the master's thesis.*

2 Theoretical background

This chapter introduces the fundamental theory underlying the analyses conducted for this master's thesis. Additional theory is given in Appendix A (i.e., Classification of landslides (A.I), Soil properties; porosity, hydraulic conductivity and spatial variations and directional trends (A.II) and failure mechanisms (A.III)). These principles are essential for a better understanding of the theory that supports the numerical tool GeoStudio (Ch. 3 and Appendix B, C). A tool used for investigating the slope stability at Eidsvoll concerning climate change.

2.1 Factors influencing slope stability

In continental climates such as Eastern Norway, most landslides occur during autumn in the months with heavy precipitation. In this part of Norway, landslides are also common in the spring during snowmelt. Infiltration of water into the ground due to rain and snowmelt can reduce the stability of the slope, as the excess water can reduce capillary suction or increase the pore pressure (NGI, 2014). Compared to infiltration from rain, infiltration from snowmelt may provide a continuous supply of moisture over a more extended period, increasing pore-water pressures beneath shallow soils (Horton, 1938; Mathewson et al., 1990).

2.1.1 Water flow and hydraulic conductivity

Saturated hydraulic conductivity measures how easily water can flow through a porous material and plays a significant role in regulating water flow (Schwartz and Zhang, 2003). The flow rate depends on grain size, degree of sorting, packing, the shape of particles, degree of saturation, and the viscosity of the water, which varies with temperature, homogeneity, anisotropy, and layering of the soil mass (Yong, 2004; Anon, 1999). E.g., Fine-grained soils (i.e., clay and silt) have a greater capacity to store water and contribute to increased suction. However, the conductivity is poor due to denser packing and fewer connections between the pores, causing pore pressures to build up (Vanapalli et al., 1999).

2.1.2 Effects on infiltration

Water infiltration into soil is one of the main triggering factors of slope instability (Chatra et al., 2019; Piciullo et al., 2022a). Infiltration into unsaturated soil may increase volumetric

water content and reduce matric suction, thereby changing the effective stresses and decreasing the soil shear strength, which may induce a slope failure (Zhang et al., 2015; Gasmo et al., 2000). The soil hydraulic characteristics, evaporation of water from the ground surface, and the thickness of the soil layer are the key factors influencing how quickly slope materials react to infiltration (Piciullo et al., 2022a; Khan et al., 2021; Rahimi et al., 2011; Hou et al., 2021). Unlike materials like clay, typically more sensitive to long-term rainfall of moderate intensity, granular soils respond quickly to intense short-term rainfall (Khan et al., 2021).

2.1.3 Porewater pressure

Porewater pressure refers to the pressure of water in the voids of a soil mass, which acts equally in all directions and contributes to holding the soil structure together as the non-compressible water carries part of the load above. Porewater pressure is an essential factor in steep soil slopes as it affects the weight component of soil shear strength (Chatwin et al., 1994) and is given as (Yong, 2004):

$$\boldsymbol{u = \gamma_w h} \qquad \textbf{(1)}$$

$$\gamma_w = unit\ weight\ of\ water (kNm^{-3}), \quad h = height\ above\ stress\ point\ or\ plane\ (m)$$

Under steady-state conditions, the porewater pressure, *u*, is hydrostatic (Figure 2-1). However, the hydrostatic pressure is no longer observed in the unsaturated zone under transient conditions (Figure 2-1). During periods where the infiltration rate is high, the porewater pressure may become positive, which is critical for slope stability. Evapotranspiration contributes to a reduction in pore water pressure creating a negative porewater pressure, also referred to as matric suction, *S*, which is, according to Yong (2004), commonly described as:

$$\boldsymbol{S = u_{air} - u_{water}} \qquad \textbf{(2)}$$

$$u_{air} = pore\ air\ pressure, \quad u_{water} = pore\ water\ pressure$$

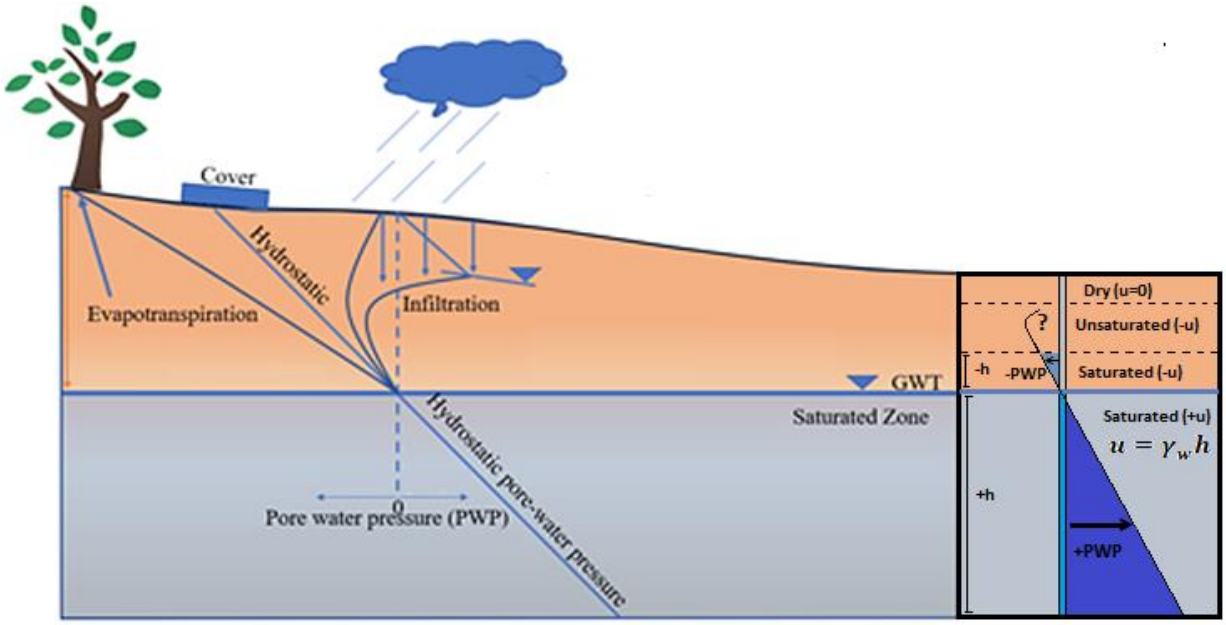

Figure 2-1. *Porewater pressure distribution. Modified from Wijaya and Leong (2018).*

In the unsaturated zone, the pore water pressures are determined by capillarity. Capillary rise is when water moves upwards due to the surface tension of water and its contact angle with the solid particles. The air/water interface exerts a tension force on the soil particles as more water is removed, which increases the soil's matric suction and shear strength (Gasmo et al., 2000). Capillary forces depend on the pore diameter, which has the same order magnitude as the particle size (Schwartz and Zhang, 2003). Tensiometers are used to detect pore water pressures in the unsaturated zone, while piezometers are used in the saturated zone (Ch. 4.3.1).

2.1.4 Volumetric water content and suction- Soil water retention curve (SWRC)

A soil water retention curve (SWRC) represents the volumetric water content (VWC) of unsaturated soil in equilibrium at a given matric suction (Tuller et al., 2004). The size and connectivity of the pore spaces strongly influence the relationship between the VWC and the matric suction and will therefore vary with soil grain size and structure (Figure 2-2). When the volumetric water content increases, the matric suction decreases (Picarelli et al., 2012). When analysing the stability of unsaturated soil slopes, the influence of matric suction coupled with volumetric water content is essential in predicting the soil's water retention capacity (Khan et al., 2021). Additionally, the SWRC parameters are necessary for estimating

unsaturated soil properties (Appendix B.II), including shear strength and unsaturated hydraulic conductivity (Fredlund et al., 1996; van Genuchten, 1980).

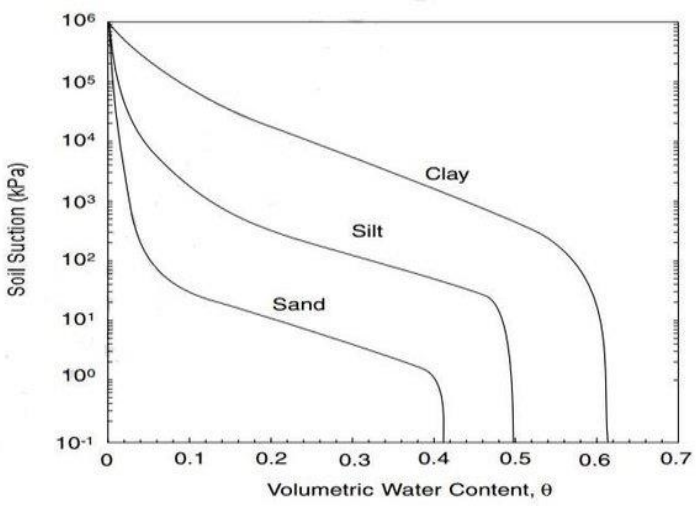

Figure 2-2. *Typical soil-water characteristic curves for soils of varying textures (Likos et al., 2010).*

2.2 Stresses in soil

Figure 2-3 illustrates a simplified free body diagram that represents stresses acting on a slope. For slopes with granular soils, the slope angle is critical because it affects slope stability in terms of cohesiveness and internal friction (Fu et al., 2020). The main driving force is gravity (g) which is proportional to the weight of the soil mass (m). Gravitational force is divisible into a normal resisting force (N) and a driving shear force ($mg\ sin\theta$). However, a force in the opposite direction ($mg\ cos\theta$) exerted by deeper soil cancels out the normal force. Shear strength, referred to as frictional resisting force (f), is consequently the most crucial resisting moment (NGI, 2014).

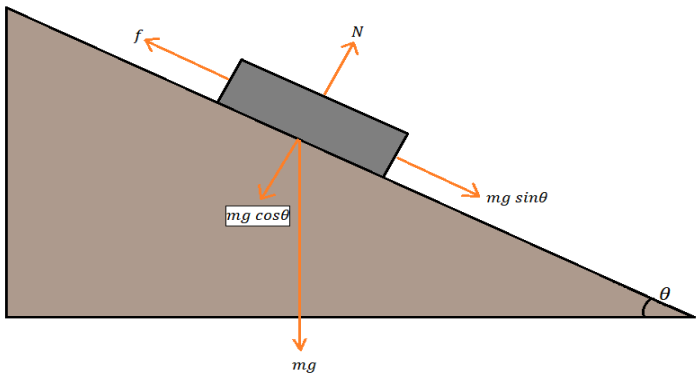

Figure 2-3. *A simplified illustration of forces acting on a slope. Modified (Geo-Studio, 2022b).*

2.2.1 Principle of effective stress

Terzaghi (1936) presented the principle of effective stress and stated, "... all measurable effects in a soil mass, such as compression, distortion, and a change in shearing resistance are due exclusively to changes in the effective stress". The principle of effective stress is the most important principle in soil mechanics, as the deformation of soils is related to effective stresses, not total stresses (Yong, 2004). Total stress refers to the load that acts on a given point or plane within the soil mass due to the overlying weight above that point or plane. Porewater pressure contributes to holding the soil structure together as the non-compressible water carries part of the load above (Ch. 2.1.3). If the water in voids drains due to permeable soil, the load is transferred to the soil particles as compressible air replaces the voids. Soil deformation is a function of total stress and the pore water pressure, as changes in total stress or porewater pressure can cause instabilities and ground movements. Loading due to foundations or unloading due to excavations will change the total stress. Porewater pressure and, therefore, the effective stress can increase due to infiltrating water from intense rainfall or decrease due to drainage, which can cause settlements (Craig, 2004). Due to the inability of porewater to resist shear stresses, these stresses are transferred to the soil particles. Thus, effective stress only applies to normal stresses (Yong, 2004). A major contributor to many slope failures is the change in effective stress caused by pore water pressures, which alter the soil's shear strength along the shear zone (Abramson et al., 2002). Effective stress is a result of the difference between total stress and the pore water pressure and is the average stress on a plane through the soil mass, expressed by Brunsden and Prior (1984) as follows:

Total Stress:

$$\boldsymbol{\sigma = \gamma_{sat} h} \qquad \textbf{(3)}$$

$\gamma_{sat} = unit\ weight\ (kNm^{-3}), \quad h = height\ above\ stress\ point\ or\ plane(m)$

Pore-Water Pressure:

$$\boldsymbol{u_w = \gamma_w h} \qquad \textbf{(4)}$$

$\gamma_w = unit\ weight\ of\ water(kNm^{-3}), \quad h = height\ above\ stress\ point\ or\ plane\ (m)$

Effective stress in saturated soil:

$$\boldsymbol{\sigma' = \sigma - u_w = \ (\gamma_{sat} - \gamma_w) h = \gamma' h} \qquad \textbf{(5)}$$

$\sigma' = effective\ stress, \sigma = \ total\ stress, u_w = porewater\ pressure, \gamma' = submerged\ unit\ weigth$

Effective stress in partially saturated soil proposed by Bishop (1959):

$$\boldsymbol{\sigma' = \sigma - u_a + x(u_a - u_w)} \quad \textbf{(6)}$$

$u_a = pore\ air\ pressure, x = degree\ of\ saturation\ (0-1), u_w = pore\ water\ pressure$

2.2.2 Shear failure in soil

A requirement for stability analysis of soil masses is the knowledge of the resistance of soil to shear failure (Craig, 2004). Failure will occur if the shear stress becomes equal to the shear strength of the soil at a point in any plane within the soil mass. This concept is expressed by Coulomb (1776) as a linear function of the normal stress at failure. The structure of solid particles can only resist shear stress in soil; therefore, shear strength is expressed as a function of effective normal stress at failure:

$$\boldsymbol{\tau = c' + \sigma' tan\varphi'} \quad \textbf{(7)}$$

$\tau = shear\ strenght, c' = cohesion, \sigma' = normal\ stress\ at\ failure, \varphi = angle\ of\ shearing\ resistance$

Cohesion and shearing resistance are developed by interparticle forces, depending on the presence of effective normal stress (Craig, 2004). Effective normal stress may influence shear strength because reduced porewater pressure and capillary forces contribute to apparent cohesion in the soil, thus increasing shear strength. During intense precipitation, this apparent cohesion decreases, resulting in decreased shear strength, which may lead to slope failure (NGI, 2014).

2.2.3 Cohesion and friction angle

The effective cohesion (c′) and friction angle (φ') are two inherent properties required for shear strength of a soil mass in any geotechnical analysis. Cohesion is the internal molecular force that holds the grains together, making the soil mass more resistant to shear failure. The water film between fine-grained soils binds together the particles and is characteristic of particle sizes below 0.002 mm, i.e., clay. Cohesion is greater in compacted soil masses as the high moisture content in the soil mass reduces cohesion (Roscoe et al., 1958). In cohesionless soils, the shear strength is mainly frictional and depends on the peak friction angle (Ameratunga et al., 2016). Proposed by Rowe (1962) the mobilised friction angle can be

expressed as the sum of the inter-particle friction angle (φ'_u), the resistance due to dilatation (φ'_d) and the resistance to crushing and rearrangement (φ'_b) (Eq. 8) (Figure 2-4).

$$\varphi'_{mob} = \varphi'_u + \varphi'_d + \varphi'_b \quad (8)$$

The critical state is reached when the dilatation is zero and granular material shears at a constant volume and stress state:

$$\varphi'_{cv} = \varphi'_u + \varphi'_b \quad (9)$$

For soils, the interparticle friction angle mainly depends on the particle surface roughness and shape characteristics. A more angular material with a rougher surface will create greater friction between the grains, which contributes to increased stability and a higher friction angle (Novotný and Klimeš, 2014). However, the high-water content in the soil will decrease the friction angle (Yong-Hong et al., 2005). Because particles have less space to rearrange when the material is dense and the void ratio is low, the dilatation rate is higher. During shearing, this forces particles to climb over each other, resulting in volume expansion and increased friction angles. A higher void ratio allows particles to shear mainly by particle rearrangement, resulting in granular material contraction during shear (Rowe, 1962; Terzaghi et al., 1996; Marzulli et al., 2021).

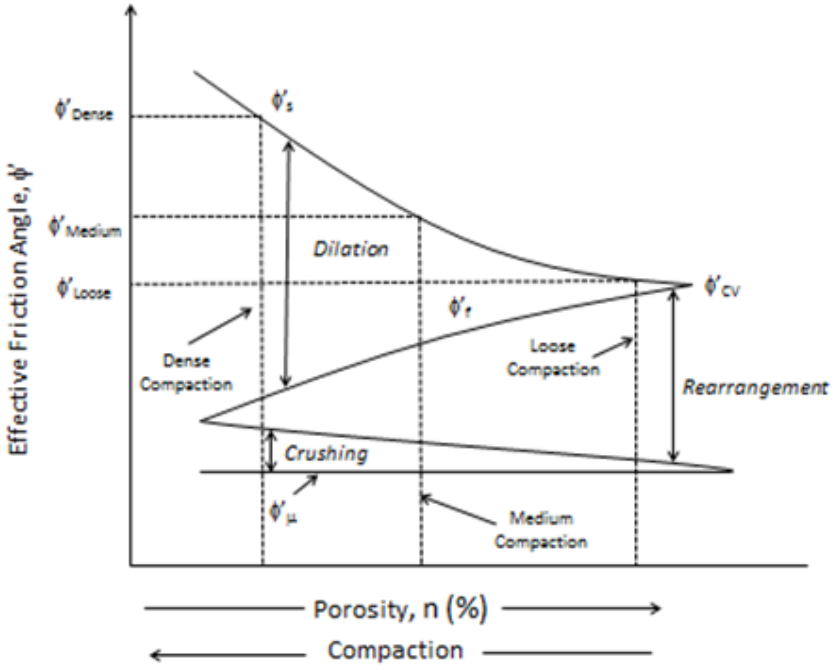

Figure 2-4. *Effect of porosity and compaction on the shear strength of granular materials (Rowe, 1962).*

2.2.4 The extended Mohr-Coulomb failure criterion

Fredlund and Rahardio (1993), extended the Mohr-Coulomb failure criterion (Eq.7) into third dimension in the shear strength equation for unsaturated soils (Figure 2-5). Using the stress state variables, the shear strength equation is given as:

$$\boldsymbol{\tau_{ff} = c' + (\sigma_f - u_a)_f tan\varphi' + (u_a - u_w)_f tan\varphi^b} \qquad \textbf{(10)}$$

$$\tau_{ff} = shear\ stress\ on\ the\ failure\ plane\ at\ failure$$

$$c' = effective\ cohesion$$

$$(\sigma_f - u_a)_f = net\ normal\ stress\ state\ on\ the\ failure\ plane\ at\ failure$$

$$(u_a - u_w)_f = matric\ suction\ on\ the\ failure\ plane\ at\ failure$$

$$\varphi' = angle\ of\ internal\ friction$$

$$\varphi^b = angle\ indicating\ the\ rate\ of\ increase\ in\ shear\ strength\ relative\ to\ the\ matric\ suction$$

When the soils become saturated, the pore-water pressure equals the pore-air pressure and the shear strength equation for saturated soils are given as:

$$\boldsymbol{\tau_{ff} = c' + (\sigma_f + u_w)_f tan\varphi'} \qquad \textbf{(11)}$$

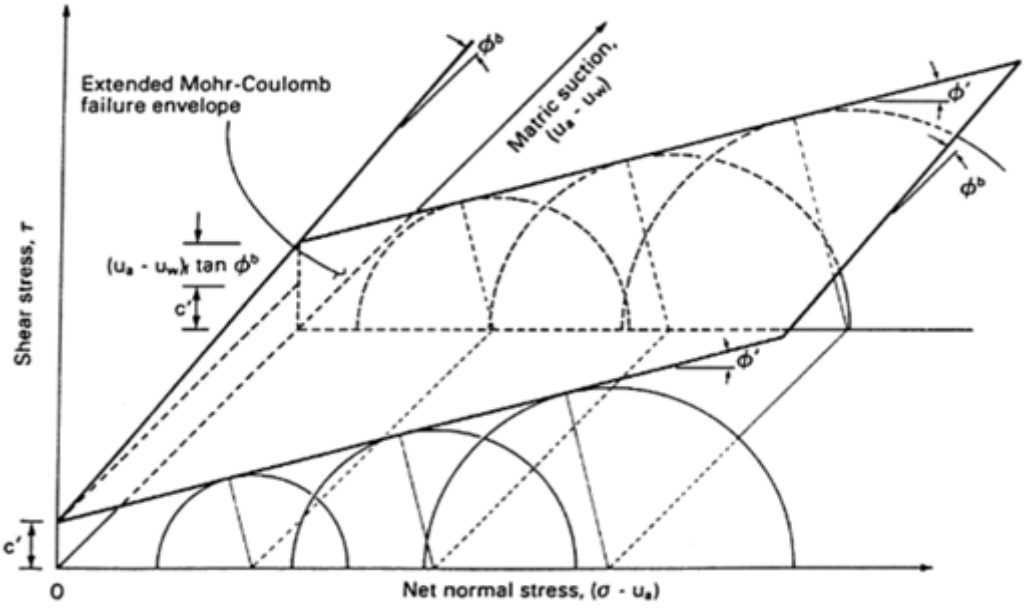

Figure 2-5. *Failure envelope for unsaturated soils (Fredlund and Rahardio, 1993).*

2.2.5 Influence of seepage in partially saturated soils

Water flow through soils, commonly referred to as seepage, may cause slope failure and is an important parameter in slope stability analysis. Calculating the rate and direction of water flow and distribution of pore water pressure within the flow regime are all part of the analysis process (Yong, 2004; Anon, 1999). The instability of soil masses due to seepage has resulted in many catastrophic failures (Yong, 2004). When water seeps through the soil's pores, a transfer of energy from the water to the solid particles takes place, and a force referred to as seepage force. In addition to the gravitational force acting on the solid particles, seepage forces govern the effective normal stress on a plane within a soil mass (Craig, 2004). Seepage force is denoted by Yong (2004) as:

$$\boldsymbol{j_s = \frac{\Delta h \gamma_w}{L} = i\gamma_w} \qquad \textbf{(12)}$$

$$\Delta h = head\ loss, \gamma_w = unit\ weight\ of\ water, L = flow\ distance, i = hydraulic\ gradient$$

In seepage conditions, seepage forces downwards are in the same direction as gravitational effective stresses and contributes to increase the effective stress

$$\boldsymbol{\sigma' = \gamma' h + j_s h = \gamma' h + ih\gamma_w} \qquad \textbf{(13)}$$

If seepage occur upwards the seepage forces are in the opposite direction to the gravitational effective stresses and thus decreases the effective stress

$$\boldsymbol{\sigma' = \gamma' h - j_s h = \gamma' h - ih\gamma_w} \qquad \textbf{(14)}$$

2.3 Failure mechanisms

A slope is an inclined body of earthwork that can either be artificial or a result of natural processes. The instability of slopes is referred to as the potential for movement, while the term 'failure' refers to the actual mass movement. The probabilities of a slope failure are influenced by gravitational forces and shear stresses exceeding the shear strength of the soil (Varnes, 1978). While seepage and gravitational forces impact the stability, the slope's geometry and the soil mass's shear strength mainly determine how resistant it is to failure

(Yong, 2004). Several factors may lead to slope failure. The most common, according to Terzaghi (1950) and Brunsden (1979), is:

- Increasing the unit weight of the soil by wetting or by external loading
- Changing the geometry of the slope, which leads to steepening of the slope by either excavation or by erosion, removing the support at the toe, or adding load at the top of the slope
- Shocks and vibrations caused by, for example, earthquakes
- Changes in the water regime leading to increased porewater pressures, a drawdown of groundwater table, or increased moisture content that contributes to loss of cohesion and shear strength
- Weathering processes like freezing and thawing

2.3.1 Types of slope failure in soil

The most important types of slope failures expected to occur in soil slopes are: translational (Figure 2-6c), compound (Figure 2-6d), and rotational failure (Figure 2-6a, b), circular slip (Figure 2-6a), and non-circular slip (Figure 2-6b) (Yong, 2004; Craig, 2004; Abramson et al., 2002).

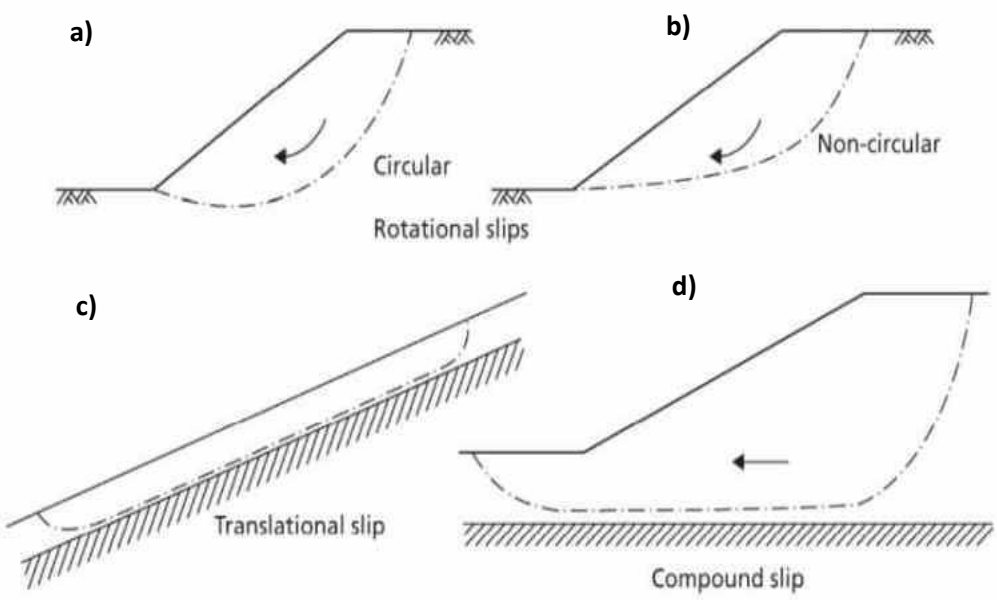

Figure 2-6. *Types of slope failure (Craig, 2004).*

At the study site in Eidsvoll, a circular rotational failure is assumed (Figure 2-6a). Circular rotational failure occurs due to a rotation along a slip surface in cohesive soils where porewater pressures along the sliding plane vary throughout the slope (NGI, 2014), and the failure surface is controlled by the strength of the groundmass (Abramson et al., 2002; Craig, 2004). More details on the different types of slope failures are given in Appendix A.III.

This chapter (Ch. 2) introduced the fundamental principles of the analyses conducted for this master's thesis. The theory given in Appendix A provides more details on soil properties, hydraulic conductivity, spatial variations, and directional trends (Appendix A.II) as a supplementary to chapter 2.1. Additionally, understanding landslides and their triggering mechanisms (Appendix A.I) gives a better understanding of a slope's mechanical behaviour and failure surfaces (Ch. 2.3 and Appendix A.III). The theory on water flow through soils (Ch. 2.1.1), the water infiltration's influence on volumetric water content and pore water pressures (Ch. 2.1.2 and 2.1.3) and the relationship between volumetric water content and suction (Ch. 2.1.4), is directly related to the theory for the SEEP/W module given in Appendix B. Further, the SLOPE/W module (Appendix C) builds on the theory which addresses driving and resisting forces and stresses acting on and within a slope (Ch. 2.2), emphasizing partially saturated soil slopes.

3 The numerical software GeoStudio

The slope stability analysis is performed using the software GeoStudio. GeoStudio is an integrated, multi-physics, multi-dimensional platform of numerical analysis tools developed by GEOSLOPE International Ltd. for geo-engineers and earth scientists. GeoStudio comprises several modules; however, for the purposes of this thesis, only SEEP/W and SLOPE/W modules will be described and used. Appendices B and C give a more detailed reading of the SEEP/W and SLOPE/W modules.

3.1 SEEP/W Module

SEEP/W is used for groundwater flow analysis which is a powerful finite element software product for modelling groundwater flow in porous media and can model saturated / unsaturated transient analyses with atmospheric coupling at the ground surface. SEEP/W uses the finite element method to simulate the water transfer through saturated and unsaturated porous media, which includes simulations of steady or transient groundwater flow within natural flow systems (Geo-Slope, 2022a).

Appendix B contains the pertinent theory for using the SEEP/W module, including an explanation of the finite element method (Appendix B.I), the input parameters required by the saturated-unsaturated material model (Appendix B.II) and the boundary conditions for Land-Climate interactions for simulating soil, vegetation, and atmospheric transfers (Appendix B.III).

3.2 SLOPE/W Module

SLOPE/W uses the limit equilibrium method (LEM) to simulate the mechanical behavior of soil to evaluate slope stability and calculate the Factor of Safety (FS). The SLOPE/W module can be useful for combining a variety of input parameters and model heterogeneous soil types, complex stratigraphic, slip surface geometry, and variable pore-water pressure conditions using a large selection of soil models (Geo-Slope, 2022b).

3.2.1 Factor of Safety

The output of the limit equilibrium analysis is a Factor of Safety (FS) which is assumed to have the same value along the entire slip surface. FS is a numerical ratio to compare the resisting shear strength of the soil with the existing shear stress on the failure surface (Figure 3-1) (Bishop, 1955). FS gives a measure of the stability of a slope and is the factor by which the strength must be divided to bring the system into a state of limiting equilibrium (Craig, 2004; Geo-Slope, 2022b). The Factor of Safety estimates the average shear stress mobilized in the slope; nevertheless, the average stress should not be mistaken for the actual stresses (Geo-Slope, 2022b). The goal is to determine the minimum Factor of Safety, which reflects the most critical surface. In order to do so, it is necessary to analyse the slope for a number of trial failure surfaces (Craig, 2004). A Factor of Safety is calculated by dividing the resisting forces by the driving forces (Figure 3-1). If the forces that resist the movement are greater than those driving the movement, the slope has FS value above 1 and is considered stable (Figure 3-1). When values are close to 1, the slope indicates marginally stable conditions, and further attention should be given. The stability of the slope is influenced by the weight of the mass, the external forces acting on the mass, shear strengths and porewater pressures along the slip surface as well as the strength of any internal reinforcement crossing potential slip surfaces (US Army Corps of Engineers, 2003).

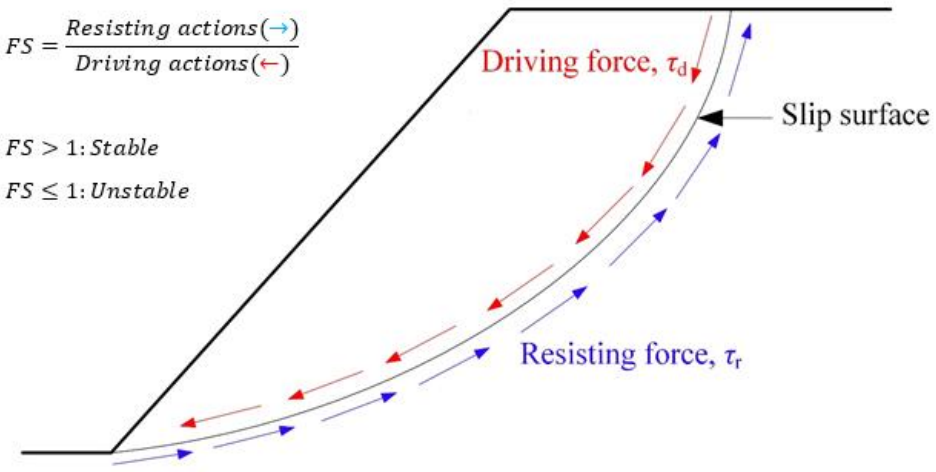

Figure 3-1. *A conceptual slope, illustrating resisting and driving forces acting on a circular slip surface. Modified from (Zhang, 2015).*

The SLOPE/W module was used to perform slope stability analysis using the limit equilibrium method (LEM) and calculate the Factor of Safety, assuming the circular rotational failure model proposed by Morgenstern and Price (1965). The SLOPE/W module calculates the Factor of Safety through the general limit equilibrium formulation, which is based on two Factor of Safety equations, one with respect to moment equilibrium (Eq.30; Appendix C.III) and the other with respect to horizontal force equilibrium (Eq.31; Appendix C.III). The Morgenstern and Price method includes both shear and normal interslice forces that satisfy both moments and force equilibrium (Morgenstern and Price, 1965; Craig, 2004). By default, the software SLOPE/W uses the half-sine function for the Morgenstern-Price method, which is also used for this analysis. The interslice shear forces typically concentrate in the middle of the sliding mass and are reduced by the half-sine function at the crest and toe regions (Geo-Slope, 2022b). More details on the limit equilibrium method are given in Appendix C.I, interslice forces in Appendix C.II, and the general limit equilibrium formulation in Appendix C.III.

4 Study Area

The study area is located in Eidsvoll municipality, situated in Eastern Norway. Eidsvoll is part of Viken, previously Akershus County, with a population of 26.716 inhabitants (2022). The slope is located between the railway line and Eidsvoll church (Figure 4-1).

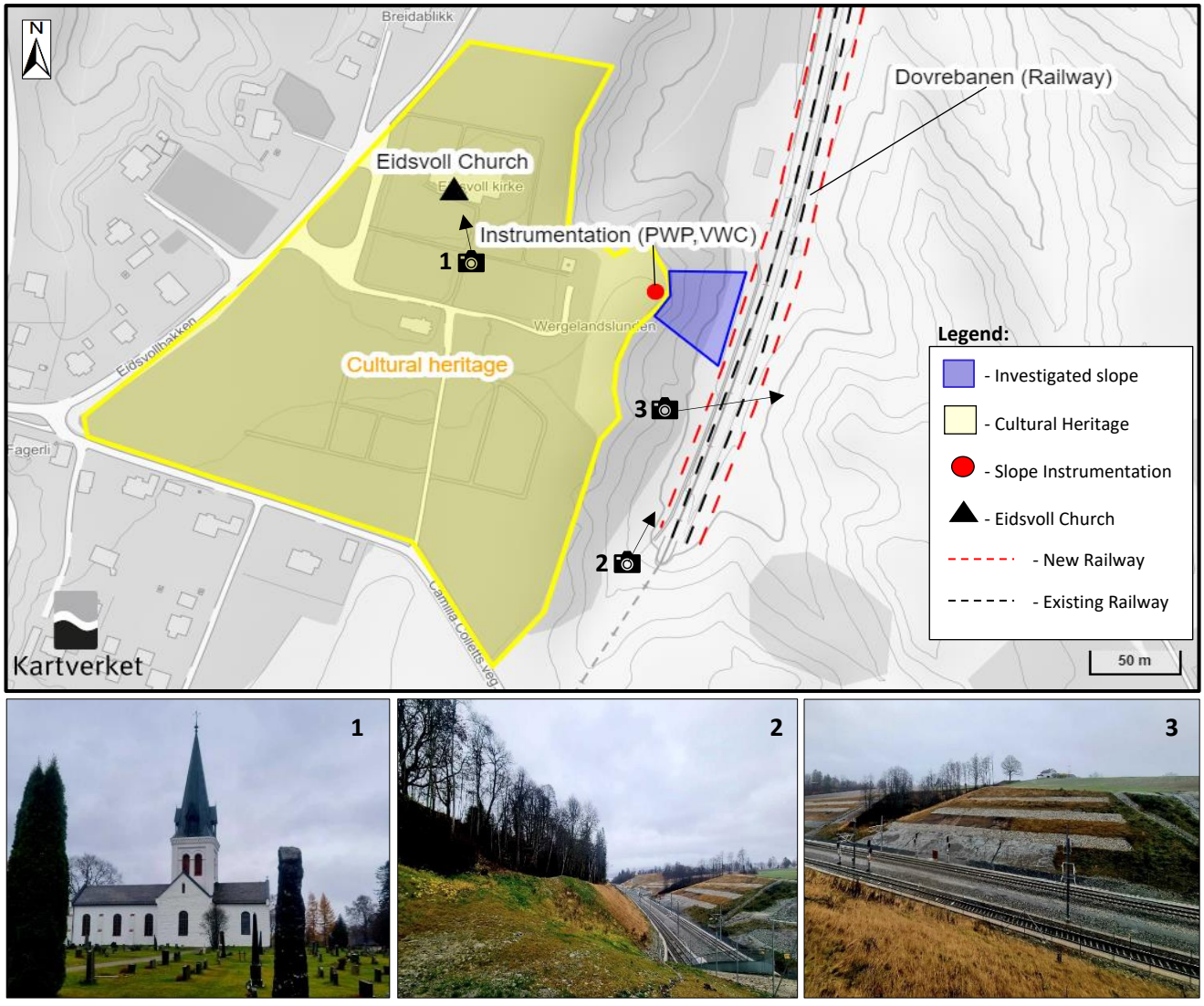

***Figure 4-1**. An overview of the study area showing the location of the instrumented slope in Eidsvoll, Eastern Norway. The Eidsvoll church is in the cultural heritage area, defined within the yellow-marked area at the west. The instrumented slope lies between the church and the railway, marked within the blue area. The numbered photos correspond to the numbers on the map, which show the location the photos were taken and the camera's orientation. Photo 1- In front of Eidsvoll Church. Photo 2- a sideview of the sloping area towards the railway line. Photo 3-the mitigated slope on the opposite side, east of the railway. Photos were taken during a visit to the site on 3.11.22. Map is created at Kartverket.no.*

The climate at Eidsvoll is characterized by moderate rainfall, low humidity, little wind, and large daily and annual temperature fluctuation (Askheim, 2020). However, the area has been exposed to frequent and long-term rainfall events. In the autumn of 2000, several landslides were triggered during almost three months of prolonged infiltration of large amounts of rainfall. Given the high air temperatures in the mountains this autumn, precipitation fell as rain instead of snow, resulting in rainfall exceeding 400% of the normal monthly values for November (Jaedicke and Kleven, 2008). The study area is located 5.4 kilometres away from the closest metrological measuring station, Eidsvoll Verk (SN11120) (Figure 4-2). Since the meteorological measuring station was established in 1916, the highest total amount of precipitation (437.3 mm) for June, July, and August was recorded during the summer of 2011 (Figure 4-2). The summer of 2011 caused flooding, extensive damage and closure of roads and railways (Askheim, 2020).

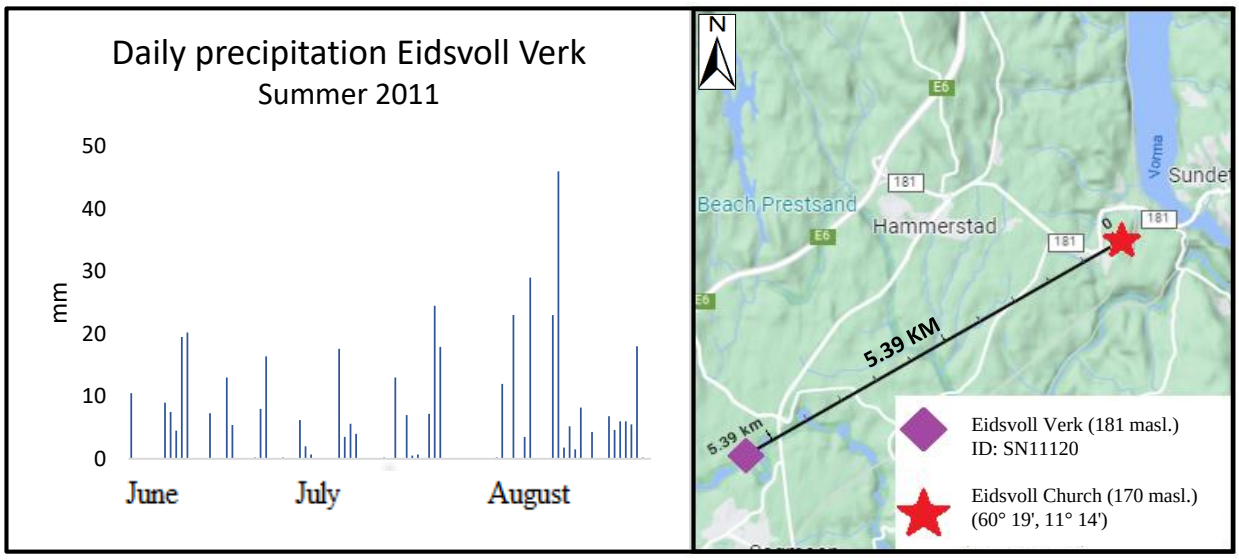

Figure 4-2. *Left: Graph showing the daily precipitation for June, July, and August in 2011, collected from observation data at Klimaservicesenter.no. Right: A map of the closest measuring station, located about 5-6 km from the study area (map created in Google Maps).*

4.1 Bedrock and Quaternary deposits in Eidsvoll

At Eidsvoll, the Precambrian Granodioritic to Tonalitic gneiss forms the bedrock underneath the Quaternary layers (Figure 4-3). The gneiss is typically identified as migmatitic and contains lenses, small granite bodies, and pegmatite (Ihlen and Lutro, 2010).

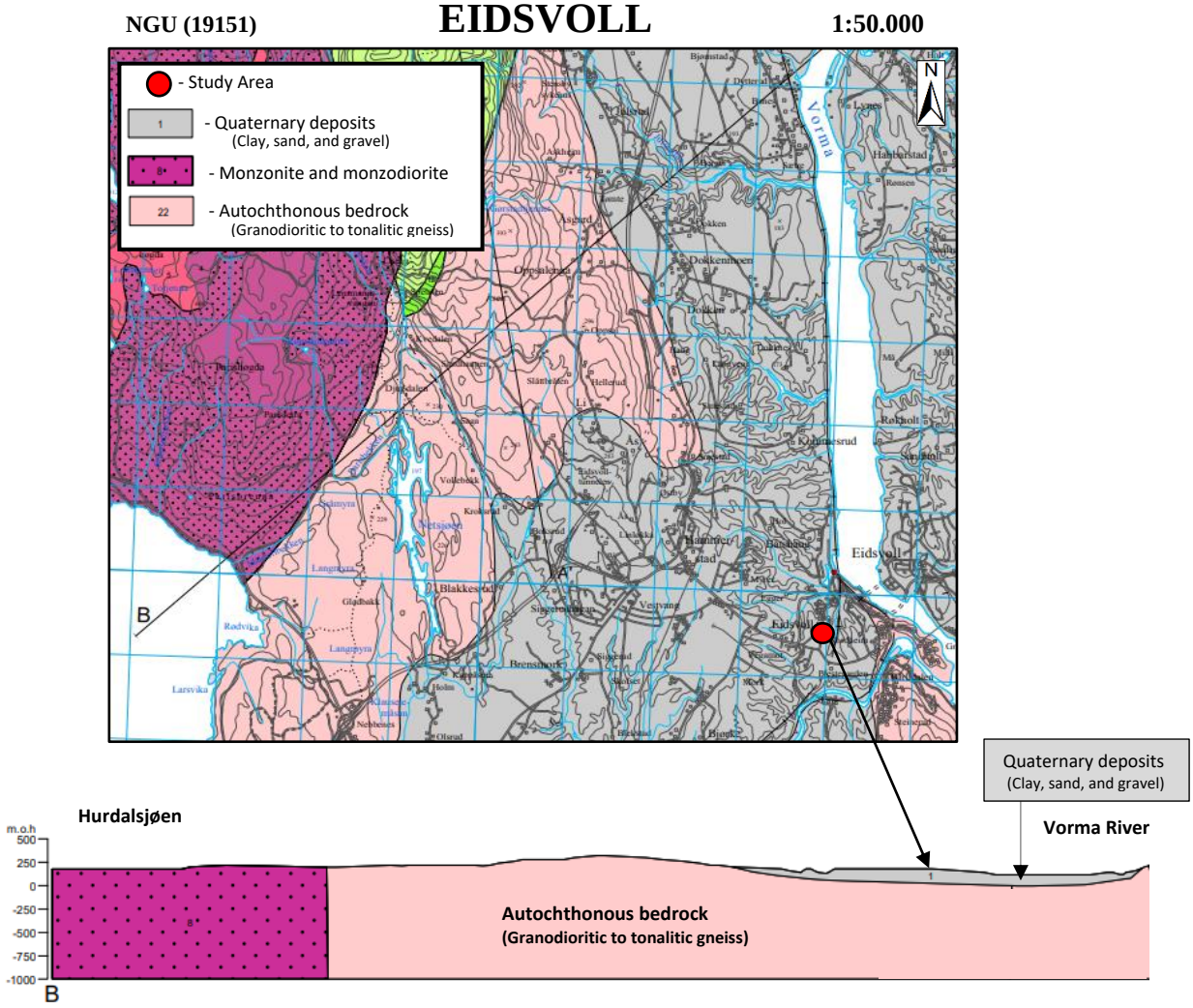

Figure 4-3. *A part of map sheet 19151: Bedrock map of Eidsvoll and a cross-section between Lake Hurdalssjen and Vorma from a location north of Eidsvoll Church. The pink covered areas consist of bedrock (gneiss) and the grey covered areas consists of Quaternary deposits. Modified from (Ihlen and Lutro, 2010).*

The Quaternary period (last 2.6 Ma) is characterized by significant climatic variations, having 40 different Ice Ages during which Scandinavia was entirely covered by ice. The landforms and sediments in Norway today result from these alternating glacial and interglacial periods (NGU, 2014). Most of the surficial sediments in Norway were formed between 13.000 and 9.000 years ago, during the Late Weichselian deglaciation (Ramberg et al., 2007). Knowledge of sedimentary structures and spatial distribution of Quaternary deposits is essential to understand soil properties and estimating the direction of water flow (Appendix A.II) which is an integral part of slope stability analysis.

"Minnesundtrinnet" is an ice-marginal deposit of sand and gravel formed while the ice front was stationary for a period of around 100 years at the outlet of Mjøsa (Figure 4-4) (Andersen, 2000). Due to isostatic depression by the Late Weichselian ice cap, the ocean followed the retreating ice front and relatively deep fjords formed in SE Norway, where fine-grained sediments (silt and clay) were deposited. Between Hurdalssjen and the Vorma River (Figure 4-4), glacial rivers transported glacial materials that accumulated into a 190-meter-high mound. As a result of post-glacial isostatic rebound, sediments deposited in the ocean were lifted above sea level, which explains why marine sediments are found exposed today (NGU, 2014). The marine limit at Minnesund is estimated to be 192 m (Andersen, 2000).

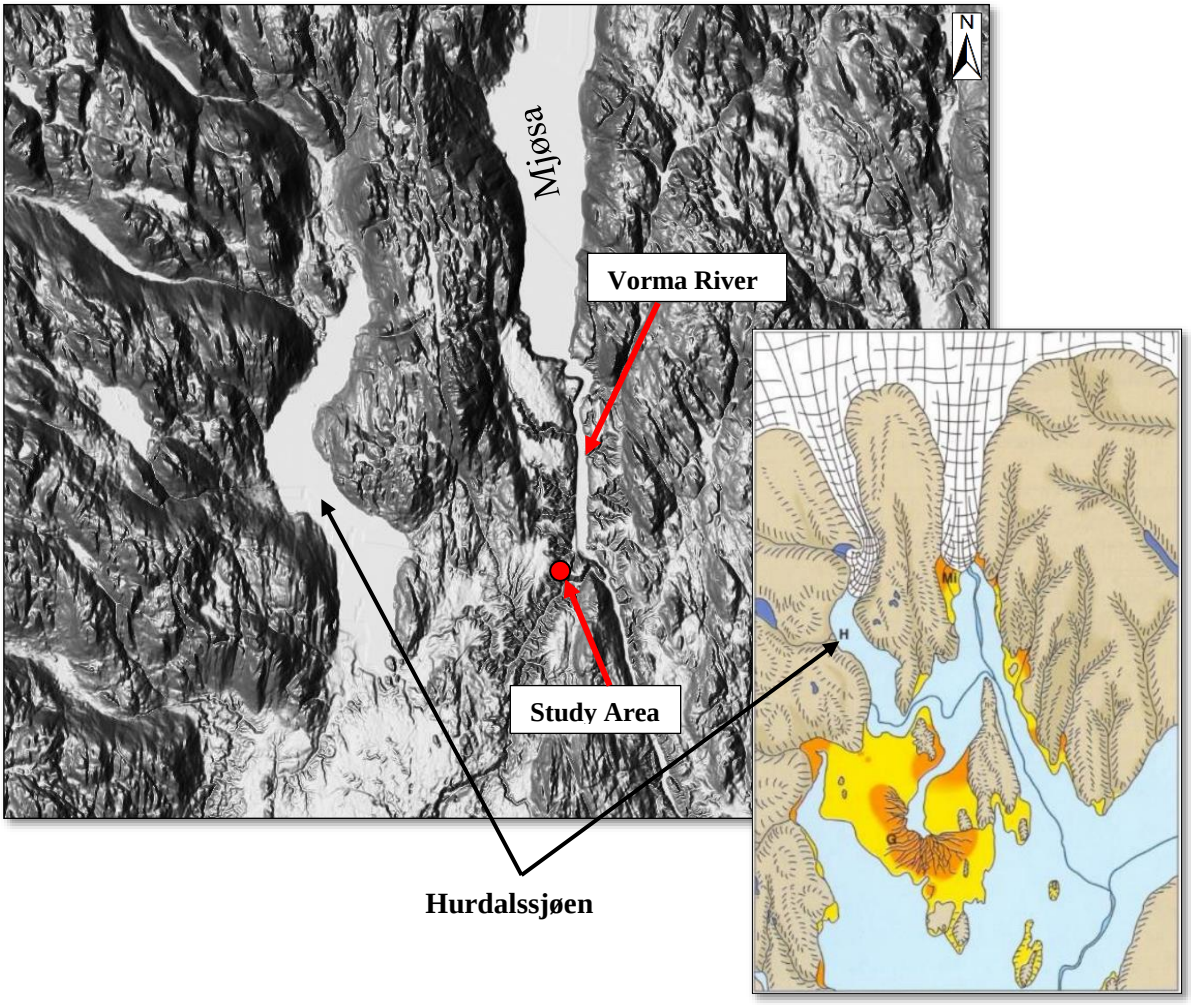

Figure 4-4. *Left: Current-state shaded relief map of Minnesund region (retrieved from NVE's thematic map service). Right: "Minnesundtrinnet" during the last Ice Age. The study site at Eidsvoll was submerged entirely under the ocean during this period, which is why marine sediments predominate here. Modified from Andersen (2000).*

Glacifluvial and fluvial sand and gravel deposits cover various locations in Eidsvoll. However, marine deposits dominate the region (Figure 4-5) (Erikstad 1992). The thickness of marine deposits ranges from 0.5 m to tens of meters, and fluvial deposits vary from 0.5 to more than 10 meters.

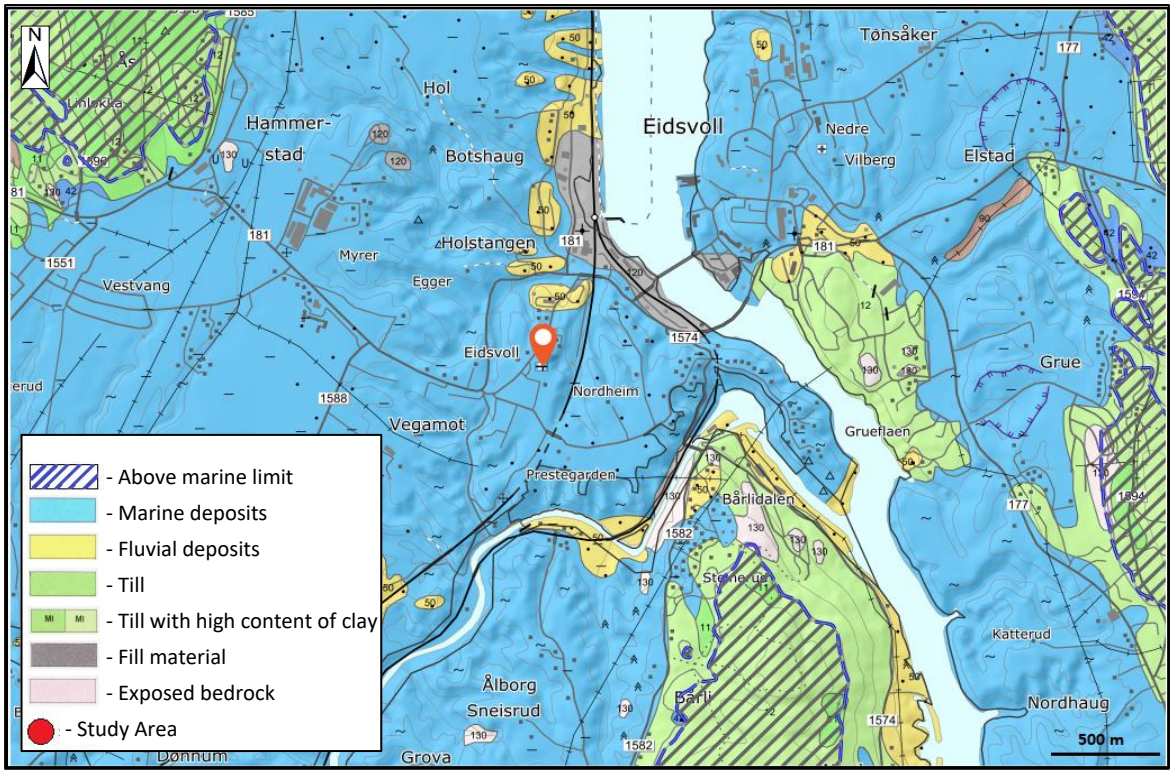

Figure 4-5. *Map of sediments in Eidsvoll area. Available at the Norwegian Geological Survey's website (https://geo.ngu.no/kart/losmasse_mobil/).*

4.1.1 Characteristics and properties of fluvial and marine deposits

The study area at Eidsvoll is covered by fluvial and marine sediments (Figure 4-5). Fluvial deposits are deposited by glacial meltwater and can be layered with different grain sizes due to seasonal variations in discharge. However, fluvial deposits are typically heterogeneous and are characterized as well-sorted fluvial sand with relatively high hydraulic conductivity and porosity (Schwartz and Zhang, 2003). Marine deposits mainly consist of clay and silt and are deposited in a calm, deeper water below the base of waves. Salt causes the clay to aggregate and sediment into massive deposits. Clay has low permeability and is vulnerable to erosion. Sandy deposits can also be found at shallower depths and are well-sorted. The high clay content in marine deposits contributes to very low hydraulic conductivity, high total porosity, and low effective porosity (Schwartz and Zhang, 2003).

4.2 Landslide activity at Eidsvoll

The national Norwegian landslide database (https://www.skredregistrering.no/) includes over 50,000 registered landslides, of which at least 18,000 are observed soil landslides in Norway. However, as landslide events were only fully registered and documented in later years, the actual numbers are much higher. There are still significant gaps in the data, and the number of reported slide events is only a small portion of the more significant number of actual incidents that are never reported. Most landslides triggered in, for example, uninhabited terrain is not registered as no damage is caused (Jaedicke et al., 2009).

Several soil landslides in the region of Eidsvoll have been reported, where most of them are triggered by intense precipitation during the snowmelt season in the spring. Furthermore, maps and geographical data can be found in the Norwegian Water Recourses and Energy Directorate (NVE) Map Catalogue (https://kartkatalog.nve.no/), which provides an overview of landslide events. In recent years, several documented landslides have been in the marine deposits in the municipality of Eidsvoll (Figure 4-6).

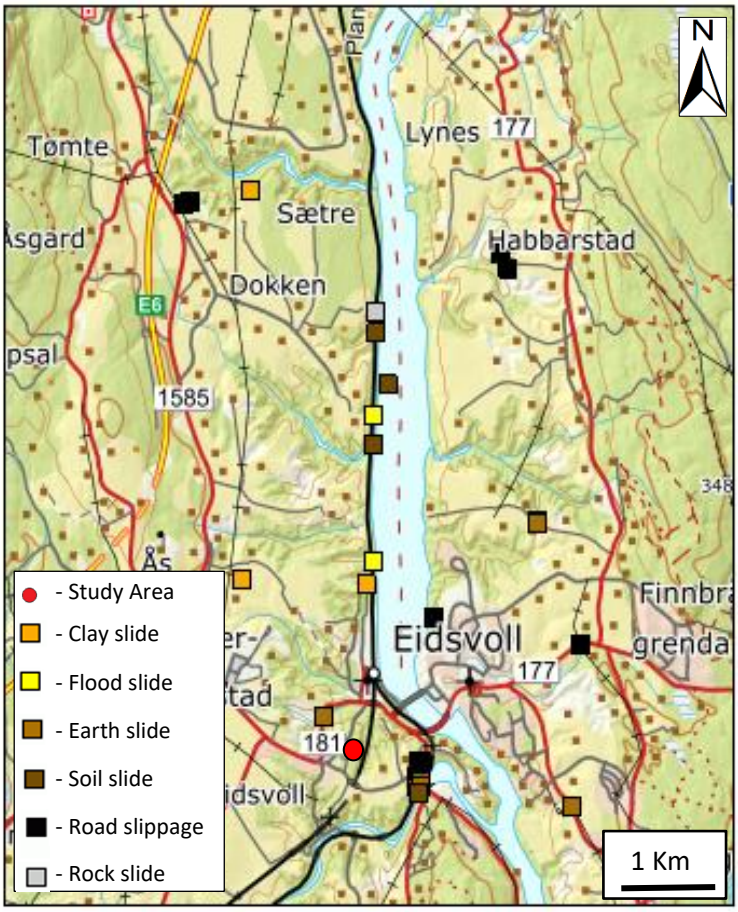

***Figure 4-6**. An overview of registered landslide incidents available at the Norwegian Water Recourses and Energy Directorate's website (NVE Atlas).*

None of these landslides have been quick clay slides but rather failures of soil masses caused by a combination of large amounts of water and steep terrain (Table 4-1) (NGU, 2021).

Table 4-1. *Registered landslide incidents in the Eidsvoll region collected from NVE (NVE Atlas).*

Year	Location	Event	Trigger
Apr 1962	Båtshaug	Clay slide	Unknown
Oct 1987	Bøn	Earth slide	Unknown
Nov 2000	Nedgarden Sander	Road slippage due to Clay slide	Unknown
Dec 2000	Søstuen Sander	Road slippage due to Clay slide	Unknown
Nov 2000	Møllerhaugen	Road slippage	Unknown
Jan 2007	Along railway line Eidsvoll-Minnesund	Soil slide	Unknown
Apr 2009	Along railway line Eidsvoll-Minnesund	Fill slippage	Unknown
May 2013	Railway north of Botnhagtangen	Flood slide (water, earth and rock)	Intense precipitation
May 2013	Below Dokenes Sørgarden	Flood slide (water, earth and rock)	Intense precipitation
May 2013	Finstadvegen next to bridge	Soil slide	Precipitation
May 2013	Fv 1574, Finstadvegen	Soil slide	Intense precipitation
Jul 2013	Dokken	Clay slide	Unknown No precipitation
Oct 2014	Fv17 (Odalsvegen)	Road slippage in filling	Precipitation -Erosion due to surface runoff
Jan 2015	Along railway line Eidsvoll-Minnesund	Rock fall < 100 m3	Unknown
May 2017	Eggerskjæringa	Soil slide <10 m3 from filling	Unknown No precipitation reg.
Apr 2018	Møllerhaugen	Road slippage	Unknown No precipitation reg.
Apr 2018	Fv 1574, Finstadvegen	Soil slide <10 m3	Unknown
Oct 2019	Røkholt/Sandholtgutua	Earth slide	Prolonged precipitation-erosion and high PWP
Feb 2020	Tømte	Road slippage/Clay slide	Precipitation
Mar 2021	Fv177	Earth slide	Unknown
Mar 2021	Vilberg ungdomskole	Clay slide	Unknown

4.2.1 Documented landslides along Dovrebanen (Venjar-Langset)

The terrain following the railway line along the west bank of the Vorma River is dominated by massive ridges formed by fine-grained sediments. The topography on the track's west side is relatively steep, with some variations due to past subsidence and slips on slopes. The

vegetation on the slopes is diverse but dominated by birch trees, although clear-cutting has occurred in several areas. Several landslides have impacted the railway (Table 4-2) for the section along the Vorma River toward Langset (Figure 4-7). Shallow landslides are the most common, according to the reports provided by BaneNor (BaneNor, 1957; BaneNor, 1967; Falstad, 2001; Jernbaneverket, 2011; Sandersen, 2011). Examination of the ground conditions reveals that the layered surface material typically consists of fine sand and clayey silt, followed by a firm and massive layer of homogeneous clay extending to greater depths (Table 4-2). No quick clay has been identified in the surroundings of the study site. The steep slopes along the railway are stable under "normal" conditions. However, heavy rainfall in spring and autumn can cause excess pore pressures in the upper layered deposits and thereby cause instability.

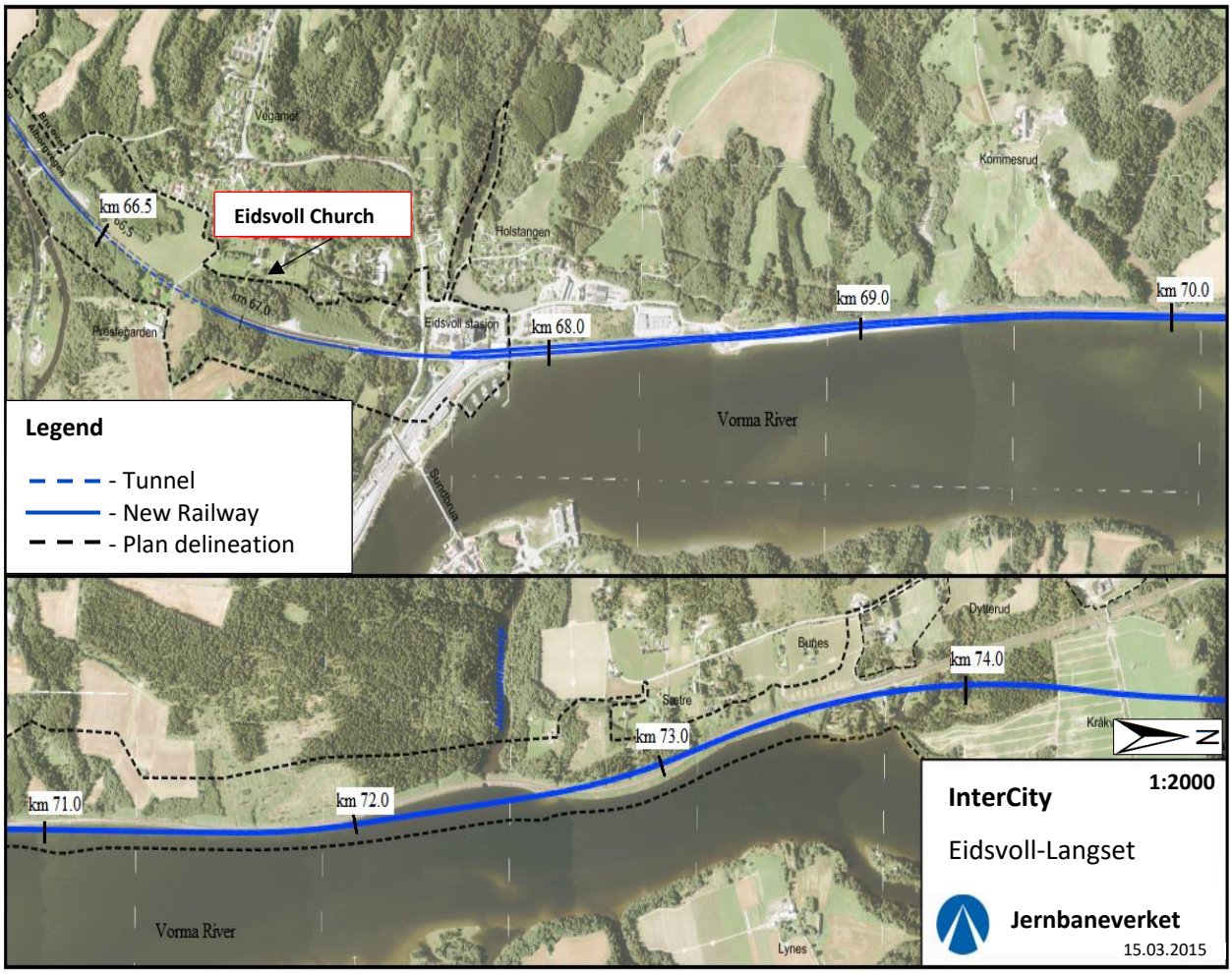

Figure 4-7. *Map showing the route for the new railway and kilometre distance from Oslo Central Station (Jernbaneverket, 2016). The kilometre-distance (km) is from Oslo Central Station, which serves as the Norwegian railway network's starting point (0 km).*

Table 4-2. *A list of known slide events that have impacted the railway between Eidsvoll and Langset along the 66.5-74.0-kilometre stretch, as well as the reported ground investigations and mitigating measures. The kilometre-distance (km) is from Oslo Central Station, which serves as the Norwegian railway network's starting point (0 km).*

Year	Location (KM)	Event	Ground conditions	Mitigation
1932/ 1958	69.208	Sliding on the slope at Båtshaug teglverk	Firm clay and fine sand High pore pressures	Ditches in slope and vertical sand drains. Drainage pipes.
1932	69.616	Subsidence in slope-filling towards Vorma	Firm clay and fine sand	Drainage ditch in filling
1932	70.368	Subsidence of sand layers at the top of the slope	Firm clay. Very high-water content in sand layer at the top of the slope	Drainage ditch in slope
1937	70.36-38	Masses sliding out. Railway closed due to major disruption on track	Firm clay underneath fine sand/ silt layer with a very high-water content	Gravel filling, drainage ditch with coal stumps and gravel. Drainage pipe.
1937	69.88	Sliding on slope. Line trench pinched	Clayey sand (2 m) above firm clay	Trenching
1942	71.05	Displaced retaining wall	Firm clay with silt	Drainage
1953	69.586-606	Top masses sliding out. Depth 1 m.	Firm clay and clayey sand layer	Slag-filled ditches. Growth of birch trees
1957	72.93	Slope filling slides out	Fine sand	Drainage pipe and refilling of pit
1967	72-77.26	Sliding, settlement and cracks due to flooding	Fine sand and coarse silt	Drainage pipes Filling
2000	69.70	Settlement in filling below railway,	High water content. Drain line clogged	Drainage pipes
2000	69.83	Traffic stops due to sliding	Masses from garbage filling	Drainage pipe (south and north)
2000	70.76	Cracks in filling/slope and settlement (length 30-40 m) towards Vorma	No drainage along track	Drainage pipe (north)
2011	86.38-97.88	Landslides, slips in fillings, settlement, and washouts due to flooding and erosion	Oversaturated fills of sandy silt, sand, and puck	Filling, drainage pipes

4.3 The slope under investigation

The investigated slope, located on the eastern side of the cultural heritage site, is 25-30 meters high and consists of a deep marine layer overlain by 8-10 meters of sand and silt (Figure 4-8).

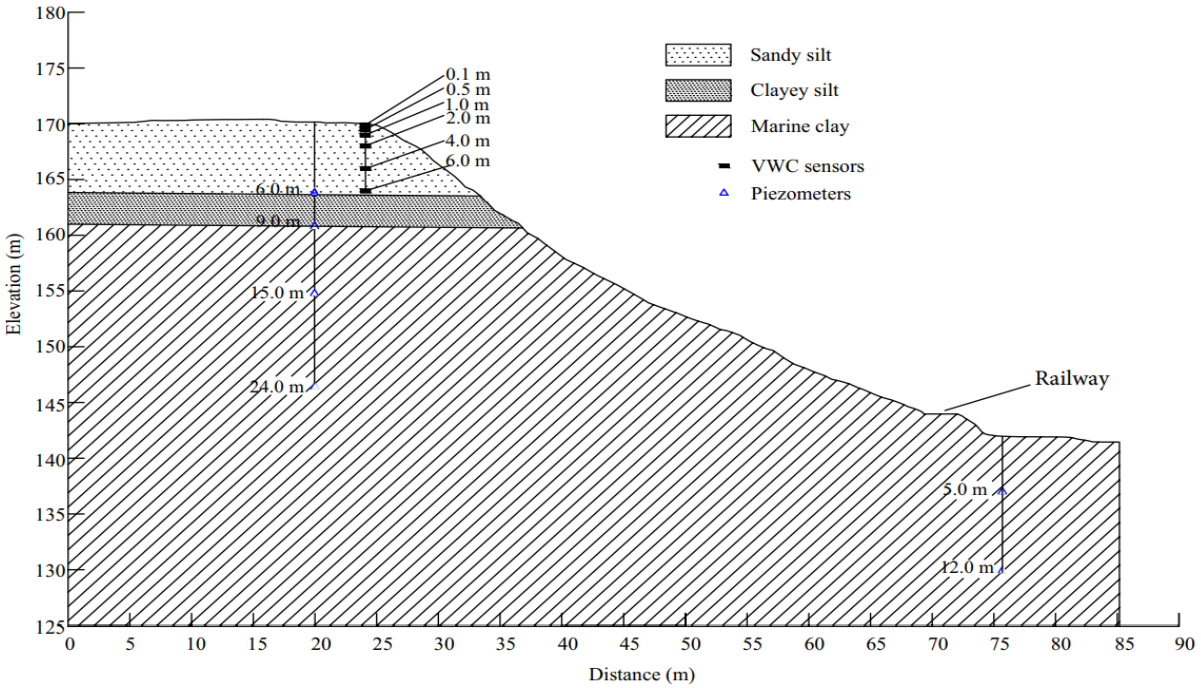

Figure 4-8. *Cross-section of the investigated slope, with soil stratigraphy and sensor locations* ***(****Piciullo et al., 2022a).*

The central Norwegian railroad (Dovrebanen) follows along the base of the slope (Figure 4-9). Landslides are the primary threat at this location and several landslides have impacted the railway in this area (Ch. 4.2). So far, no slope deformation has been observed (Piciullo et al., 2022b); however, the theoretically unstable upper slope with an inclination of > 45˚is of concern.

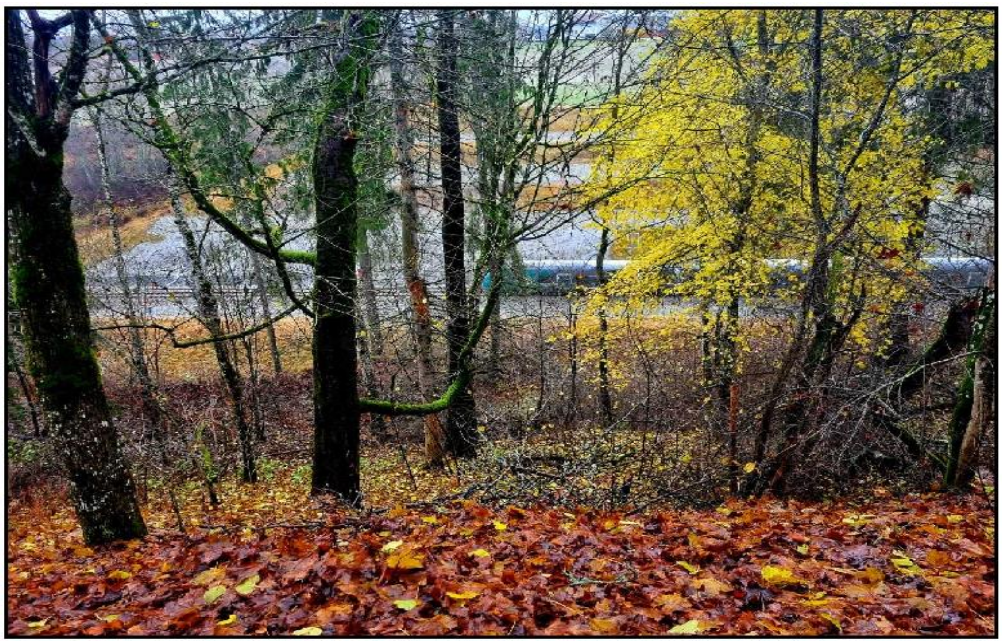

Figure 4-9. *Slope facing east towards the operating railway line "Dovrebanen" (Photo taken during visit to the study area 3.11.22).*

Heyerdahl et al. (2018) conducted a grain size distribution analysis at various depths in the upper layer of approximately 9 m. The results show that the silt fraction increases with depth while the sand fraction decreases (Figure 4-10). Clay content is stable in the entire fraction down to 9 m, while at 10 m depth, the soil is entirely characterized as clay (Figure 4-8). According to Heyerdahl et al. (2018), it may be challenging to characterize the slope for modelling purposes due to the gradual change in grain size distribution and the absence of distinct boundaries.

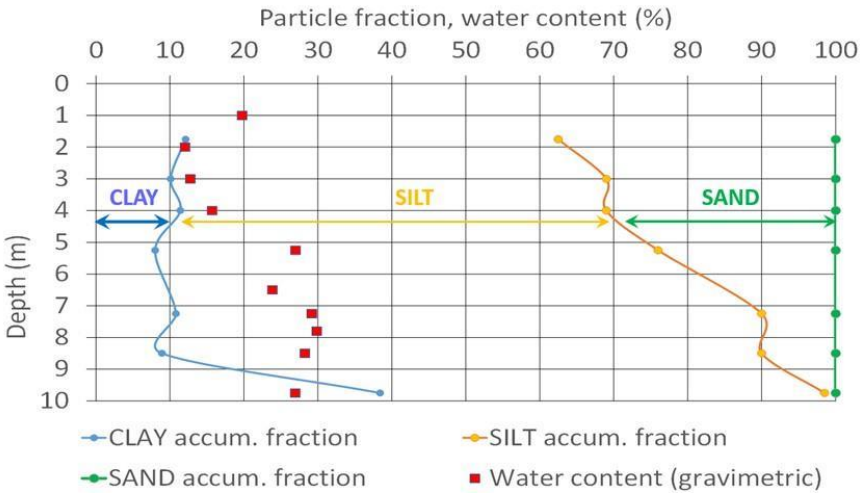

Figure 4-10. *Grain size distribution of sand and silt layer (Heyerdahl et al., 2018)*

4.3.1 Instrumentation and a IoT-based monitoring system

The information in this chapter is collected from Piciullo et al. (2022a, b).

In the spring/summer of 2016, soil water content sensors for monitoring temperature and soil moisture in the unsaturated zone and piezometers for measuring pore-water pressure in all layers were installed at various depths in the slope (Figures 4-8 and 4-11). The combined measurements of soil moisture and temperature sensors were installed at 0.1 m, 0.5 m, 1.0 m, 2.0 m, 4.0 m, and 6.0 m depth (Figure 4-8). The electronical piezometers were installed at 6 m, 9 m, 15 m, and 23 m depths on top of the slope (ca. 171 m.a.s.l.) (Figures 4-8 and 4-11). These depths cover the clay layers (15- and 23 m), the silt layer (6 m), and the transition zone between the silt and clay layers (9 m). Later, two additional piezometers were installed at the toe of the slope (ca. 144 m.a.s.l.) at 5- and 12 m depths. All sensors are connected to a data logger and a solar-powered modem that transmits data for PWP and VWC to Deltalink-cloud software with an hourly monitoring frequency (Figure 4-12) (Piciullo et al., 2022b).

Figure 4-11. *Left: A geotechnical drilling rig was used for the installation of the slope instruments (Heyerdahl et al., 2018). Right: Installed piezometers at 6m, 9m, 15m, and 23 m (photo during visit to the study area 3.11.22)*

Additional instruments were installed on May 27, 2022. A total of six sensors were installed where two sensor types (TEROS 12 and TEROS 21) were coupled for detecting volumetric water content (VWC) and soil suction at three different depths in the unsaturated layer at 0.1 m, 0.5 m, and 0.9 m. By coupling the VWC measurements with the newly installed instruments, the datasets will provide additional information regarding the slope in situ wetting cycles. In addition, a local weather station (ATMOS 41) was installed in June 2022, allowing for more precise measurements of climate variables (Figure 4-12). Data from these instruments were not included in the analysis of this thesis. However, they can improve the modelling and monitoring phase of future evaluations (Ch. 9.1).

Figure 4-12. *Pictures of the installed instruments.*
Left: The Delta-T GP2 datalogger. Middle: Atmos 41 local weather station. Right: Solar-powered 3G/2G Modem Gateway. (Photos taken during visit to the slope 3.11.22).

4.3.2 Slope Vegetation

Large deciduous trees are prevalent in the surroundings of Eidsvoll church (Figure 4-13a). The slope area on the west side of the ravine between Eidsvoll church and the railway line is dominated by a rich deciduous forest, mainly by tall birch trees, mixed grass, and shrubs (Figure 4-13b) (Bratli et al., 2005).

Figure 4-13. *a- Left: Park landscape by Eidsvoll church at the top of the slope area, and b- Right: Dense deciduous forest east of Eidsvoll church and west of the railway where the slope is located (Photos taken during visit to the slope 3.11.22).*

4.3.3 Mitigation work against slope failure in soils

As the 12th-century church and cemetery at the Eidsvoll site is a cultural heritage, physical slope stabilizing measures that change or otherwise impact the landscape must be avoided. There are several different mitigation measures available. This chapter will focus on the mitigation measure that could be relevant at the Eidsvoll site, considering its status as a protected cultural heritage site.

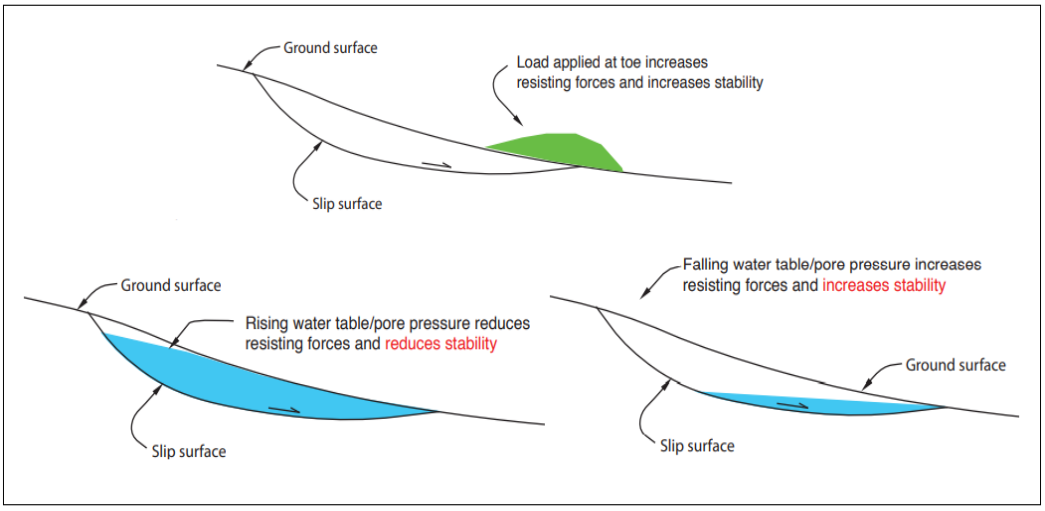

Figure 4-14. *Illustration of how water and applied load may affect slope stability. From Highland and Bobrowsky (2008).*

At Eidsvoll, various strategies for slope stabilization, which do not involve large landscape modifications, could be considered (Highland and Bobrowsky, 2008):

- Channelling surface water away from the slope
- Draining excess water from the slope to reduce the chance of a rising groundwater level
- Weight or retaining structures constructed at the foot of the slope
- Planting or encouraging the natural growth of vegetation

Water or applied load at the toe of the slope may affect slope stability (Figure 4-14). Since removing soil from the top of the slope and lowering the slope's height conflicts with cultural heritage conservation regulations, adding weight to the slope's base may be an alternative. According to Highland and Bobrowsky (2008), it is recommended to use rockfill rather than finer soil materials for slope base filling. Finer soil materials may cause impending groundwater flow, whereas rockfill provides greater frictional resistance to shear forces and higher permeability, allowing water to drain efficiently. Another crucial aspect of a slope stabilization technique is adequate water drainage, which can be handled by surface or subsurface drainage (Figure 4-15). Adequate drainage increases the soil's stability by reducing the weight of the sliding mass and preventing pore overpressure. Subsurface drainage is often associated with slides induced by groundwater. In contrast, surface drainage reduces erosion of the slope's face and limits water infiltration, thereby preventing the build-up of pore water pressures. Because the pore pressure regime influences the slope at Eidsvoll, surface drainage may be appropriate at the site if any mitigation would be considered in the future.

Figure 4-15. *Left: Shallow surface drains. Right: Horizontal subsurface drainpipes for landslide prevention in road construction (Chatwin, 1994).*

4.4 Future climate based on climate models

Annual temperatures have increased in Norway by 1°C during the past 100 years, while precipitation has increased by 18% across the country (Hanssen-Bauer et al., 2015). Climate models project that temperatures and precipitation will continue to increase nationwide in most seasons until the end of the century. Since the research in this master thesis is most concerned with understanding inherent physical risks that future climate may pose to slope stability, the focus has been on the higher-emission scenario, i.e., RCP 8.5 (Figure 4-16). Moreover, utilizing the RCP 8.5 emission scenario enables a comparison of future temperature and precipitation changes between the estimated changes at the Eidsvoll study site and the climate profile expected changes for Oslo and Akershus County (Table 4-4). Appendix D describes how climate projections were made (Appendix D.I) and the various emission scenarios (Appendix D.II).

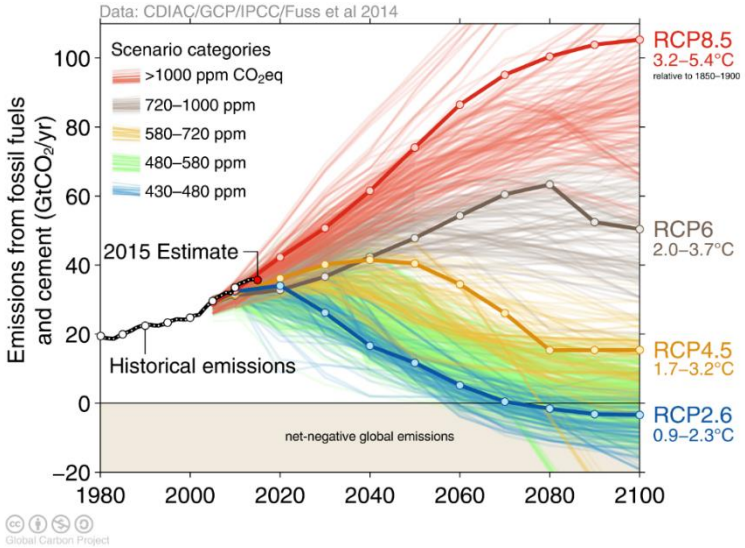

Figure 4-16. *Emissions scenarios for various Representative Concentration Pathways (RCPs) with historical and current emissions overlaid (available at: http://www.globalcarbonproject.org/).*

4.4.1 Future climate predictions for Oslo and Akershus County

This chapter is based on the climate profile for Oslo and Akershus County taken from the Norwegian Centre for Climate Services (NCCS) (klimaservicesenter.no).

Climate profiles have been developed for each county with recommended climate guidelines to estimate, among other factors, intense precipitation (Hanssen-Bauer et al., 2015). These guidelines can contribute to avoid or reduce damage in connection with climate change. Future climate prediction for Oslo and Akershus County indicates a need for adaptation to

climate change since there will be several challenges as more extreme precipitation, floods, and landslides are expected (Figure 4-17). The climate profile focuses on changes towards the end of the century (2071–2100) compared to a reference period 1971–2000. The calculations are based on analyses of downscaled climate models (Appendix D.I), taken from IPCC's fifth main report from 2013 (AR5).

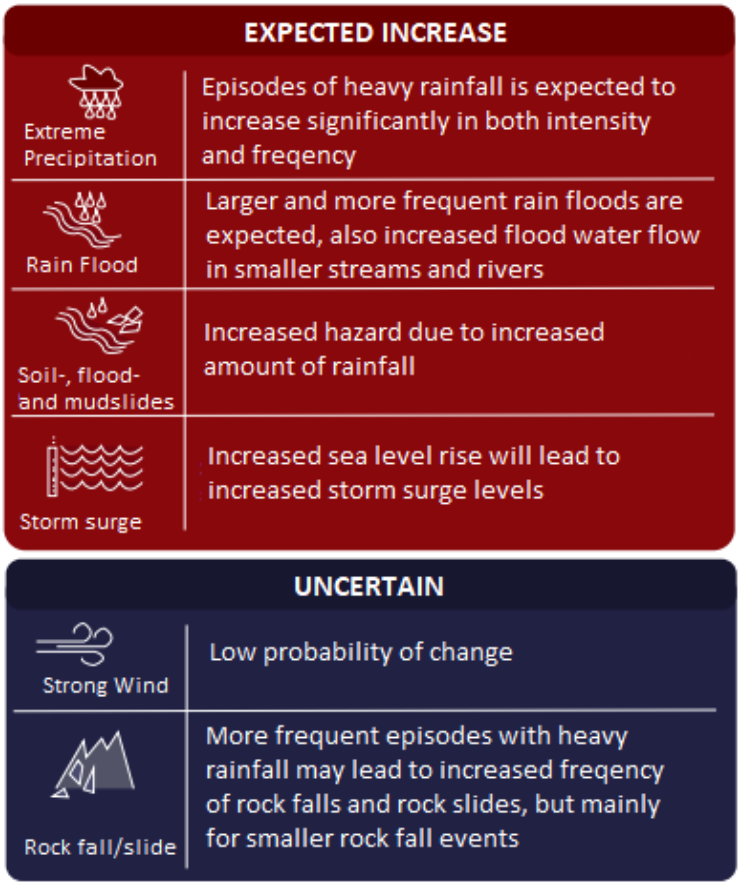

Figure 4-17. *Expected changes for Oslo/Akershus from the reference period 1971–2000 towards the projected period 2071–2100. Changes in climate, hydrological-conditions, and natural hazards relevant to this thesis. Modified from (Klimaservicesenter.no).*

Precipitation and Temperature

Recommendations for estimating climate effects have been developed in response to the predicted increase in extreme rainfall in the future (Table 4-3). The guidelines are meant for overall planning when climate adaptation must be considered. The guidelines for climate effects of heavy rainfall specifies how much today's extreme value should be increased to account for future climate change (Table 4-3). It represents the predicted consequences of climate change for Oslo and Akershus County due to high greenhouse gas emissions (RCP 8.5) until the end of the century.

Table 4-3*. From climate profile Oslo/Akershus- Climate guidance for short-term precipitation as part of climate adaption for Akershus County. The climate guidance is based on the expected change in design precipitation until the end of the century and depends on the duration and design return period.*

	Dimensioning return period < 50 years	Dimensioning return period ≥ 50 years
≤ 1 hour	40 %	50 %
> 1 – 3 hours	40 %	40%
> 3 – 24 hours	30 %	30%

For Oslo and Akershus, the annual amount of precipitation is expected to increase by 15 %, and average annual temperatures anticipate rising by 4 °C, with the most noticeable change for winter and spring (Table 4-4). Rainfall intensity and frequency will increase in all seasons.

Table 4-4. *The climate profile for Oslo/Akershus and the expected annual and seasonal change in precipitation (%), and temperature increase (°C).*

Oslo and Akershus Climate Profile		
	Precipitation (%)	**Temperature (°C)**
Winter	+ 30	+ 4.5
Spring	+ 25	+ 4.5
Summer	+ 5	+ 3.5
Autumn	+ 10	+ 4.0
Annual	**+15**	**+ 4.0**

The expected change (%) in annual (Figure 4-18), and seasonal (Figure 4-19) precipitation for Oslo and Akershus County are based on the reference period 1971-2000 to 2071-2100, using emission scenario RCP8.5. For Eidsvoll, the average annual temperatures and precipitation from the reference period 1971-2000 are 4.3°C and 785 mm, respectively.

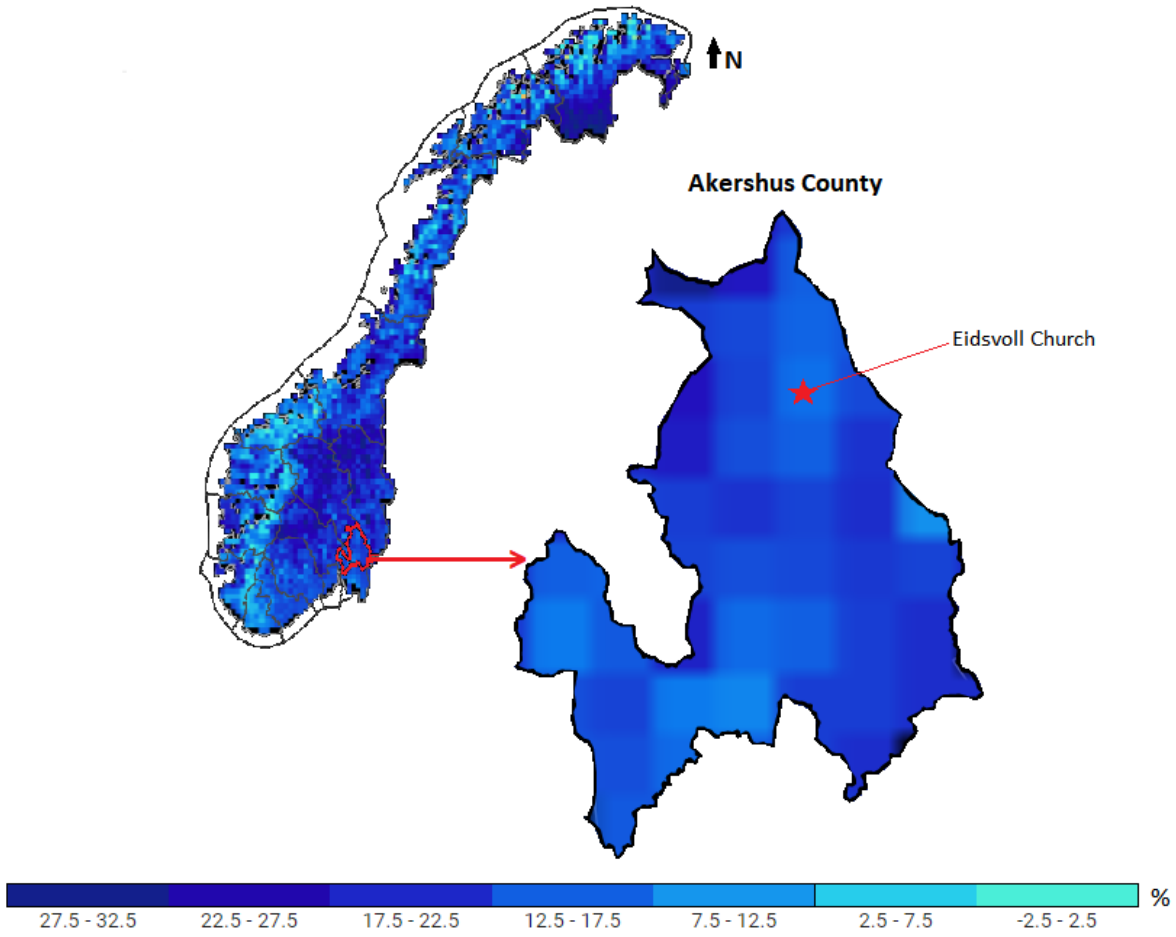

Figure 4-18. *Overview map over Norway and Akershus County where the study area Eidsvoll church is marked. The map shows the annual change in precipitation (%) from the period 1971-2000 to 2071-2100 with emissions scenario RCP8.5. Map is modified from klimaservicesenter.no.*

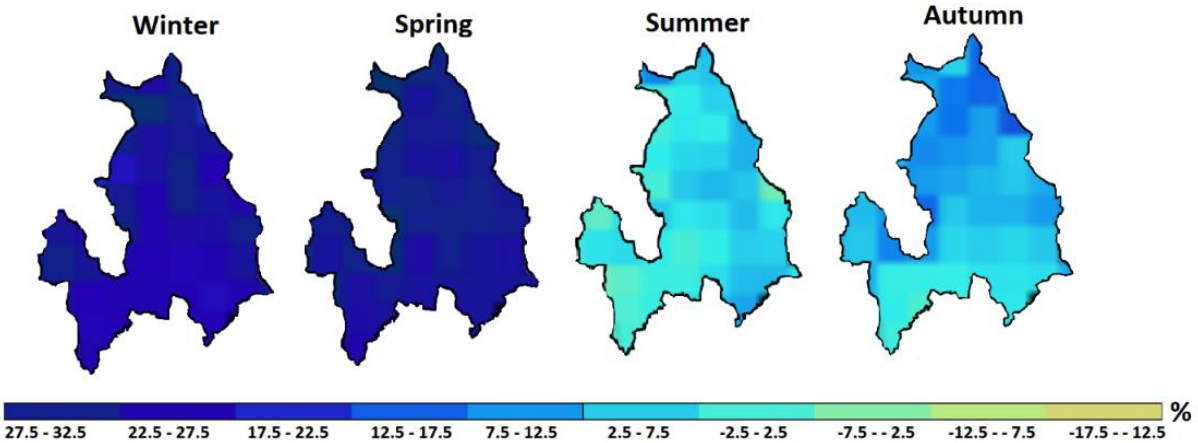

Figure 4-19. *The map shows seasonal change in total precipitation (%) from the period 1971-2000 to 2071-2100 with emissions scenario RCP8.5 for Akershus County. Maps are modified from klimaservicesenter.no.*

Figure 4-20 presents the development of precipitation as deviation (%) from the period 1971-2000 up to 2100.

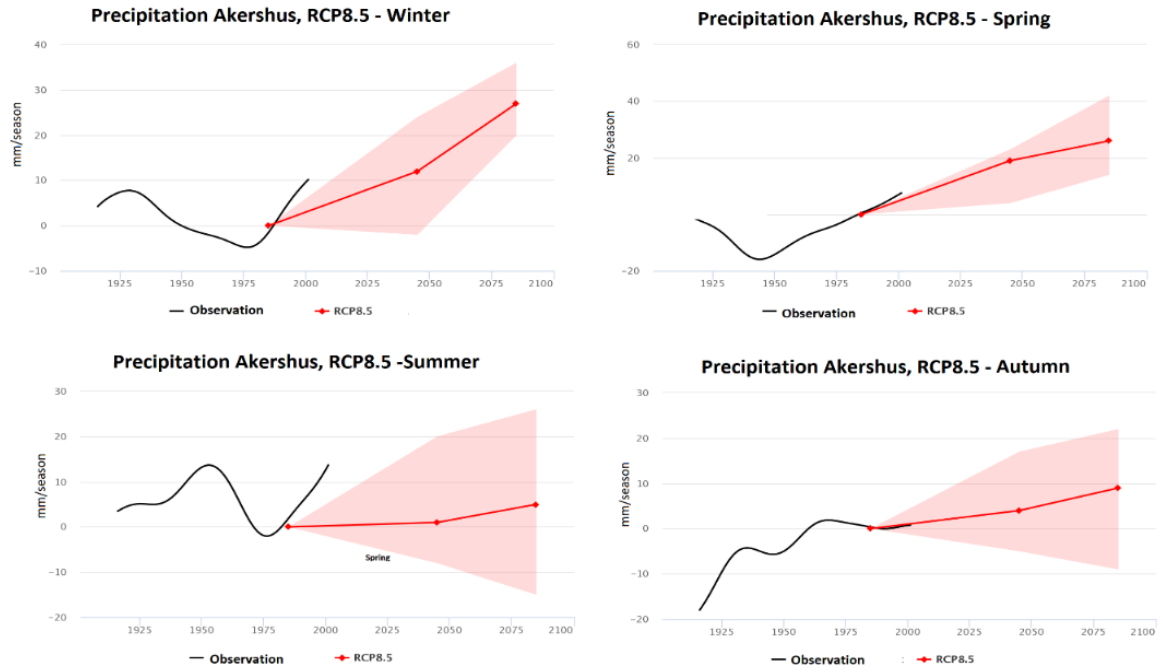

Figure 4-20. *Development of precipitation as deviation (%) from 1971-2000 up to 2100. The black curve represents observational data, smoothed to illustrate variations on a 30-year scale. The colored curve shows the trend in the median value for several RCM simulations, up to 2031-2060 and 2071-2100. The shaded area indicates a spread between low and high climate projections (10 and 90 percentiles). Available at Klimaservicesenter.no.*

Snow

A 2–4-month shorter snow season is anticipated for Akershus County, along with a significant reduction in snowfall frequency and accumulation. However, there will still be years with significant snowfall. Low-lying regions with winter temperatures now hovering around 0 °C will experience the largest reduction. Throughout the winter, there will be increased melting incidents as the temperature rises.

Landslides

Because floods and landslides may become more frequent and more destructive in the future, there is a particular reason for enhanced awareness of these hazards. Although the weather is one of the most critical triggering factors for landslides, the probability of landslides is closely related to the local terrain conditions. In steep terrain, climate change could lead to an increased frequency of landslides linked to downpours/floods and snowmelt, which primarily applies to landslides, flash floods, and debris flows for Akershus County.

5 Eidsvoll slope model set-up and data inputs

A slope stability analysis is performed using the software GeoStudio where the two modules, SEEP/W (Ch.3.1) and SLOPE/W (Ch.3.2), were coupled. These modules are based on the principles described in chapters 2 and 3 and the supplementary theory given in Appendix A. The relevant theory for the two modules used in this analysis is obtained from the GeoStudio textbooks (SEEP/W and SLOPE/W) and presented in Appendix B for the SEEP/W module and Appendix C for the SLOPE/W module. This chapter describes how the soil parameters and slope characteristics were obtained from previous research by Heyerdahl et al. (2018) and Piciullo et al. (2022a, b) and how the final hydrological model was developed.

5.1 Ground conditions and soil properties

Heyerdahl et al. (2018) conducted field investigations in the area and studied the ground conditions by calculating the stability of the slope using unsaturated soil parameters extracted from retention curves measured by pressure plate test and shear strengths by triaxial tests (Table 5-1). Heyerdahl et al. (2018) found that the top layer is 6 meters thick and consists of unsaturated sandy silt. This layer is followed by a 3-meter thick and partially saturated clayey silt layer, which lies above a saturated firm layer of marine clay that continues to great depth.

Table 5-1. S*lope characteristics and material properties used in the analysis, based on the previous work of Heyerdahl et al. (2018) and Piciullo et al. (2022a).*

Layer	**1**	**2**	**3**
Soil type	Sandy silt	Clayey silt	Firm marine clay
Elevation (m)	164-170	161-164	130-161
Layer thickness (m)	6	3	>30
Saturated water content (Lab test) (%)	45	45	-
Range of natural gravimetric water content (%)	12-20	24-29	>29
Conditions	Unsaturated	Unsaturated/saturated	Saturated
Unit weight γ (kN/m^3)	18	18	20
Cohesion c' (kPa)	8	8	5
Friction angle $\varphi' = 2\varphi^b$ (°)	36	32	26

The natural gravimeter water content values were measured on samples at different depths. The material properties for the sandy silt layer and the friction angle for all layers (Table 5-1) are obtained from the research by Heyerdahl et al. (2018). For clayey silt, the material properties were obtained from the literature (Statens Vegvesen, 2018; Melchiorre and Frattini, 2012), and for the clay layer (Table 5-1) (NGI, 2017). The process of acquiring these parameters is described in detail by Heyerdahl et al. (2018) and Piciullo et al. (2022a).

In order to find the shear strength of the material, the shear strength equation for unsaturated soils was used (Eq. 10; Ch. 2.2.4). The soil hydraulic properties were determined through laboratory tests from Heyerdahl et al. (2018), which were used to define the best-fit parameters through the Van Genuchten soil water retention curve equation (Eq. 25; Appendix B.II). Despite determining the SWRCs for the wetting curve being recommended for unsaturated flow conditions, only tests during the drying phase were performed (Heyerdahl et al., 2018; Piciullo et al., 2022a, b). The best-fit parameters (n, m) and scaling factor (α) (Table 5-2), together with saturated hydraulic conductivity (k_{sat}), residual- (θ_r) and saturated water content (θ_s), were used to estimate the actual soil water content (θ) and hydraulic conductivity (k_w) (Eq. 25 and Eq. 26; Appendix B.II).

Table 5-2. *Soil hydraulic properties estimated by laboratory testing and best-fit parameters using the SWRC for the drying phase, determined through research by Heyerdahl et al. (2018) and Piciullo et al. (2022a, b).*

Layer	n	m	$\alpha\ (kPa)$	$\theta_s\ \left(\frac{m^3}{m^3}\right)$	$\theta_r\ \left(\frac{m^3}{m^3}\right)$	$k_{sat}\ \left(\frac{m}{s}\right)$
1	1.9	0.474	5.92	0.45	0.03	2.4E-06
2	1.76	0.432	8.47	0.45	0.03	1.0E-07

5.2 Evaporation flux

SEEP/W module uses, by default, the Penman-Monteith (1948) equation (Eq.28; Appendix B.III) to assess the evaporation flux where a set of meteorological variables and information regarding vegetation are needed (Table 5-3) (Piciullo et al., 2022a, b; Allen et al., 1998). As no specific investigation has been carried out on the slope, reference values are used for the vegetation features, which is further explained by Piciullo et al. (2022a, b).

Table 5-3. *The vegetation features needed as input for the SEEP/W module and the values used for the hydrological model based on previous work by Piciullo et al. (2022a, b).*

Vegetation features	Description	Input
LAI	Leaf Area Index	1.5 summer/ 0 autumn-winter
RD	Root Depth	1 m
PML	Plant Moisture Limit	Default value
NRD	Normalized Root Density	Negative linear trend
SCF	Soil Cover Fraction	1 summer/ 0 autumn-winter
VH	Vegetation Height	3 m

5.3 The hydrological model

The hydrological model used for this thesis was developed by Piciullo et al. (2022a, b) (Figure 5-1). The pore water pressure values monitored from the installed instruments were used to determine an assumed groundwater level at 7 meters depth which follows the topographic contour 1.5 meters beneath the sloping surface. A total of 2460 elements and 2566 nodes, quadrilateral, and triangular elements with a resolution of about 1 meter were applied to discretize the domain (Figure 5-1). Based on the four piezometers installed at the top and the two piezometers installed at the toe of the slope, the initial total head values were defined as 163 m on the left and 142 m on the right side of the model (Piciullo et al., 2022b).

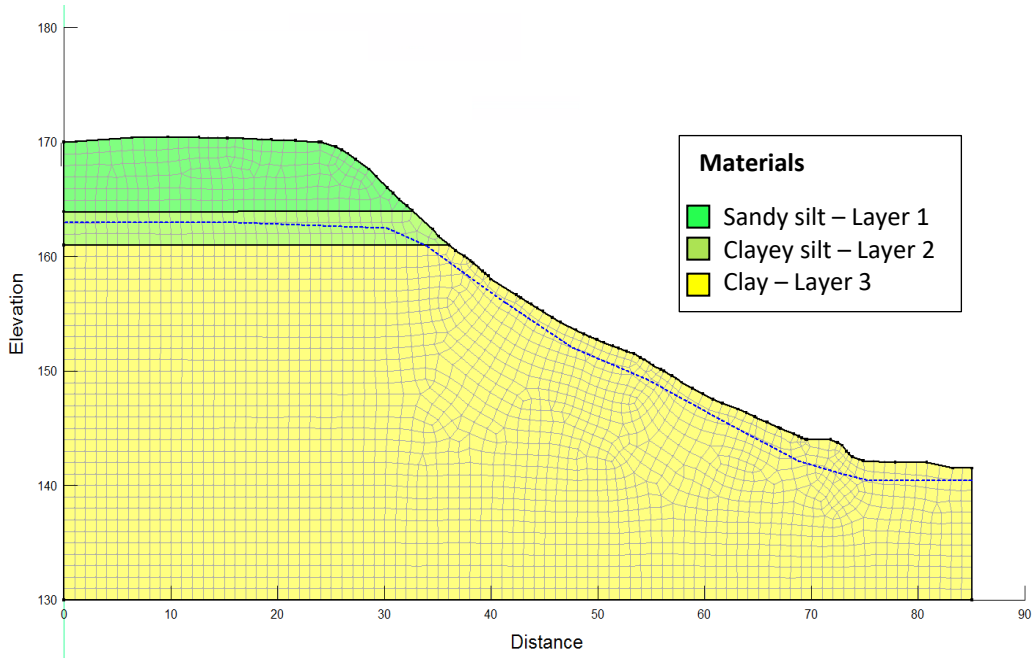

Figure 5-1. *Slope geometry with mesh distribution, material boundaries and the defined groundwater level at 7 meters depth following the sloping surface (Piciullo et al., 2022b).*

5.3.1 Calibration and validation of the hydrogeological model

Piciullo et al. (2022a, b) performed a preliminary hydrological adjustment. A calibrated VWC profile could be obtained by fitting the measured VWC profile with the modelled VWC profile by applying an initial condition of steady-state analysis with a constant surface unit flux. The water flux boundary condition along the slope surface was defined by the monthly rainfall recorded in the month preceding the simulation's initiation. Furthermore, a series of simulations were carried out considering different boundary conditions. The hydrogeological model was validated to determine the simulation that best meets the in-situ conditions. Using Taylor diagrams and linear regression analysis, a comparison was made between predicted and measured VWC for each simulation. Based on these results, the best hydrogeological model was the one that incorporated vegetation (Piciullo et al., 2022a, b). The calibrated and validated hydrogeological model used for the analysis part of this thesis (Figure 5-2), is the one including vegetation (NC_Cl_VE).

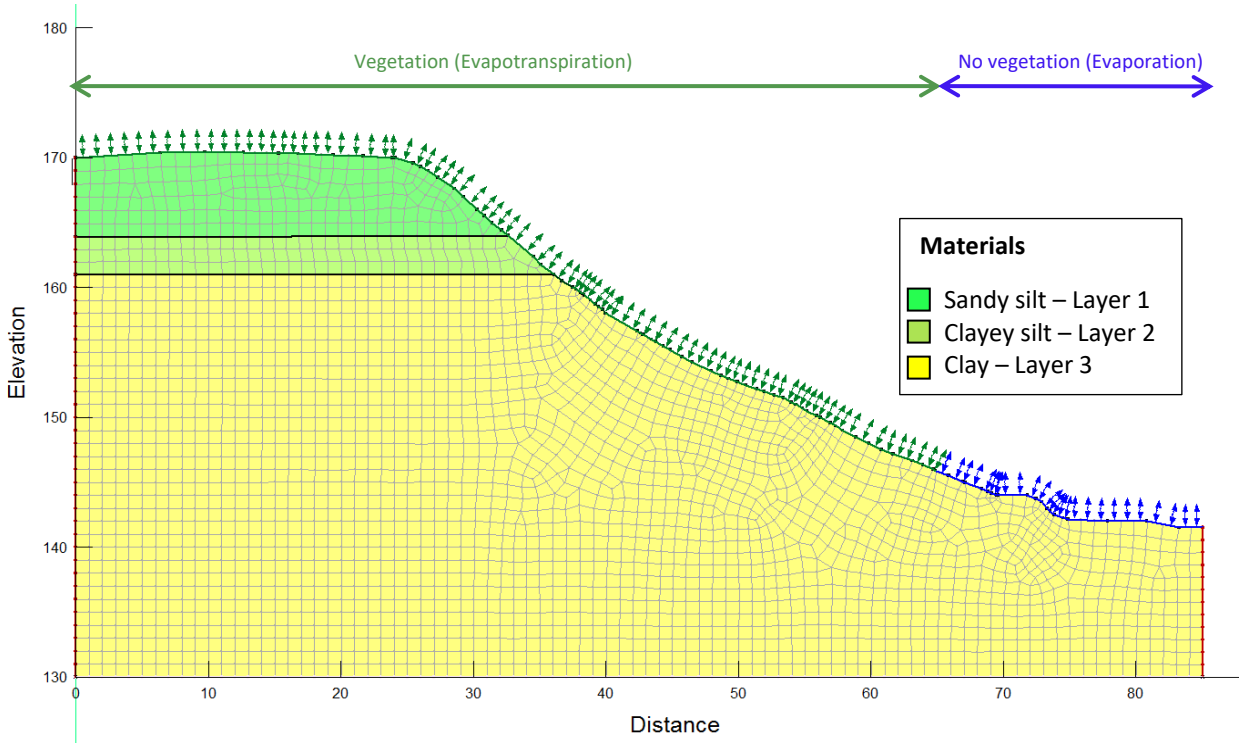

Figure 5-2. *The calibrated hydrological model applied in the simulations, illustrating the boundary conditions for the model including vegetation.*

6 Method

This chapter covers the methods used to evaluate the slope stability at Eidsvoll in terms of future climate change. Initially, a continued sensitivity analysis is conducted to improve the hydrological model further (Ch. 5.3). In order to validate and define input data for the SEEP/W model, various steps are performed;

- Future changes in precipitation and temperature at Eidsvoll are estimated until 2100 and compared with the climate profile estimations for Oslo/Akershus County provided by Klimaservicesenter.no (Table 4-4).
- Water supply and temperature values at Eidsvoll, representing two future periods, 2046-2075 and 2076-2100, are estimated by adding the expected changes to the measured year 2000-2001.
- Water supply and temperature projections until 2100 are derived from one climate model representing two years within each of the estimated intervals (2046-2075 and 2076-2100).

Finally, a slope stability analysis is performed using 1) the estimated changes and 2) one selected climate model's predicted water supply and temperature changes. The slope's water supply and temperature thresholds are also determined based on numerical stress testing using artificial water supply and temperature data for the hydrological model with and without vegetation.

6.1 Sensitivity analysis for VWC and PWP

A sensitivity analysis of the hydraulic conductivity and the anisotropy ratio was conducted based on the best simulation (NC_Cl_VE) of the existing hydrogeological model (Figure 5-1). The predicted volumetric water content (VWC) and pore water pressure (PWP) were compared to the measured values from the instruments at each of the measured depth points (0.1 m, 0.5 m, 1 m, 2 m, 4 m, and 6 m). The effect of permeability was investigated by adjusting the horizontal saturated hydraulic conductivity k_x and the anisotropy ratio between vertical and horizontal hydraulic conductivity $\frac{k\prime_y}{k\prime_x}$ for each of the three layers (Figure 4-8).

Multiple simulations were run in GeoStudio to improve the agreement between measured and predicted values for VWC and PWP. The saturated hydraulic conductivity and the

permeability anisotropy ratio that gave the best fit were then employed as inputs to improve the hydrogeological model before undertaking the stability calculations.

6.2 Historical observation data

The hydrological variables for historical observations were extracted from the daily gridded raster fields on the Norwegian website senorge.no (http://www.senorge.no) (Figure 6-1). SeNorge provides observation-based maps with high-resolution fields of daily total precipitation and daily average temperatures. The maps are based on 3D spatial interpolation from available nearby meteorological stations. The datasets are updated daily and presented on high resolution gridded raster fields (1 km of grid spacing), exhibiting past climate data dating back to 1957 (Lussana et al., 2018). The values for snow water equivalent are based on a snow map model, which uses the precipitation and temperature maps as a basis. The snow model is based on the HBV model (Hydrologiska Byråns Vattenbalansavdelning model) and calculates the snow conditions based on the air temperature and precipitation from each grid field. The HBV model is a rainfall-drainage model that estimates drainage from a watercourse based on recorded rainfall and air temperature (Holmqvist, 2017). When temperatures are below 0.5 °C, the snow model interprets precipitation as snow; otherwise, it is interpreted as rain (Bergstøm, 1995; Saloranta, 2014). Values for snow water equivalent (SWE), temperatures (TM), and precipitation (RR) were extracted for the study site at Eidsvoll (Figure 6-1).

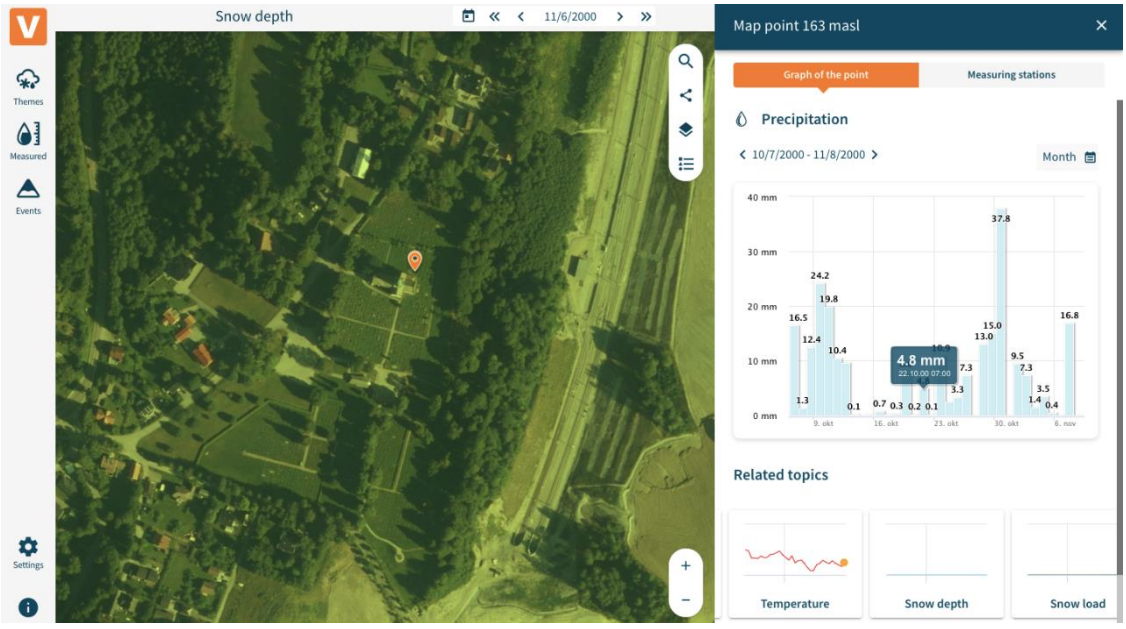

Figure 6-1. *The measured hydrological variables (Snow Water Equivalent, Precipitation and Temperatures) were extracted for the study site at Eidsvoll from the daily gridded raster fields through SeNorge.no.*

6.3 Climate data as input to SEEP/W

According to studies conducted by Piciullo et al. (2022a, b), the accuracy and performance of the hydrological model diminished with time. However, the model's predictions of in-situ conditions are still accurate and satisfactory up to one year before any recalibration is necessary. In order for the SEEP/W model to use climate data as input, the hydrological variables for each simulation must reflect one year. The hydrological model is calibrated with a start time from 3rd June; hence climate data was collected from 3rd June to 2nd June (Figure 6-2). The year 2000-2001 is chosen as a reference year from measured data as this was a year with historically high precipitation levels (Jaedicke and Kleven, 2008). Additionally, this year falls within the reference period for the projected climate data (1971-2000). To account for snowmelt in the computations, precipitation and snowmelt must be coupled as a single input for the hydrological model in GeoStudio. Snowmelt is calculated from the snow water equivalent (SWE), which represents changes in total amount of snow. Snowmelt is found by calculating the difference between yesterday and todays SWE (Figure 6-3). The difference between the SWE is either accumulated or melted snow where only the negative values are considered for the snowmelt, these values are added as positives when estimating water supply (precipitation + snowmelt).

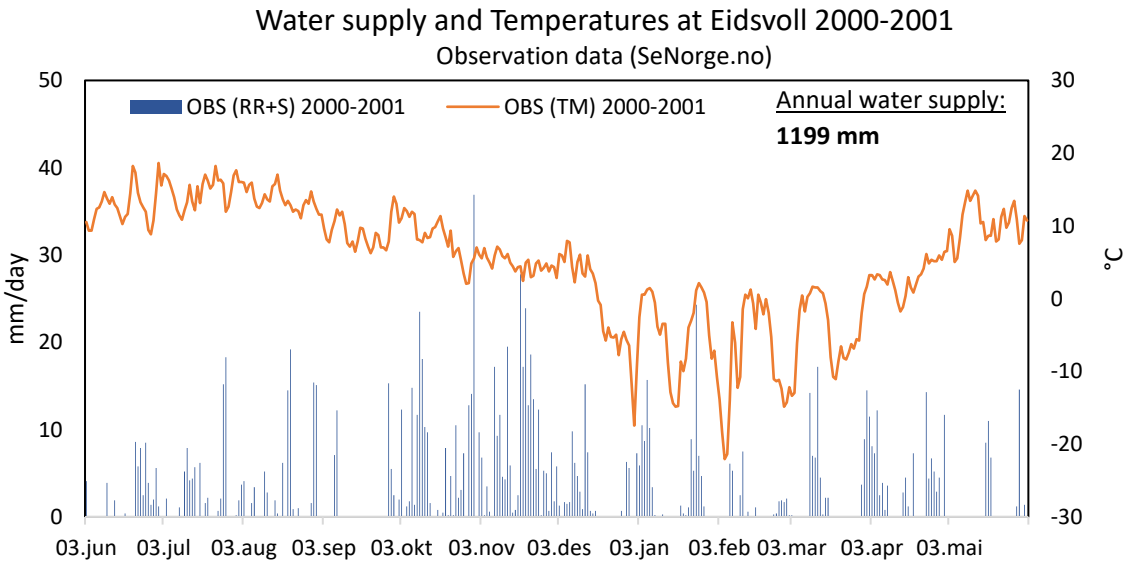

Figure 6-2. *Measure daily water supply and temperature values at Eidsvoll 3rd June 2000 to 2nd June 2001.Collected at SeNorge.no.*

	A	B	C	D
1	Date	SWE (SeNorge.no) Eidsvoll 2000	Accumulated Snow / Snowmelt =(B4-B3)	Snowmelt =IF(C3>0,0,C3)
3	1 Jan	13.8	8	0
4	2 Jan	21.8	6.4	0
5	3 Jan	28.2	1.6	0
6	4 Jan	29.8	-1.6	-1.6
7	5 Jan	28.2	-3.3	-3.3
8	6 Jan	24.9	-3.9	-3.9
9	7 Jan	21	-2.6	-2.6
10	8 Jan	18.4	0.2	0
11	9 Jan	18.6	0	0
12	10 Jan	18.6	0.1	0
13	11 Jan	18.7	0.2	0
14	12 Jan	18.9	0.1	0
15	13 Jan	19	0	0
16	14 Jan	19	0	0
17	15 Jan	19	0	0
18	16 Jan	19	0	0
19	17 Jan	19	0.1	0
20	18 Jan	19.1	1.4	0
21	19 Jan	20.5	0.4	0
22	20 Jan	20.9	0.2	0
23	21 Jan	21.1	1.2	0
24	22 Jan	22.3	9.7	0
25	23 Jan	32	5.8	0
26	24 Jan	37.8	0.9	0
27	25 Jan	38.7	-5.9	-5.9
28	26 Jan	32.8	-4.3	-4.3
29	27 Jan	28.5	-2.4	-2.4
30	28 Jan	26.1	0	0
31	29 Jan	26.1	0	0

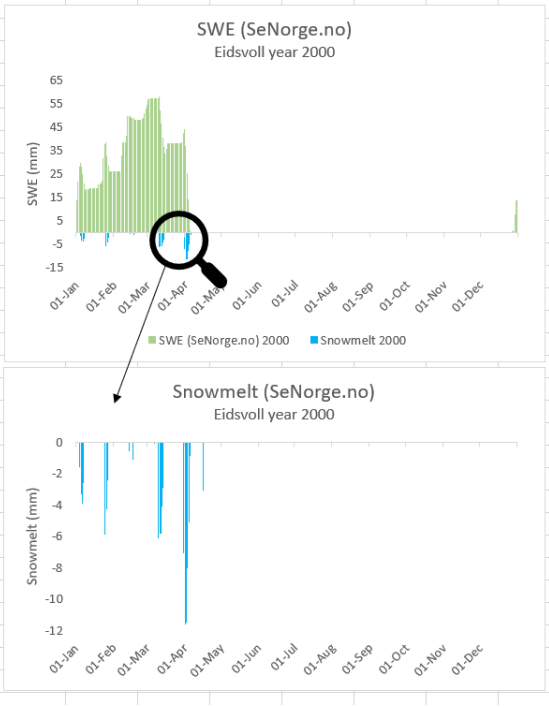

***Figure 6-3**. Illustration of how snowmelt is determined by calculating the difference between yesterday and todays SWE.*

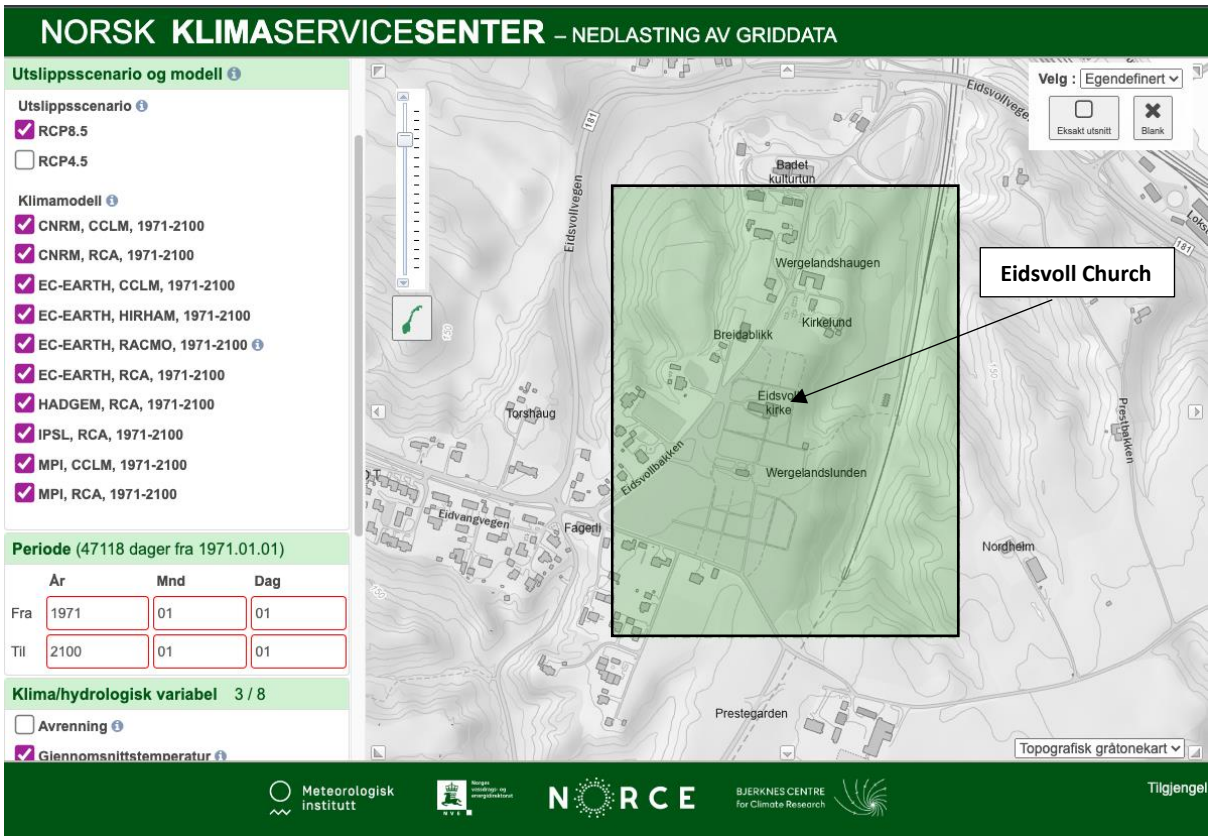

***Figure 6-4.** The hydrological values RR (precipitation), TM (average temperature) and SWE (snow water equivalent), was downloaded for the area marked in green. Data was downloaded from 1971-2100 for all 10 climate models based on emission scenario RCP 8.5. The data is available for download at klimaservicesenter.no.*

6.4 Extracting hydrological variables from projected climate models

The climate projections (Wong et al., 2016; Jacob et al., 2014) downloaded for use in this thesis, are collected online at Klimaservicesenter.no. The climate projections come from an ensemble of ten EURO-CORDEX resulting from five GCM and four RCM combinations (Table 6-1). Due to the Norwegian topography, only the finest grid resolution is used (EUR-11) (Wong et al., 2016). Climate data for precipitation (RR), snow water equivalent (SWE), and the average temperature (TM) were downloaded for the area shown in Figure 6-4. The climate data were downloaded for the time range 1971-2100 for all ten climate models, based on emission scenario RCP 8.5. The hydrological variables for each year and model were imported directly to ArcGIS Pro as netCDF files. Then, the hydrological values from the raster cells encompassing the research region were retrieved for further analysis in Excel.

***Table 6-1**. An overview of the combinations of Global and Regional climate models collected from EURO-CORDEX included in the climate projection from Klimaservicesenter.no.*

Global climate model	Ensemble member	Regional climate model	Time period	Institution
CNRM-CERFACS-CM5	r1i1p1	CCLM4-8-17	1971-2100	Climate Limited-area Modelling Community
CNRM-CERFACS-CM5	r1i1p1	RCA4	1971-2100	Swedish Meteorological and Hydrological Institute
ICHEC-EC-EARTH	r12i1p1	CCLM4-8-17	1971-2100	Climate Limited-area Modelling Community
ICHEC-EC-EARTH	R3i1p1	HIRHAM5	1971-2100	Danish Meteorological Institute
ICHEC-EC-EARTH	r1i1p1	RACMO22E	1971-2100	Royal Netherlands Meteorological Institute
ICHEC-EC-EARTH	r12i1p1	RCA4	1971-2100	Swedish Meteorological and Hydrological Institute
MOHC-HadGEM2-ES	r12i1p1	RCA4	1971-2100	Swedish Meteorological and Hydrological Institute
IPSL-CM5A-MR	r1i1p1	RCA4	1971-2100	Swedish Meteorological and Hydrological Institute
MPI-ESM-LR	r1i1p1	CCLM4-8-17	1971-2100	Climate Limited-area Modelling Community
MPI-ESM-LR	r1i1p1	RCA4	1971-2100	Swedish Meteorological and Hydrological Institute

Due to the large dataset and time-consuming procedures in ArcGIS Pro, the study was continued in a Python software (Spyder 3.9) as both software generated similar findings. A premade script (provided by K. Gisnås, NGI, 2022) was used for extracting the hydrological

values. The downloaded climate data (Figure 6-4) were transformed to a particular coordinate (292500E, 66932500N) for the Eidsvoll slope as JSON files before running the script. Using this script, each climate model could provide the hydrological values at the precise research area coordinates and deliver data for 1971-2100 in a single run. The script was run for all ten models, and the values for precipitation (RR), snow water equivalent (SWE), and average temperature (TM) were further analysed in Excel.

The values from the downloaded data are stored as integers instead of floats. To increase the precision of these values, a scaling factor for each variable needs to be included (Table 6-2). The units for precipitation and snow water equivalent are state variables given in km/m^2which describes the average conditions of the hydrological components in a grid cell with unit mm. As the hydrological data represent daily values, the km/m^2 are equivalent to mm/day (Wong et al., 2016). The unit for average temperature is given in Kelvin which are converted to Celsius after scaling the values.

Table 6-2. *Scaling factors used for the downloaded data.*

Variables		***Scale Factor***	***Unit***
Precipitation	(RR)	0.1	Km/m^2
Snow water equivalent	(SWE)	1	Km/m^2
Average temperature	(TM)	0.1	K

6.5 Validation of projected climate data for SEEP/W model input

As the hydrological model is only verified for one-year simulations, the hydrological input values from the climate projections must reflect one year (Ch. 6.3). However, there are two aspects to consider when using climate projection data:

1. Climate projections are intended to provide statistics until the end of the century rather than weather data in a single year (A. Dyrrdal, pers. Comm., 2022).

2. The climate models interpret the world differently depending on their design and will produce different results; thus, all ten climate models should be combined to compensate for such uncertainties (Nilsen et al., 2022; Wong et al., 2016).

The following strategies are used to account for the suggested applications of climate projection data:

1. To account for statistical climate prediction, the SEEP/W model's hydrological input variables for one year are calculated across 25-30 years (Figure 6-5)

2. All ten climate models may be combined by calculating the median value (Figure 6-6).

A year with daily values of precipitation, snowmelt, and temperatures could be determined (Figure 6-5) by summarizing the same days of each year across a 25- or 30-year period for all ten climate models (Table 6-1). Furthermore, selecting a daily median value over a year could combine the ten climate models (Figure 6-6). These strategies (Figures 6-5 and 6-6) could compensate for the uncertainties of the statistical climate models.

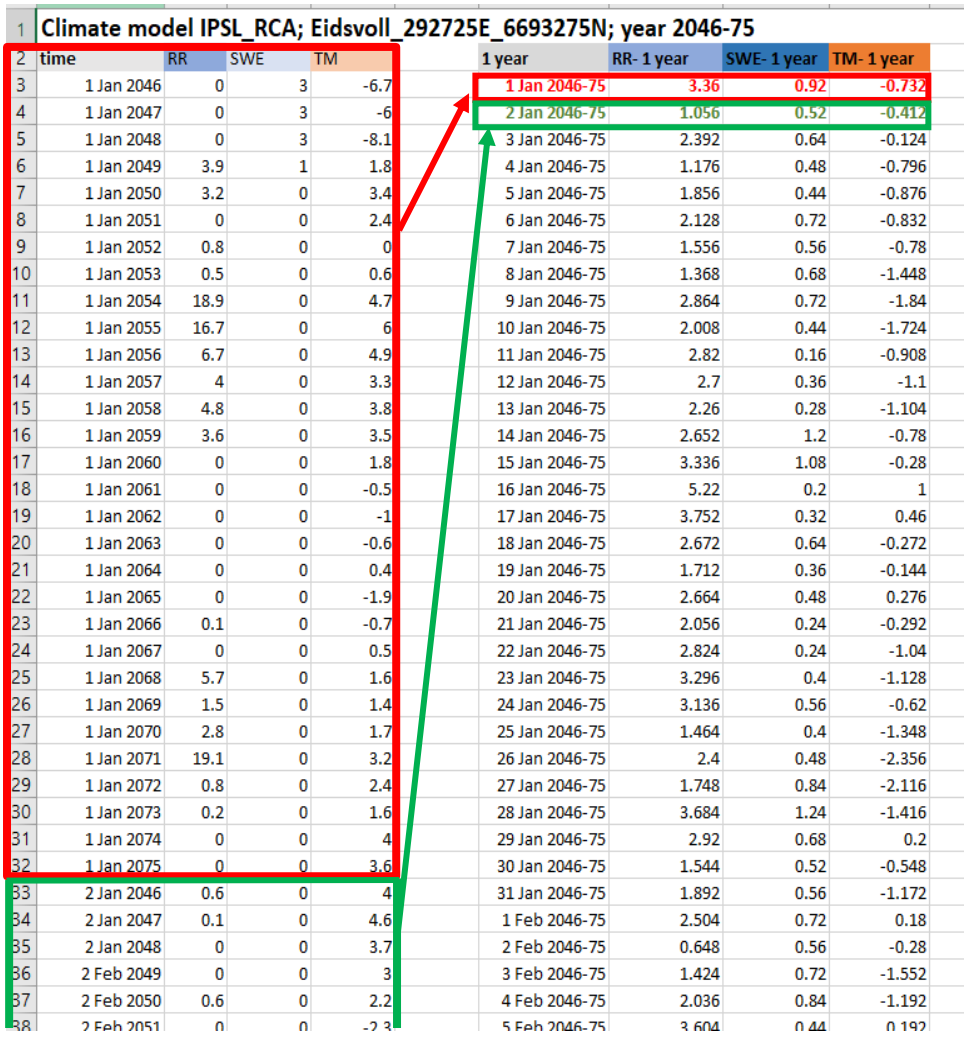

	Climate model IPSL_RCA; Eidsvoll_292725E_6693275N; year 2046-75							
2	time	RR	SWE	TM	1 year	RR- 1 year	SWE- 1 year	TM- 1 year
3	1 Jan 2046	0	3	-6.7	1 Jan 2046-75	3.36	0.92	-0.732
4	1 Jan 2047	0	3	-6	2 Jan 2046-75	1.056	0.52	-0.412
5	1 Jan 2048	0	3	-8.1	3 Jan 2046-75	2.392	0.64	-0.124
6	1 Jan 2049	3.9	1	1.8	4 Jan 2046-75	1.176	0.48	-0.796
7	1 Jan 2050	3.2	0	3.4	5 Jan 2046-75	1.856	0.44	-0.876
8	1 Jan 2051	0	0	2.4	6 Jan 2046-75	2.128	0.72	-0.832
9	1 Jan 2052	0.8	0	0	7 Jan 2046-75	1.556	0.56	-0.78
10	1 Jan 2053	0.5	0	0.6	8 Jan 2046-75	1.368	0.68	-1.448
11	1 Jan 2054	18.9	0	4.7	9 Jan 2046-75	2.864	0.72	-1.84
12	1 Jan 2055	16.7	0	6	10 Jan 2046-75	2.008	0.44	-1.724
13	1 Jan 2056	6.7	0	4.9	11 Jan 2046-75	2.82	0.16	-0.908
14	1 Jan 2057	4	0	3.3	12 Jan 2046-75	2.7	0.36	-1.1
15	1 Jan 2058	4.8	0	3.8	13 Jan 2046-75	2.26	0.28	-1.104
16	1 Jan 2059	3.6	0	3.5	14 Jan 2046-75	2.652	1.2	-0.78
17	1 Jan 2060	0	0	1.8	15 Jan 2046-75	3.336	1.08	-0.28
18	1 Jan 2061	0	0	-0.5	16 Jan 2046-75	5.22	0.2	1
19	1 Jan 2062	0	0	-1	17 Jan 2046-75	3.752	0.32	0.46
20	1 Jan 2063	0	0	-0.6	18 Jan 2046-75	2.672	0.64	-0.272
21	1 Jan 2064	0	0	0.4	19 Jan 2046-75	1.712	0.36	-0.144
22	1 Jan 2065	0	0	-1.9	20 Jan 2046-75	2.664	0.48	0.276
23	1 Jan 2066	0.1	0	-0.7	21 Jan 2046-75	2.056	0.24	-0.292
24	1 Jan 2067	0	0	0.5	22 Jan 2046-75	2.824	0.24	-1.04
25	1 Jan 2068	5.7	0	1.6	23 Jan 2046-75	3.296	0.4	-1.128
26	1 Jan 2069	1.5	0	1.4	24 Jan 2046-75	3.136	0.56	-0.62
27	1 Jan 2070	2.8	0	1.7	25 Jan 2046-75	1.464	0.4	-1.348
28	1 Jan 2071	19.1	0	3.2	26 Jan 2046-75	2.4	0.48	-2.356
29	1 Jan 2072	0.8	0	2.4	27 Jan 2046-75	1.748	0.84	-2.116
30	1 Jan 2073	0.2	0	1.6	28 Jan 2046-75	3.684	1.24	-1.416
31	1 Jan 2074	0	0	4	29 Jan 2046-75	2.92	0.68	0.2
32	1 Jan 2075	0	0	3.6	30 Jan 2046-75	1.544	0.52	-0.548
33	2 Jan 2046	0.6	0	4	31 Jan 2046-75	1.892	0.56	-1.172
34	2 Jan 2047	0.1	0	4.6	1 Feb 2046-75	2.504	0.72	0.18
35	2 Jan 2048	0	0	3.7	2 Feb 2046-75	0.648	0.56	-0.28
36	2 Feb 2049	0	0	3	3 Feb 2046-75	1.424	0.72	-1.552
37	2 Feb 2050	0.6	0	2.2	4 Feb 2046-75	2.036	0.84	-1.192
38	2 Feb 2051	0	0	-2.3	5 Feb 2046-75	3.604	0.44	0.192

Figure 6-5. *Illustration of how daily values across a 30-year period (2046-2075) could be averaged to represent a single year.*

Mean of all climate models; Eidsvoll_292725E_6693275N; year 2046-75; RR (mm/d)											All Climate Models
1 year	IPSL_RCA	CNRM_RCA	CNRM_CCLM	ECEARTH_CCLM	ECEARTH_HIRHAM	ECEARTH_RCA	ECEARTH_RACMO	HADGEM_RCA	MPI_CCLM	MPI_RCA	MEDIAN 2046-75
1 Jan 2046-75	0.9	2.7	2.5	2.0	3.2	2.3	2.3	2.3	1.6	2.9	2.3
2 Jan 2046-75	0.6	2.7	2.9	2.9	1.6	2.4	2.2	1.1	2.2	1.9	2.2
3 Jan 2046-75	2.4	2.0	2.3	1.8	1.9	2.7	1.9	1.8	2.3	2.5	2.1
4 Jan 2046-75	2.7	2.4	2.4	2.5	2.3	2.0	3.4	2.7	3.9	3.3	2.6
5 Jan 2046-75	1.5	2.4	1.9	3.1	3.3	1.7	2.7	2.8	2.1	2.2	2.3
6 Jan 2046-75	2.1	1.2	1.4	1.6	1.0	3.3	2.2	2.3	2.1	2.1	2.1
7 Jan 2046-75	2.3	1.7	1.7	2.3	1.3	2.2	1.9	2.4	2.4	0.6	2.1
8 Jan 2046-75	2.4	2.0	1.6	1.7	2.0	1.3	1.6	2.8	2.1	1.6	1.8
9 Jan 2046-75	2.1	1.5	2.5	2.4	2.9	1.3	2.1	2.8	2.0	2.0	2.1
10 Jan 2046-75	2.5	1.6	1.4	2.0	2.3	1.2	2.1	2.7	2.5	2.1	2.1
11 Jan 2046-75	1.0	2.1	3.6	0.9	1.7	2.4	0.6	3.6	3.2	2.2	2.2
12 Jan 2046-75	2.6	3.5	2.0	1.7	1.6	2.3	1.9	2.1	1.5	2.6	2.1
13 Jan 2046-75	2.0	2.1	1.1	0.9	3.1	1.9	1.4	2.7	0.8	0.9	1.6
14 Jan 2046-75	1.6	1.8	2.0	2.1	3.4	3.0	2.1	1.3	1.8	1.6	1.9
15 Jan 2046-75	2.3	1.5	1.3	0.8	2.2	3.5	1.2	3.0	1.8	2.1	1.9
16 Jan 2046-75	3.1	0.9	0.6	1.8	1.8	1.8	1.2	1.6	1.5	2.0	1.7
17 Jan 2046-75	2.7	0.7	1.0	1.1	3.0	2.5	1.5	0.7	1.8	1.9	1.7
18 Jan 2046-75	3.7	0.9	1.6	1.0	2.5	2.3	0.9	1.3	0.9	0.6	1.1
19 Jan 2046-75	2.5	1.5	1.8	1.1	1.8	1.7	1.5	2.1	1.8	1.7	1.7
20 Jan 2046-75	2.0	2.2	1.8	3.6	2.6	2.4	2.1	1.3	2.1	2.4	2.2
21 Jan 2046-75	2.7	1.7	1.7	2.7	1.0	1.6	2.1	1.8	2.1	2.3	1.9
22 Jan 2046-75	2.3	1.6	1.9	1.9	2.2	2.8	4.0	0.9	1.1	2.1	2.0
23 Jan 2046-75	2.5	1.4	1.7	2.5	3.2	2.3	1.8	1.4	2.2	3.0	2.3
24 Jan 2046-75	3.7	1.9	1.7	2.0	2.2	1.2	1.5	0.7	2.6	2.6	1.9
25 Jan 2046-75	1.6	2.7	2.1	2.1	2.5	1.3	2.1	0.9	2.4	1.8	2.1
26 Jan 2046-75	1.9	1.0	1.4	3.0	1.9	2.1	2.9	1.4	1.0	0.4	1.6
27 Jan 2046-75	2.6	1.1	1.2	1.5	2.4	2.5	1.4	1.4	1.8	1.2	1.5

Figure 6-6. *Illustration of how calculating daily median values over a year could combine the ten climate models.*

Three different years were chosen to represent a reference period (1971-2000), a middle period (2046-2075), and a final period (2076-2100) based on the climate projection data. The goal is to use the hydrological values of these three years as inputs for the hydrological model in GeoStudio to investigate the impact of climate change on slope stability until the end of the century. In this context, the hydrological variables' credibility is further assessed for intended use as SEEP/W model inputs (Ch. 6.5.1 and 6.5.2).

6.5.1 Assessing the credibility of the projected hydrological variables

The average daily values of the hydrological variables calculated from the climate models (Figures 6-5 and 6-6) provide a reasonable annual water supply value (918 mm). However, as a consequence of employing an average value (Figure 6-5), values above 0 mm are provided daily (Figure 6-7).

A daily contribution of snowmelt and/or precipitation results in vastly underestimated values (2-3 mm a day), which do not represent a realistic year for water supply at Eidsvoll (Figure 6-2). Also, the temperatures throughout the year (Figure 6-7) are higher than expected (Table 4-4) compared to measurements at Eidsvoll (Figure 6-2). Another strategy was investigated (in the search for appropriate projected hydrological input values) by following the same approach as the initial (Figures 6-5 and 6-6). However, before combining all climate models,

a maximum is used rather than an average value (Figure 6-5). This approach might provide more accurate daily values for water supply (peaks up to 30 mm); however, the annual water supply (7196 mm) is vastly exaggerated as the values for water supply still appear above 0 mm each day (Figure 6-8). Furthermore, daily temperatures are too high, with no days appearing below 0°C (Figure 6-8).

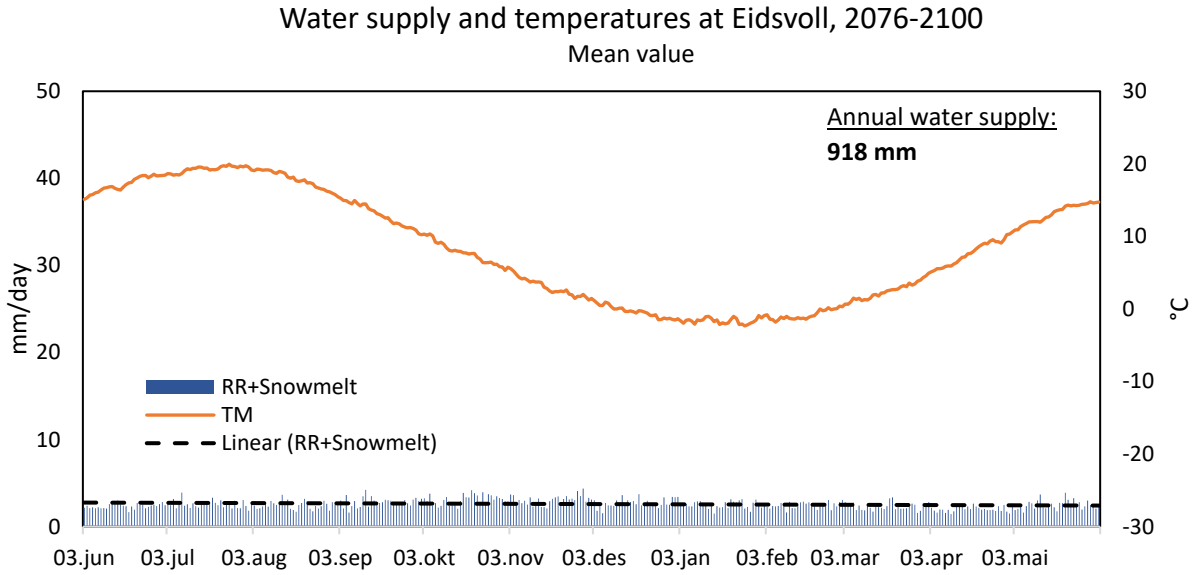

Figure 6-7. *A daily mean value over a year representing the period 2076-2100 combined with all climate models. Very low daily values are provided; however, the annual water supply values (precipitation + snowmelt) are reasonable (918 mm).*

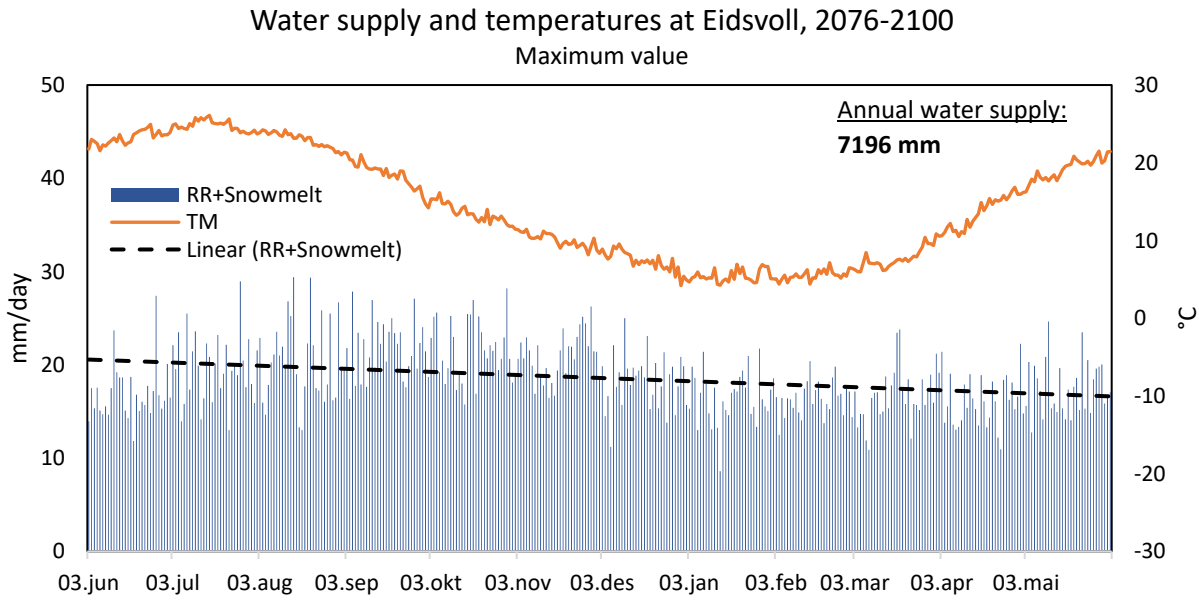

Figure 6-8. *A daily maximum value over a year representing the period 2076-2100 combined with all climate models. Reasonable daily values are provided; however, the annual water supply values (precipitation + snowmelt) are vastly exaggerated (7196 mm).*

As a result of these observations (Figures 6-7 and 6-8), the three projected years (1971-2000, 2046-2075, and 2076-2100) (Ch. 6.5) cannot be directly fed into the hydrological model since they do not provide realistic hydrological values, and further investigation is necessary to validate projected climate data as input for the SEEP/W model.

6.5.2 Eidsvoll climate change estimation and Oslo/Akershus climate profile

The expected annual and seasonal changes in temperature and precipitation are predicted for Oslo/Akershus County until 2100 (Table 4-4) provided by Klimaservicesenter.no. In this context, the annual and seasonal precipitation, snowmelt (Figure 6-3) and temperature changes for Eidsvoll until 2100 were estimated and compared to the expected changes for Oslo/Akershus County. The estimates for Eidsvoll were accomplished by calculating the difference between the year corresponding to the 1971-2000 reference period and the two years representing the future periods, 2046-2075 and 2076-2100 (Figures 6-5 and 6-6). The daily changes in precipitation, snowmelt and temperatures were calculated (Figure 6-9).

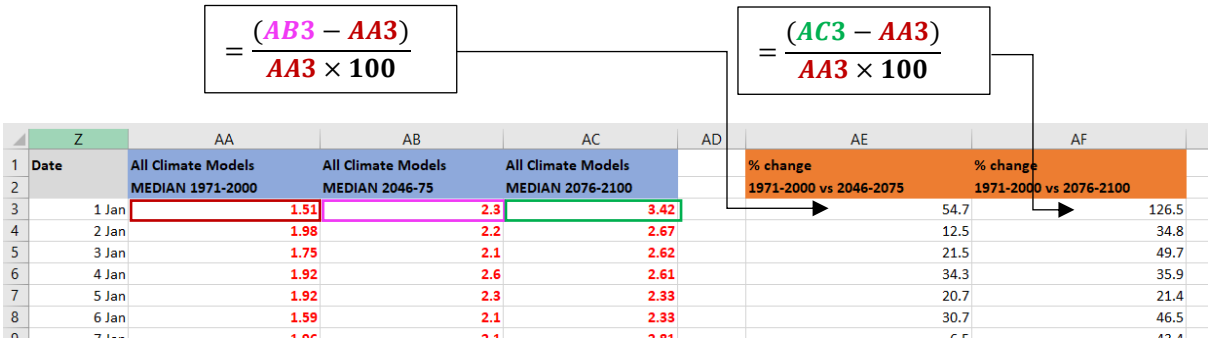

	Z	AA	AB	AC	AD	AE	AF
1	Date	All Climate Models	All Climate Models	All Climate Models		% change	% change
2		MEDIAN 1971-2000	MEDIAN 2046-75	MEDIAN 2076-2100		1971-2000 vs 2046-2075	1971-2000 vs 2076-2100
3	1 Jan	1.51	2.3	3.42		54.7	126.5
4	2 Jan	1.98	2.2	2.67		12.5	34.8
5	3 Jan	1.75	2.1	2.62		21.5	49.7
6	4 Jan	1.92	2.6	2.61		34.3	35.9
7	5 Jan	1.92	2.3	2.33		20.7	21.4
8	6 Jan	1.59	2.1	2.33		30.7	46.5

Figure 6-9. *Future climate values for Eidsvoll were estimated based on the difference between the projected reference year (1971-2000) and the two future years (2046-2075 and 2076-2100). The difference was estimated regarding changes in % for snowmelt and precipitation and in °C for temperatures.*

Based on the difference between the reference year and the two years representing the future periods, changes in precipitation, snowmelt, and temperatures could be estimated and evaluated in %, %, and °C, respectively (Figure 6-9). The years 2046-2075 and 2076-2100 were combined to represent the seasonal and annual changes until 2100 relative to the 1971-2000 reference period at Eidsvoll. This way, the estimated changes at Eidsvoll until 2100 could be compared to those for Akerhus/Oslo (Table 4-4). Furthermore, the precipitation and temperature changes at Eidsvoll may be verified, where the expected changes for the Oslo/Akershus climate profile serve as reference values.

6.5.3 Estimated future climate values based on measured data

To get future climate values, the daily % change in water supply (precipitation+snowmelt) and the °C change in temperatures at Eidsvoll for the two years (2046–2075 and 2076-2100) (Figure 6-9) were added to the 2000–2001 measurements at Eidsvoll (Figure 6-2). Because future water supply values are only estimated for days with water supply above 0 mm (Figure 6-10), the same number of days with water supply as in 2000-2001 are provided, but with different daily values (Figure 6-11). When a % change is added to the measured data to represent the year 2076-2100, the water supply values have increased on most days. However, certain days will have lower water supply values than those observed in 2000-2001(Figure 6-11). Contrary to what the climate models provided (Figures 6-7 and 6-8), this method delivers realistic future daily and annual water supply and temperature values, which could be applied as input values for the SEEP/W model.

$$=\left(\frac{AE3 \times AG3}{100}\right) + AE3$$

$$=\left(\frac{AE3 \times AF3}{100}\right) + AE3$$

	AD	AE	AF	AG	AH	AI
1	Date	Observation RR (mm)	% change	% change	Expected RR (mm)	Expected RR (mm)
2		2000-2001	1971-2000 vs 2046-2075	1971-2000 vs 2076-2100	2046-2075	2076-2100
3	03-Jun	4.1	7.8	8.9	4.4	4.5
4	04-Jun	0.0	65.3	10.6	0.0	0.0
5	05-Jun	0.0	27.6	18.3	0.0	0.0
6	06-Jun	0.0	16.5	23.7	0.0	0.0
7	07-Jun	0.0	-16.0	12.3	0.0	0.0
8	08-Jun	0.0	15.4	15.6	0.0	0.0
9	09-Jun	0.1	66.0	12.9	0.2	0.1
10	10-Jun	0.0	-6.6	-9.7	0.0	0.0
11	11-Jun	3.9	-6.1	20.4	3.7	4.7
12	12-Jun	0.0	29.4	60.8	0.0	0.0
13	13-Jun	0.0	1.4	26.7	0.0	0.0
14	14-Jun	1.9	-17.9	25.3	1.6	2.4
15	15-Jun	0.0	-2.1	25.7	0.0	0.0
16	16-Jun	0.0	16.0	3.6	0.0	0.0
17	17-Jun	0.0	26.4	7.2	0.0	0.0
18	18-Jun	0.4	-2.6	-17.1	0.4	0.3

Figure 6-10. *The future hydrological values were estimated by multiplying the estimated % change (Fig. 6-9) with 2000-2001 measurement data. This figure demonstrates how this was completed for the daily precipitation for the years 2046-2075 and 2076-2100, respectively. For snowmelt, the same procedure was used. The temperature changes in °C were added directly to the 2000-2001 measurement data.*

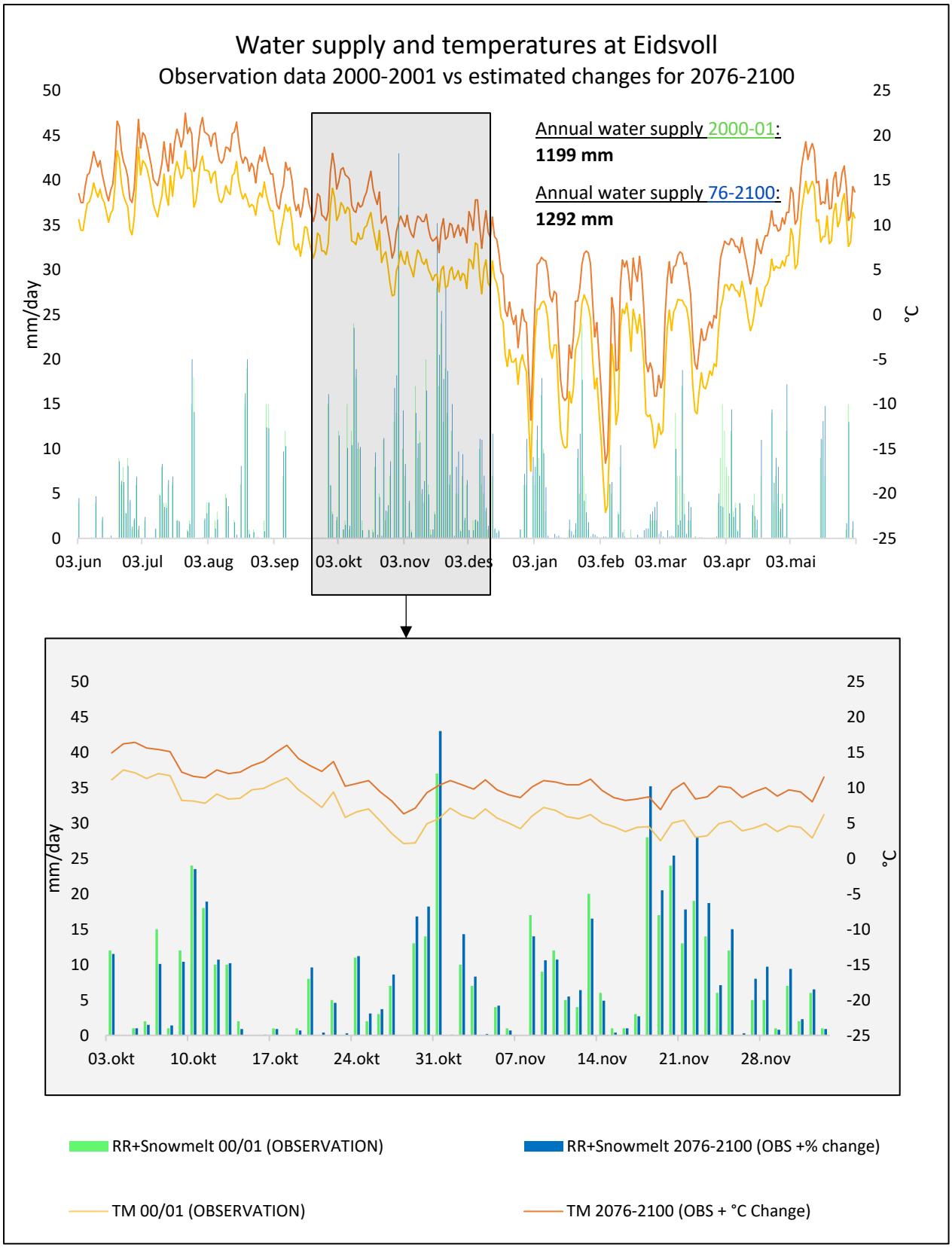

Figure 6-11. Top: *Measured water supply (green) and temperatures (yellow) at Eidsvoll 2000-2001 compared to the water supply- (blue) and temperature changes (orange) added to the 2000-2001 measurements to represent the year 2076-2100.* ***Bottom:*** *A closer view of the data (3 October-3 December), Although values for water supply have increased on most days for 2076-2100, some days will have lower values for water supply than those measured in 2000-2001 (Fig. 6-10).*

6.5.4 Selecting a climate model based on estimated climate changes

The measured annual water supply for 2000-2001 and the estimated annual water supply for the two years 2046-2075 and 2076-2100 (Ch. 6.5.3) were compared with the annual water supply predicted by each climate model (Table 6-1) for corresponding years (Table 6-3). The measured year 2000-2001 were compared to climate model predictions for the same year, representing the reference period. For the estimated year representing 2046-2075, each climate model for the years within the interval 2046-2075 was evaluated. The same approach was carried out for 2076-2100 (Table 6-3). The purpose was to determine which climate model best predicts the annual values for water supply corresponding to the estimated intervals (Ch. 6.5.3). Climate model's predicted seasonal temperatures were also compared to the estimated seasonal temperatures (Ch. 6.5.3). The goal was to validate a set of input values predicted by a single climate model that could best represent a year within each of the estimated intervals.

Table 6-3. *Annual water supply (mm) predictions for the years 2076-2100 for each climate model.*

Year RR+S	CNRM_ CCLM	CNRM_ RCA	MPI_C CLM	HIRH AM	IPSL _RCA	RAC MO	MPI_ RCA	HAD GEM	EC_R CA	EC_C CLM
2076-77	1112	969	967	1018	1012	916	935	790	824	846
2077-78	1058	1067	1161	1229	1303	985	920	871	971	1273
2078-79	1252	1010	1128	863	975	1140	1184	1203	581	854
2079-80	1042	861	1193	870	998	1276	1085	1262	852	1052
2080-81	1118	822	1032	884	1003	920	1105	954	1093	1271
2081-82	770	697	962	889	1221	936	1042	1095	665	715
2082-83	1046	930	1084	1198	1158	819	1022	882	1073	1151
2083-84	807	812	1192	1273	1180	999	1130	922	829	791
2084-85	1195	1078	1081	1364	919	1194	1124	1035	1000	838
2085-86	805	1071	1053	1153	1085	1004	1019	1214	701	690
2086-87	1034	848	856	800	888	1071	891	1076	1198	1313
2087-88	1047	1140	825	1245	1282	833	793	1226	1018	1114
2088-89	1039	1187	1031	954	916	1004	796	1002	833	645
2089-90	1038	982	893	796	1026	1015	899	1055	882	1022
2090-91	1068	1084	1343	970	1130	1067	1338	891	761	754
2091-92	1218	877	1175	1144	1001	1184	875	1031	1028	847
2092-93	1193	1361	1228	1054	1073	1035	972	794	904	1028
2093-94	1097	831	1073	919	968	1037	1023	979	989	950
2094-95	1238	994	1128	1057	860	1048	1070	1170	819	895
2095-96	1225	1295	1159	925	1170	1130	816	863	928	1211
2096-97	1065	797	1048	1131	1475	658	936	897	1022	897
2097-98	1033	816	1032	1240	1049	964	861	1055	1085	1122
2098-99	846	848	1431	1356	989	1094	1203	1271	1004	1125
99-2100	1190	937	1081	659	1189	896	979	1486	889	943

6.6 Other climate drivers as input

To compute evaporation flux under climate boundary conditions, meteorological variables such as solar radiation, albedo, wind speed, and relative humidity are needed as input for the SEEP/W model (Appendix B.III). The meteorological variables for relative humidity and windspeed were provided by the visual crossing's website (visualcrossing.com), which uses the closest available weather station (EW4699 Eidsvoll). Visual Crossing collects historical weather data using the Integrated Surface Database (ISD) from National Oceanic and Atmospheric Administration (NOAA) and real-time weather history data from the Meteorological Assimilation Data Ingest System (MADIS) weather observations database. The dataset contains sub-hourly, hourly, and daily weather observations from meteorological stations throughout the globe. ISD datasets use the nearest station (or group of stations) to the intended site to deliver records for that location (Wigmore, 2019). The solar radiation was computed by the SEEP/W model, and the albedo was estimated using values from the literature.

6.6.1 Estimated solar radiation flux

SEEP/W provides an option to select incoming solar radiation flux so that net radiation is calculated during solve-time. An albedo function must be defined such that the net solar radiation can be calculated as:

$$\boldsymbol{q_{ns} = (1 - \alpha)_{q_s}} \qquad \textbf{(15)}$$

Where, q_{ns}, is the net solar radiation reaching earth's surface (direct and diffuse), also known as short-wave radiation q_s. The solar radiation is measured on a horizontal surface and the albedo, α, is often based on field measurements or estimated from literature values, the latter is the case for this analysis where the albedo values are estimated from Cherubini et al. (2017).

The net longwave radiation is computed using the equation given by (van Bavel and Hillel, 1976):

$$\boldsymbol{q_{nl} = \varepsilon_s \sigma {T_g}^4 - \varepsilon_a \varepsilon_s \sigma {T_a}^4} \qquad \textbf{(16)}$$

$\varepsilon_a = air\ emissivity, T_a = air\ temperature, \varepsilon_s = surface\ emissivity,$
$\sigma = Stefan\ Boltzmann\ constant, T_g = absolute\ temperature\ of\ the\ surface$

The net radiation is calculated as the difference between net shortwave and net longwave radiation by the surface energy balance equation as follows:

$$(\boldsymbol{q_{ns} - q_{nl}}) = \boldsymbol{q_{sens} + q_{lat} + q_g} \quad \textbf{(17)}$$

Where q_{ns} is net solar (shortwave) radiation, q_{nl} is net terrestrial (longwave) radiation, $(q_{ns} - q_{nl})$ is net radiation, q_{sens} is sensible heat flux, q_{lat} is latent heat flux, q_g is ground heat flux.

6.7 Simulations combining SEEP/W and SLOPE/W modules

In previous research by Piciullo et al. (2022a, b), the hydrological model was constructed and calibrated using the numerical software GeoStudio. For this master's thesis, a sensitivity analysis was conducted to improve the agreement between measured and predicted values for volumetric water content (VWC) and pore water pressure (PWP) in the hydrological model (Ch. 6.1). The hydrological model is used for simulating the variation of the hydrological parameters in the slope from estimated and projected future climate scenarios (Ch. 6.5). The two modules, SEEP/W and SLOPE/W are combined to determine the influence of climate drivers on slope stability, such as air temperature, relative humidity, solar radiation, albedo, wind speed, vegetation, rainfall, and snowmelt at a 24h time interval (Figure 6-12). Transient seepage (Ch. 2.2.5) is analysed using the powerful 2D finite element module SEEP/W (Ch. 3.1 and Appendix B) for unsaturated groundwater flow in porous soil. The transient seepage analysis identifies pore-water pressure distribution (PWP) and variations in soil volumetric water content (VWC) over time. The SEEP/W transient analysis is then used as input in the form of pore-water pressure (PWP) distribution for the slope stability analysis performed in the SLOPE/W module (Ch. 3.2). The SLOPE/W module uses the limit equilibrium method (LEM) (Appendix C.I), for calculating the Factor of Safety, assuming the circular rotational failure model proposed by Morgenstern-Price (1965). When calculating the Factor of Safety in granular soil, the slippery mass should be divided into an optional number of slices. Internal forces and inter-part forces are then obtained for each slice (Appendix C.II). The more slices, the higher degree of accuracy is achieved. A conceptual illustration of the coupled analysis of SEEP/W and SLOPE/W are shown in Figure 6-12.

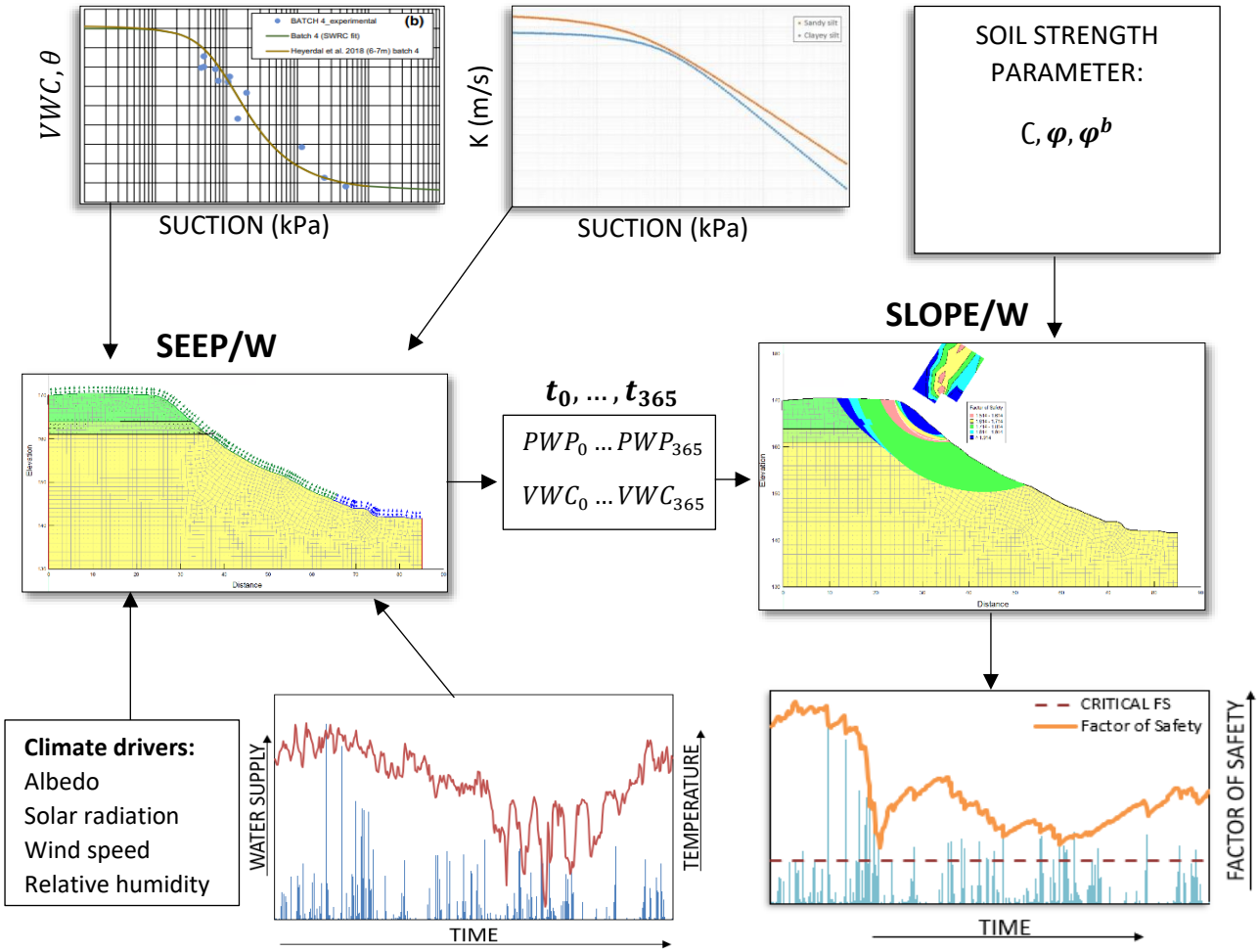

Figure 6-12. *Illustration of coupled analysis of SEEP/W and SLOPE/W created by Falkeid, inspired by Suryo et al. (2013).*

6.7.1 Slope stability at Eidsvoll based on future climate until 2100

Investigations on how climate until 2100 influences slope stability at Eidsvoll (Ch. 6.5.3 and 6.5.4) at 24-hour intervals over a year will be considered through six simulations (Table 6-4):

- The 2000-2001 reference period, based on measured A) and projected B) climate data for water supply and temperatures.
- Future estimated C) and projected D) water supply and temperature data for a future year representing 2046-2075.
- Future estimated E) and projected F) water supply and temperature data for a future year representing 2076-2100.

Table 6-4. *Input methods for simulations conducted to investigate the influence of future climate on slope stability at Eidsvoll.*

Simulation	*Input*	*Source*
A	Measured year 2000-2001	SeNorge.no (Ch. 6.2)
B	Projected year 2000-2001	Climate Model (Ch 6.5.4)
C	Estimated climate change 2046-2075 (%, °C)	(Ch 6.5.3)
D	Projected year within the period 2046-2075	Climate Model (Ch 6.5.4)
E	Estimated climate change 2076-2100 (%, °C)	(Ch 6.5.3)
F	Projected year within the period 2076-2100	Climate Model (Ch 6.5.4)

6.7.2 Slope stability based on numerical stress-tests of artificial data

By investigating the possible effects of climate change on slope stability in connection to extreme events, thresholds can be defined using artificial data during stress testing. The artificial data is based on historical observation data from 3rd June 2000 to 2nd June 2001, where values progressively increase through 14 simulations by a 10-350% increase for daily water supply and through 14 simulations by a 1-30°C rise of daily temperatures (Table 6-5). First, water supply and temperatures impact on slope stability are considered separately. Then, simulations combining water supply and temperatures are conducted using the hydrological model with and without vegetation (Table 6-5).

Table 6-5. *Simulations conducted for stress-testing slope stability at Eidsvoll.*

Simulation input	*Quantity*
10-350% increasing water supply	14
1-30°C increasing temperatures	14
Water supply and temperature increase (10-350%, 1-30°C) - Vegetation	14
Water supply and temperature increase (10-350%, 1-30°C) - No Vegetation	14
Total simulations	**56**

7 Results

This thesis builds on the study conducted by Piciullo et al. (2022a, b). In particular, the hydrological model (Piciullo et al., 2022a, b) was used to assess the effects of climate change on slope stability at Eidsvoll. The unique aspect of the present study is the analysis of how future climate influences the slope conditions at Eidsvoll in terms of the development of porewater pressures and volumetric water content until 2100. Future climate variables are extracted from climate projections based on the RCP 8.5 emission scenario and included in the hydrological model as inputs. Then, by combining the hydrological model with a slope model, the influence of future climate on slope stability until 2100 could be evaluated. The sensitivity analysis conducted by Piciullo et al. (2022a) was also continued. The intention was to further improve the hydrological model by determining new input values for hydraulic conductivity and anisotropy ratio.

7.1 Sensitivity analysis on the hydraulic conductivity and anisotropy ratio

Due to the gradual change in grain sizes within the slope layers (Ch. 4.3), a sensitivity analysis on the hydraulic conductivity and the anisotropy ratio was conducted (Piciullo et al., 2022a) to define the input data and improve the model's reliability. In this thesis, the sensitivity analysis was continued to further improve the hydrological model and to investigate how changes in anisotropy ratio and hydraulic conductivity in layer 3 influence the predicted PWP and VWC in layer 1 and the interface between layers 1 and 2. A portion of the 110 simulations (Appendix E; Table E-1) conducted are presented (Table 7-1).

At 6 meters depth (interface between layer 1 and layer 2), sensors are located in the water table's fluctuation zone, which shows long-term variations compared to the shallower layers. The simulations (Table 7-1) are mainly compared with the measurements at 6m depth (Figure 7-1), allowing for both variables (PWP, VWC) to be analysed simultaneously. The sensitivity analysis compares predicted and measured PWP and VWC through observations from each simulation. Adjusting the saturated hydraulic conductivity for all three layers (Figure 7-1a, c) yielded the hydraulic conductivity values that could best predict the shape of the PWP and VWC curves compared to the measured curves. The hydraulic conductivity providing the best fit was used when adjusting the anisotropy ratio, which improved the timing of the predicted PWP and VWC curves to the measured ones.

Table 7-1. *List of the selected simulations used to present the results of the sensitivity analysis. The simulations were carried out varying the saturated horizontal hydraulic conductivity and the anisotropy ratio for layer 1 (6m sandy silt), layer 2 (3m clayey silt) and layer 3 (marine clay). The saturated horizontal hydraulic conductivity varies in simulations 67, 68, 69, 70, and 72, whereas the anisotropy ratio varies in simulations 47, 51, 60, and 43. The hydraulic conductivity and anisotropy ratio of layer 3 was evaluated further based on simulation 47-1 to 47-6.*

ID	k'_y/k'_x **ratio**			$k_{x,sat}$ *(m/s)*		
	Layer 1	**Layer 2**	**Layer 3**	**Layer 1**	**Layer 2**	**Layer 3**
67	1.25	0.75	1	5.00E-06	5.00E-07	5.00E-10
68	1.25	0.75	1	3.00E-06	5.00E-07	5.00E-10
69	1.25	0.75	1	1.00E-06	5.00E-07	5.00E-10
70	1.25	0.75	1	5.00E-06	1.00E-07	5.00E-10
72	1.25	0.75	1	5.00E-06	9.00E-07	5.00E-10
47	1.5	1.25	1	5.00E-06	5.00E-07	5.00E-10
47-1	1.5	1.25	1	5.00E-06	5.00E-07	5.00E-09
47-2	1.5	1.25	1	5.00E-06	5.00E-07	5.00E-11
47-3	1.5	1.25	0.5	5.00E-06	5.00E-07	5.00E-09
47-4	1.5	1.25	0.5	5.00E-06	5.00E-07	5.00E-11
47-5	1.5	1.25	0.25	5.00E-06	5.00E-07	5.00E-09
47-6	1.5	1.25	0.25	5.00E-06	5.00E-07	5.00E-11
51	1	1	1	5.00E-06	5.00E-07	5.00E-10
60	1.75	1.25	1	5.00E-06	5.00E-07	5.00E-10
43	2	1.5	1	5.00E-06	5.00E-07	5.00E-10

7.1.1 Changing the saturated hydraulic conductivity, $k_{x,sat}$

Typically, the saturated hydraulic conductivity varies from E-03 to E-07 m/s for sandy silt (layer 1), E-07 to E-10 m/s for clayey silt (layer 2), and E-09 to E-13 m/s for marine clay (layer 3) (Freeze and Cherry, 1979) (Appendix A.II; Figure A-3).

In the simulations 67, 68, and 69 (Figure 7-1a, c), when only decreasing the hydraulic conductivity in layer 1, from 5E-06 to 3E-06 and 1E-06 (m/s), the infiltration rate in layer 1 reduces, which causes the VWC at 6 m to decrease (Figure 7-1a). Consequently, a delayed response in the VWC and PWP results in lower predicted values than measured values.

When comparing simulations 67 and 70 (Figure 7-1a, c), by lowering the hydraulic conductivity in layer 2 from 5E-07 to 1E-07 (m/s), the infiltration rate in layer 2 reduces and causes water to accumulate at the interface between layers 1 and 2. In this condition, simulation 70 reveals a higher VWC (Figure 7-1a) and PWP (Figure 7-1c) but a less accurate curve shape at 6 meters depth than simulation 67.

Increasing the hydraulic conductivity of layer 2 from 5E-07 to 9E-07 (m/s) in the simulations 67 and 72 (Figure 7-1a, c) leads to a higher infiltration rate between layers 1 and 2, resulting in underestimated PWP (Figure 7-1c) and VWC (Figure 7-1 a) values at 6m. In contrast to simulation 70, the peak is reduced, and the shape is smoother in simulation 72 as the curve is less steep and better replicates the shape of the measured data for both VWC (Figure 7-1a) and PWP (Figure 7-1c). Changing the hydraulic conductivity in layer 2 has influenced only the deepest VWC sensor, located at 6m (Figure 4-8), at the interface between layers 1 and 2.

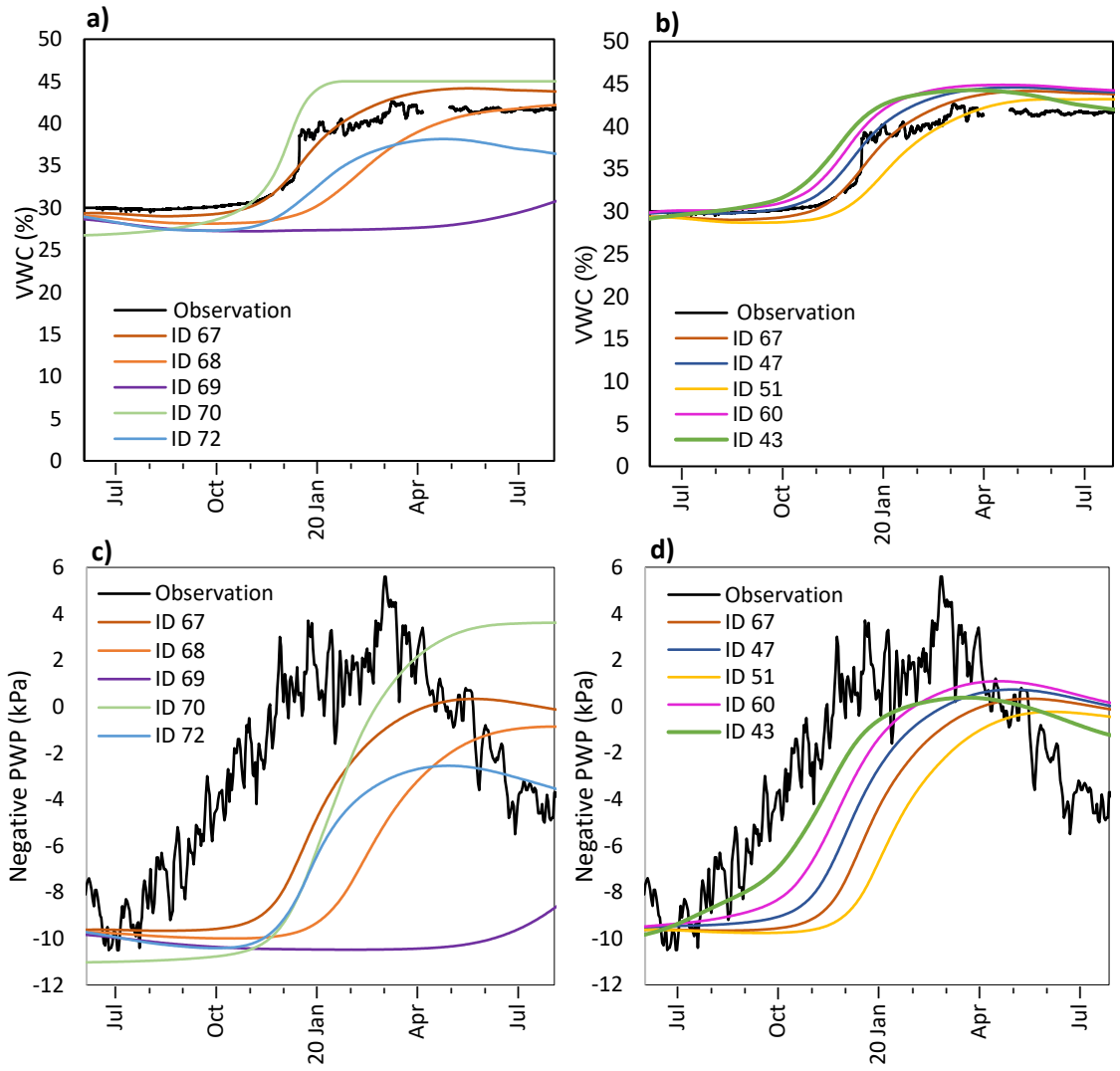

Figure 7-1. *Comparison between simulation (Table 7-1) predictions (black) and the observed VWC (a,b) and PWP (c,d) at 6-m depth at the layer 1 and layer 2 interface. a) and c) changing only the hydraulic conductivity. b) and d) changing anisotropy ratio for the best simulated match (ID 67).*

The simulation in which the hydraulic conductivity of layers 1 and 2 is increased (i.e., ID 67, Figure 7-1a, c) provides the best agreement with the measured PWP and VWC curves, obtaining PWP and VWC trends between simulations 68 and 70. The obtained VWC curve

(ID 67) corresponds well to the measured one (Figure 7-1a). The measured and predicted PWP curves (ID 67) feature similar shapes, but the predicted one appears to be shifted in time (Figure 7-1c).

When simply adjusting each layer's hydraulic conductivity, it is observed that simulation 67 provides the best corresponding shape to the measured PWP and VWC curves at 6 meters depth (Figure 7-1a, c) and was, therefore, further evaluated in a parametric analysis of the anisotropy ratio to improve the timing of the predicted curves (Figure 7-1 b, d).

7.1.2 Parametric analysis of the anisotropy ratio, k'_y/k'_x

A parametric analysis of the anisotropy ratio is performed by changing the ratio in layers 1 and 2 based on the hydraulic conductivity values of simulation 67 (Table 7-1, Figure 7-1a, c). This analysis assists in determining the hydrological model's input values for the anisotropy ratio by observing which ratio best predicts the curves' timing to match the measured ones (Table 7-1, Figure 7-1b, d).

Comparing simulation 67 and the two simulations 51 and 47 (Figure 7-1b, d); In simulation 51, the ratio in layer 1 decreases from 1.25 to 1 and increases from 0.75 to 1 in layer 2 (Table 7-1), resulting in more shifted PWP (Figure 7-1d) and VWC (Figure 7-1b) curves than simulation 67 due to a reduced vertical flow in layer 1. Whereas in simulation 47, the ratio increases from 1.25 to 1.5 in layer 1 and from 0.75 to 1.25 in layer 2 (Table 7-1) and displays a less shifted curve than simulation 67 (Figure 7-1b, d) due to a higher vertical hydraulic conductivity compared to the horizontal one in layers 1 and 2. Simulation 47 shows better accuracy than simulation 67 and is further used in comparison with simulation 60.

In simulation 60, the ratio in layer 1 increases from 1.5 to 1.75, while the ratio in layer 2 remains unchanged (Table 7-1). The timing of the PWP curve is improved (Figure 7-1d), whereas the VWC curve respond earlier (Figure 7-1b) compared to simulation 47. Simulation 60 demonstrates more accurate timing for the predicted PWP curve than simulation 47 and is further used to compare simulation 43.

In simulation 43, the ratio increases from 1.75 to 2 in layer 1 and from 1.25 to 1.5 in layer 2 (Table 7-1), which further improves the timing of PWP curve (Figure 7-1d), but the VWC curve continues to show an earlier response (Figure 7-1b) than simulation 60.

The results show an improving PWP (Figure 7-1d) when a higher ratio is set, particularly in layer 1 (i.e., ID 43, Table 7-1). Simulations 67 and 47, with a lower ratio for layers 1 and 2 (Table 7-1), provide a better fit for the measured VWC (Figure 7-1b). A higher ratio gives higher vertical hydraulic conductivity than the horizontal one, and with a higher ratio (>1.25) at the 6 m depth interface between layers 1 and 2, the VWC show a quicker response in simulation 43 (Figure 7-1b). However, simulation 43, with a ratio of 2 for layer 1 and 1.5 for layer 2 (Table 7-1), could most accurately represent the measured PWP curve and is smoother than the other simulations (ID 67,47,51 and 60) at a depth of 6 m (Figure 7-1d).

7.1.3 The best accuracy of PWP and VWC

Overall, simulation 43 provides the best accuracy when considering both the VWC (Figure 7-1b) and the PWP (Figure 7-1d) trends together at 6 m depth. However, the PWP shows less accuracy at the deeper layers (Figure 7-2b, c, d). At 9 m (Figure 7-2b) the predicted curve is overestimated and at 15 m (Figure 7-2c) the curve is more smoothed and slightly overestimated. At 23 meters depth (Figure 7-2d) the predicted curve is underestimated and has a flattening trend compared to the in-situ measurements by the sensors.

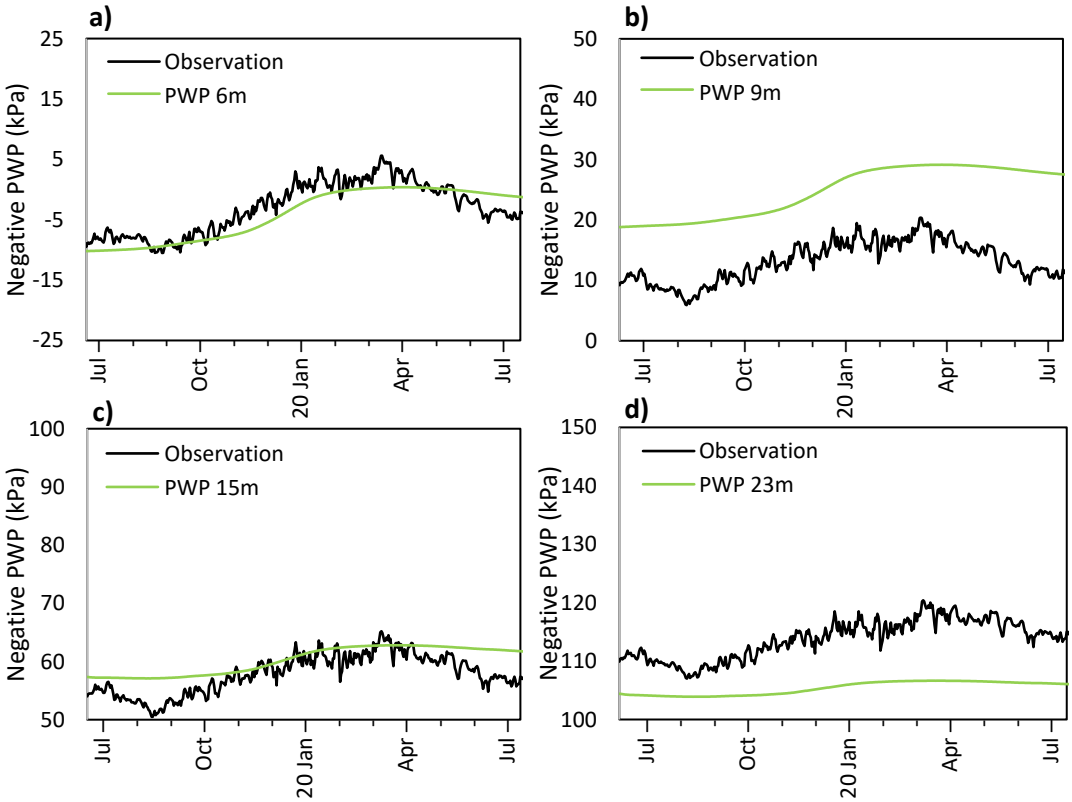

Figure 7-2. *Comparison between the predicted (green) and the observed (black) PWP at depths of a) 6m, b) 9m, c) 15m, and d) 23m for the best simulation (ID 43, Table 7-1; Figure 7-1d).*

Although the predicted VWC curves at 0.1 and 0.5 m (Figure 7-3a, b) are underestimated, and the predicted VWC curves at 1 m and 6 m (Figure 7-3c, f) are overestimated, the predicted and measured VWC for simulation 43 shows satisfactory trends at 0.1-, 0.5-,1- and 6-m depths (Figure 7-3a, b, c, and f). However, the model failed to predict adequate VWC trends at 2- and 4-m depths (Figure 7-3d, e). The predicted VWC at 6m (Figure 7-3f) shows slightly overestimated values, however, it is the best result for VWC when also considering the PWP at 6 m (Figure 7-2a).

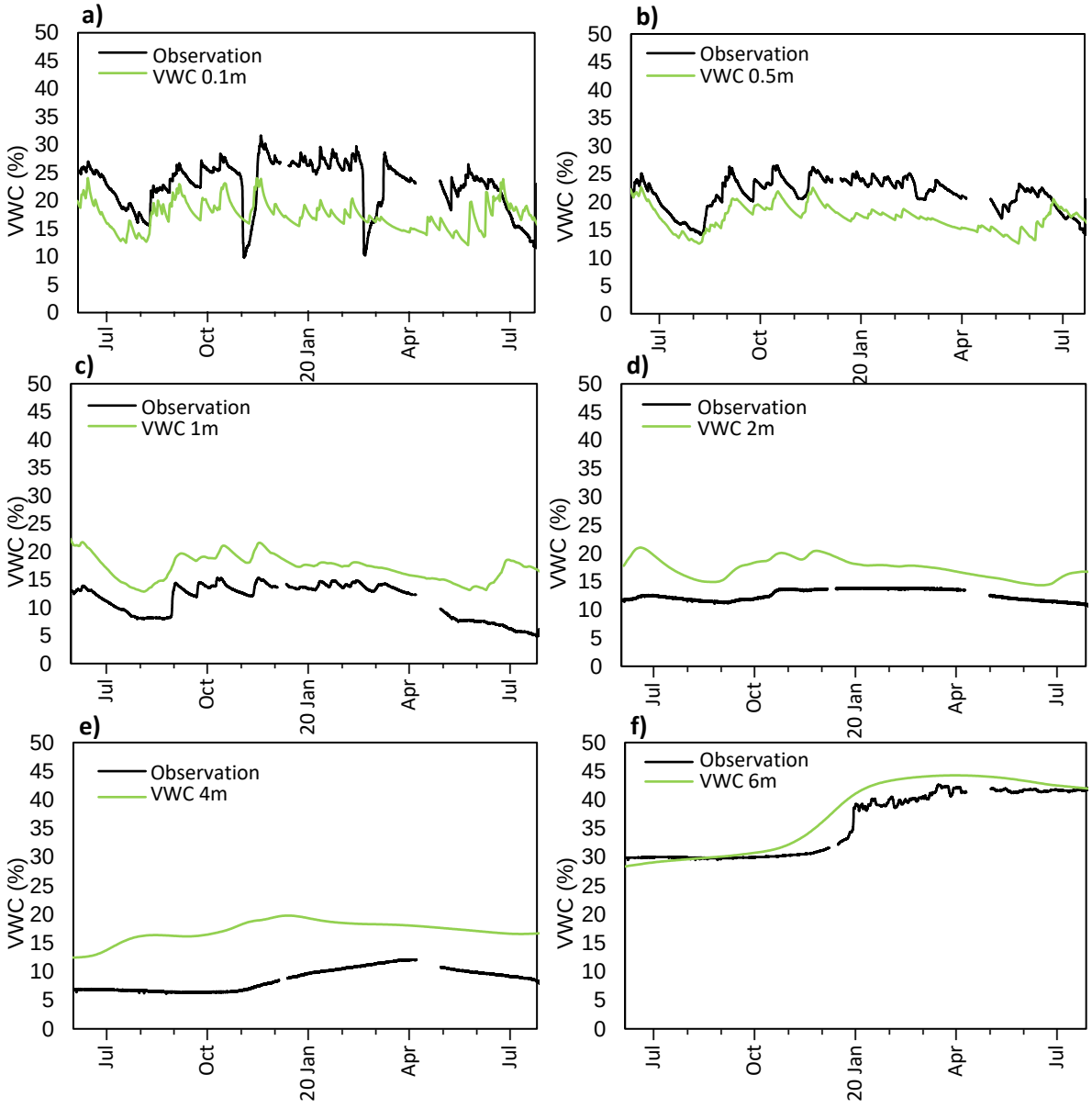

Figure 7-3. *Comparison between the predicted (green) and the observed (black) VWC at depths of a) 0.1m, b) 0.5m, c) 1m, d) 2m, e) 4m, and f) 6m for the best simulation (ID 43, Table 7-1; Figure 7-1b).*

7.1.4 Varying the hydraulic conductivity and anisotropy ratio of layer 3

The hydraulic conductivity and anisotropy ratio of layer 3 was further evaluated based on simulation 47 (Table 7-1). By doing a rough calculation of hydraulic conductivity in combination with systematic changes in the anisotropy ratio for layer 3, no significant variations in PWP and VWC were observed within layer 1 for hydraulic conductivity values lower than E-10 m/s or by changing the anisotropy ratio. However, suppose the hydraulic conductivity for layer 3 is higher (i.e., E-09 m/s). In that case, the VWC and PWP at 6 m depth get significantly underestimated. When changing the anisotropy ratio, the timing slightly varies but improves as the ratio decreases for the PWP curve. However, the opposite is observed for the VWC curve (Simulation 47-1 vs. 47-5 in Table 7-1).

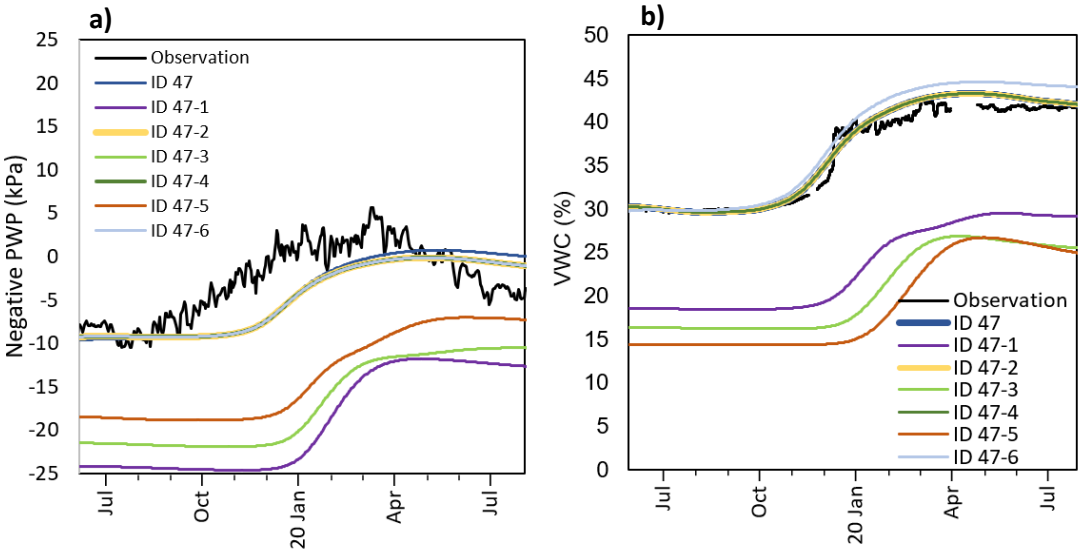

Figure 7-4. *Comparison between the predicted and the observed (black) a) PWP and b) VWC at 6-meter depth when varying the hydraulic conductivity and anisotropy ratio in layer 3 based on simulation 47 (Table 7-1; Figure 7-1b, d).*

The sensitivity analysis was conducted by observing how the predicted and measured (PWP, VWC) data for layer 1 and the interface between layers 1 and 2 responded when adjusting the hydraulic conductivity and the anisotropy ratio for layers 1, 2, and 3 (Table 7-1). The sensitivity analysis helped improve the agreement between measured and predicted PWP and VWC, and the hydraulic conductivity and anisotropy ratio could be defined. Simulation 43 provided the best accuracy when the VWC and the PWP were considered together at the interface between layers 1 and 2 (6 m depth). A hydraulic conductivity of 5E-06, 5E-07, and 5E-10 (m/s) with corresponding anisotropy ratios of 2, 1.5, and 1 is further used as input to the SEEP/W model for layers 1, 2, and 3, respectively.

7.2 Eidsvoll and Oslo/Akershus precipitation and temperature changes

The climate profile for Oslo/Akershus provides the expected annual and seasonal precipitation (%) and temperature (°C) changes for the county until 2100 (Table 4-4), provided by Klimaservicesenter.no. In this context, the annual and seasonal precipitation (Table 7-2) and temperature (Table 7-3) changes for the period 2046 to 2100 were estimated for Eidsvoll. The results for Eidsvoll are compared with the climate profile estimations for Oslo/Akershus (Tables 7-2 and 7-3) to evaluate how they differ and to establish the credibility of the Eidsvoll estimates.

Table 7-2. *The differences between the estimated precipitation changes (%) at the Eidsvoll study site and the climate profile's expected increase for Akershus/Oslo County until 2100. The increase is estimated until 2100 based on the 1971-2000 reference period.*

	Oslo/Akershus RR (%)	***Eidsvoll RR (%)***	***Difference RR (%)***
Winter	30	29.2	-0.8
Spring	25	31.1	+6.1
Summer	5	1.5	-3.5
Autumn	10	9.8	-0.2
Annual	**15**	**17.6**	**+2.6**

The expected changes for both Oslo/Akershus County and Eidsvoll indicate that the most significant increases in precipitation will occur during winter and spring (Figure 7-5). However, the increase will be minor during the summer (Figure 7-5). The results predict a 2.6% higher increase in annual precipitation for Eidsvoll compared to estimates for Akershus/Oslo (Table 7-2). The summer and spring months exhibit the most significant deviation, with a 6.1% increase and a 3.5% decrease, respectively. On the contrary, winter and autumn months show comparable results, with just a 0.2% and 0.8% decrease for Eidsvoll (Table 7-2).

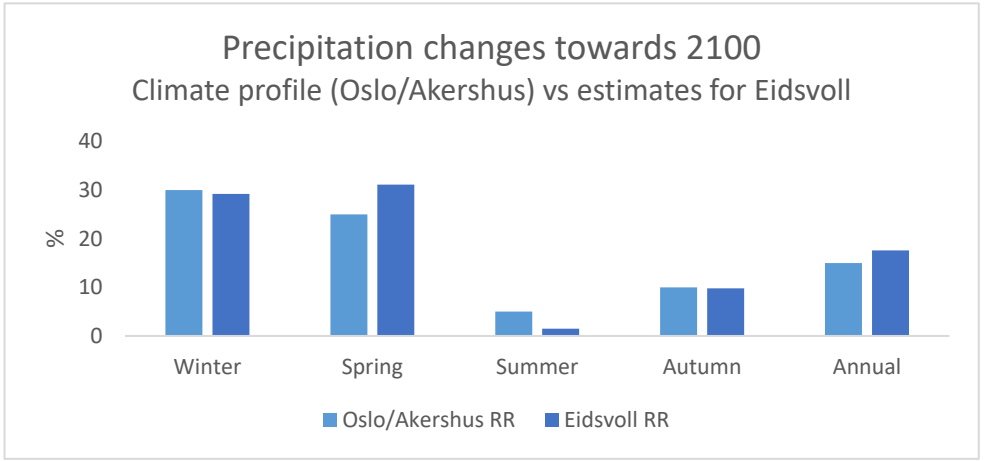

Figure 7-5. *The results for seasonal and annual precipitation changes (%) at the Eidsvoll study site and Akershus/Oslo County until 2100 based on the 1971-2000 reference period.*

Winter and spring will experience the highest temperature increases, while the summer season will have the lowest increases (Table 7-3; Figure 7-6). Generally, every season will have a consistent temperature increase (Figure 7-6).

Table 7-3. *The differences between the estimated temperature changes (°C) at the Eidsvoll study site and the climate profile's expected increase for Akershus/Oslo County until 2100. The increase is estimated until 2100 based on the 1971-2000 reference period.*

	Oslo/Akershus TM (°C)	***Eidsvoll TM (°C)***	***Difference TM (°C)***
Winter	4.5	4.5	0
Spring	4.5	3.9	-0.6
Summer	3.5	3.0	-0.5
Autumn	4	3.7	-0.3
Annual	**4**	**3.7**	**-0.3**

The estimated temperature at Eidsvoll predict a 0.6°C and 0.5°C decrease in spring and summer temperatures and a 0.3°C decrease in autumn and the annual temperatures compared to the climate profile estimations for Oslo/Akershus (Table 7-3). For the winter season, both Oslo/Akershus and Eidsvoll anticipate equal changes (Table 7-3).

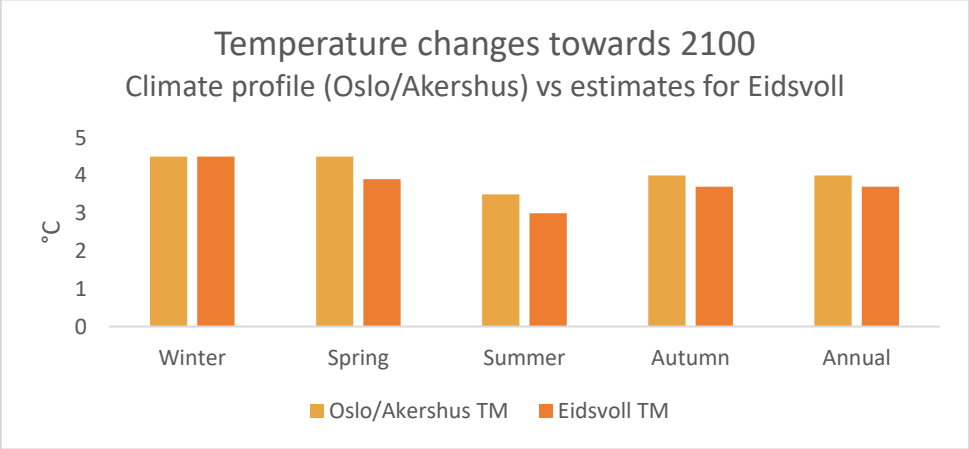

Figure 7-6. *The results for seasonal and annual temperature changes (°C) at the Eidsvoll study site and Akershus/Oslo County until 2100 based on the 1971-2000 reference period.*

Based on these results (Tables 7-2 and 7-3), the estimated changes at Eidsvoll provide reasonable precipitation and temperature changes compared to the expected changes from the climate profile estimates for Oslo/Akershus. This approach is therefore continued when determining changes for two future periods, 2046-2075 and 2076-2100 (Ch. 7.2.1). The goal is to establish input values for precipitation, snow water equivalent, and temperature for the two periods to the hydrological model in SEEP/W (Ch. 7.3). However, the climate profile estimates do not provide any values for snow water equivalent and cannot be validated.

7.2.1 Eidsvoll RR, SWE and TM changes for 2046-2075, 2076-2100 and 2046-2100

To analyse the slope stability at Eidsvoll based on two future periods, the estimated precipitation (RR) and temperature (TM) changes (%, °C) at Eidsvoll are estimated individually for the periods 2046-2075 (Table 7-4) and 2076-2100 (Table 7-5), respectively. These estimated changes are a step closer to determining reliable values for use as input to the SEEP/W model for these two periods. Another new feature in this chapter is the calculation of snow water equivalent (SWE) changes during these periods to determine snowmelt changes, which will be combined with precipitation to represent water supply, a component of the SEEP/W model's input.

The results show that the spring and winter seasons will experience the most significant increases in precipitation, with a 19.8% and 23.2% increase until 2075 (Table 7-4) and a 39% and 38.5% increase until 2100 (Table 7-5). Compared to the 1971-2000 reference period, summer precipitation will increase by 2.8% towards 2075 (Table 7-4), whereas only a 0.2% increase is expected until 2100 (Table 7-5).

Table 7-4. *Seasonal and annual changes in precipitation (RR), temperature (TM), and snow water equivalent (SWE) at Eidsvoll, between the reference period 1971-2000 and the first future period 2046-2075.*

	Change RR (%)	***Change TM (°C)***	***Change SWE (%)***
Winter	19.8	3.6	-75.5
Spring	23.2	3.0	-89.2
Summer	2.8	2.2	-
Autumn	8.2	3.0	-91.1
Annual	**13.3**	**2.9**	**-82.8**

Table 7-5. *Seasonal and annual changes in precipitation (RR), temperature (TM), and snow water equivalent (SWE) at Eidsvoll, between the reference period 1971-2000 and the second future period 2076-2100.*

	Change RR (%)	***Change TM (°C)***	***Change SWE (%)***
Winter	38.5	5.4	-84.8
Spring	39.0	4.9	-100
Summer	0.2	3.8	-
Autumn	11.4	4.4	-99.0
Annual	**21.9**	**4.5**	**-92.2**

The winter months will experience the highest temperature increases, with a rise of 3.6°C for 2046-2075 (Table 7-4) and 5.4°C for 2076-2100 (Table 7-5), while the summer seasons will experience the lowest temperature rise of 2.2°C and 3.8°C, respectively.

The snow water equivalent (SWE) will decrease by around 90% for the spring and autumn seasons and by 75% for the winter for the first period (Table 7-4). For the second period (Table 7-5), the winter season will experience a reduction of about 85%. In contrast, the SWE will be gone entirely during spring and reduced by 99% in autumn. There are no estimates for the summer season, in either period, due to the lack of snow cover.

The entire period (2046-2100) represents the total change until the end of the century (Table 7-6) based on the reference period 1971-2000. The change in precipitation and temperatures are already mentioned and compared with the climate profile (Tables 7-2 and 7-3). However, there are no statistics for snow water equivalent (SWE) in the climate profile for Oslo/Akershus; hence the validity of the estimated SWE changes at Eidsvoll cannot be verified (Figure 7-9). The estimated change in SWE at Eidsvoll shows that the most significant reduction will be during the spring and autumn seasons, with a 95% reduction, while the winter seasons will have an 80% reduction towards the end of the century (Table 7-6).

Table 7-6. *Seasonal and annual changes in precipitation (RR), temperature (TM), and snow water equivalent (SWE) at Eidsvoll, between the reference period 1971-2000 and the entire period 2046-2100.*

	Change RR (%)	***Change TM (°C)***	***Change SWE (%)***
Winter	29.2	4.5	-80.2
Spring	31.1	3.9	-94.7
Summer	1.5	3.0	-
Autumn	9.8	3.7	-95.1
Annual	**17.6**	**3.7**	**-87.5**

When the estimated changes until 2100 are separated into two periods, 2046-2075 and 2076-2100, precipitation and temperatures increase towards 2046-2075, while the most significant increase is expected in the last period, 2076-2100 (Figures 7-7 and 7-8). On the contrary, the snow water equivalent will reduce more in 2076-2100 than in 2046-2075 (Figure 7-9).

Higher precipitation and temperature increases (Figures 7-7 and 7-8), in addition to a decrease in snow water equivalent (Figure 7-9), are anticipated and compatible with RCP 8.5 emission scenario (Hanssen-Bauer et al., 2017) and the climate profile's expectations (Oslo/Akershus) (Klimaservicesenter.no); hence these results are not surprising, but rather confirms reasonable estimates for Eidsvoll.

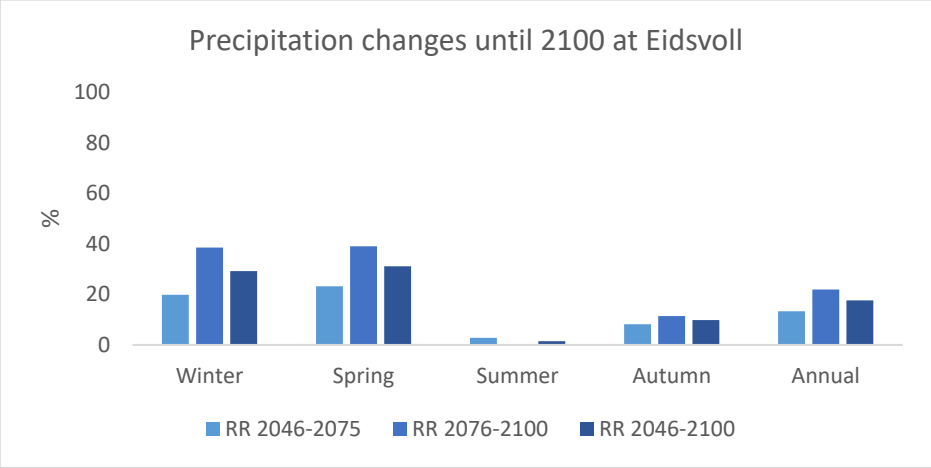

Figure 7-7. *The results for seasonal and annual precipitation (RR) changes (%) at the Eidsvoll study site for the periods 2046-2075, 2076-2100, and the entire period 2046-2100 based on the 1971-2000 reference period.*

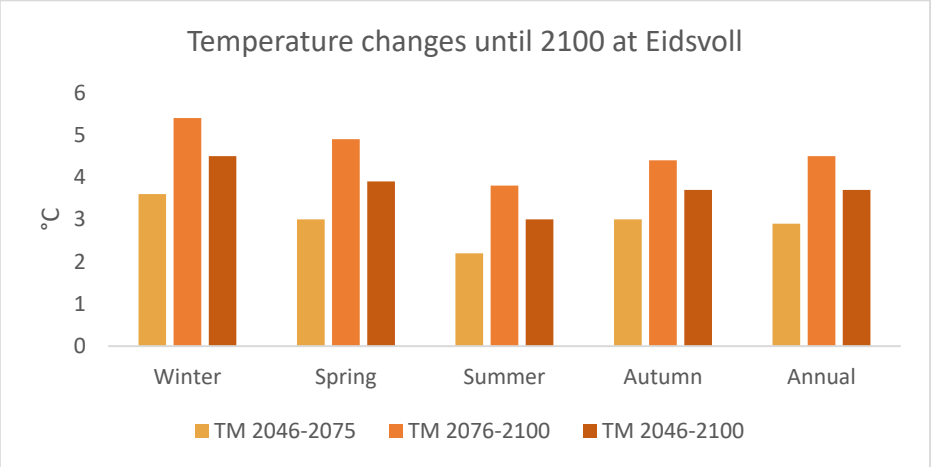

Figure 7-8. *The results for seasonal and annual temperature (TM) changes (°C) at the Eidsvoll study site for the periods 2046-2075, 2076-2100, and the entire period 2046-2100 based on the 1971-2000 reference period.*

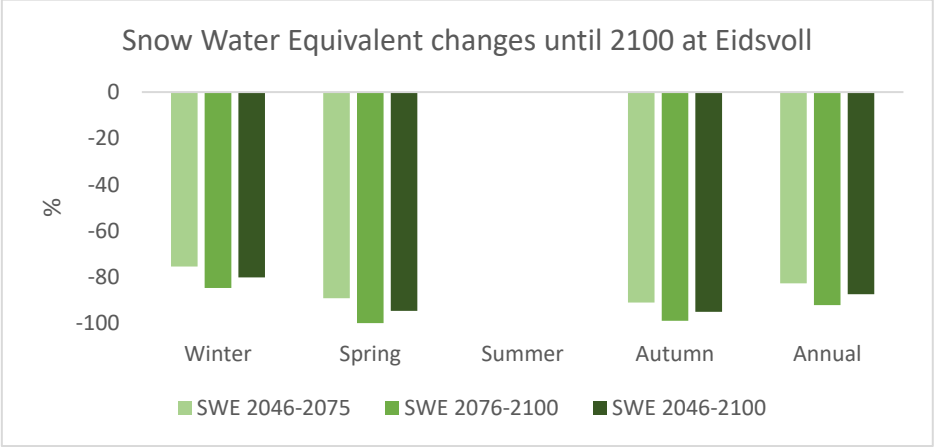

Figure 7-9. *The results for seasonal and annual snow water equivalent (SWE) changes (%) at the Eidsvoll study site for the periods 2046-2075, 2076-2100, and the entire period 2046-2100 based on the 1971-2000 reference period.*

7.3 Future precipitation, snowmelt, and temperature values at Eidsvoll

Estimated daily water supply (%) and temperature (°C) changes (Figure 6-10) are added to historical observation data from 2000-2001 (SeNorge.no) (Figure 6-11). The goal is to generate a future year with realistic daily and annual values as input to the SEEP/W model. Precipitation and snowmelt are combined as one input to the SEEP/W model to reflect the water supply. The calculation of snowmelt is based on the snow water equivalent (Figure 6-3). Future daily values are calculated for two years, 2046-2075 and 2076-2100, using the 2000-2001 measurements as a reference. To make the results of each period more readily apparent, the daily values are presented as annual and seasonal values for the intervals 2046-2075 and 2076-2100 for precipitation, snowmelt, and total water supply (Table 7-7) and temperatures (Table 7-8).

Table 7-7. *The annual and seasonal precipitation (RR) and snowmelt (S), and annual water supply (RR+S) at Eidsvoll based on the observation data for 2000-2001 and the added climate changes (Tables 7-4 and 7-5) for both years representing the future periods 2046-2075 and 2076-2100.*

	2000-2001 ***Observation (mm)***	***2046-2075*** ***Estimated (mm)***	***2076-2100*** ***Estimated (mm)***
Winter RR	193	234	253
Spring RR	169	197	219
Summer RR	232	231	227
Autumn RR	507	550	575
Annual RR	**1101**	**1212**	**1274**
Winter Snowmelt (S)	26	11	13
Spring Snowmelt (S)	72	18	5
Summer Snowmelt (S)	0	0	0
Autumn Snowmelt (S)	0	0	0
Annual Snowmelt	**98**	**29**	**18**
RR+S	**1199**	**1241**	**1292**

The results show that annual precipitation (Table 7-7) and temperature (Table 7-8) values will increase towards 2100, whereas snowmelt will decrease (Table 7-7), which is consistent with the prior results (Ch.7.2.1). Autumn will continue to have the most significant amount of precipitation in the future, and precipitation will increase in all seasons towards 2100, except for summer (Table 7-7). In summer, the results for precipitation show a slight decrease towards 2100 compared to the reference 2000-2001 (Table 7-7), which might be because summer has moderate future changes (Tables 7-4 and 7-5). The snowmelt is prominent in winter and even more in spring. However, the trend is switched for 2076-2100, where more snowmelt is expected in winter compared to spring (Table 7-7).

Table 7-8. *The annual and seasonal temperatures(°C) at Eidsvoll based on the observation data for 2000-2001 and the added climate changes (Tables 7-4 and 7-5) for both years representing the future periods 2046-2075 and 2076-2100.*

	2000-2001 ***Observation (°C)***	***2046-2075*** ***Estimated (°C)***	***2076-2100*** ***Estimated (°C)***
Winter	-4.1	-0.6	1.2
Spring	2.8	5.8	7.7
Summer	13.8	16.1	17.7
Autumn	7.5	10.5	11.8
Annual	**5.0**	**7.9**	**9.5**

The 2000-2001 measurements show an annual water supply of 1199 mm, of which 98 mm is snowmelt and 1101 mm is precipitation (Table 7-7), which is higher than an average year at Eidsvoll. For instance, from 1971–2000, the average annual temperature and precipitation at Eidsvoll were estimated to 4.3 °C and 785 mm (Klimaservicesenter.no).

During the autumn of 2000, high air temperatures in the mountains caused more precipitation to fall as rain instead of snow, resulting in nearly three months of persistent precipitation (Jaedicke and Kleven, 2008). Therefore, the year 2000 was deliberately selected as part of the reference period when estimating future values (RR, Snowmelt, and TM) to ensure that the future stability calculations could account for an irregular year. The hydrological model in SEEP/W is validated for one year, starting on 3rd June and ending on 2nd June of the following year; thus, the year 2000 will continue into 2001 to ensure that autumn 2000 is included. Hence, the reference period is defined from 3rd June 2000 to 2nd June 2001.

Consequently, when estimating future values using 2000-2001 as a reference, 2046-2075 and 2076-2100 will inherently have higher precipitation values (Table 7-7) than if an average year had been chosen. However, the correlation between the reference year 2000-2001 and the increased values for the future periods shows less agreement than the expected increase from the estimated changes at Eidsvoll (Tables 7-4 and 7-5). For 2046-2075, the difference between estimated values (Tables 7-7 and 7-8) and estimated changes (Tables 7-4 and 7-5) for increased annual precipitation is -7.5% (Table 7-9), and temperatures are -0.8°C (Table 7-10). For 2076-2100, the difference for increased annual precipitation is -6.2% (Table 7-11), whereas the increased annual temperatures are consistent and show no difference (Table 7-12) compared to the estimated changes (Tables 7-4 and 7-5). These differences are expected as the changes are added to a measured year instead of a statistical average year with values provided daily (Ch. 6.5.1).

Table 7-9. *Estimated precipitation changes (Table 7-4) compared to 2046-2075 values at Eidsvoll (Table 7-7). To compare the value results (mm) to the expected changes (%) (Ch. 7.2.1), the values are converted from mm to % by determining the difference between the reference values (2000-2001) and the 2046-2075 values.*

	2046-2075 ***Estimated change (%)***	***2046-2075*** ***Estimated values mm → (%)***	***Difference*** ***(%)***
Winter	29.2	21.2	- 8.0
Spring	31.1	16.6	- 14.5
Summer	1.5	0.4	- 1.1
Autumn	9.8	8.5	- 1.3
Annual RR	17.6	**10.1**	**- 7.5**

Table 7-10. *Estimated temperature changes (Table 7-4) compared to 2046-2075 values at Eidsvoll (Table 7-8). To compare the value results to the expected changes (Ch. 7.2.1), the difference between the reference values (2000-2001) and the 2046-2075 values are determined.*

	2046-2075 ***Estimated change (°C)***	***2046-2075*** ***Estimated values (°C)***	***Difference*** ***(°C)***
Winter	4.5	4.7	+ 0.2
Spring	3.9	3	-0.9
Summer	3.0	2.3	-0.7
Autumn	3.7	3	-0.7
Annual TM	**3.7**	**2.9**	**-0.8**

Table 7-11. *Estimated precipitation changes (Table 7-5) compared to 2076-2100 values at Eidsvoll (Table 7-7). To compare the value results (mm) to the expected changes (%) (Ch. 7.2.1), the values are converted from mm to % by determining the difference between the reference values (2000-2001) and the 2076-2100 values.*

	2076-2100 ***Estimated change (%)***	***2076-2100*** ***Estimated values mm → (%)***	***Difference*** ***(%)***
Winter	38.5	31.1	- 7.4
Spring	39.0	29.6	- 9.4
Summer	0.2	2.1	+ 1.9
Autumn	11.4	13.4	+ 2.0
Annual RR	**21.9**	**15.7**	**- 6.2**

Table 7-12. *Estimated temperature changes (Table 7-5) compared to 2076-2100 values at Eidsvoll (Table 7-8). To compare the value results to the expected changes (Ch. 7.2.1), the difference between the reference values (2000-2001) and the 2076-2100 values are determined.*

	2076-2100 ***Estimated change (°C)***	***2076-2100*** ***Estimated values (°C)***	***Difference*** ***(°C)***
Winter	5.4	5.3	- 0.1
Spring	4.9	4.9	0
Summer	3.8	3.9	+ 0.1
Autumn	4.4	4.3	- 0.1
Annual TM	**4.5**	**4.5**	**0**

7.3.1 Predicted water supply and temperature values from climate models

The predicted annual water supply was determined for all climate models for the reference year 2000-2001 (Table 7-13) and the years within the first (Table 7-14) and second (Table 7-15) estimated intervals. Based on the expected values at Eidsvoll (Tables 7-7 and 7-8), the climate model that most closely predicts corresponding annual water supply and seasonal temperature values could be determined for all periods (Tables 7-13, 7-14, and 7-15). The model and year were primarily chosen based on the annual water supply. However, before determining the best model, seasonal temperature values were verified (Table 7-21) with the estimated seasonal temperature changes at Eidsvoll (Table 7-8). The purpose was to obtain water supply and temperature data represented by a single climate model for a year within each interval (2000-2001, 2046-2075, and 2076-2100) as input to the SEEP/W model.

***Table 7-13**. Finding the best fit for annual water supply (RR+S) based on Table (7-8) results to select one climate model's water supply values for one year. The relevant climate models are highlighted in **red**, accepting an annual water supply variance of ± 2%. Water supply values are given in mm.*

Year RR+S	CNRM_ CCLM	CNRM _RCA	MPI_ CCLM	HIR HAM	IPSL_ RCA	RAC MO	MPI_ RCA	HAD GEM	EC_ RCA	EC_ CCLM
2000-01	1000	**1186**	877	788	1006	922	976	1271	1143	934

***Table 7-14.** Finding the best fit for annual water supply (RR+S) based on Table (7-8) results to select one climate model's water supply values for one year. The relevant years for 2046-2075 are highlighted in **red** for each climate model, accepting an annual water supply variance of ± 2%. Water supply values are given in mm.*

Year RR+S	CNRM_ CCLM	CNRM _RCA	MPI_ CCLM	HIR HAM	IPSL_ RCA	RAC MO	MPI_ RCA	HAD GEM	EC_ RCA	EC_ CCLM
2046-47	1200	873	1051	1300	1165	1033	950	1058	842	1139
2047-48	1208	946	987	959	831	807	794	839	984	1110
2048-49	947	819	1029	987	1040	1115	953	764	656	829
2049-50	901	750	1158	**1240**	991	624	945	850	891	944
2050-51	1016	1018	1174	1111	792	1198	927	1103	996	1110
2051-52	943	1000	1145	1061	1145	1081	1083	879	974	1115
2052-53	808	776	995	1040	1017	794	1021	824	1093	963
2053-54	936	820	1007	1043	1105	904	913	813	888	1049
2054-55	1000	824	904	1117	1306	1101	892	928	694	899
2055-56	1142	1092	**1241**	986	993	997	1012	909	1146	1106
2056-57	1091	1017	1065	1069	**1258**	1062	889	788	872	984
2057-58	1016	969	869	818	1059	**1232**	755	859	815	810
2058-59	1176	998	1010	995	1092	585	908	677	1005	1053
2059-60	1091	1014	1112	818	863	692	785	754	1137	1280
2060-61	960	921	878	1000	997	1063	741	870	615	873
2061-62	1059	1008	1005	1128	896	1348	959	837	780	876
2062-63	1110	1029	1022	1173	949	1128	858	851	778	835

2063-64	**1219**	1063	**1234**	**1219**	979	842	1081	978	765	982
2064-65	1130	**1235**	1046	1077	995	**1245**	938	803	871	1082
2065-66	1034	1018	958	964	1046	878	952	823	684	586
2066-67	996	652	1066	952	1098	1135	**1262**	1286	854	827
2067-68	**1249**	1011	1000	**1266**	1089	1055	729	825	1084	947
2068-69	992	927	1159	1048	991	995	983	712	1030	**1233**
2069-70	882	805	1071	1083	719	693	1014	807	928	1319
2070-71	1014	1131	877	970	908	1003	715	1123	681	714
2071-72	682	856	**1220**	1318	1059	886	1131	1042	**1224**	1284
2072-73	1324	1009	895	971	1191	890	903	939	1134	1082
2073-74	980	754	882	974	936	1280	905	1043	953	1152
2074-75	803	789	1063	1107	922	867	1175	806	1029	**1222**

Table 7-15. *Finding the best fit for annual water supply (RR+S) based on Table (7-8) results to select one climate model's water supply values for one year. The relevant years for 2076-2100 are highlighted in* ***red*** *for each climate model, accepting an annual water supply variance of ± 2%. Water supply values are given in mm.*

Year RR+S	**CNRM_ CCLM**	**CNRM _RCA**	**MPI_C CLM**	**HIR HAM**	**IPSL_ RCA**	**RAC MO**	**MPI_ RCA**	**HAD GEM**	**EC_ RCA**	**EC_ CCLM**
2076-77	1112	969	967	1018	1012	916	935	790	824	846
2077-78	1058	1067	1161	1229	**1303**	985	920	871	971	**1273**
2078-79	1252	1010	1128	863	975	1140	1184	1203	581	854
2079-80	1042	861	1193	870	998	**1276**	1085	1262	852	1052
2080-81	1118	822	1032	884	1003	920	1105	954	1093	**1271**
2081-82	770	697	962	889	1221	936	1042	1095	665	715
2082-83	1046	930	1084	1198	1158	819	1022	882	1073	1151
2083-84	807	812	1192	**1273**	1180	999	1130	922	829	791
2084-85	1195	1078	1081	1364	919	1194	1124	1035	1000	838
2085-86	805	1071	1053	1153	1085	1004	1019	1214	701	690
2086-87	1034	848	856	800	888	1071	891	1076	1198	**1313**
2087-88	1047	1140	825	1245	**1282**	833	793	1226	1018	1114
2088-89	1039	1187	1031	954	916	1004	796	1002	833	645
2089-90	1038	982	893	796	1026	1015	899	1055	882	1022
2090-91	1068	1084	1343	970	1130	1067	1338	891	761	754
2091-92	1218	877	1175	1144	1001	1184	875	1031	1028	847
2092-93	1193	1361	1228	1054	1073	1035	972	794	904	1028
2093-94	1097	831	1073	919	968	1037	1023	979	989	950
2094-95	1238	994	1128	1057	860	1048	1070	1170	819	895
2095-96	1225	**1295**	1159	925	1170	1130	816	863	928	1211
2096-97	1065	797	1048	1131	1475	658	936	897	1022	897
2097-98	1033	816	1032	1240	1049	964	861	1055	1085	1122
2098-99	846	848	1431	1356	989	1094	1203	**1271**	1004	1125
99-2100	1190	937	1081	659	1189	896	979	1486	889	943

Altogether, the CNRM_RCA model for the years 2000-2001, 2064-2065, and 2095-2096 (Table 7-16) could replicate the expected annual water supply values (Table 7-7) for each period with the highest accuracy. The annual and seasonal temperatures provided by the CNRM_RCA model for the same years also show reasonable values (Table 7-20) compared

to the estimated seasonal temperature changes at Eidsvoll (Table 7-8). The daily precipitation, snow water equivalent, snowmelt, and temperatures values projected by the CNRM RCA model, and the estimated changes, are further detailed in the Appendix E (Figure E-1, E-2, and E-3).

Table 7-16. *The annual and seasonal precipitation (RR), snowmelt (S), and annual water supply (RR+S) result of the CNRM_RCA model for the years 2000-2001, 2064-2065, and 2095-2096.*

CLIMATE MODEL	***2000-2001 CNRM_RCA (mm)***	***2064-65 CNRM_RCA (mm)***	***2095-96 CNRM_RCA (mm)***
Winter RR	208	103	259
Spring RR	108	260	177
Summer RR	226	462	438
Autumn RR	303	385	411
Annual RR	**845**	**1210**	**1285**
Winter Snowmelt (S)	140	17	6
Spring Snowmelt (S)	186	8	4
Summer Snowmelt (S)	0	0	0
Autumn Snowmelt (S)	15	0	0
Annual Snowmelt	**341**	**25**	**10**
RR+S	**1186**	**1235**	**1295**

Table 7-17. *The difference between the CNRM_RCA model (Table 7-16) and the estimated values for Eidsvoll (Table 7-7). The precipitation (RR), snowmelt (S), and water supply (RR+S) value deviations are given in %.*

Climate model vs. estimated values	***2000-2001 (%)***	***2046-2075 vs 2064-2065 (%)***	***2076-2100 vs 2095-2096 (%)***
Winter RR	+7.7	-55.9	+2.3
Spring RR	-36.0	+31.9	-19.1
Summer RR	-2.5	+100	+92.9
Autumn RR	-40.2	-30.0	-28.5
Annual RR	**-23.2**	**-0.1**	**+0.8**
Winter Snowmelt (S)	+438.4	+54.5	-53.8
Spring Snowmelt (S)	+158.3	-55.5	-20.0
Summer Snowmelt (S)	-	-	-
Autumn Snowmelt (S)	-	-	-
Annual Snowmelt	**+247.9**	**-13.8**	**-44.4**
RR+S	**-1.0**	**- 0.5**	**+0.2**

The seasonal precipitation predicted by the CNRM_RCA model (Table 7-16), show a more varied pattern (Table 7-17) than the estimated values (Table 7-7). Typically, snowmelt is associated in spring, but for the predicted years 2064-2065 and 2095-2096, the snowmelt will be more dominant in winter (Table 7-16). The CNRM_RCA predicts less annual precipitation and a more significant contribution of snowmelt for 2000-2001 compared to observational data (Table 7-17). The estimated annual precipitation values for the future periods (Table 7-7) correspond well with those predicted by the CNRM_RCA model (Table 7-16). However, the model predicts a higher reduction of annual snowmelt for both future years compared to the estimated changes at Eidsvoll (Table 7-17). The annual water supply varies by 0.2-1% between the climate model predicted values (Table 7-16) and the estimated values (Table 7-7) for all periods (Table 7-17). However, to account for snowmelt in the modelling phase, precipitation and snowmelt must be coupled as a single input for the hydrological model in GeoStudio (Tables 7-18 and 7-19) as the hydrological model does not consider snowmelt and precipitation separately.

Table 7-18. *Seasonal and annual water supply (RR+S) of the observation data of 2000-2001 and the estimated future changes for the intervals 2046-2075 and 2076-2100.*

	2000-2001 Observation (mm)	***2046-2075 Estimated (mm)***	***2076-2100 Estimated (mm)***
Winter RR+S	219	245	266
Spring RR+S	241	215	224
Summer RR+S	232	231	227
Autumn RR+S	507	550	575
Annual RR+S	**1199**	**1241**	**1292**

Table 7-19. *Seasonal and annual water supply (RR+S) by the CNRM_RCA model for the selected years 2000-2001, 2064-2065, and 2095-2096 within the intervals 2000-2001, 2046-2075, and 2076-2100, respectively.*

CLIMATE MODEL	***2000-2001 CNRM_RCA (mm)***	***2064-65 CNRM_RCA (mm)***	***2095-96 CNRM_RCA (mm)***
Winter RR+S	348	120	265
Spring RR+S	294	268	181
Summer RR+S	226	462	438
Autumn RR+S	318	385	411
Annual RR+S	**1186**	**1235**	**1295**

Generally, the predicted temperature values (Table 7-20) are lower than the estimated future temperatures at Eidsvoll (Table 7-8). The most significant disparity between predicted and estimated values appears in autumn for all periods and in winter for the reference year and the first period (Table 7-21). Still, predicted annual temperatures agree well with the estimated ones (Table 7-21).

Table 7-20. *The annual and seasonal temperature (in °C) result by the CNRM_RCA model for the years 2000-2001, 2064-2065, and 2095-2096.*

CLIMATE MODEL	***2000-2001 CNRM_RCA (°C)***	***2064-65 CNRM_RCA (°C)***	***2095-96 CNRM_RCA (°C)***
Winter	-6.5	-2.7	0.5
Spring	3.9	5.3	7.8
Summer	15.5	16.0	18.5
Autumn	3.9	8.6	8.4
Annual	**4.3**	**6.8**	**8.8**

Table 7-21. *The difference between the CNRM_RCA model (Table 7-20) and the estimated values for Eidsvoll (Table 7-8). The seasonal and annual temperature value deviations are given in °C.*

Climate model vs. estimated values	***2000-2001 (°C)***	***2046-2075 vs 2064-2065 (°C)***	***2076-2100 vs 2095-2096 (°C)***
Winter	-2.4	-2.1	-0.7
Spring	1.1	-0.5	0.1
Summer	1.7	-0.1	0.8
Autumn	-3.6	-1.9	-3.4
Annual	**-0.7**	**-1.1**	**-0.7**

Given that the estimated future values for daily water supply and temperature are calculated from the same measured data, they reflect the same trend and patterns as the year 2000-2001 (Figure 7-10 a, c, e). Based on 2000-2001 observations (Figure 7-10a), the estimated water supply and temperatures continue to increase towards 2046-2075 (Figure 7-10c) and 2076-2100 (Figure 7-10e). The corresponding daily water supply and temperature values predicted by the climate model CNRM_RCA show a varying pattern for both temperatures and water supply for all years, as they are chosen independently (Figure 7-10b, d, f).

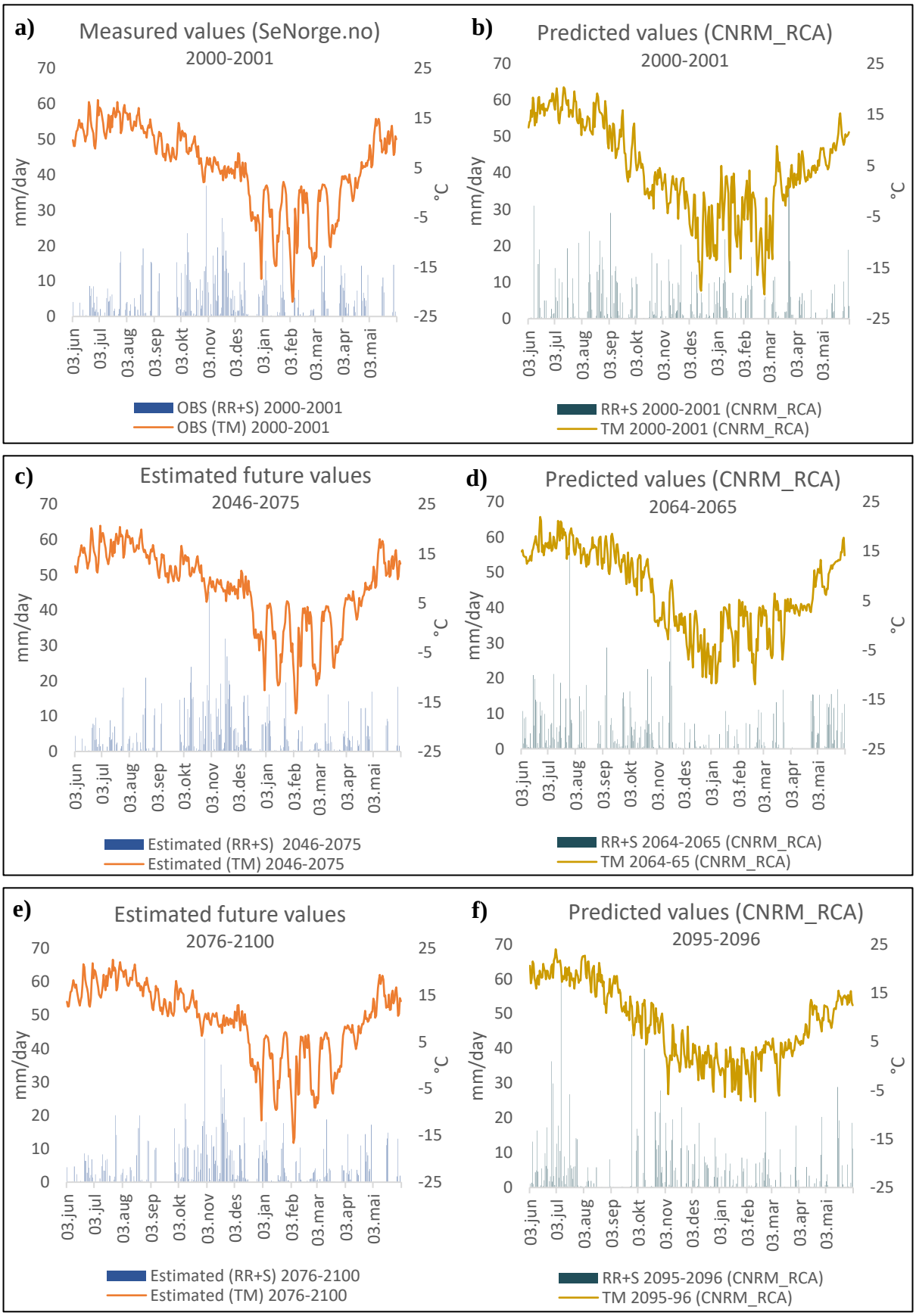

Figure 7-10. *Daily water supply and temperature values at Eidsvoll from 3 June 2000 to 2 June 2001 for a) observational data and the corresponding b) predictions from the CNRM_RCA model. Daily water supply and temperature values at Eidsvoll from 3 June to 2 June for c) estimated changes for* the intervals *2046-2075 and e) 2076-2100, and predictions from the CNRM_RCA model for selected years d) 2064-2065 and f) 2095-2096 within the intervals 2000-2001, 2046-2075, and 2076-2100, respectively.*

Based on the expected changes (in %, ±°C) (Ch. 7.2), this chapter presented the estimated daily, seasonal, and annual values (in mm, °C) for Eidsvoll. Precipitation and temperatures show increasing values towards the end of the century, while snowmelt will decrease. The CNRM_RCA climate model is selected for three years (2000-2001, 2064-2065, and 2095-2096) within the intervals 2000-2001, 2046-2075, and 2076-2100, as this model predicts the estimated annual water supply and seasonal temperature values best. The estimated annual and seasonal values are then compared to the CNRM_RCA's projected values to identify the differences (Tables 7-17 and 7-21). The climate model's predictions reveal a more shifting precipitation pattern and some fluctuations in snowmelt and temperatures compared to the estimated values for Eidsvoll (Table 7-17). The overall purpose is to have reasonably similar annual water supply and seasonal temperature values from estimated and predicted values to be used as input to the SEEP/W model. The slope stability calculations can then be determined based on predicted values that show more changing weather (Figure 7-10b, d, f) and by estimated values based on a realistically measured year with expected future increases (Figure 7-10a, c, e).

7.4 Slope stability analysis based on estimated and predicted values

The slope stability analysis was conducted using the estimated and predicted temperature and water supply values (Figure 7-10a-f), and other climate drivers, such as wind speed, relative humidity, albedo, and solar radiation, as inputs to the SEEP/W model before combining it with the SLOPE/W model in GeoStudio. The slope stability was assessed through six different simulations based on two different methods (Table 6-4). The first method calculates the Factor of Safety based on measured data for 2000-2001 (Figure 6-2) and estimated future values for two intervals (Tables 7-7 and 7-8). The second method uses predicted values from the CNRM_RCA model (Tables 7-16 and 7-20) for three single years (2000-2001, 2064-2065, and 2095-2096).

The simulations conducted for the estimated intervals (Figure 7-11a, c, e) show that as the water supply increases (Figure 7-11c, e), the minimum Factor of Safety (FS) decreases from 1.46 in 2000-2001 to 1.44 and 1.43 in 2046-2075 and 2076-2100, respectively (Table 7-22). The minimum Factor of Safety also occurs earlier in 2076-2100 than in 2046-2075 and the measured year 2000-2001 (Table 7-22). Furthermore, the Factor of Safety after each simulation shows different values for 2000-2001 (FS 1.52), 2046- 2075 (FS 1.53), and 2076-

2100 (FS 1.51) (Table 7-22). The contribution from snowmelt in the spring of 2001 is drastically reduced in 2046-2075 and 2076-2100, which may explain why 2000-2001 has a lower Factor of Safety after the simulation compared to 2046-2075 (Table 7-22). However, 2076-2100 shows the lowest Factor of Safety at the end of the simulation, which can be because the total water supply increases the most during this period (Table 7-18).

The slope stability analysis using precipitation, snowmelt, and temperature input predicted by the CNRM_RCA climate model for the years 2000-2001, 2064-65, and 2095-96 (Figure 7-11b, d, f) demonstrates a decrease in the minimum Factor of Safety towards 2100 (Table 7-23) but indicates a better slope stability due to a higher minimum Factor of Safety than what is shown for the estimated intervals (Tables 7-22 and 7-23).

Both reference years 2000-2001 (Figure 7-11a, b) show similar precipitation during summer (Tables 7-18 and 7-19). However, the CNRM_RCA model provides much less precipitation during autumn, which could be explained by the historically high precipitation amount measured during the autumn of 2000 that the CNRM_RCA model does not capture as it is based on statistics and not actual measurements.

Table 7-22. *The maximum, average, initial, final, and minimum Factor of Safety (FS) of the observation data of 2000-2001 and the estimated future changes for the intervals 2046-2075 and 2076-2100.*

	2000-2001 (Observation)	***2046-2075 (Estimated)***	***2076-2100 (Estimated)***
Maximum FS	1.71	1.72	1.73
Average FS	1.58	1.57	1.57
Initial FS	1.65	1.65	1.65
Final FS	1.52	1.53	1.51
Minimum FS	**1.46** (31 Jan)	**1.44** (29 Jan)	**1.43** (27 Jan)

Table 7-23. *The maximum, average, initial, final, and minimum Factor of Safety (FS) of the CNRM_RCA model for the years selected years 2000-2001, 2064-2065, and 2095-2096 within the intervals 2000-2001, 2046-2075, and 2076-2100, respectively.*

	2000-2001 CNRM_RCA	***2064-65 CNRM_RCA***	***2095-96 CNRM_RCA***
Maximum FS	1.70	1.66	1.68
Average FS	1.61	1.56	1.55
Initial FS	1.65	1.65	1.65
Final FS	1.59	1.54	1.51
Minimum FS	**1.56** (13 Apr)	**1.49** (21 Nov)	**1.47** (25 Feb)

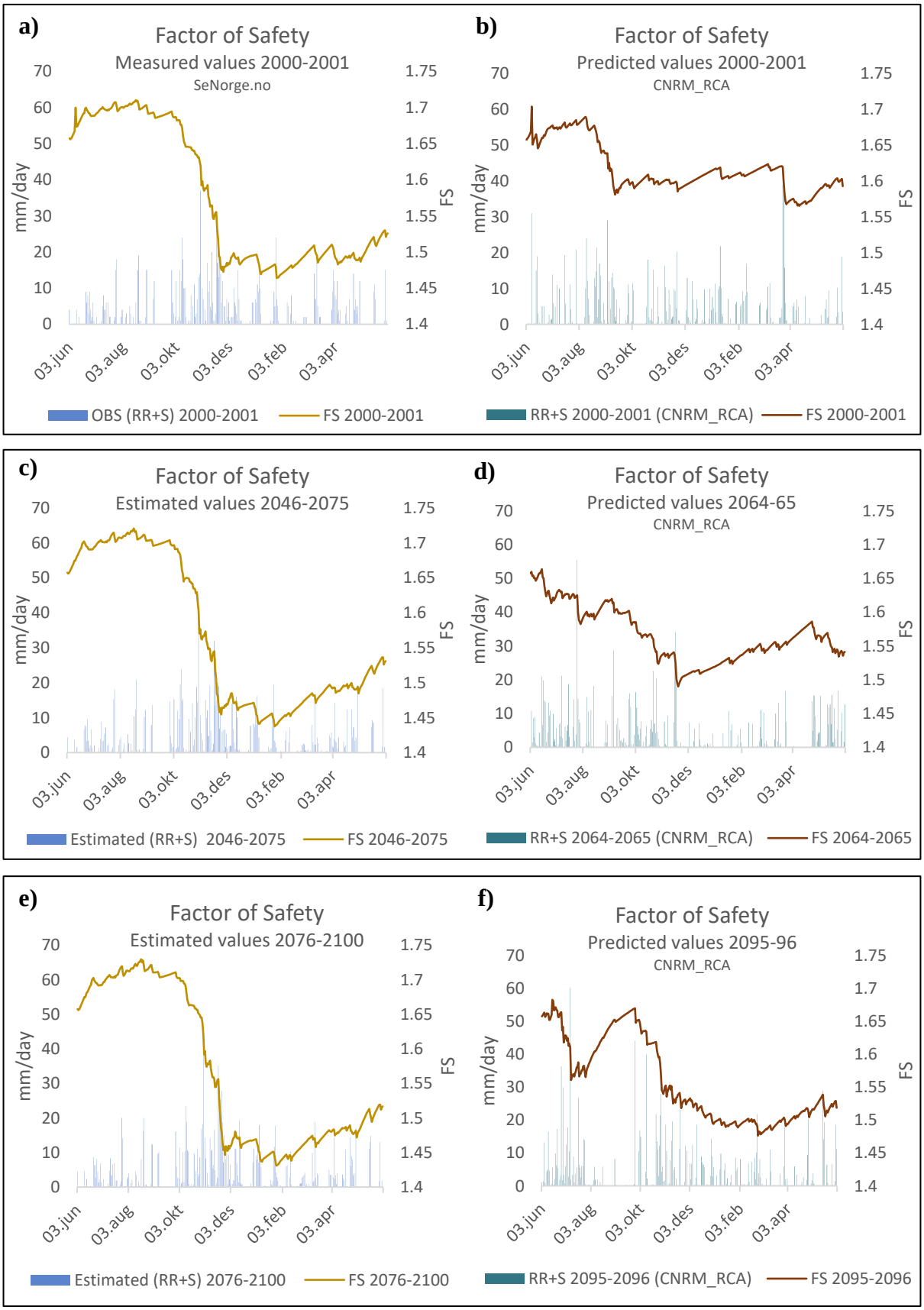

Figure 7-11. *The Factor of Safety (FS) for a) observation data of 2000-2001, and the estimated future changes for the intervals c) 2046-2075 and e) 2076-2100. FS predicted by the CNRM_RCA model corresponding to selected years b) 2000-2001, d) 2064-2065, and f) 2095-2096 within the intervals 2000-2001, 2046-2075, and 2076-2100, respectively.*

During winter, however, the CNRM_RCA predicts a lot higher amount of water supply and slightly higher in spring than the measurements from 2000-2001 due to the high snowmelt contribution during winter and spring (Tables 7-18 and 7-19). The high snowmelt peaks from 23rd to 25th March cause the Factor of Safety to drop, and a minimum Factor of Safety (FS 1.56) is observed on 13th April. A value of 1.59 is shown at the end of the simulation (Table 7-23).

The CNRM_RCA predicted year 2064-65 provides a doubled amount of water supply during summer; although less water supply is predicted in autumn compared to the interval 2046-2075, the Factor of Safety decreases during summer and autumn but does not drop as drastically as the Factor of Safety in autumn 2046-2075 due to a more spread precipitation pattern and the lower precipitation amount predicted in autumn 2064-65 (Table 7-19). After high precipitation peaks on 17-19th November (Figure 7-11d), the minimum Factor of Safety is reached on 21st November (FS 1.49) (Table 7-23). Furthermore, as the CNRM_RCA predicts a low water supply during winter (Table 7-19), the Factor of Safety starts to increase before it decreases again in late spring due to the increased water supply. A Factor of Safety of 1.54 is shown at the end of the simulation (Table 7-23).

The CNRM_RCA predicted year 2095-96 provides almost a doubled amount of water supply during summer compared to the 2076-2100 interval, causing the Factor of Safety to drop. However, very little rain during August and September causes the Factor of Safety to increase (Figure 7-11f). Then, the high peaks in October and the continuous water supply during autumn and winter cause the Factor of Safety to decrease again and reach its minimum on 25th February (FS 1.47) (Table 7-23). Due to less contribution of snowmelt and lower water supply values in the spring of 2095-96, the Factor of Safety slightly increases during spring and ends up with a Factor of Safety of 1.51 at the end of the simulation (Table 7-23).

The Factor of Safety is mainly influenced by high water supply peaks and persistent water supply over extended periods (Figure 7-11). Another observation is that the minimum Factor of Safety decreases (Tables 7-22 and 7-23) as the annual water supply increases (Tables 7-18 and 7-19) for the middle and last periods towards 2100. The measured and estimated years follow the same trend for Factor of Safety (Figure 7-11a, c, e). However, the predicted years follow a varied trend for Factor of Safety (Figure 7-11b, d, f), which is mainly connected to the shifting water supply pattern used as input to the hydrological model (Table 7-19). The CNRM_RCA model predict a higher Factor of Safety for all years (Figure 7-11b, d, f)

compared to the Factor of Safety of the measured and estimated input (Figure 7-11a, c, e). For the slope at Eidsvoll, the geotechnical Factor of Safety (FS) must be at least 1.4 (Jernbaneverket, 2016). However, all simulations show a Factor of Safety above 1.4 (Figure 7-12), indicating that the slope stability is within the requirements.

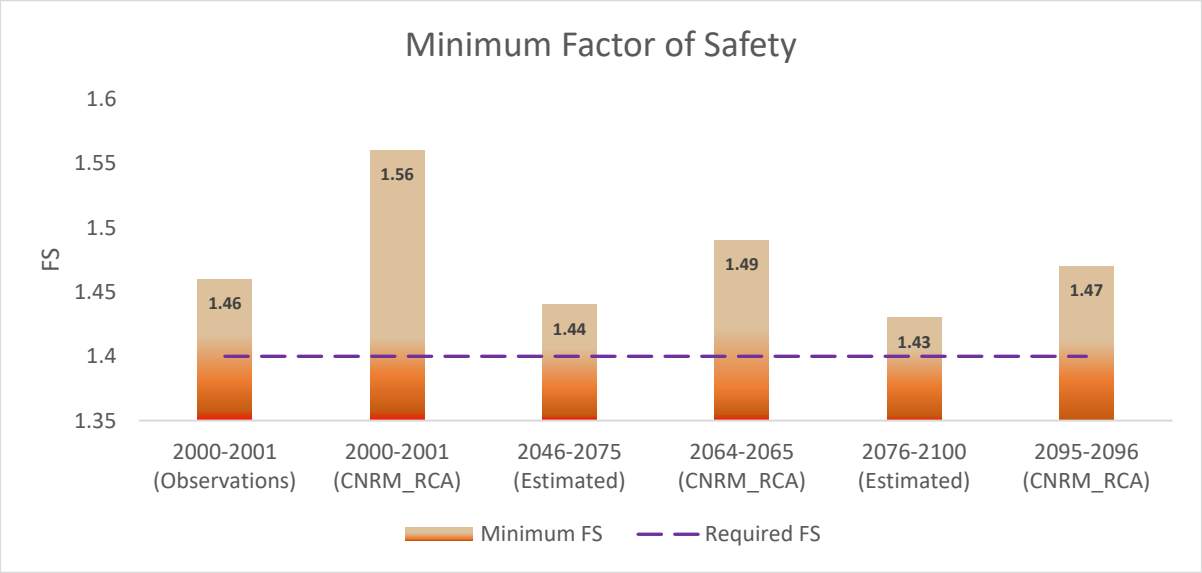

Figure 7-12. *The minimum Factor of Safety of each simulation (Table 6-4). For the slope at Eidsvoll, the geotechnical Factor of Safety must be at least 1.4 (Jernbaneverket, 2016). All simulations show values above the required Factor of Safety of 1.4 (Purple line).*

7.5 Defining thresholds through numerical stress-testing

Determining thresholds is essential for comprehending how a future climate with higher temperatures and increased precipitation intensity and duration would impact the slope. Stress tests on slope stability are performed using artificial data and systematically increasing the water supply and temperature values to determine the slope's thresholds. These stress tests assist in detecting when the slope's Factor of Safety is below the geotechnical requirements (FS 1.4), when it is at failure (FS =1), and which variables (RR+S, TM) influence the slope stability significantly. A Factor of Safety below 1 implies a slope failure. Additionally, any Factor of Safety below 1.4 does not meet the requirements, as this is the minimum geotechnical Factor of Safety required for the Eidsvoll slope (Jernbaneverket, 2016).

7.5.1 Increasing the daily water supply

Historical observation data for daily water supply from June 3rd 2000 to June 2nd 2001 (Figure 6-2) were gradually increased by 10 to 350% (Figure 7-13), while temperatures

remained unchanged. The minimum and average Factor of Safety was determined for each simulation (Table 7-24). When the water supply value increases by 20% (Figure 7-14), the slope's stability condition falls below the required Factor of Safety (FS 1.4) (Table 7-24). A slope failure (FS < 1) occurs when the water supply value increases by an unrealistically high value of 300 % (Figure 7-15).

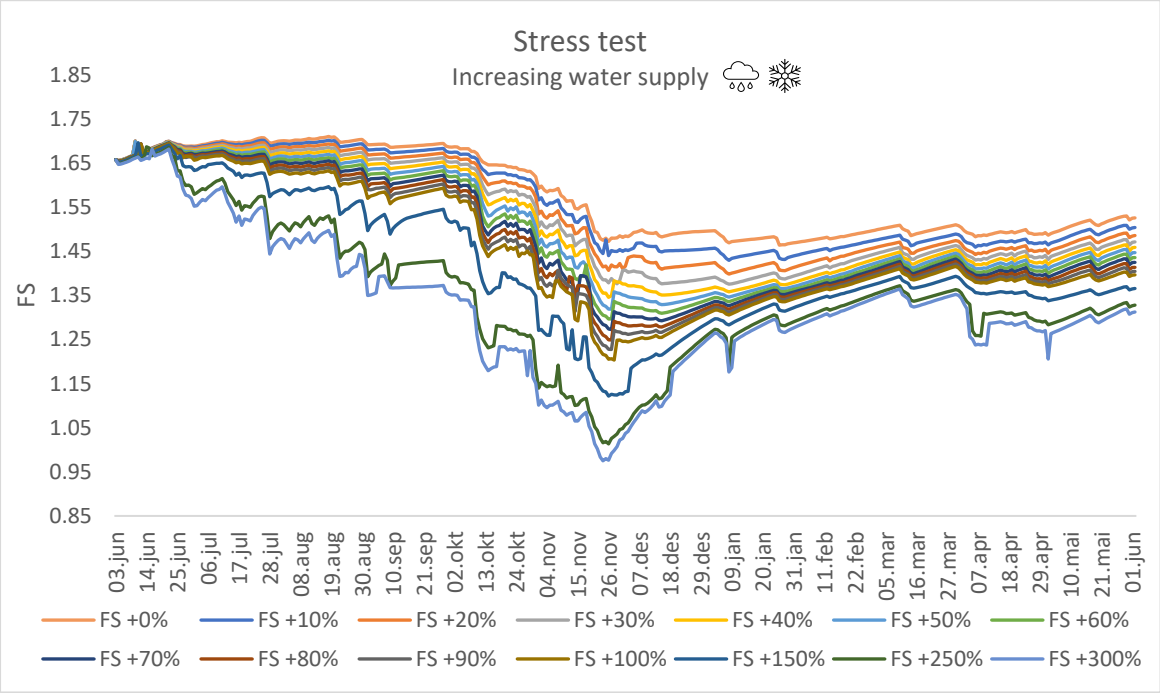

Figure 7-13. *Stress test by increasing only water supply by progressively adding 10-300% to the measured water supply at Eidsvoll from 3rd June 2000 to 2nd June 2001, while temperature values stayed unchanged.*

Table 7-24. *Simulations were conducted by systematically increasing 10-300% to the measured daily water supply (RR+S) at Eidsvoll from 3rd June 2000 to 2nd June 2001, while maintaining the same temperature (TM) values. A FS below the requirements (FS 1.4) is marked in purple. The FS after failure (<1) is marked in **red**.*

Year and increase (%)	*Water supply (mm)*	*Minimum FS*	*Average FS*
2000-2001 + 0%	1199	1.46	1.58
2000-2001 + 10%	1327	1.42	1.56
2000-2001 + 20%	1447	1.39	1.54
2000-2001 + 30%	1568	1.37	1.52
2000-2001 + 40%	1688	1.34	1.51
2000-2001 + 50%	1809	1.31	1.50
2000-2001 + 60%	1930	1.29	1.49
2000-2001 + 70%	2050	1.27	1.48
2000-2001 + 80%	2171	1.24	1.47
2000-2001 + 90%	2291	1.22	1.46
2000-2001 + 100%	2412	1.20	1.45
2000-2001 + 150%	3015	1.12	1.41
2000-2001 + 250%	4221	1.01	1.35
2000-2001 + 300%	4824	**0.97**	1.32

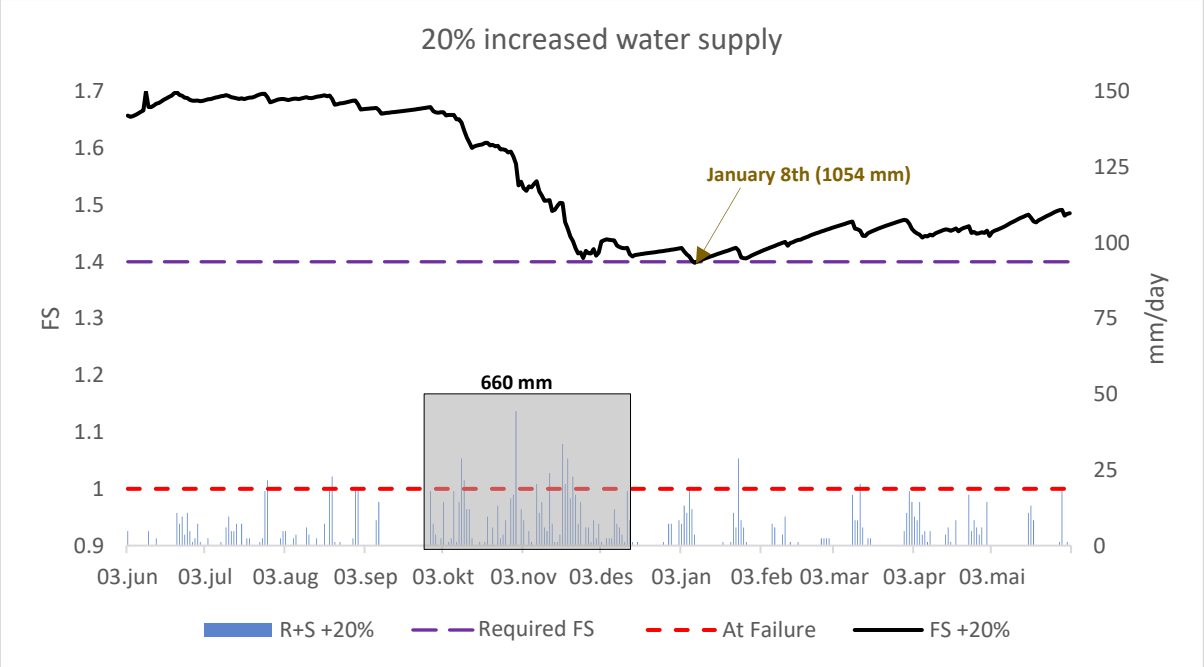

Figure 7-14. *Increasing water supply by 20% to the measured daily water supply at Eidsvoll from June 3rd 2000 to June 2nd 2001. Temperatures stay unchanged. The Factor of Safety falls below the requirements (FS 1.4) on January 8th. The period from June 3rd to January 8th has a total water supply of 1054 mm, whereas the period of consistent precipitation, September 28th to December 17th, provides a water supply of 660 mm.*

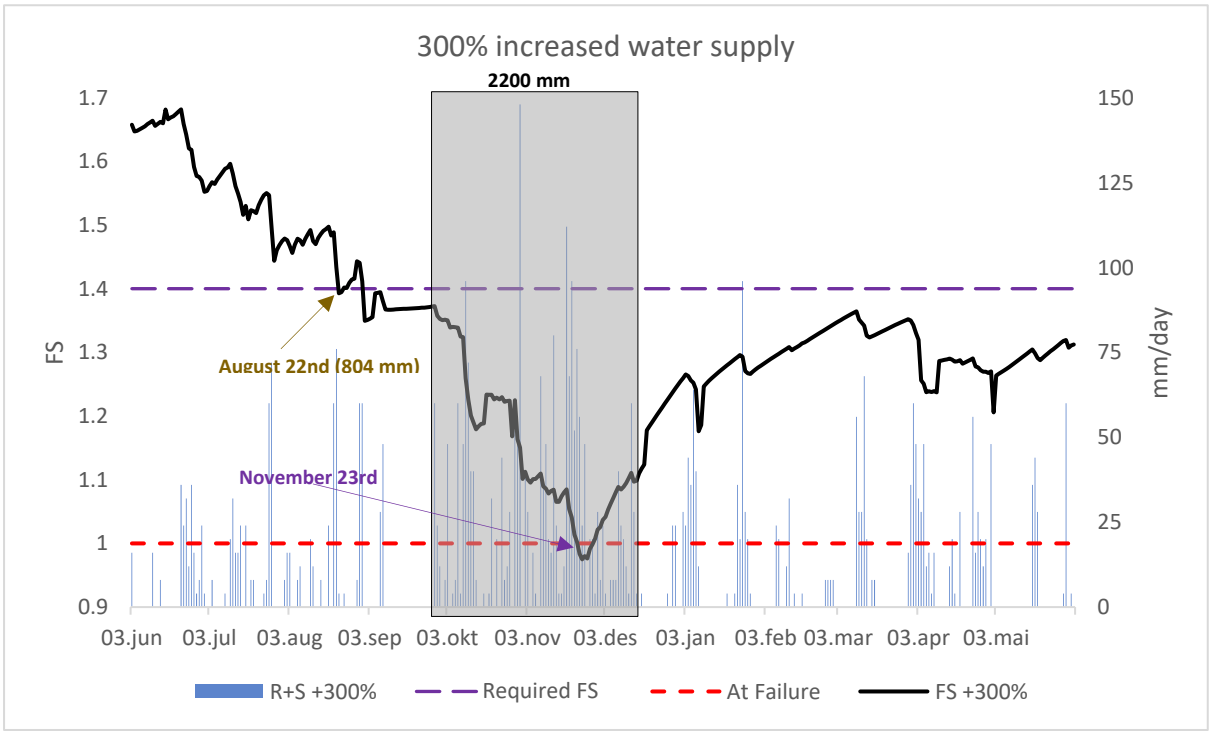

Figure 7-15. *Increasing water supply by the unrealistically high value of 300% to the measured daily water supply at Eidsvoll from June 3rd2000 to June 2nd 2001. Temperatures stay unchanged. The Factor of Safety falls below the requirements (FS 1.4) already on August 22nd, where the total water supply from June 3rd to August 22nd is 804 mm. A slope failure is indicated on November 23rd, where the water supply since June 3rd has reached 2812 mm.*

A 20% water supply increase from 3rd June 2000 to 2nd June 2001 (Figure 7-14) brings the slope's stability condition below the required Factor of Safety (FS 1.4) by January 8th. The period from June 3rd to January 8th has a total water supply of 1054 mm, whereas the period of consistent precipitation, September 28th to December 17th, provides a water supply of 660 mm (Figure 7-14). By increasing the daily water supply by the unrealistically high value of 300% from 3rd June to 2nd June (Figure 7-15), the Factor of Safety already falls below the requirements by August 22nd, due to high peaks and a total water supply of 804 mm from June 3rd to August 22nd. Furthermore, the simulation results indicate a slope failure on November 23rd, where the water supply since 3rd June has reached 2812 mm.

7.5.2 Increasing the daily temperatures

The historical observation data for daily temperatures from 3rd June 2000 to 2nd June 2001 (Figure 6-2) were gradually increased by 1 to 30°C (Figure 7-16) while the water supply remained unchanged. The minimum and average Factor of Safety for each simulation were determined (Table 7-25). The Factor of Safety does not fall below the geotechnical requirement (FS 1.4) by simply adjusting the temperature. The Factor of Safety increases as temperatures increase until 15 °C, suggesting a more stable slope. However, for temperatures above 15°C, the hydrological model does not produce appropriate results (Figure 7-16) (Table 7-25).

Table 7-25. *Simulations were conducted by systematically adding 1-30°C to the measured daily temperatures (TM) at Eidsvoll from 3rd June 2000 to 2nd June 2001, while maintaining the same water supply values (RR+S). The marked areas (grey) having temperatures exceeding 15°C indicate erroneous results and are not further used. The Factor of Safety is presented as the minimum and average value for each simulation.*

Year and increase (°C)	***Temperatures (°C)*** *Summer/Autumn/Winter/Spring*	***Minimum FS***	***Average FS***
2000-2001 + 0°C	13.8/ 7.5/ -4.1/ 2.8	1.46	1.58
2000-2001 + 1°C	14.8/ 8.5/ -3.1/ 3.8	1.46	1.58
2000-2001 + 2°C	15.8/ 9.5/ -2.1/ 4.8	1.46	1.58
2000-2001 + 3°C	16.8/ 10.5/ -1.1/ 5.8	1.46	1.58
2000-2001 + 4°C	17.8/ 11.5/ -0.1/ 6.8	1.47	1.58
2000-2001 + 5°C	18.8/ 12.5/ 0.9/ 7.8	1.47	1.59
2000-2001 + 6°C	19.8/ 13.5/ 1.9/ 8.8	1.47	1.59
2000-2001 + 7°C	20.8/ 14.5/ 2.9/ 9.8	1.47	1.59
2000-2001 + 8°C	21.8/ 15.5/ 3.9/ 10.8	1.48	1.60
2000-2001 + 9°C	22.8/ 16.5/ 4.9/ 11.8	1.48	1.60
2000-2001 + 10°C	23.8/ 17.5/ 5.9/ 12.8	1.48	1.61
2000-2001 + 15°C	28.8/ 22.5/ 11.0/ 17.8	1.53	1.67
2000-2001 + 25°C	38.8/ 32.5/ 21.1/ 27.8	1.65	1.92
2000-2001 + 30°C	43.8/ 37.5/ 26.2/ 32.8	1.45	1.73

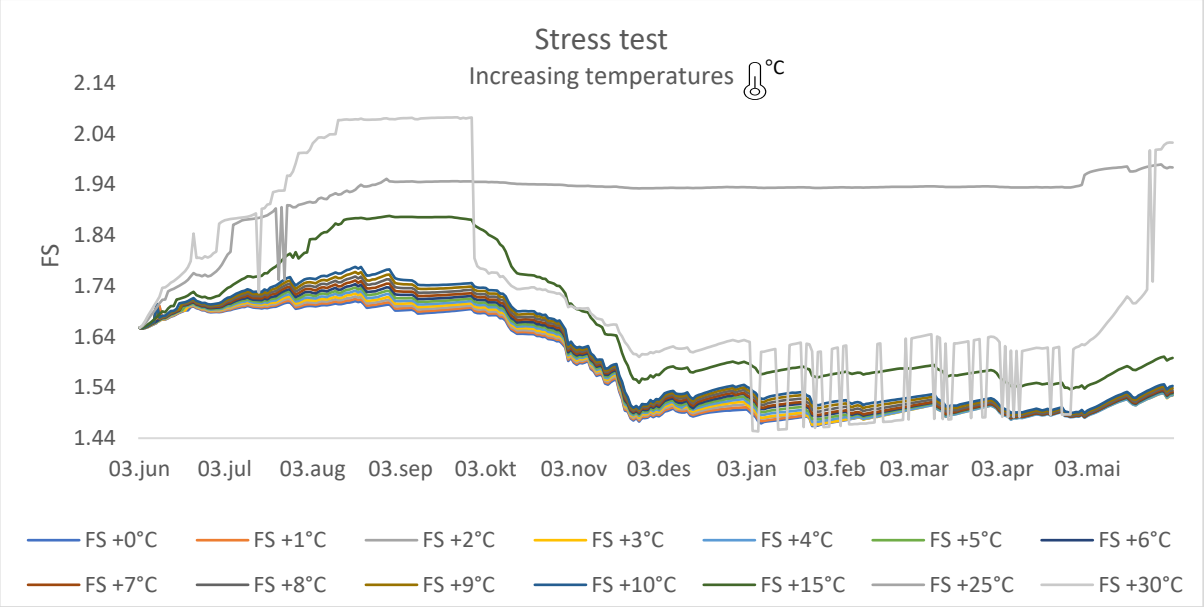

Figure 7-16. *Stress test by increasing only temperatures by progressively adding 1-30°C to the measured temperatures at Eidsvoll from 3rd June 2000 to 2nd June 2001, while water supply values stayed unchanged.*

7.5.3 Combining water supply and temperature increase with and without vegetation

Stress tests combining increasing water supply (1-300%) and temperatures (1- 15°C) (Ch 7.5.1 and 7.5.2) were performed using the hydrological model with and without vegetation (Figure 7-17a, b) where the minimum Factor of Safety was determined for each simulation (Table 7-26).

Using the vegetated model (Figure 7-17a) and the coupling of water supply and temperature increase, the Factor of Safety falls below the required geotechnical Factor of Safety (FS 1.4) at a 30%/3°C increase (Table 7-26). Generally, the Factor of Safety is slightly higher than the results obtained by only increasing the water supply (Table 7-24), which could be related to the models' incorporation of increasing temperatures. Temperature increases have been shown to improve the Factor of Safety in the slope (Table 7-25). Furthermore, the Factor of Safety suggests that the slope will not fail until an unlikely increase of 300%/15°C is reached (Table 7-26). The simulations using the hydrological model without vegetation (Figure 7-17b) shows a Factor of Safety below the requirements (FS 1.4) even before increased water supply, and temperatures are added to the measured data from 3rd June 2000 to 2nd June 2001 (0%/+0°C). In addition, a failure is shown to occur when water supply and temperature are increased by 250%/15 °C, implying that the slope will fail earlier without vegetation than with vegetation (Table 7-26). Furthermore, the minimum Factor of Safety decreases more rapidly in the model without vegetation than in the model with vegetation (Table 7-26).

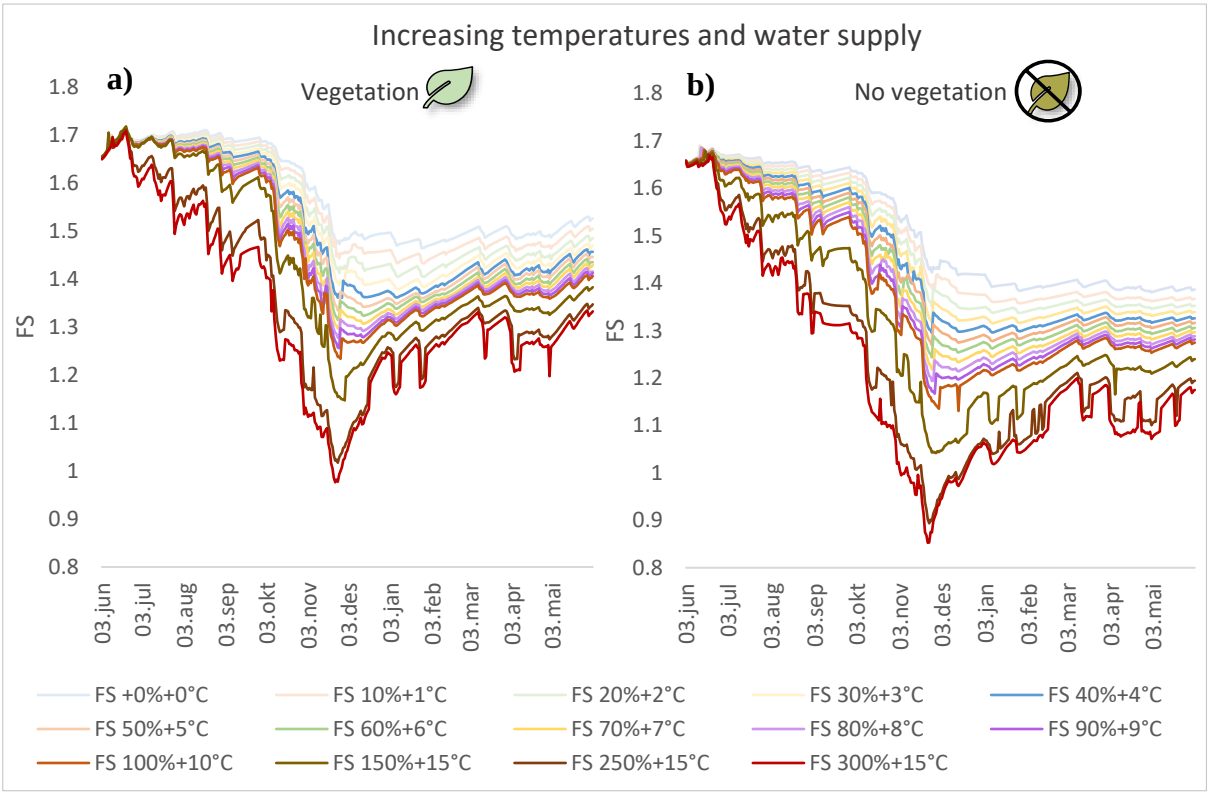

Figure 7-17. *Simulations were conducted by systematically increasing 10-300% and adding 1-30°C to the measured daily water supply and temperatures at Eidsvoll from June 3rd 2000 to June 2nd 2001. These simulations are run with the hydrological model in SEEP/W with vegetation (a) and without vegetation (b).*

Table 7-26. *Simulations were conducted by systematically increasing 10-300% and adding 1-30°C to the measured daily water supply (RR+S) and temperatures (TM) at Eidsvoll from 3rd June 2000 to 2nd June 2001. A Factor of Safety below the requirements (FS 1.4) is marked in purple. The FS after failure (<1) is marked in **red**. These simulations are run with the hydrological model in SEEP/W with vegetation (green column) and without vegetation (grey column) and are presented with the minimum Factor of Safety for each simulation.*

Year and increase (%/°C)	***Water supply (mm)***	***Temperature (°C) Summer/Autumn/ Winter/Spring***	***Minimum FS***	***Minimum FS (no veg)***
2000-2001+ 0% + 0°C	1199	13.8/ 7.5/ -4.1/ 2.8	1.46	**1.38**
2000-2001 + 10% +1°C	1327	14.8/ 8.5/ -3.1/ 3.8	1.43	1.35
2000-2001 + 20% +2°C	1447	15.8/ 9.5/ -2.1/ 4.8	1.40	1.33
2000-2001 + 30% +3°C	1568	16.8/ 10.5/ -1.1/ 5.8	**1.37**	1.31
2000-2001 + 40% +4°C	1688	17.8/ 11.5/ -0.1/ 6.8	1.36	1.29
2000-2001 + 50% +5°C	1809	18.8/ 12.5/ 0.9/ 7.8	1.33	1.26
2000-2001 + 60% +6°C	1930	19.8/ 13.5/ 1.9/ 8.8	1.31	1.24
2000-2001 + 70% +7°C	2050	20.8/ 14.5/ 2.9/ 9.8	1.29	1.21
2000-2001 + 80% +8°C	2171	21.8/ 15.5/ 3.9/ 10.8	1.27	1.19
2000-2001 + 90% +9°C	2291	22.8/ 16.5/ 4.9/ 11.8	1.25	1.16
2000-2001 + 100% +10°C	2412	23.8/ 17.5/ 5.9/ 12.8	1.23	1.13
2000-2001 + 150% +15°C	3015	28.8/ 22.5/ 11.0/ 17.8	1.14	1.04
2000-2001 + 250% +15°C	4221	38.8/ 32.5/ 21.1/ 27.8	1.01	**0.89**
2000-2001 + 300% +15°C	4824	43.8/ 37.5/ 26.2/ 32.8	**0.97**	0.85

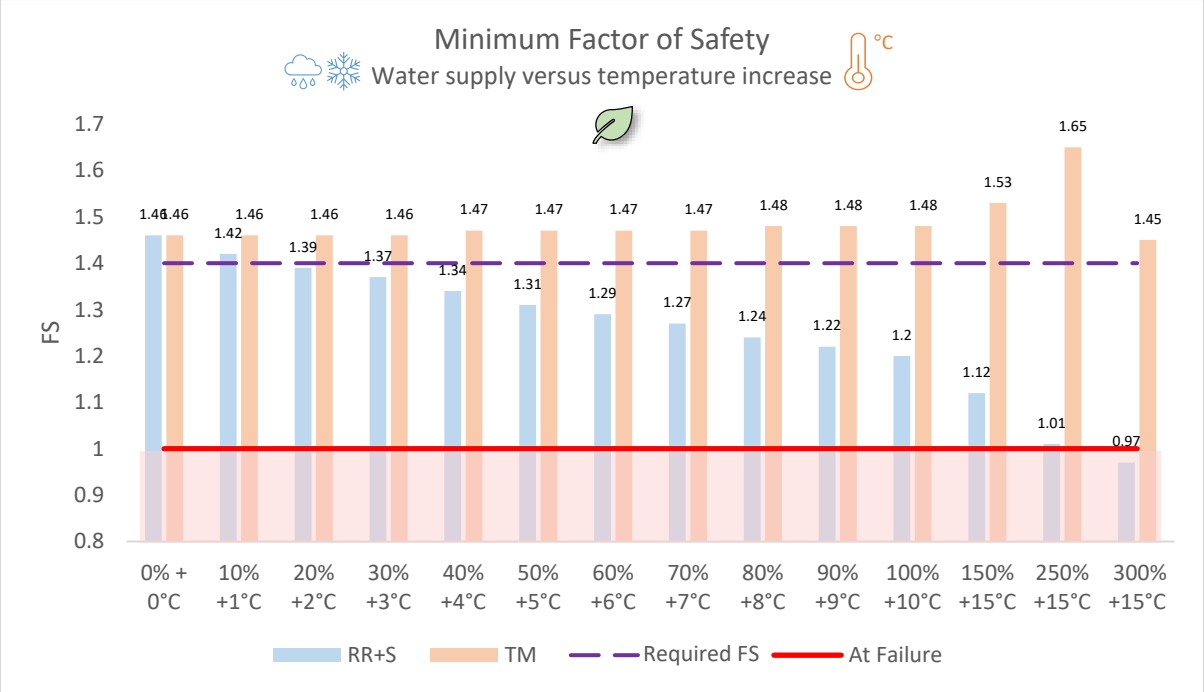

Figure 7-18. *The minimum Factor of Safety and a comparison of simulations where only the water supply(RR+S) is increased (blue) and only the temperatures(TM) increase (orange). The solid red line represents the slope at failure (FS=1), while the purple striped line represents the geotechnical requirement for the Factor of Safety (FS =1.4). The area below the red line indicates that the slope has already failed (FS<1). Between the purple striped and the red lines, the slope has not failed but is below the requirement for the FS (Jernbaneverket, 2016). These simulations are run with the hydrological model in SEEP/W with vegetation.*

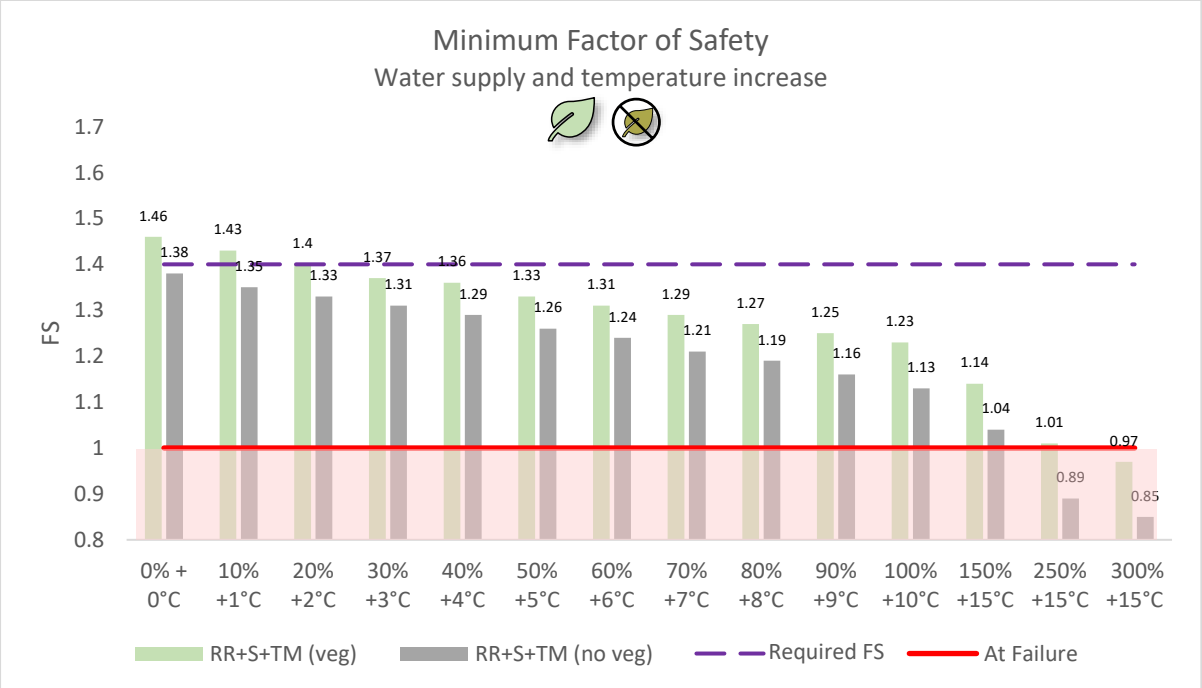

Figure 7-19. *The minimum Factor of Safety and a comparison of simulations where the water supply (RR+S) and temperatures (TM) systematically increase together (0%+0°C - 300%+15°C). The simulations are run with the hydrological model in SEEP/W with vegetation (green) and without vegetation (grey). The solid red line represents the slope at failure (FS=1), while the purple striped line represents the geotechnical requirement for the Factor of Safety (FS =1.4). The area below the red line indicates that the slope has already failed (FS<1). Between the purple striped and the red lines, the slope has not failed but is below the requirement for the Factor of Safety (Jernbaneverket, 2016).*

The stress test results show that increasing only the water supply reduces the slope's Factor of Safety (Table 7-24). The slope is predicted to fail at an improbable 300% increase in water supply (Figure 7-15). However, a 20% increase in water supply is predicted for the slope to fall below the required geotechnical Factor of Safety (FS 1.4) (Figure 7-14). Increasing the temperatures improves the Factor of Safety (Table 7-25) and indicates an opposite impact on slope stability than the water supply (Figure 7-18).

When temperatures and water supply increases together using the vegetated model (Table 7-26 and Figure 7-17a), the Factor of Safety falls below the required geotechnical Factor of Safety (FS 1.4) at a 30%/3°C increase, indicating that by also increasing the temperatures, the Factor of Safety decreases more gradually than when only the water supply is increased (Table 7-24).

Stability calculations using the hydrological model without vegetation (Figure 7-17b) show a Factor of Safety below the geotechnical requirements (FS 1.4) before increasing the temperatures or water supply (0%/+0°C) (Table 7-26). The slope will fail at a 250%/15°C increase, which is still a very unrealistic value but reflects that the stability of the slope is more sensitive if vegetation is removed (Figure 7-19).

8 Discussion

The following chapters discuss the elements which may cause uncertainty in the modelling phase, where all uncertainty factors and limitations that can affect the results are assessed. Then, the hydrological model's input parameters and how several factors may influence slope stability in a future climate are evaluated.

8.1 Calibration of the hydrological model

Piciullo et al. (2022a, b) discovered that antecedent precipitation conditions influenced the soil's VWC at the beginning of the analysis period in 2019. Rainfall-induced landslides are frequently triggered by wet antecedent conditions followed by days of intense rainfall (Baum et al., 2005). Before initiating simulations in SEEP/W, the initial state of the hydrological model must correspond to the actual conditions of the slope. However, it is not feasible to manually assign a customized VWC profile in the SEEP/W module (GEO-SLOPE 2022a). A prelaminar calibration was conducted to replicate the in-situ conditions recorded by the installed sensors by fitting the measured VWC profile to the modelled one (Piciullo et al., 2022a, b; Figure 8-1).

Real-time in-situ measurements cannot provide information on future VWC and PWP; thus, no comparison could be made between the in-situ measurements and hypothetical future predicted VWC profiles in the slope. Consequently, the hydrological model could not be re-calibrated for future slope conditions. Therefore, the calibrated initial slope conditions in

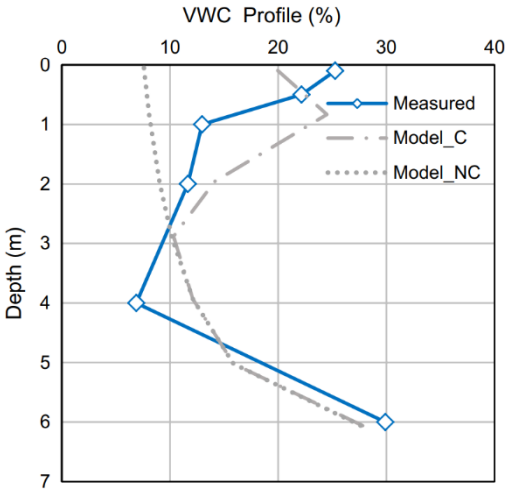

***Figure 8-1**. Initial VWC profiles: measured to date 03 June 2019 (continuous blue line), modelled non-calibrated (NC) and modelled calibrated (C) (Piciullo et al., 2022a, b).*

2019 are used when conducting simulations based on future climate data. However, due to the anticipated increase in precipitation, the conditions in 2019 cannot accurately reflect the future VWC and PWP conditions. Since VWC and PWP evolve over time, ideal VWC and PWP levels representative of future slope conditions are only attained after a period of time. This might result in wrong predictions at the beginning of each simulation and a higher Factor of Safety than if the future slope conditions were adjusted before starting the simulations.

8.2 Constraints on the examination of ground conditions and soil properties for modelling purposes

The soil water retention curves (SWRCs) were obtained in the laboratory using a pressure plate apparatus (Heyerdahl et al., 2018). Experimental in situ tests can give different SWRCs results where the variability of hydraulic parameters for a field-based SWRC is less than for a laboratory-based SWRC (Thomas et al., 2018). Significant discrepancies may exist between predicted and observed results if wetting and drying hysteresis' influence on soil hydraulic and mechanical behaviour is neglected (Kool and Parker, 1987; Mitchel and Mayer, 1998). Since standard stationary equilibrium measurements of drying and wetting curves for a broad range of soil water pressures can take several months (Shein and Mady, 2018), it is easier to derive van Genuchten model parameters from the initial drying SWRC (Zhao et al., 2020). At a given suction, the soil moisture for the drying curve is usually more significant than the value for the wetting curve (Hillel, 1980; Shein and Mady, 2018). Wetting and drying curves are recommended for irrigation mode calculations and research on other soil moisture migration problems (Gurin and Terleev, 2012; Poluektov and Terleev, 2002). In natural slopes with unsaturated clayey and silty sand that can undergo significant shear strength changes upon wetting or shallow landslides that can be triggered by wetting, accurate assessments of unsaturated strength parameters are important (Patil et al., 2017). Although the wetting curve is recommended for better characterizing unsaturated flow conditions leading to slope failure (Ebel et al., 2008; Chen et al., 2017), SWRCs could only be calculated for the drying phase (Heyerdahl et al., 2018). A better evaluation of the slope's in-situ wetting–drying cycles at Eidsvoll could improve the modelling phase (Piciullo et al., 2022a, b).

Cohesion is one of the main strength parameters and substantially impacts slope stability (Harabinová and Panulinová, 2020). High moisture content in the soil mass reduces cohesion (Roscoe et al., 1958). During intense precipitation, the apparent cohesion decreases, resulting in decreased shear strength, possibly leading to slope failure (NGI, 2014). However, the slope's cohesion was not easily determined as only one cylinder sample of undisturbed material was successfully retrieved due to difficulties of firm ground and was only partially filled with soil when extracted. Due to limited test samples, cohesion was chosen arbitrarily, and Heyerdahl et al. (2018) concluded that the shear strength parameters might be better than assumed. Therefore, the cohesion used in the analysis may not reflect the actual in-situ conditions.

8.3 Sensitivity analysis of the hydraulic properties

The soil's hydraulic properties are a primary contributor to controlling the rate of water infiltration into soils (Hou et al., 2021; Ashok et al., 2020; Reid et al., 1988), which are mainly influenced by various inherent soil properties such as the hydraulic conductivity and the anisotropy ratio of the soil profile (Reid et al., 1988; Greco et al., 2017; Haghnazari et al., 2015; Johnson, 1963; Rahimi et al., 2011). Also, the material's hydraulic conductivity plays a significant role in regulating water flow. Water flow through a material with varying conductivity impacts the pore water pressure distribution and can cause increased pore pressure locally, thereby increasing the risk of failure (Reid et al., 1988). The failure surface is assumed to be beneath the water table in most landslide hazard assessment methods, and the perception of water-induced landslides is that the failure surface is saturated and influenced by positive pore-water pressures (Godt et al., 2009). Furthermore, the prevalent theory for failure surfaces occurring above the water table proposes that positive pore water pressures develop when part of the soil becomes saturated during the transient infiltration processes (Sidle and Swanston, 1982; Reid et al., 1988; Johnson and Sitar, 1990). However, Godt et al. (2009) discovered that a shallow landslide occurred under partially saturated soil conditions despite the apparent absence of positive pore water pressures, indicating that a shallow slope failure may occur before the development of positive pore pressures. Godt et al. (2009) also identified that the transient reduction of suction stress during infiltration could reveal failure-prone stress and moisture conditions. These findings emphasize the importance of using reliable input values for the slope's hydraulic properties when performing a slope

stability analysis, as they may significantly influence the development of VWC and PWP and, thus, impact slope stability.

Generally, the saturated hydraulic conductivity is assumed to be the same in both directions in engineering practice; however, this does not account for possible inhomogeneities in the soil texture often found in situ (Hong et al., 2019; Piciullo et al., 2022a; Wang et al., 2018). At the Eidsvoll slope, the upper soil layers of approximately 9 m (layers 1 and 2) are not homogeneous as the silt fraction increases with depth while the sand fraction decreases (Heyerdahl et al., 2018). Due to the gradual change in grain size distribution and the absence of distinct boundaries, it is challenging to characterize the slope for modelling purposes, as only homogenous layers can be simulated (Piciullo et al., 2022a), which can substantially limit the modelling of the actual hydraulic conditions (Yeh and Tsai, 2018). The anisotropy ratio in SEEP/W must be specified carefully and cautiously, as laboratory-measured anisotropy may not represent the actual field conditions (Geo-Slope,2022a). However, in this thesis, the sensitivity analysis on the hydraulic conductivity and the anisotropy ratio was specified by adjusting model predictions to in-situ measurements of the VWC and PWP sensors.

The sensitivity analysis improved the agreement between predicted and measured VWC and PWP. The input data (i.e., hydraulic conductivity and anisotropy ratio) was defined to further improve the reliability of the hydrological model, with the best agreement being targeted at 6 m depth. Furthermore, because there are installed sensors for both variables at 6 m depth, it allows for simultaneously comparing both VWC and PWP at this depth.

The PWP and VWC sensors have been installed and monitored since May 2016. The measurements have shown a fluctuating PWP at 6 m, with positive PWP observed during rainfall and snowmelt seasons (October-April), indicating that PWP is influenced by a seasonally changing water table that shifts between roughly 7 and 5.5 m depth (Piciullo et al., 2022a) due to increased water infiltration. As water infiltrates, the water content increases, matric suction decreases and reduces the shear strength, which may induce slope failure (Reid et al., 1988; Yong, 2004; Anon, 1999; Zhang et al., 2015; Gasmo et al., 2000). According to Godt et al. (2009), the reduction of suction stress during infiltration may be an effective mechanism for shallow failures on steep slopes and where permeable substrates underlie soils. The steep upper part of the slope (>45°) at Eidsvoll is made up of a 6 m thick unsaturated layer underlain by a 3 m partially saturated and permeable layer further

emphasizes the significance of concentrating the sensitivity analysis at the PWP fluctuation zone at 6 m depth.

Overall, simulation 43 provided the best accuracy when considering the VWC (Figure 7-1b) and the PWP (Figure 7-1d) trends together at 6 m depth. The predicted and the measured VWC for simulation 43 shows satisfactory trends at 0.1-, 0.5-,1- and 6-m depths (Figure 7-3a, b, c, and f). At depths of 2 and 4 m, however, the model could not predict the observed VWC, which preserves a relatively flat trend with quite low measured VWC values. This disparity can be traced to using drying curves as SWRC (Ch. 8.1) and the potential existence of a higher hydraulic conductivity soil lens between 2 and 4 m depth (Piciullo et al., 2022a). However, a 2D model cannot adequately capture the spatial variability of the slope's moisture content (Piciullo et al., 2022a; Uhlemann et al., 2017). Although the predicted and the measured PWP for simulation 43 shows satisfactory trends at 6m, the PWP is less accurate in deeper layers (Figure 7-2b, c, and d). Since this study concentrates on the unsaturated upper portion of the slope (sandy silt) at Eidsvoll, as this section is of concern (Heyerdahl et al., 2018), the agreement between predicted and measured PWP and VWC at 6 m depth, i.e., the interface of layers 1 and 2, was the primary focus of the sensitivity analysis.

8.3.1 Future changes in anisotropy ratio and hydraulic conductivity

The hydraulic conductivity and anisotropy ratio were adjusted to best fit the in-situ measurements. These adjustments are made for measurements obtained between 2019 and 2020. Several factors, however, could cause hydraulic conductivity and anisotropic ratio to change in the future.

The hydraulic conductivity of soil is strongly influenced by particle size and packing. Since air is compressible, the volume of the soil pack can be reduced if the particles can reorganize, thereby changing the hydraulic conductivity and anisotropic ratio over time (Craig, 2004). Also, because the hydraulic conductivity of soils depends upon a fluid's viscosity, seepage velocity would increase due to global warming and increased temperatures (Fabius, 2008).

Moreover, changes in vegetation can either reduce or increase the near-surface permeability of the soils (Balzano et al., 2019). Rising air temperatures will result in a higher evapotranspiration rate and more abundant vegetation, resulting in a higher hydraulic conductivity (Crozier, 2010). Over time, the presence of roots may also reduce the permeability and hydraulic conductivity of soils, as roots can occupy the pores as they grow

and develop (Capobianco et al., 2020). However, roots may also form soil macro-pores and preferred flow paths, which improve soil permeability (Capobianco et al., 2021). How roots influence soil water conductivity remains unclear. Since this study did not address these issues, the same hydraulic properties of the unsaturated layers were used in all simulations.

8.4 Vegetation properties and additional atmospheric variables as input to SEEP/W

At Eidsvoll, vegetation may have a noticeable effect on slope stability. To account for the hydrological influence of vegetation on slope stability, the SEEP/W module uses, by default, the Penman–Monteith equation (Eq.28; Appendix B.III) for calculating potential evapotranspiration (Allen et al., 1998). When evapotranspiration is included, additional atmospheric conditions are needed (i.e., air temperature, relative humidity, wind speed, and solar radiation) to feed the Penman–Monteith equation, along with vegetation properties. This chapter discusses the influence of vegetation and prospective future changes to atmospheric variables where the hydrological model's input parameters are evaluated.

8.4.1 Vegetation's influence on slope stability

Several factors, including vegetation, must be considered when assessing slope stability. It has been proven that vegetation significantly influences slope stability; in particular, Meehan (1991) discovered that clear-cutting of forests increases the likelihood of slope failure by more than six times. According to Johnson et al. (2007), the same quantity of water saturation in the soil was obtained after only 39% of the rainfall compared to the conditions before vegetation clearing. For the hydrological modelling and evaluation of the pore water pressure regime in the ground at Eidsvoll, vegetation affects the stability where root reinforcement and hydraulic processes are essential.

In particular, the hydrological effect of vegetation on soil shear strength in partially saturated slopes is primarily given by a reduction in pore-water pressure due to the interception of rainfall that would otherwise have infiltrated into the soil and the resulting increase in soil suction through root water uptake for transpiration (Indraratna et al., 2006). The mechanical contribution of vegetation to soil reinforcement provided by plant roots contributes to increased shear strength, which is largely dominated by root diameter and depth (Preti and

Laio, 2010). Roots also bind soil particles, reducing their susceptibility to erosion. Loss of vegetation and, consequently, root cohesion contributes to shallow erosion, with the associated increases in water infiltration (Fabius, 2008). Increased infiltration could lead to loss of soil suction and a rise in the groundwater level.

However, suction due to evapotranspiration, particularly in the summer, is the most important potential benefit to slope stability in terms of vegetation (Pollen and Simon, 2010). Conversely, vegetation interception during rainfall events is almost negligible (Capobianco et al., 2021). In a ravine in South-Eastern Norway with similar geology to the Eidsvoll site, Capobianco et al. (2021) found that suction due to evapotranspiration is more pronounced in spring than autumn, which is not surprising since plant activity varies seasonally (Mancuso and Viola, 2015). Similar studies in different climate regions (Gonzalez and Mickovski, 2017; Comegna et al., 2013) confirmed that due to evapotranspiration, vegetation exerts its maximum suction during the dry seasons, confirming that plant–water uptake is the primary hydrological mechanism contributing to slope stability in the dry season. These findings are consistent with the instrumented sensor observations from the Eidsvoll slope, which shows a PWP increase from October to April and PWP decrease starting at the beginning of summer (Piciullo et al., 2022a, b).

8.4.2 Hydrological model settings for future vegetation characteristics

Capobianco et al. (2021) establish that combining trees, shrubs, and grass gives the highest reinforcement, suggesting this would be the best option for slope stability. In the spring, low-height vegetation has been shown to provide effective suction due to evapotranspiration, while trees provide the highest mechanical reinforcement. The slope at Eidsvoll is mainly dominated by birch trees but also consists of some degree of shrubs and grass in the sloping area. As input to the hydrological model, the vegetation height was set to 3 m, representing an average of the heights of shrubs and trees along the slope (Piciullo et al., 2022a, b).

To accurately assess vegetation's influence on slope stability, root reinforcement and the hydrological effect of vegetation should be considered (Capobianco et al., 2021). Mechanical reinforcement from root shear resistance is usually added to soil cohesion to obtain the total cohesion of the root–soil material (Dias et al., 2017). However, since no vegetation investigations have been conducted on the slope, this study did not include additional root cohesion in the slope stability analysis.

Climate change impacts on slope vegetation include a loss of root reinforcement due to changes in vegetation type or dying vegetation. Roots can be lost due to higher air temperatures, stronger winds, and thereby reduced air humidity (causing drought), or increased surface runoff and erosion from storms and severe rainfall events (Fabius, 2008; Mohsen and Ashtiani, 2019). Crozier (2010), on the other hand, examined many factors linking landslides to climate change and discovered that increased air temperatures would cause a higher evapotranspiration rate and more abundant vegetation, which may have positive effects on slope stability. Liptak et al. (2017) state that warming in high latitudes may extend growing seasons and promote vegetation growth. In the winter, higher air temperatures cause increased evapotranspiration; however, a lack of sunlit hours during the winter months may limit the vegetation's transpiration rates (Walker et al., 2010).

Although climate change will impact atmospheric variables (Chapters 8.4.3, 8.4.4 and 8.4.5) and thus the effect of vegetation, no additional changes to vegetation features were made considering future climate changes due to the limited information on the slope's vegetation features. The vegetation features were thus the same as in previous work by Piciullo et al. (2022a, b), selected from reference values and default values in the SEEP manual (Heat and Mass Transfer Modeling).

8.4.3 Future solar radiation and albedo as input to the hydrological model

Several sources of uncertainty are linked to future changes in natural forcings, such as solar radiation (Førland et al., 2007). The solar radiation was computed during solve-time by the SEEP/W model, where an albedo function must be defined. Studies by Stjern et al. (2009) discovered that variations in surface solar radiation in northern Europe showed a significant decreasing trend from the 1950s to the 1980s, followed by a slight increase, and pointed out that cloud cover and atmospheric circulation were the main influencing factors (Stjern et al., 2009). In high latitudes, reduced albedo variability is expected, resulting from melting snow and sea ice (Huntingford et al., 2013; Brown et al., 2017). The effect of albedo is influenced by the incoming solar radiation and cloud covers. However, due to the complexity of simulating cloud processes and microphysics (MacCracken et al., 2012; Stuart et al., 2013; Stjern et al., 2018), considerable uncertainty is connected to future changes in albedo at a local scale. Due to the challenges and complexity involved in predicting future albedo values, no further research on future albedo changes was made in this study. Additionally,

since vegetation cover was assumed to remain unchanged in the future (Ch. 8.4.2), the same albedo values obtained from the literature (Cherubini et al., 2017) were used for future slope stability calculations.

8.4.4 Future wind speed as input to the hydrological model

Global warming will involve new wind conditions (Fabius, 2008). High trees exposed to wind, transfer wind forces to the soil and decrease the shear strength on steeper slopes (Buma and Johnson, 2015; Pawlik, 2013). Also, high wind with direction downslope provides a lateral load to trees, creating an additional downward force acting on the slope (Wu et al., 1979). Storm-induced tree fall displaces soil, opens pits for enhanced water infiltration, and creates excess pore-water pressure in saturated soils, thus promoting slope instability (Valtera and Schaetzl, 2017; Wang et al., 2019). The wind is a prevalent driver of forest disturbance (Baumann et al., 2014; Peterson et al., 2019), where denser forest stands are more prone to landslides than open stands (Parra et al., 2021). Additionally, susceptibility increases on steep slopes (>40°) with high wind exposure (Buma and Johnsen, 2015) and are frequently disturbed by shallow landslides (Kramer et al., 2001).

The slope stability in Eidsvoll has shown to be more susceptible in the absence of vegetation (Ch. 8.7), implying that root reinforcements may play an important part in slope stability. However, since this is a steep slope (>45°) with dense and tall birch trees, the effect of winds may have an adverse impact on the stability.

Several studies indicate that the most intense mid-latitude storms may become more frequent in a warmer climate (Lee et al., 2021). However, Førland et al. (2007) found no evident trend in strong wind frequency or changes in wind speed from 1961 to 2006 or for future wind conditions in Norway over the next 50-100 years. Furthermore, a low probability of changes in strong wind is anticipated for Akershus County until 2100, according to the climate profile (Figure 4-17). However, considerable uncertainty is connected to how wind speed and patterns will change in the future (Hanssen-Bauer et al., 2015).

Since the climate profile anticipates a negligible change in strong winds for Akershus County, the climate variables for wind speed used in the slope stability calculations were obtained from the nearest meteorological station (Senorge.no) using average wind speed records from June 3rd, 2021, to June 2nd, 2022. However, average daily wind speed may poorly reflect the effects of gusts of windstorms since average regional wind speed records

smooth out local variations (Parra et al., 2021). Therefore, it is reasonable to assume that wind speeds are higher than the average daily wind speeds used in the hydrological model.

8.4.5 Future relative humidity as input to the hydrological model

Relative humidity will vary significantly with the time of day and inversely with air temperature; warm air can hold more water vapor and has lower relative humidity than cold air (Allen et al., 1998). Due to global warming and more significant warming rates over land than the ocean, relative humidity over land is expected to decrease (Byrne and O'Gorman, 2018; Chadwick et al., 2016). However, IPCC's sixth main report from 2021 estimates a 0-2% decrease in relative humidity in Norway towards 2100 based on results from an ensemble of 30 climate models (Lee et al., 2021).

Several different values for relative humidity were tested in the initial simulations but showed no effect on the stability at Eidsvoll. Since the IPCC's estimates only suggest a fairly small change in relative humidity for Norway, the parameters for relative humidity were kept the same as in previous work by Piciullo et al. (2022a, b).

8.5 The use of climate model projections

General circulation models (GCMs) can describe the governing processes in the atmosphere, ocean, land surface, and sea ice. However, GCMs are insufficient for many aspects of regional and local scale estimates due to coarse horizontal and temporal scales. They are therefore downscaled using RCMs to represent the local effects of climate change. For RCMs resolution (~12 x 12 km), many important details are still lacking in areas with complex and variable topography, such as Norway. Data of higher spatial resolution is therefore required. Climate models can usually not provide higher spatial resolution, and further downscaling is necessary (Wong et al., 2016). The climate projections used in this thesis were downloaded at Klimaservicesenter.no; each grid cell from the regional climate model was divided into grid cells of 1 x 1 km to look at detailed processes at a local scale (Hanssen-Bauer et al., 2015).

Uncertainty linked to climate projections includes future anthropogenic emissions, natural climate variations, imperfect climate models, and weaknesses in downscaling techniques (Førland et al., 2007; Wong et al., 2016). Future anthropogenic emissions depend on several factors and can, to some extent, be compensated for by using several emission scenarios;

however, only the emission scenario RCP8.5 was used in the analysis of this master's thesis. Natural climate variations are due to internal variations in the climate system leading to unpredictable natural variability and unknown variations in natural external forces (e.g., solar radiation and volcanic eruptions), which can affect temperature and precipitation where the uncertainty is most substantial on a regional scale (Førland et al., 2007). There is also uncertainty linked to the various climate models' limitations and simplifications, which are a consequence of limited knowledge of the climate system where the main uncertainty is linked to parameters (e.g., description of clouds) and the structure of the model system (e.g., unknown forcing, physical and numerical treatment of processes and poor resolution in the global models). There are weaknesses in downscaling techniques in which simulations with different climate models and emission scenarios may give different projections (Førland et al., 2007; Nilsen et al., 2022). Furthermore, considerable uncertainty is linked to extreme events at specific localities. Natural variance, downscaling methods, and model error can all be partially compensated for by combining several climate models and determining the median of the models (Hanssen-Bauer et al., 2015). In this way, part of the uncertainty can be limited, but it cannot be ruled out that future climate change may fall outside the intervals. An ensemble of ten EURO-CORDEX simulations resulting from five GCM and four RCM were used in this master's thesis to limit the uncertainty associated with the use of climate projections and make the estimates more robust.

8.5.1 Advantages and disadvantages using climate projections in slope stability modelling

The primary drawback of downscaling methods is that the fundamental hypotheses are difficult to verify and cannot be proven. However, the data can be calibrated when projected precipitation and temperature records for the past and future are accessible (Gariano and Guzzetti, 2016). Additionally, many downscaling methods do not generate a sufficiently extensive set of parameters at short intervals (i.e., hourly), which is essential for hydrological modelling (Walker et al., 2010). For several reasons, climate models can contain systematic deviations from observations, such as lower temperatures or more precipitation than observed. Bias adjustment corrects systematic deviations when analysing threshold-dependent changes. If climate model systematic deviations are not adjusted against observations, a cold climate model may extend the snow season, and a wet climate model may shorten it (Wong et al., 2016). Despite their drawbacks, high-resolution climate and

hydrological projections represent a valuable data source for different types of climate impact studies at a national and local scale (Wong et al., 2016). Evaluating the effects of climate variables on investigated slopes that provide information on the expected trend of stability conditions is a straightforward but time-consuming and computationally intensive process. The advantages of downscaling techniques are their physical compatibility with GCM output as they provide high-resolution climate information and manage weather extremes and prevalent weather patterns locally (Walker et al., 2010), as well as their applicability to existing slope stability engineering and hydrological modelling frameworks and associated software tools (Gariano and Guzzetti, 2016).

8.5.2 Obtaining future water supply and temperature values for model input

The proposed method for implementing climate projections is not suitable for the analysis conducted in this thesis (Ch. 6.5 and 6.5.1). Instead, precipitation, snowmelt and temperatures were estimated in terms of changes (in %, % and °C) (Ch. 6.5.2) and added to the measurements from 2000-2001 to determine future daily values (mm, °C) (Ch. 6.5.3) for model input (Figure 7-10a, c, e). This approach yields acceptable future daily, seasonal, and annual values because it accounts for the anticipated future changed trends with higher temperatures throughout the year, increased precipitation, and less snowmelt, particularly during winter and spring, as more precipitation will fall as rain rather than snow (Hansen-Bauer et al., 2015). However, the future estimated values do not consider different future scenarios for precipitation patterns, as expected in the future (Hansen-Bauer et al., 2015), which has been shown to affect the variation and outcome of the Factor of Safety (Figures 8-2c, d and 8-3). Instead, they build upon and reflect the same trend established by the measurements from 2000-2001.

In order to evaluate different future trends, one climate model was selected (Ch. 7.3.1). However, using only one climate model introduces significant uncertainty since various climate models may produce different outcomes (Figure 8-2a-d). Not only do they vary between models, but they also predict considerable variation (i.e., snowmelt and precipitation) from one year to the next within the same climate model (Tables 7-14 and 7-15). Thus, model selection has a substantial impact on the results (Figure 8-2a-d).

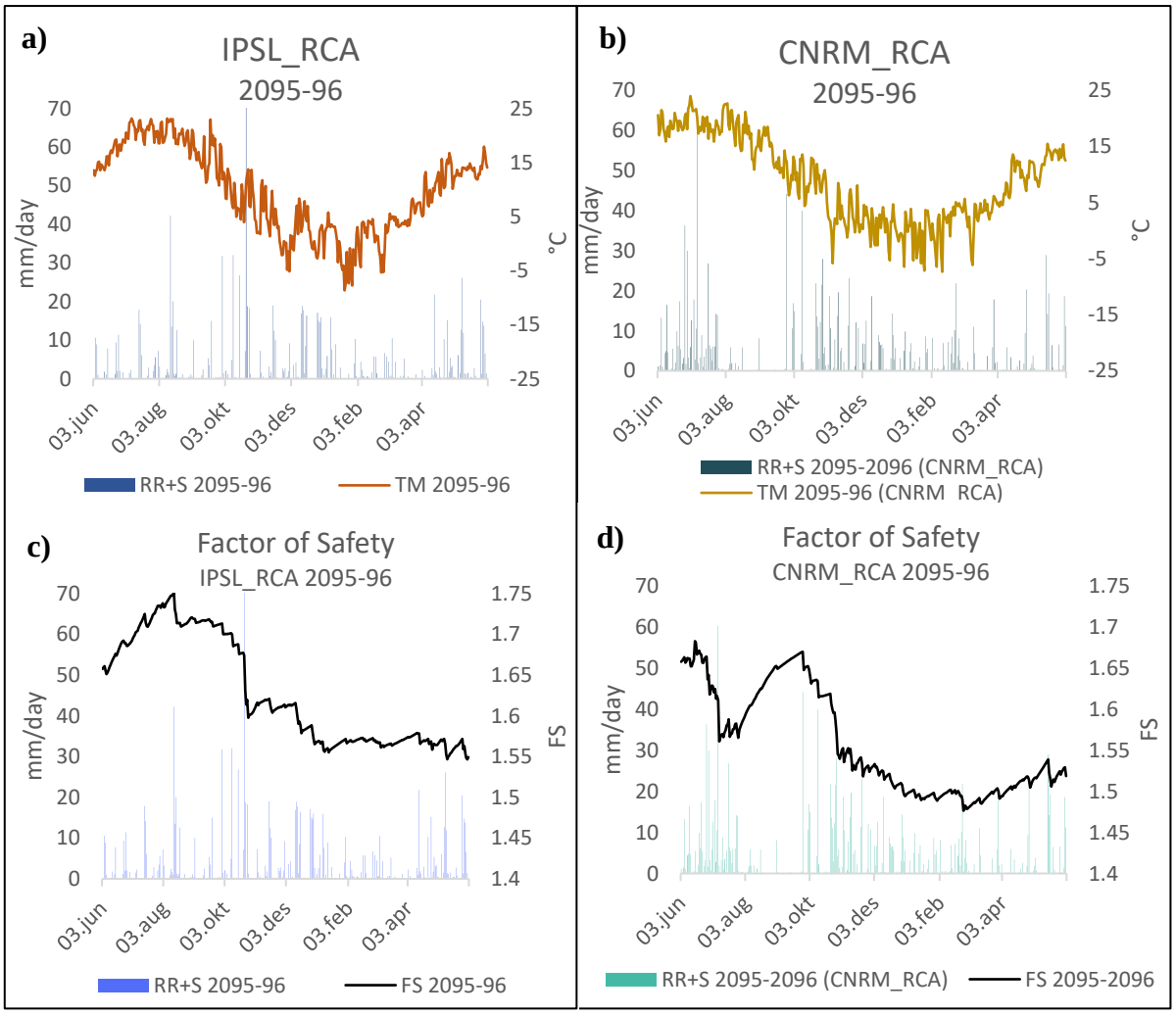

Figure 8-2. *Various climate models may produce very different results. Water supply and temperature patterns for a) IPSL_RCA model and b) CNRM_RCA model for the year 2095-96. The different outcome of Factor of Safety for c) IPSL_RCA model and d) CNRM_RCA model for the same year 2095-96.*

The CNRM_RCA model captured the annual water supply values for each of the estimated intervals (2046–2075 and 2076-2100) best. However, if a climate model was chosen based on the reference value for annual precipitation at Eidsvoll (785 mm) and the expected annual precipitation increase of 17.6 % (923 mm) by the end of the century, the CNRM RCA model for the year 2095-96 provides overestimated annual precipitation values (1285 mm); thus, other climate models may be better at capturing actual precipitation amount towards 2100. However, those analyses go beyond the purview of this study, as this work concentrates on extreme cases, such as the year 2000 (Jaedicke and Kleven, 2008).

The PWP regime mainly influences the slope at Eidsvoll due to water infiltration. It is, therefore, essential to point out that water supply has been emphasized when selecting the climate model. Temperature changes also influence slope stability and have been validated as a second priority after precipitation, showing good agreement. Climate models have shown to

be more consistent in predicting temperatures showing less disparity, and do not fluctuate as much as predictions for precipitation and snowmelt. To account for snowmelt in the computations, precipitation and snowmelt must be coupled as a single input for the hydrological model in GeoStudio; This also explains why the CNRM_RCA model was selected based on the best annual water supply agreement rather than considering annual precipitation and snowmelt separately.

8.5.3 Future water supply and temperature values

The results show good agreement between the estimated changes at Eidsvoll and the climate profiles estimates for Oslo/Akershus towards 2100. The highest increase in precipitation is expected during winter and spring (25-30 %), whereas summer will have minor increases (1.5-5 %) (Figure 7-5 and Table 7-2). In comparison, the CNRM_RCA model for the year 2095-96 predicts similar increases in precipitation during winter within the interval 2076-2100 (Table 7-17). Besides that, the model predicts a lower increase in the spring and a substantial increase in the summer. The model also predicts lower values during autumn compared to the interval 2076-2100 (Table 7-17), which could be explained by the historically high precipitation amounts recorded in the autumn of 2000, which the climate model does not consider.

The climate profile for Akershus/Oslo describes a 2–4-month shorter snow season anticipated for Akershus County at the end of the century, along with a significant reduction in snowfall frequency and accumulation. The estimated changes at Eidsvoll towards 2100 indicate significant reductions in the contribution of snowmelt, which drastically reduces during spring and winter compared to the reference year (Table 7-7), which is also supported by the CNRM_RCA model (Table 7-16). However, there are no snow water equivalent (SWE) or snowmelt statistics in the climate profile for Oslo/Akershus; hence, the estimated change in snowmelt at Eidsvoll cannot be verified.

8.6 Future slope stability

Because all simulations start with the same calibrated ground conditions (Ch. 8.1), they all exhibit the same initial Factor of Safety (FS 1.65) (Figure 8-3a, b). Since the hydrological model was not calibrated to future conditions, the slope stability's response to future water

infiltration may be slower than actual, as climate change is anticipated to result in wetter antecedent conditions, which require less precipitation to reach a critical level (Tacher and Bonnard, 2007). The slope is prone to shifting rainfall patterns, including rainfall intensity and duration, snowmelt contribution, and fluctuating temperatures throughout the year. These changes will impact the soil's VWC and PWP, which depend on the amount and rate of water infiltration into the soil. The simulations conducted for the estimated intervals (Figure 7-11a, c, e) follow the same trend and precipitation pattern as the measurements from 2000-2001 (Ch. 8.5.2), resulting in a similar trend for Factor of Safety (FS) in these simulations (Figure 8-3a). In comparison, the simulations conducted for the CNRM_RCA climate model predictions for the years 2000-2001, 2064-65, and 2095-96 (Figure 7-11b, d, f) shows a varying trend for the Factor of Safety because the distribution of water supply and temperature variables are different in each year (Ch. 8.5.2) (Figure 8-3b).

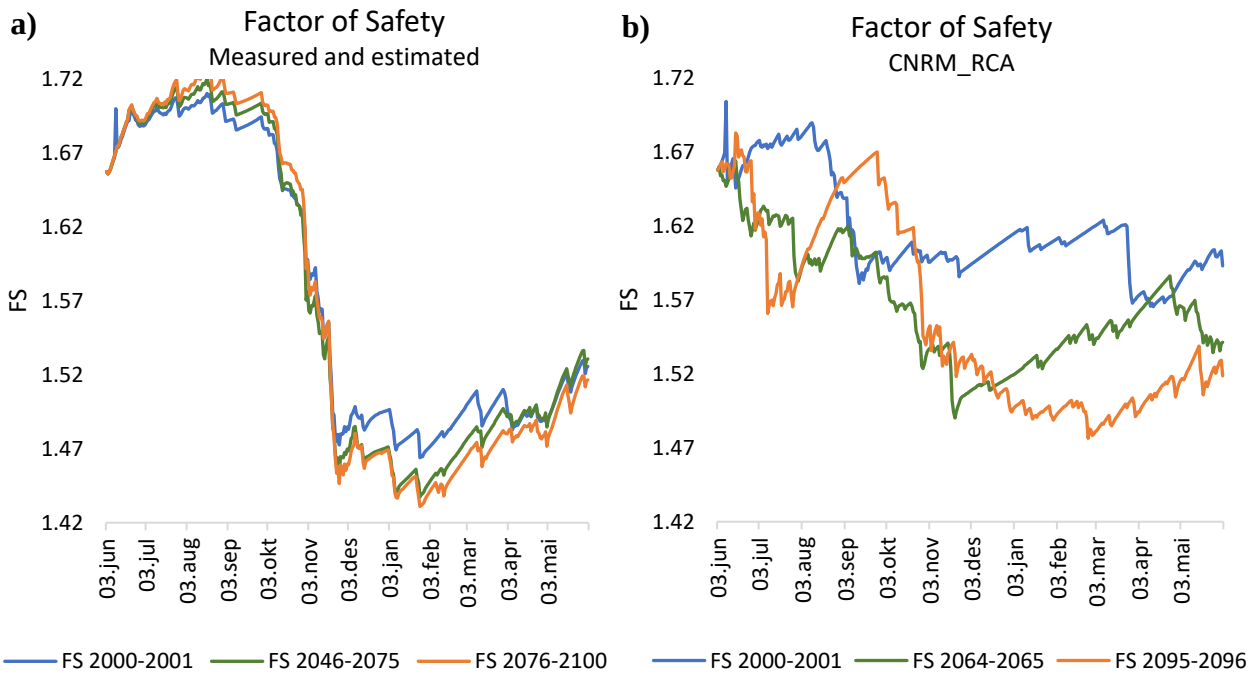

Figure 8-3. *The Factor of Safety (FS) over time (3 june-2 June) for;*
a) observation data of 2000-2001 and the estimated future changes for the intervals 2046-2075 and 2076-2100.
b) predictions by the CNRM_RCA model corresponding to selected years 2000-2001, 2064-2065, and 2095-2096 within the intervals 2000-2001, 2046-2075, and 2076-2100, respectively.

Prolonged precipitation and high precipitation- and snowmelt peaks reduce the Factor of Safety, particularly during and after persistent rainfall events, which is also confirmed by Heyerdahl et al. (2018). Furthermore, PWP and VWC sensor observations demonstrate that water infiltration significantly impacts slope stability at Eidsvoll (Piciullo et al., 2022a, b).

When the soil fails to drain water at the same rate as the excess water infiltrates, the volumetric water content increases, and the matric suction decreases as pore water pressures build up (Picarelli et al., 2012). Increased pore water pressures could reduce the soil's shear strength (Gasmo et al., 2000), which is critical for slope stability (Yong, 2004; Zhang et al., 2015; Gasmo et al., 2000). Landslides are frequently caused by rainwater infiltration (Chatra et al., 2019), and combined rainfall intensity and duration often trigger shallow landslides during extreme rainfall events (Turner and Schuster, 1996). Extreme precipitation leading to a high infiltration rate increases landslide probability by 90% (Haque et al., 2016; Sepúlveda, 2015; Wienhöfer et al., 2011). Chiang and Chang (2011) discovered that a 15% increase in the average annual maximum precipitation until the end of the century would reduce slope stability by 12%.

The CNRM RCA model predicts a higher Factor of Safety for all years (Table 7-23) than the measured and estimated intervals (Table 7-22), which may be due to the CNRM RCA model predicting a different distribution of water supply with less persistent rainfall that concentrates more in high peaks, allowing the soil to drain and adjust to the additional excess water during the dry periods (Turner and Schuster, 1996). However, when daily input data is used, the effect of short-term (<24-hour) precipitation is neglected, which may significantly impact slope stability (Ch. 8.8). Additionally, the CNRM_RCA model predicts that the most significant water supply will occur during the summer (Table 7-19). Ciabatta et al. (2016) discovered a substantial decrease in soil moisture in the warm/dry season due to evapotranspiration, and a moderate increase in rainfall intensity did not influence slope stability. The effect of evapotranspiration (Ch. 8.4.2) could suggest that the CNRM RCA's high prediction of water supply in the summer has less impact on the Factor of Safety than if an increase in water supply would occur in the cold/wet season.

Ciabatta et al. (2016) found that higher rainfall during the cold/wet season increased landslide frequency by more than 40% in the winter. Similarly, Bracko et al. (2022) estimated changes in precipitation levels by 2050 and found that increased precipitation is most important for slope stability, where the most significant changes are expected in the winter when precipitation in the lowlands is projected to fall as rain rather than snow. This is also observed for simulations conducted for the estimated intervals (Figure 7-11a, c, e), which reveal a minimum Factor of Safety occurring in the winter for all simulations (Table 7-22) due to the persistent precipitation throughout autumn, followed by a winter with continuous precipitation and snowmelt contributions. However, simulations conducted for the

CNRM_RCA climate model for the years 2000-2001, 2064-65, and 2095-96 (Figure 7-11b, d, f) (Table 7-23) show a minimum Factor of Safety occurring in April, November, and February, respectively. The minimum Factor of Safety occurring in April could be due to less persistent rainfall periods and more spread distribution of water supply (2000-01) and in November due to a higher water supply amount over the summer with continuous water supply in the autumn (2064-65) and in late February due to longer dry periods in late summer/early autumn (2095-96) which causes pore water pressure to stabilize in this period. Furthermore, the CNRM RCA model predicts higher winter temperatures in the future with less snowmelt compared to the simulations for the estimated intervals, which has been shown to affect slope stability positively (Ch. 8.7).

8.7 Slope stability using artificial temperature and water supply data

When increasing the water supply systematically (Table 7-24), the Factor of Safety falls below the required Factor of Safety (FS 1.4) after a water supply of 1054 mm (i.e., a 20% increase) (Figure 7-14). However, after a 300% increase, the Factor of Safety is below the required Factor of Safety (FS 1.4) after only 804 mm of water supply (Figure 7-15). This could be due to a higher water supply intensity causing more excess water to infiltrate the soil in a shorter period of time, resulting in a faster VWC and PWP response as the water cannot drain at the same rate as it infiltrates, and thus decreasing slope stability faster. In several studies (Hansen-Bauer et al., 2015; Lee and Kim, 2009; Chiang and Chang, 2011; Turkington et al., 2016; Comegna et al., 2013; Rianna et al., 2014; Saez et al., 2013; Stoffel et al., 2014), rainfall intensity has been shown to promote slope instability. Rainfall intensity is further discussed in chapter 8.8.

The 300% increase suggests a slope failure on November 23rd, following 2200 mm of continuous rainfall during the autumn (Figure 7-15). Although a 300% increase in the water supply is unrealistic, the results demonstrated that the combined intensity and duration of the water supply produce slope failure. On contrary, gradually increasing the temperatures improves slope stability (Table 7-25). Thota and Vahedifard (2021), Crozier (2010), Collison et al. (2000), Comegna et al. (2013), Glade (2003), Sidle and Ochiai (2006), and Wu (2013) all confirmed that an increase in temperature promotes slope stability. For example, Thota and Vahedifard (2021) discovered that raising temperatures from 25 °C to 55 °C produced

increased evaporation, reduced water content, increased suction, and thus improved slope stability.

When increasing both temperatures and water supply, the vegetated hydrological model requires a more considerable increase (i.e., 30%) for the Factor of Safety to fall below the requirements (FS 1.4) (Table 7-26). Due to the stabilizing effect of increased temperatures, the Factor of Safety decreases more gradually than when only increasing the water supply (Table 7-24). Consequently, the Factor of Safety is marginally higher than the results obtained when increasing the water supply alone (Table 7-25). However, using the hydrological model without vegetation when increasing the temperatures and water supply, the Factor of Safety is below the requirements (FS 1.4) before any additional increases in water supply, or temperatures (i.e., 0%/0°C) are introduced (Table 7-26). The slope is shown to fail at a temperature and water supply increased of 250%/15°C, suggesting that the slope will fail at a lower threshold if slope vegetation is not present (Figure 7-19).

The slope stability is more susceptible to water infiltration if vegetation is removed (Figure 7-19), also discussed in chapters 8.4.1 and 8.4.2. As a result, the minimum Factor of Safety decreases more quickly when vegetation is absent (Figure 8-4b) than when it is present (Figure 8-4a). A nearby slope at Eidsvoll experienced a slope failure in 2018 due to vegetation removal between 2016 and 2018, which increased precipitation and snowmelt infiltration into the ground (NGI, 2020). This incident highlights the impact of vegetation on slope stability, which may also be very important for the study site at Eidsvoll.

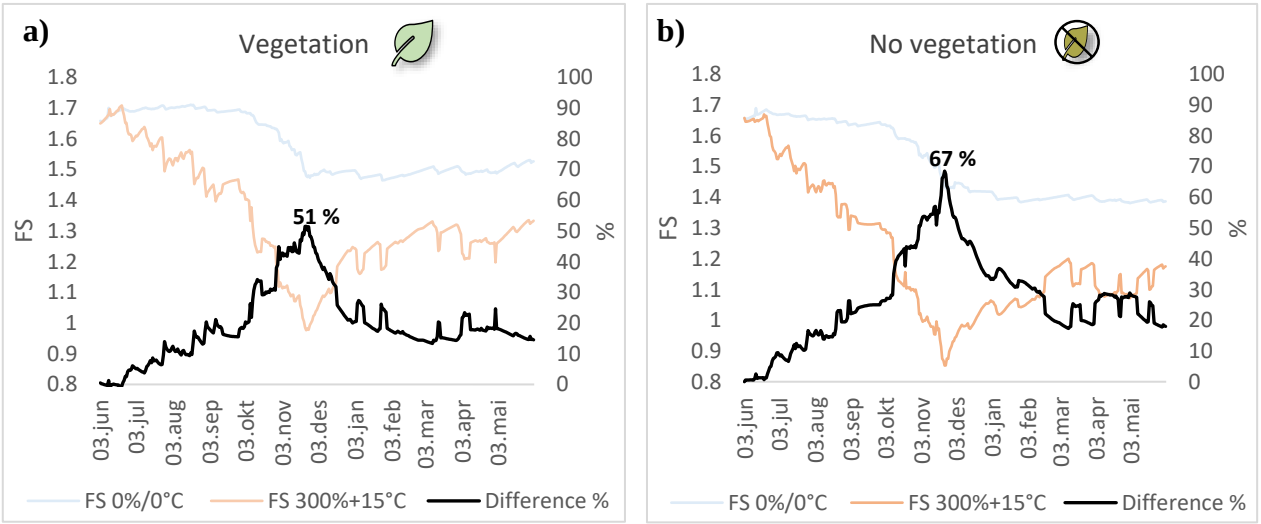

Figure 8-4. *Difference (in %) between FS from the 3rd June 2000 to 2nd June 2001 measurements (0%/0°C) and the FS for temperatures and water supply increases (300%/15°C) with a) Vegetated model b) Model without vegetation.*

8.8 The influence of rainfall intensity on slope stability at Eidsvoll

Climate change leads to shifts in rainfall patterns, with the mean annual precipitation predicted to concentrate on fewer rainy days, resulting in more intense rainfall events (IPCC, 2014) and more days with no rainfall (Strauch et al., 2015). Several studies have shown that extreme rainfall will increase more than average rainfall, both in intensity and frequency (Hanssen-Bauer et al., 2015; Førland et al., 2015; Dolva et al., 2016; Lawrence, 2016), and it is likely that under the RCP8.5 scenario, the number of days with intense rainfall will more than double by the end of the century in all seasons (Hansen-Bauer et al., 2015; Dyrrdal, 2019). Kristo et al. (2017) combined seepage and slope stability analyses and discovered a significant decrease in the Factor of Safety from 2003 to 2050 due to an increase in rainfall intensity. Saez et al. (2013) and Stoffel et al. (2014) anticipate that increased rainfall intensity will result in more frequent slope failures. A possible explanation is that a rise in atmospheric temperature will allow more water vapor to be stored in the atmosphere before falling back as precipitation, resulting in prolonged and more intense rainfall (Kristo et al., 2017). In steep terrain, these climate changes could increase the frequency of landslides linked to heavy rainfall and downpours in Akershus County (Hansen-Bauer et al., 2017).

How accurately downscaled values describe short-term precipitation in Norway using climate models are still being established and a more reliable basis for projections of intense short-term precipitation is necessary (Hansen-Bauer et al., 2017). According to preliminary research, the increase in intense rainfall for shorter durations (<24 hours) may be more substantial (i.e., 30% for 3-hour rainfall with a 5-year return period for RCP8.5) (Hansen-Bauer et al., 2017). Additionally, The Norwegian Centre for Climate Services (NCCS) is currently working on revising its report, "Climate in Norway 2100," which will be published in 2024, and the associated climate profiles in 2025. Based on the latest scientific evidence, the climate profiles will include updated climate adaptation guides for each county.

In this thesis, the slope stability analysis concentrates on daily water supply, which does not consider the impact of intense rainfall for shorter durations (<24 hours). However, intense short-duration rainfall may significantly impact slope stability at Eidsvoll and may even serve as the primary trigger of slope failure.

An attempt to determine the influence of hourly precipitation on slope stability at Eidsvoll was however conducted (Figure 8-5). Since the uncertainty associated with downscaled projections for short and intense rainfall are much higher than for prolonged rainfall (Gariano

and Guzzetti, 2016), simulations using hourly precipitation from historical observations were obtained instead. The hourly precipitation records were simulated over a 2-week period; however, as no changes were detected, only a rough increase of 0, 100, 300, and 500% were tested. Although better estimates can be obtained by following the recommendations for estimating climate effects for climate adaptations (Table 4-3) by the Norwegian Centre for Climate Services (NCCS). However, due to hydrological model constraints, these simulations did not yield acceptable results (Figure 8-5) and no further investigations were conducted. Since climate change predicts more intense rainfall by the end of the century, it emphasizes the importance of these calculations, which should be further evaluated in future studies to properly determine the impact of future climate on slope stability at Eidsvoll.

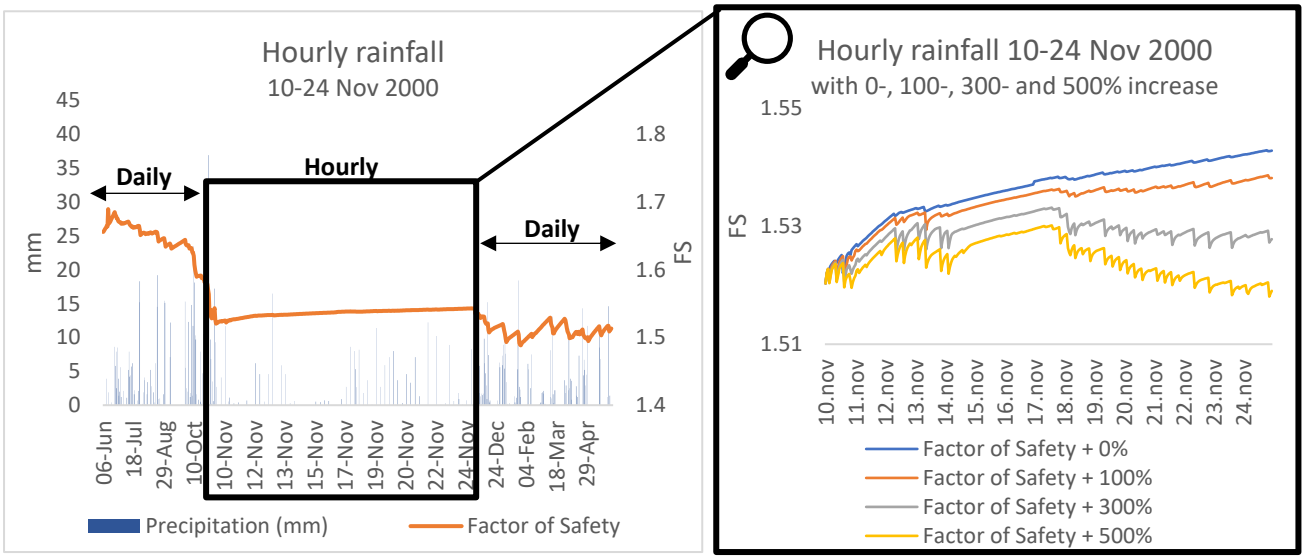

Figure 8-5. *Analysis on 2 weeks of intense hourly precipitation with roughly increasing the hourly rainfall values by 0, 100, 300 and 500%. However, as these simulations did not provide any reasonable results no further investigation were made.*

8.9 Summary of the main modelling uncertainties and limitations

- The hydrological model could not be re-calibrated for future slope conditions, which might result in wrong predictions at the beginning of each simulation and a higher Factor of Safety than if the future slope conditions were adjusted before starting the simulations.
- Due to limited test samples, cohesion was chosen arbitrarily and may not reflect the actual in-situ conditions. Additionally, since no vegetation investigations have been conducted on the slope, this study did not include additional root cohesion in the slope stability analysis.
- The sensitivity analysis improved the agreement between predicted and measured VWC and PWP from 2019-2020. However, several factors could cause hydraulic conductivity and anisotropic ratio to change in the future (e.g., higher evapotranspiration rates and the presence of roots).
- Using only one climate model introduces significant uncertainty. Not only do they vary between models, but they also predict considerable variation (i.e., snowmelt and precipitation) from one year to the next within the same climate model, which has been shown to affect the variation and outcome of the Factor of Safety. Therefore, model selection has a substantial impact on the results.

9 Conclusion

The main objective of this thesis was to investigate the influence of future climate on slope stability, define slope stability thresholds, and identify triggering factors leading to slope failure at the Eidsvoll case study.

A slope stability analysis was conducted by coupling a transient seepage analysis using the finite element method with a slope stability analysis using the limit equilibrium method through the numerical software GeoStudio (SEEP/W and SLOPE/W). Climate drivers (i.e., relative humidity, wind speed, albedo, solar radiation) and vegetation features obtained from literature as well as future snowmelt, precipitation, and temperature series obtained from downscaled climate projections, were introduced in an existing hydrological model. The slope's Factor of Safety was calculated for two future periods, 2046-2075 and 2076-2100, under the RCP 8.5 "business as usual" emission scenario. The slope's thresholds and triggering factors causing slope failure were determined through numerical stress testing of artificial water supply and temperature data.

The results of the analyses suggested:

- When expected precipitation and temperature changes until 2100 are added to the irregular year 2000, or a climate model with a higher annual water supply than the average is selected, the Factor of Safety still indicates a stable slope for all simulated cases. Additionally, all simulations show a Factor of Safety above the required geotechnical Factor of Safety of 1.4, which is the limit set by the railroad authorities.

- Despite increased water supplies and temperatures until 2100, the modelled change in Factor of Safety is relatively small.

- The slope stability is mainly influenced by intense and prolonged water supply due to water infiltration causing VWC and PWP to build up.

- Increased temperatures promote slope stability, which could be explained by increasing evapotranspiration rates reducing the pore water pressures.

- When simulations are conducted without vegetation, the Factor of Safety is below the required geotechnical Factor of Safety (FS 1.4) before introducing an increased water supply or higher temperatures. Removing vegetation could significantly influence slope stability as the VWC and PWP respond more quickly to water infiltration.

Despite the effect of climate change, the analysis shows a satisfactory Factor of Safety, indicating stable slope conditions. However, the analysis has limitations and may not accurately reflect the actual outcome when considering the following:

- Wet antecedent conditions are not considered due to the hydrological model's lack of calibration to future climate conditions, which may result in a higher Factor of Safety throughout the simulation.

- Since the climate projections are intended to provide statistics until the end of the century and because climate models interpret the world differently depending on their design, they should be combined rather than interpreted separately. Thus, determining the Factor of Safety using a single year from only one climate model is uncertain and could produce misleading results.

- Not including the impact of intense hourly precipitation in the analysis limits the overall understanding of future climate's influence on slope stability, as this is an important triggering factor for slope stability.

9.1 Suggestions for future work

Better and more precise climate predictions can be made as scientific evidence improves and a more reliable basis for climate projections is established (e.g., intense short-term precipitation), including the revised "Climate in Norway 2100" report from the Norwegian Centre for Climate Services (NCCS) and the updated climate adaptation guides, which will be published in 2024/25. Furthermore, the local weather station will provide more precise measurements of climate variables and may enhance future evaluations' modelling and monitoring phases. In addition, the new instruments installed in May 2022 will provide additional information regarding the slope in situ wetting cycles, enabling the SWRC to describe unsaturated flow conditions better and improve the modelling phase. Other elements that can improve the assessment of future slope stability at Eidsvoll include:

- The modelling phase might benefit from more details on the actual vegetation characteristics for the slope (i.e., vegetation types, root cohesion, and root depth).

- When testing with synthetic data, the input parameters for future albedo, solar radiation, relative humidity, and wind speed exhibit insignificant impacts on slope stability. However, in future studies, these parameters should be considered concerning local climate change to improve the accuracy of the analysis.

- The hydrological model did not produce acceptable results for hourly precipitation. However, the impact of intense hourly precipitation may be the most crucial factor in rainfall-induced landslides. Further assessments of the influence of climate change on slope stability at this site should include the impact of hourly precipitation.

Bibliography

Abramson, Lee W., Lee, Thomas S., Sharma S., Boyce, Glenn M. (2002). Slope Stability and Stabilization Methods (2nd ed.), *New York, USA: John Wiley & Sons.* ISBN 0-471-38493-3

Allen R. G., Pereira L. S., Raes D., Smith M. (1998). Crop evapotranspiration—guidelines for computing crop water requirements - FAO Irrigation and drainage paper 56. *Food and Agriculture Organization of the United Nation*s. ISBN 92-5-104219-5

Ameratunga J., Sivakugan N., Das B.M. (2016). Correlations of soil and rock properties in geotechnical Engineering. *Springer. Developments in Geotechnical Engineering. Das BM (ed), Henderson; Nagaratnam S (ed), Townsville.* ISBN 978-81- 322-2627-7. https://doi.org/10.1007/978-81-322-2629-1

Andersen, Bjørn G. (2000). Ice age Norway: landscapes formed by ice age glaciers. *Scandinavian University Press; Oslo: Universitetsforlaget.* ISBN 978-82-004-5366-6

Anon (1999). Definition of geotechnical engineering. *Ground Engineering, the magazine of the British Geotechnical Association, Vol. 32, No. 11,* 35-39.

Ashok Kumar Indoria, Kishori Lal Sharma and Kotha Sammi Reddy (2020). Hydraulic properties of soil under warming climate. *Climate Change and Soil Interactions, Elsevier,* 473-508. ISBN 978-01-281-8032-7. https://doi.org/10.1016/B978-0-12-818032-7.00018-7

Askari, F., and Farzaneh, O. (2008). Pore Water Pressure in Three Dimensional Slope Stability Analysis, *International Journal of Civil Engineering,6(1),* 10-23.

Askheim, S. (2020). Eidsvolls natur. *Store norske leksikon* (3.06.2022) https://snl.no/Eidsvolls_natur

Askheim, S. (2022). Eidsvoll stasjon. *Store norske leksikon* (3.06.2022) https://snl.no/Eidsvoll_stasjon

Aven, T. (2017). Improving risk characterizations in practical situations by highlighting knowledge aspects, with applications to risk matrices. *Reliability Engineering and System Safety*, 167, 42–48.

Balzano B., Tarantino A., Ridley A. (2019). Preliminary analysis on the impacts of the rhizosphere on occurrence of rainfall-induced shallow landslides. *Landslides 16(10).* pp.1885–1901. https://doi.org/10.1007/s10346-01901197-5

BaneNor, (1957). Eidsvoll-Minnesund km 72.93 - Ras i fyllingsskråning. *Rapport nr.: Gk 2403*

BaneNor (1967). Eidsvoll-Hamar km 70-80-Virkninger av flommen 1967. *Norges Statsbaner. Rapport nr.: Gk 3616*

Bane NOR (2016). Beskrivelse av pilotprosjekt: Skredvarsling basert på instrumentering. https://static1.squarespace.com

Baum R.L., McKenna J.P., Godt J.W., Harp EL, McMullen S.R. (2005). Hydrologic monitoring of landslide-prone coastal bluffs near Edmonds and Everett, Washington, 2001–2004. *U.S. Geological Survey Open-File Report 2005–1063,* 42 p.

Baumann, M., Ozdogan, M., Wolter, P.T., Krylov, A., Vladimirova, N., and Radeloff, V.C. (2014). Landsat remote sensing of forest windfall disturbance. *Remote Sensing of Environment, 143*. pp.171– 179. https://doi.org/10.1016/j.rse.2013.12.020

Benson, Craig and Chiang, I. and Chalermyanont, Tanit and Sawangsuriya, Auckpath (2014). Estimating van Genuchten Parameters α and n for Clean Sands from Particle Size Distribution Data. *Geotechnical Special Publication.* 410-427. https://doi.org/10.1061/9780784413265.033

Bergström, S. (1995). The HBV model. *In: Singh, V.P. (Ed.), Computer Models of Watershed Hydrology. Water Resources Publications, Highlands Ranch,* 443-476.

Bishop, A. W. (1955). The Use of The Slip Circle in the Stability Analysis of Earth Slope, *Geotechnique, 5(1),* 7-17.

Bishop, A. W. (1959). The principle of effective stress. *Teknisk Ukeblad, 106 (39),* 859–863.

Bondevik, S. and Sorteberg, A. (2020). Groundwater fluctuations during a debris flow event in Western Norway – triggered by rain and snowmelt. *Hydrology and Earth System Sciences, 25 (7),* 4147-4158. https://doi.org/10.5194/hess-25-4147-2021

Bracko, T., Žlender, B., Jelušic, P. (2022). Implementation of Climate Change Effects on Slope Stability Analysis. *Appl. Sci., 12, 8171.* https://doi.org/10.3390/app12168171

Bratli, H., Larsen, B. H. and Gaarder, G. (2005). Kartlegging av vilt og naturtyper i Eidsvoll kommune. *NIJOS rapport 13/2005.*

Brown, P.T., Y. Ming, W. Li, and S.A. Hill (2017). Change in the magnitude and mechanisms of global temperature variability with warming. *Nature Climate Change, 7(10),* pp. 743–748. DOI: 10.1038/nclimate3381.

Brundsen, D. (1979). Mass movements. In: Progress in geomorphology. *(C.E. Embleton and J.B. Thornes, Eds), Arnold,* 130-186.

Brunsden D. and Prior D.B. (1984). Slope instability. *John Wiley, Chichester. Earthquake Engng. Struct. Dyn, 13.* https://doi.org/10.1002/eqe.4290130313

Buma, J., and Dehn, M. (1998). A method for predicting the impact of climate change on slope stability. *Environmental Geology, 35,* 190-196.

Buma, J. (2000). Finding the most suitable slope stability model for the assessment of the impact of climate change on a landslide in southeast France. *Earth Surf. Process. Landf. 25, 565–582.* http://dx.doi.org/10.1002/1096-9837(200006)25

Buma, J., Dehn, M. (2000). Impact of climate change on a landslide in Southeast France, simulated using different GCM scenarios and downscaling methods for local precipitation. *Clim. Res. 15*, 69–81. http://dx.doi.org/10.3354/cr015069

Buma B., and Johnson, A.C. (2015). The role of windstorm exposure and yellow cedar decline on landslide susceptibility in southeast Alaskan temperate rainforests. *Geomorphology, Vol. 228. pp. 504-511.* DOI: 10.1016/j.geomorph.2014.10.014

Byrne, M.P., and O'Gorman, P.A. (2018). Trends in continental temperature and humidity directly linked to ocean warming. *Proceedings of the National Academy of Sciences, 115(19), 4863–4868*. DOI: 10.1073/pnas.1722312115

Capobianco, V., Cascini, L., Cuomo, S., Foresta, V. (2020). Wetting-Drying Response of an Unsaturated Pyroclastic Soil Vegetated with Long-Root Grass. *Environ. Geotech. 2020, 1–18.* DOI: 10.1680/jenge.19.00207

Capobianco, Vittoria, Kate Robinson, Bjørn Kalsnes, Christina Ekeheien, and Øyvind Høydal (2021). Hydro-Mechanical Effects of Several Riparian Vegetation Combinations on the Streambank Stability-A Benchmark Case in Southeastern Norway. *Sustainability* 13, no. 7: 4046. https://doi.org/10.3390/su13074046

Chadwick, R., Good, P., and Willett, K. (2016). A Simple Moisture Advection Model of Specific Humidity Change over Land in Response to SST Warming. *Journal of Climate, 29(21), 7613–7632*. DOI: 10.1175/jcli-d-16-0241.1

Chaithong, Thapthai and Soralump, Suttisak and Pungsuwan, D., and Komori, Daisuke (2017). Assessing the effect of predicted climate change on slope stability in northern thailand: A case of doi pui. *International Journal of Geomate, 13*. 38-48. DOI: 10.21660/2017.38.209764.

Chatra A.S., Dodagoudar G.R., Maji V.B. (2019). Numerical modelling of rainfall effects on the stability of soil slopes. *Int J Geotech Eng 13(5):* 425–437. https://doi.org/10.1080/19386362.2017.1359912

Chatwin, S.C., Howes, D.E., Schwab, J.W., and Swanston, D.N. (1994). A guide for management of landslide prone terrain in the Pacific Northwest, 2nd edition: *Research Branch, Ministry of Forests, Province of British Columbia, Victoria, British Columbia, Crown Publications.* ISBN 97-807-726-2059-0

Chen P., Mirus B., Ning L., Godt J.W. (2017). Effect of hydraulic hysteresis on stability of infinite slopes under steady infiltration. *J. Geotech Geoenviron Eng. 143(9):04017041*. https://doi.org/10.1061/(ASCE)GT.1943-5606.0001724

Cherubini, F., Vezhapparambu, S., Bogren, W., Astrup R., and Hammer A. (2017). Spatial, seasonal, and topographical patterns of surface albedo in Norwegian forests and cropland. *International Journal of Remote Sensing, 38:16,* 4565-4586, DOI: 10.1080/01431161.2017.1320442

Chiang, S.H., and Chang, K.T. (2011). The potential impact of climate change on typhoon-triggered landslides in Taiwan, 2010–2099. *Geomorphology*, *133*(3-4), pp. 143-151. https://doi.org/10.1016/j.geomorph.2010.12.028

Ciabatta, L., Camici, S., Brocca, L., Ponziani, F., Stelluti, M., Berni, N., and Moramarco, T. J. J. O. H. (2016). Assessing the impact of climate-change scenarios on landslide occurrence in Umbria Region, Italy. *Journal of Hydrology*, *541*, 285-295. https://doi.org/10.1016/j.jhydrol.2016.02.007

Cicero (2018). Oppdatering av kunnskap om konsekvenser av klimaendringer i norge. *CICERO Center for International Climate and Environmental Research, M-1209.* http://hdl.handle.net/11250/2582720

Coe, Jeffrey and Godt, Jonathan (2012). Review of approaches for assessing the impact of climate change on landslide hazards. *Landslides and Engineered Slopes, Protecting Society Through Improved Understanding: Proceedings 11th International and 2nd North American Symposium on Landslides and Engineered Slopes, Banff, Canada, 1, Taylor & Francis Group, London*, 371-377.

Colleuille, Boje, Devoli, Krøgli, Sund, Skaslien, Humstad, Frekhaug and Wiréhn (2017). Jordskredvarslingen. *Nasjonal varslingstjeneste for jord-, sørpe- og flomskredfare, NVE report nr.75*. ISBN 978-82-410-1628-8

Collison, A., Wade, S., Griffiths, J., and Dehn, M. (2000). Modelling the impact of predicted climate change on landslide frequency and magnitude in SE England. *Engineering Geology*, *55*(3), 205-218. https://doi.org/10.1016/S0013-7952(99)00121-0

Comegna, L., Damiano, E., Greco, R., Guida, A., Olivares, L., Picarelli, L. (2013). Effects of the vegetation on the hydrological behavior of a loose pyroclastic deposit. *Procedia Environ. Sci. 19*. pp. 922–931. https://doi.org/10.1016/j.proenv.2013.06.102

Coulomb, C. A. (1776). Essai Sur Une Application Des Maximis et Minimis a Queques problems Des Statique Relatifsa1‟ Architecture. *Nem. Div. Sav. Acad, Sci, 7*.

Craig, R.F. (2004). Craig's soil mechanics 7th edition. 2 Park Square. *Milton Park, Abingdon, Oxon.* https://doi.org/10.4324/9780203494103

Crozier M.J. (2010). Deciphering the effect of climate change on landslide activity: a review. *Geomorphology, 124, pp.* 260-267. DOI: 10.1016/j.geomorph.2010.04.009

Dehn, M., Buma, J. (1999). Modelling future landslide activity based on general circulation models. *Geomorphology 30 (1),* 175–187. http://dx.doi.org/10.1016/s0169-555(99)00053-7

Dehn, Martin and Bürger, Gerd and Buma, Jelle and Gasparetto, Paolo (2000). Impact of climate change on slope stability using expanded downscaling. *Engineering Geology. 55(3),*193-204. DOI:10.1016/S0013-7952(99)00123-4.

Dias, A.S., Pirone, M., Urciuoli, G. (2017). Review on the methods for evaluation of root reinforcement in shallow landslides. *In Proceedings of the World Landslide Forum, Ljubljana, Slovenia, 30 May–2 June*; *Springer: Cham, Switzerland*. pp. 641–648. DOI: 10.1007/978-3-319-53498-5_74

Dikau, R. and Schrott L. (1999). The temporal stability and activity of landslides in Europe with respect to climatic change (TESLEC): main objectives and results. *Geomorphology, 30*, pp. 1-12.

Dolva, Aunaas, Humstad, Myrabø, Petkovic, Thakur, Viklund, Øvrelid and Øydvin (2016). NIFS-sluttrapport: FoU-programmet Naturfare, Infrastruktur, Flom og Skred. *NVE-rapport 43/2016.*

Domenico, P.A. and Schwartz, F.W. (1998). Physical and Chemical Hydrogeology. *2nd Edition, John Wiley & Sons Inc., New York.* ISBN: 978-0-471-59762-9

Duncan J.M. (1996). State of the Art: Limit Equilibrium and Finite-Element Analysis of Slopes. *Journal of Geotechnical Engineering, 122,* 577-596. https://doi.org/10.1061/(ASCE)0733-9410(1996)122:7(577)

Dyrrdal, A. (2019). Klimapåslag for korttidsnedbør – Anbefalte verdier for Norge.*NCCS-report 5/2019.* Available online: NCCS-report 5/2019

Ebel B.A., Loague K., Montgomery D.R., Dietrich W.E. (2008). Physics-based continuous simulation of long-term near-surface hydrologic response for the Coos Bay experimental catchment. *Water Resour Res 44:W07417.* https://doi.org/10.1029/2007WR006442

Engen, Inger Karin (2016). Varsling av flom og jordskredfare:Hva gjør vi? Hva forventer vi? Gjeldende varslingsrutiner. *NVE.* (22.09.2022) https://www.statsforvalteren.no

Erikstad, L. and Halvorsen, G. (1992). Områder med nasjonal og internasjonal naturverdi ved Hauerseter-trinnet, Akershus fylke. *Norsk institutt for naturforskning; NINA oppdragsmelding 136.*

Fabius, Mike and K. Fabius (2008). Impact of global warming on stability of natural slopes. Available online: https://www.semanticscholar.org/paper/

Falstad, B. (2001). BanePartner: Stabilitetsproblematikk Dovrebanen, Oslo-Hamar, km 69-71. *Jernbaneverket Region Øst. Rapport nr.: Gk 4608-1*

Fredlund, D.G. (1984). Analytical Methods for Slope Stability Analysis. *Proceeding of the Fourth International Symposium on Landslides, State-of-the-Art, Toronto, Canada,* 229-250.

Fredlund D.G., Rahardjo, H. (1993). Soil mechanics for unsaturated soils. *New York: John Wiley & Sons.* DOI:10.1002/9780470172759

Fredlund, Delwyn and Xing, Anqing and Fredlund, Murray and Barbour, Sidney (1996). The relationship of the unsaturated soil shear strength to the soil-water characteristic curve. *Canadian Geotechnical Journal - CAN GEOTECH J. 33.* DOI: 440-448.10.1139/t96-065

Fredlund D.G., Rahardjo H, Fredlund M.D. (2012). Unsaturated soil mechanics in engineering practice. *New York: John Wiley & Sons.* DOI:10.1002/9781118280492

Freeze, R.A., and Cherry, J.A. (1979). Groundwater. *Prentice-Hall Inc., Englewood Cliffs, Vol. 7632, 604.* ISBN 978-0133653120

Fu, Jian-Jun; Chen, Cheng; Ferellec, Jean-Francois and Yang, Juan (2020). Effect of Particle Shape on Repose Angle Based on Hopper Flow Test and Discrete Element Method. *Advances in Civil Engineering. 2020: 1–10.* DOI:10.1155/2020/8811063

Furseth, A. (2006). Skredulykker i Norge (1st Ed.). *Tun Forlag, Oslo.* ISBN: 9788252930436

Førland, E., et al. (2007). Climate change and natural disasters in Norway – An assessment of possible future changes. *met.no report 6/2007*. ISSN 1503-8025. Available online: MET-report-06-2007

Førland, E.J., Mamen, J., Dyrrdal, A.V., Grinde, L. and Myrabø, S. (2015). Dimensjonerende korttidsnedbør. *MET rapport 24-2015 / NVE rapport nr 134-2015*.

Gariano, S.L., and Guzzetti, F. (2016). Landslides in a changing climate. *Earth-Science Reviews, Volume 162,* pp. 227-252. ISSN 0012-8252. https://doi.org/10.1016/j.earscirev.2016.08.011

Gasmo, J.M., and Rahardjo, H., and Leong, E. (2000). Infiltration effects on stability of a residual soil slope. *Computers and Geotechnics, 26.* 145-165. https://doi.org/10.1016/S0266-352X(99)00035-X

GEO-SLOPE (2022a). Heat and Mass Transfer Modelling with GeoStudio. *International Ltd*. 73 p. Available online: Heat and Mass Transfer Modeling.pdf (geoslope.com)

GEO-SLOPE (2022b). Stability Modelling with GeoStudio. *International Ltd.* 255 p. Available online: Stability Modeling with SLOPE/W (geoslope.com)

Glade, T. (2003). Landslide occurrence as a response to land use change: a review of evidence from New Zealand. *Catena*, *51*(3-4), 297-314. https://doi.org/10.1016/S0341-8162(02)00170-4

Godt, J. W., Baum, R. L., and Lu, N. (2009). Landsliding in partially saturated materials, *Geophys. Res. Lett.*, *36, L02403,* DOI:10.1029/2008GL035996

Gonzalez-Ollauri, A., Mickovski, S.B. (2017). Hydrological effect of vegetation against rainfall-induced landslides. *J. Hydrol. 2017, 549, 374–387.* https://doi.org/10.1016/j.jhydrol.2017.04.014

Greco R, Comegna L, Damiano E, Guida A. (2017). Investigation on the hydraulic parameters affecting shallow landslide triggering in a pyroclastic slope. In: *Mikoš M et al (eds) Fourth world landslide forum. Advancing culture of living with landslides. vol 2*, 659–667. https://doi.org/10.1007/978-3-319-53498-5

Gurin, P.D., and Terleev, V.V. (2012). The way to simulate soil water retention capability considering hysteresis. *Proc. Int. Conf. Agriculture Physics under Climate Change: Development Trends (Agrophysical Scientific Research Institute, St. Petersburg, Sept. 20–21, St. Petersburg, 2012.*

Guthrie, R.H., Mitchell, S.J., Lanquaye-Opoku N., Evans S.G. (2010). Extreme weather and landslide initiation in coastal British Columbia. *Q. J. Eng. Geol. Hydrogeol., 43,* pp. 417-428. DOI: 10.1144/1470-9236/08-119

Haghnazari, F., Shahgholi, H., and Feizi, M. (2015). Factors affecting the infiltration of agricultural soils. *International Journal of Agronomy and Agricultural Research*, *6*(5), 21-35.

Hanssen-Bauer et al. (2015). Klima i Norge 2100 – Kunnskapsgrunnlag for klimatilpasning oppdatert i 2015. Available online: NCCS report no. 2/2015

Hanssen-Bauer I, Førland EJ, Hisdal H, Mayer S (2017). Climate in Norway 2100 – a knowledge base for climate adaptation. *NCCS Report no. 1/2017.* Available online: www.klimaservicesenter.no

Harabinová, S., Panulinová E. (2020). Impact of shear strength parameters on slope stability. *MATEC Web Conf. 310 00040*. DOI: 10.1051/matecconf/202031000040

Harr, R.D. (1981). Some Characteristics and Consequences of snowmelt during Rainfall in Western Oregon. *Journal of Hydrology*, Vol. 53, pp. 277-304.

Haque, Blum, Da Silva, Andersen, Pilz, Chalov, Malet, Auflič, Andres, Poyiadji (2016). Fatal landslides in Europe. *Landslides, 13,* 1545–1554.

Heyerdahl H, Hoydal O A, Kvistedal Y, Gisnas K G, Carotenuto P. (2018). Slope instrumentation and unsaturated stability evaluation for steep natural slope close to railway line. In UNSAT 2018: *The 7th International Conference on Unsaturated Soils.*

Highland, L.M., and Bobrowsky, P. (2008). The landslide handbook—A guide to understanding landslides: Reston, Virginia, U.S. *Geological Survey Circular 1325.* ISBN 978-1411322264

Hillel, D. (1980). Fundamentals of soil physics (pp. 413). *New York:Academic Press Inc.*

Hisdal, H. (2017). Evaluering av snø- og jordskredvarslingen, *NVE report 38.* Available online: http://publikasjoner.nve.no/rapport/2017/rapport2017_38.pdf

Hong B., Li X.A., Wang L., Li L.C. (2019). Temporal variation in the permeability anisotropy behavior of the Malan loess in northern Shaanxi Province, China: an experimental study. *Environ Earth Sci 78(15).* https://doi.org/10.1007/s12665-019-8449-z

Holmqvist, E. (2017). Norges vannbalanse i TWh basert på HBV-modeller. *Norges vassdrags- og energidirektorat. Rapport nr 87-2017.* Available online: Rapport (nve.no)

Horton, R.E. (1938). Phenomena of the Contact Zone Between the Ground Surface and a Layer of Melting Snow. *Bulletin No. 23, Association Internationale d'Hydrologie Scientifique, Paris,* 545-561.

Hou X, Li T, Qi S, Guo S, Li P, Xi L, Xing X. (2021). Investigation of the cumulative influence of infiltration on the slope stability with a thick unsaturated zone. *Bull Eng Geol Environ 80:5467–5480.* https://doi.org/10.1007/s10064-021-02287-2

Huang, W., Leong, E. C. and Rahardjo, H. (2015). Translational slip failures on slope incorporating unsaturated soil mechanics. *Proceedings of the 6th Asia Pacific Conference on Unsaturated Soils*, Guilin, China, 771-775.

Huang, W., Leong, E., and Rahardjo, H. (2018). Simplified stability analysis of unsaturated soil slopes under rainfall. *Proc., Proc., 7th Int. Conf. on Unsaturated Soils. Hong Kong: Hong Kong Univ. of Science and Technology*

Huntingford, C., P.D. Jones, V.N. Livina, T.M. Lenton, and P.M. Cox (2013). No increase in global temperature variability despite changing regional patterns. *Nature, 500(7462), pp.* 327–330. DOI:10.1038/nature12310.

Huysmans, Marijke and Alain Dassargues (2005). Review of the use of Péclet numbers to determine the relative importance of advection and diffusion in low permeability environments. *Hydrogeology Journal* 13: 895-904. https://doi.org/10.1007/s10040-004-0387-4

Ihlen, P. og Lutro, O. (2010): Berggrunnskart EIDSVOLL 1915 I, M 1:50.000. *Foreløpig utgave Norges geologiske undersøkelse.*

Indraratna, B., Fatahi, B., and Khabbaz, H. (2006). Numerical analysis of matric suction effects of tree roots. *Proceedings of the Institution of Civil Engineers, ICE, 159(GE2)*. pp. 77-90. https://doi.org/10.1680/geng.2006.159.2.77

IPCC – Intergovernmental Panel on Climate Change (2014). Synthesis Report. *Contribution of Working Groups I, II and III to the Fifth Assessment Report of the Intergovernmental Panel on Climate Change, Geneva, Switzerland,* pp. 151

Jacob, D., Petersen, J., Eggert, B. et al. (2014). EURO-CORDEX: new high-resolution climate change projections for European impact research. *Reg Environ Change* 14, 563–578. https://doi.org/10.1007/s10113-013-0499-2

Jaedicke, Christian and Kleven, Arne (2008). Long-term precipitation and slide activity in south-eastern Norway, autumn 2000. *Hydrological Processes. 22. 495 - 505.* DOI: 10.1002/hyp.6878

Jaedicke C, Lied K, Kronholm K. (2009). Integrated database for rapid mass movements in Norway. *Natural Hazards and Earth System Science 9.* 469–479. https://doi.org/10.5194/nhess-9-469-2009

Jeong, Sangseom and Lee, Kwangwoo and Kim, Junghwan and Kim, Yongmin (2017). Analysis of rainfall-induced landslide on unsaturated soil slopes. *Sustainability 9(7):1280.* DOI: 10.3390/su9071280

Jernbaneverket (2011). Flomsituasjonen på Dovrebanen 15-20.08.2011. *Jernbaneverket Region Øst. Dokumentasjons nr.: UB.154781-000.*

Jernbaneverket (2016). Venjar - Eidsvoll: Forslag til reguleringsplan, med endringer etter høring og offentlig ettersyn. *Detaljreguleringsplan for Gardermobanen Venjar-Eidsvoll i Eidsvoll kommune.* Available online: https://www.banenor.no/

Johnson, A.I. (1963). A field method for measurement of infiltration. *Water Supply Paper 1544-F.* https://doi.org/10.3133/wsp1544F

Johnson, K. A., and Sitar, N. (1990). Hydrologic conditions leading to debris-flow initiation. *Canadian Geotechnical Journal*, *27*(6), 789-801.

Johnson, A. C., Edwards, R. T., and Erhardt, R. (2007). Ground-water response to forest harvest: Implications for hillslope stability. *Journal of the American Water Resources Association, vol. 43,* 134-147. https://doi.org/10.1111/j.1752-1688.2007.00011.x

Kalsnes, Bjørn and Nadim, Farrokh and Hermanns, Reginald and Hygen, Hans and Petkovic, G and Dolva, B and Berg, Hallvard and Høgvold, D. (2016). Landslide risk management in Norway. DOI: 10.1201/9781315387789-9

Kalatehjari, Roohollah and Ali, N. (2013). A Review of Three-Dimensional Slope Stability Analyses based on Limit Equilibrium Method. *EJGE. 18.* 119-134. Available online: researchgate.net

Khan, K.U.J., Wang, Cm., Khan, M.W.J. et al. (2021). Influence of rainfall infiltration on the stability of unsaturated coal gangue accumulated slope. *J. Mt. Sci. 18,* 1696–1709. https://doi.org/10.1007/s11629-020-6567-4

Klose, M., Maurischat, P., Damm, B. (2016). Landslide impact in Germany: A historical and socioeconomic perspective. *Landslides, 13.* 183-199. https://doi.org/10.1007/s10346-015-0643-9

Kool, J. B., and Parker, J. C. (1987). Development and evaluation of closed-form expressions for hysteretic soil hydraulic properties. *Water Resources Research, 23(1).* pp. 105–114. https://doi.org/10.1029/WR023i001p00105

Kramer, M. G., Hansen, A. J., Taper, M. L., and Kissinger, E. J. (2001). Abiotic controls on long-term windthrow disturbance and temperate rain forest dynamics in southeast Alaska. *Ecology*, 82(10), 2749–2768. https://doi.org/10.1890/0012-9658(2001)082[2749:acoltw]2.0.co;2

Kristo, C., Rahardjo, H., Satyanaga, A. (2017). Effect of variations in rainfall intensity on slope stability in Singapore. *International Soil and Water Conservation Research,Volume 5, Issue 4.* pp. 258-264. ISSN 2095-6339. https://doi.org/10.1016/j.iswcr.2017.07.001

Krøgli, I.K., Devoli, G., Colleuille, H., Boje, S., Sund, M. and Engen, I.K. (2018). The Norwegian forecasting and warning service for rainfall- and snowmelt-induced landslides. *Nat. Hazards Earth Syst. Sci., 18,* 1427-1450. https://doi.org/10.5194/nhess-18-1427-2018

Lawrence, D. (2016). Klimaendringer og fremtidige flommer. NVE Rapport 81-2016. Available online: Rapport (nve.no)

Lee, Min-Seok and Kim, Gyo-Won. (2009). Relationship between Rainfall Intensity and Slope Stability based on Numerical Analysis. *The Journal of Engineering Geology. 19.*

Lee, J.Y., and J. Marotzke, et. al. (2021). Future Global Climate: Scenario-Based Projections and NearTerm Information. In Climate Change 2021: The Physical Science Basis. *Contribution of Working Group I to the Sixth Assessment Report of the Intergovernmental Panel on Climate Change. Cambridge University Press, Cambridge, United Kingdom and New York, NY, USA,* pp. 553–672, DOI: 10.1017/9781009157896.006.

Li A.G., Tham L.G., Yue Z.Q., Lee C.F., Law K.T. (2005). Comparison of field and laboratory soil–water characteristic curves. *J Geotech Geoenviron Eng., 131.1176–1180.* DOI: 10.1061/(ASCE)1090-0241(2005)131:9(1176)

Lied, K. (1993). Snow avalanche experience through 20 years. *Laurits Bjerrums Memorial Fund, Norwegian Geotechnical Institute,NGI.*

Likos, W.J., Wayllace, A., Godt, J., and Lu, N. (2010). Modified Direct Shear Apparatus for Unsaturated Sands at Low Suction and Stress. *Geotechnical Testing Journal, Vol. 33, No. 4.*

Liptak, J., G. Keppel-Aleks, and K. Lindsay (2017). Drivers of multi-century trends in the atmospheric CO2 mean annual cycle in a prognostic ESM. *Biogeosciences, 14(6),* pp. 1383–1401. DOI: 10.5194/bg-14-1383-2017.

Liu, Y.J., Wang, T.W., Cai, C.F., Li, Z.X., and Cheng, D.B. (2014). Effects of vegetation on runoff generation, sediment yield and soil shear strength on road-side slopes under a simulation rainfall test in the Three Gorges Reservoir Area, China. *Science of the Total Environment,volum 485-486*. https://doi.org/10.1016/j.scitotenv.2014.03.053

Liu J, Yang C, Gan J, Liu Y, Wei L, Xie Q. (2017). Stability analysis of road embankment slope subjected to rainfall considering runoff-unsaturated seepage and unsaturated fluid–solid coupling. *Int J Civil Eng. 15(6)*. 865–876. DOI: 10.1007/s40999-017-0194-7

Logan, Daryl L. (2011). A first course in the finite element method. *Cengage Learning*. ISBN 978-0495668251.

Lussana, C., Saloranta, T., Skaugen, T., Magnusson, J., Tveito, O. E., and Andersen, J. (2018). seNorge2 daily precipitation, an observational gridded dataset over Norway from 1957 to the present day, *Earth Syst. Sci. Data*, *10*, 235–249, https://doi.org/10.5194/essd-10-235-2018

MacCracken, Michael and Shin, H.J., and Caldeira, Ken and Ban-Weiss, G. (2012). Climate response to imposed solar radiation reductions in high latitudes. *Earth System Dynamics Discussion. 3.* DOI: 10.5194/esdd-3-715-2012.

Mancuso, S., Viola, A. (2015). Brilliant Green: The Surprising History and Science of Plant Intelligence; *Island Press: London, UK*. ISBN 978-1610916035

Marzulli, V., Sandeep, C.S., Senetakis, K., Cafaro, F., Pöschel, T. (2021). Scale and water effects on the friction angles of two granular soils with different roughness. *Powder Technology. Volume 377*. pp. 813-826. https://doi.org/10.1016/j.powtec.2020.09.060

Mathewson, C.C., Keaton, J.R., and Santi, P.M. (1990). Role of Bedrock Ground Water in the Initiation of Debris Flows and Sustained Post-storms Streams Discharge. *Bulletin of the Association of Engineering Geologists, Vol. 27, No. 1*, pp. 73-78.

Meehan, W.R. (1991). Influences of Forest and Rangeland Management on Salmonid Fishes and Their Habitats. *American Fisheries Society, Bethesda, MD, USA.*

Melchiorre, C., Frattini, P. (2012). Modelling probability of rainfall-induced shallow landslides in a changing climate, Otta, Central Norway. *Climatic Change* 113, 413–436. https://doi.org/10.1007/s10584-011-0325-0

Miklin, L., Podolszki, L., Gulam, V., and Markotić, I. (2022). The impact of Climate Changes on Slope Stability and Landslide Conditioning Factors: An Example from Kravarsko, Croatia. *Remote Sensing, 14*(8). DOI:10.3390/rs14081794

Mirus, B. B., Smith, J. B., and Baum, R. L. (2017). Hydrologic impacts of landslide disturbances: implications for remobilization and hazard persistence. *Water Resources Research*, 53, 8250– 8265. https://doi.org/10.1002/2017WR020842

Mitchel, R.J., and Mayer, A.S. (1998). The significance of hysteresis in modeling solute transport in unsaturated porous media. *Soil Science Society of America Journal, 62, 1506–1512*. https://doi.org/10.2136/sssaj1998.03615995006200060005x

Mohsen, Emadi-Tafti and Ashtiani, Behzad (2019). A Modeling Platform for Landslide Stability: A Hydrological Approach. *Water 11, no. 10: 2146*. https://doi.org/10.3390/w11102146

Morgenstern, N., and Price, V. (1965). The analysis of the stability of general slip surfaces, *Geotechnique,Vol 15, pp.* 79-93.

NBC News (2010). Landslide buries cars, cuts highway in Taiwan.
Available online: Landslide buries cars, cuts highway in Taiwan (nbcnews.com) (14.11.22)

Ng C.W.W., Springman S.M., Alonso E.E. (2008). Monitoring the performance of unsaturated soil slopes. *Geotech Geol Eng 26(6):*799–816. https://doi.org/10.1007/s10706-008-9203-6

NGI-Norges Geotekniske Institutt (2013). Impacts of extreme weather events on infrastructure in Norway (InfraRisk) - Sluttrapport til NFR-prosjekt 200689. *NGI rapport nr. 20091808- 01-R.*

NGI-Norges Geotekniske Institutt (2014). Skred-Skredfare og sikringstiltak-praktiske erfaringer og teoretiske prinsipper. *Univeritetsforlaget. 256 p.* ISBN: 9788215023915

NGI-Norges Geotekniske Institutt (2017). ICP Venjar-Langset, Byggeplan: Sammenstilling av tidligere utførte grunnundersøkelser. *NGI Report 20160131-02-R.*

NGI- Norges Geoteknisk Institutt (2020). Geoteknisk bistand, nedsunket vegskulder, Holstangen, Eidsvoll. *NGI Report 20190940-01-TN*

NGU (2014). Kvartærgeologi.. *Norges geologiske undersøkelse (NGU).*
Available online: https://www.ngu.no/Kvartærgeologi

NGU (2021). Skred. *Norges geologiske undersøkelse (NGU).* Available online: https://www.ngu.no/skred

Nilsen, I.B., Hanssen-Bauer, I., Dyrrdal, A.V., Hisdal, H., Lawrence, D., Haddeland, I., Wong, W.K. (2022). From climate model output to actionable climate information in Norway. *Frontiers in Climate 4.* https://doi.org/10.3389/fclim.2022.866563

Norsk Naturskadepool (2016). Naturskadestatistikk. Available online:
https://www.finansnorge.no/Naturskadestatistikk (NASK) (22.09.22).

Novotný, J. and Klimeš, J. (2014). Grain size distribution of soils within the Cordillera Blanca, Peru: An indicator of basic mechanical properties for slope stability evaluation. *Journal of Mountain Science,volum 11*, p. 563-577. DOI: 10.1007/s11629-013-2836-9

NVDB (2019). Skred og nedfall på veg registret per 2019. *Norway's national road database (NVDB).*
Available online: https://www.vegvesen.no/ (12.05.2022)

Oggero, M., Insana, A., Barla, M. (2021). Climate Change Effects on Slope Stability. Challenges and Innovations in Geomechanics (IACMAG 2021). *Lecture Notes in Civil Engineering, vol 126. Springer, Cham.* https://doi.org/10.1007/978-3-030-64518-2_56

Olje- og energidepartementet (2012). Hvordan leve med farene – om flom og skred. *Meld. St. 15*. Available online: https://www.regjeringen.no/ (11.06.2022)

Pagano L, Reder A, Rianna G. (2014). Experiments to investigate the hydrological behaviour of volcanic covers. *Procedia Earth Planet Sci 9.* 14–22. https://doi.org/10.1016/j.proeps.2014.06.013

Parra, Eric and Mohr, Christian and Korup, Oliver (2021). Predicting Patagonian Landslides: Roles of Forest Cover and Wind Speed. *Geophysical Research Letters. 48*. DOI: 10.1029/2021GL095224.

Patil, Ujwalkumar and Puppala, Anand and Hoyos, Laureano and Pedarla, Aravind (2017). Modeling critical-state shear strength behavior of compacted silty sand via suction-controlled triaxial testing. *Engineering Geology. 231*. pp. 21-33. DOI: 10.1016/j.enggeo.2017.10.011.

Pawlik, Ł. (2013). The role of trees in the geomorphic system of forested hillslopes - A review. *Earth-Science Reviews*, 126. pp. 250–265. https://doi.org/10.1016/j.earscirev.2013.08.007

Pei, Y., Qiu, H., Yang, D., Liu, Z., Ma, S., Li, J., Cao, M., Wufuer, W. (2023). Increasing landslide activity in the Taxkorgan River Basin (eastern Pamirs Plateau, China) driven by climate change. *CATENA, Volume 223*, https://doi.org/10.1016/j.catena.2023.106911

Peranić J, Jagodnik V, Arbanas Ž. (2019). Rainfall infiltration and stability analysis of an unsaturated slope in residual soil from fysch rock mass. In: *Proceedings of the XVII ECSMGE-2019 "geotechnical engineering foundation of the future", Reykjavik, Iceland*, pp. 1–6. https://doi.org/10.32075/17ECSMGE-2019-0906

Peterson, C.J., De Mello Ribeiro, G., Negrón-Juárez, R., Marra, D., Chambers, J.Q., Higuchi, N., et al. (2019). Critical wind speeds suggest wind could be an important disturbance agent in Amazonian forests. *Forestry*, 92(4). pp. 444– 459. https://doi.org/10.1093/forestry/cpz025

Picarelli, L., Leroueil, S., Lolivares, L., Pagano, L., Tommasi, P., and Urciuoli, G. (2012). Groundwater in slopes. *iClague, J. J. & Stead, D. (red.) Landslides -Types, Mechanisms and Modeling.New York: Cambrindge University Press.*

Piciullo, L., Capobianco, V., and Heyerdahl, H. (2022a). A first step towards a IoT-based local early warning system for an unsaturated slope in Norway. *Nat Hazards* 114, 3377–3407. https://doi.org/10.1007/s11069-022-05524-3

Piciullo, P, Capobianco, V., and Heyerdal, H. (2022b). A monitored unsaturated slope in Norway: Eidsvoll case study. *Klima 2050 Report 35. Oslo*. ISBN: 978-82-536-1760-2

Pollen-Bankhead, N., Simon, A. (2010). Hydrologic and hydraulic effects of riparian root networks on streambank stability: Is mechanical root-reinforcement the whole story? *Geomorphology, 116*. pp. 353–362. https://doi.org/10.1016/j.geomorph.2009.11.013

Poluektov, R.A., and Terleev, V.V. (2002). The way to simulate water retention capability and differential water capacity for soil. *Meteorol. Gidrol, no. 11*.

Preti, F., Dani, A., Laio, F. (2010). Root profile assessment by means of hydrological, pedological and above-ground vegetation information for bio-engineering purposes. *Ecol. Eng. 36, 305–316.* https://doi.org/10.1016/j.ecoleng.2009.07.010

Prince Philip S. (2019). A sand model landslide compared to the 2018 Llusco event. *Virginia Division of Geology and Mineral Resources.* Available online: https://blogs.agu.org/thefield/2019/06/20/ (9/11/22)

Rahimi A., Rahardjo H., Leong E.C. (2011). Effect of antecedent rainfall patterns on rainfall-induced slope failure. *J Geotech Geoenviron Eng 137 (5)*. https://doi.org/10.1061/(ASCE)GT.1943-5606.0000451

Ramberg, I.B., Bryhni, I., Nøttvedt, A. and Rangnes. K. (2007). Landet blir til - Norges geologi. *Trondheim. Norsk Geologisk Forening*. pp. 656. ISBN 978-82-92344-31-6

Reid, M.E., Nielsen, H. P. and Dreiss, S.J. (1988). Hydrologic factors triggering a shallow hillslope failure. *Bulletin of the Association of Engineering Geologists,volum 25,* pp. 349-361.

Rianna G., Pagano L., Urciuoli G. (2014). Rainfall patterns triggering shallow flowslides in pyroclastic soils. *Eng Geol 174:22–35.* https://doi.org/10.1016/j.enggeo.2014.03.004

Roscoe, K., Schofield, Andrew and Wroth, C. (1958). On The Yielding of Soils. *Geotechnique. 8.* pp. 22-53. DOI: 10.1680/geot.1958.8.1.22.

Rowe P.W. (1962). The stress-dilatancy relation for static equilibrium of an assembly of particles in contact *Proc. R. Soc. Lond. A* 269: 500–527. http://doi.org/10.1098/rspa.1962.0193

Saez, J. L., Corona, C., Stoffel, M., and Berger, F. (2013). Climate change increases frequency of shallow spring landslides in the French Alps. *Geology*, *41*(5), 619-622. https://doi.org/10.1130/G34098.1

Saloranta, T. M. (2014). New version (v.1.1.1) of the SeNorge snow model and the snow maps for Norway. *NVE-rapport 6-2014*. ISBN: 978-82-410-0951-8.
Available online: https://nve.brage.unit.no/nve (16.12.2022)

Sandersen, F., Bakkehøi, S., Hestnes, E., and Lied, K. (1996). The influence of meteorological factors on the initiation of debris flows, rockfalls, rockslides and rock mass stability. *Landslides, Proceedings of the 7th symposium on landslides*. pp. 97–114.

Sandersen F. (2011). NGI- Tekninsk notat: Eidsvoll-Tangen, km 81.730 og km 87.500. *Jernbaneverket Region Øst. Dokument nr.: 20110661-00-1-TN*

Schiliro, L., Cepeda, J., Devoli, G., and Piciullo, L. (2021). Regional Analyses of Rainfall-Induced Landslide Initiation in Upper Gudrandsdalen (South-Eastern Norway) Using TRIGRS Model**.** *Geosciences* 2021, 11, 35. https://doi.org/10.3390/geosciences11010035

Schwartz, F.W., and Zhang, H. (2003). Fundamentals of Groundwater. *John Wiley & Sons, New York*. ISBN: 978-0-471-13785-6

Sepúlveda, S.A., and Petley, D.N. (2015). Regional trends and controlling factors of fatal landslides in Latin America and the Caribbean. *Nat. Hazards Earth Syst. Sci, 15*, 1821–1833. https://doi.org/10.5194/nhess-15-1821-2015

Shein, E.V., Mady, A.Y. (2018). Hysteresis of the Water Retention Curve: Wetting Branch Simulation Based on the Drying Curve. *Moscow Univ. Soil Sci. Bull. 73*, pp. 124–128. https://doi.org/10.3103/S0147687418030080

Sidle, R. C., and Swanston, D. N. (1982). Analysis of a small debris slide in coastal Alaska. *Canadian geotechnical journal*, *19*(2), 167-174.

Sidle, R.C. and Ochiai, H. (2006). Landslides: processes, prediction, and land use. *Water Resour. Monogr. Ser., 18, American Geophysical Union, Washington, 525. DC*. DOI: 10.1029/WM018

Spencer, E. (1967). A method of analysis of the stability of embankments assuming parallel interslices forces. *Geotechnique 17(1), 11-26*.

Statens vegvesens handbook (2018). Geoteknikk i vegbygging- Håndbok V220. Available online: https://www.vegvesen.no/ (12.07.2022)

Stjern, Camilla and Jón, Egill and Kristjánsson, J. and Walløe Hansen, Aksel (2009). Global dimming and global brightening: An analysis of surface radiation and cloud cover data in northern Europe. *Int. J. Climatol. 29.* DOI: 10.1002/joc.1735.

Stjern, C.W., et al. (2018). Response to marine cloud brightening in a multimodel ensemble. *Atmospheric Chemistry and Physics, 18(2),* pp.621–634, DOI: 10.5194/acp-18-621-2018.

Stoffel, M., Tiranti, D., and Huggel, C. (2014). Climate change impacts on mass movements—case studies from the European Alps. *Science of the Total Environment*, *493*, 1255-1266. https://doi.org/10.1016/j.scitotenv.2014.02.102

Strauch, A. M., MacKenzie, R. A., Giardina, C. P., and Bruland, G. L. (2015). Climate driven changes to rainfall and streamflow patterns in a model tropical island hydrological system. *Journal of Hydrology*, *523*, 160-169. https://doi.org/10.1016/j.jhydrol.2015.01.045

Stuart, G.S. et al. (2013). Reduced efficacy of marine cloud brightening geoengineering due to in-plume aerosol coagulation: parameterization and global implications. *Atmospheric Chemistry and Physics, 13(20), 10385–10396*, DOI:10.5194/acp-13-10385-2013.

Suryo, Eko and Gallage, Chaminda and Trigunarsyah, Bambang (2013). A Method for Predicting Rain-induced Instability of an Individual Slope. DOI: 10.13140/2.1.2542.2084.

Tacher, L., and Bonnard, C. (2007). Hydromechanical modelling of a large landslide considering climate change conditions. In *Landslides and Climate Change: Challenges and Solutions Proceedings of the International Conference on Landslides and Climate Change. Taylor & Francis, Ventnor* (pp. 131-141). https://doi.org/10.1201/noe0415443180.ch17

Terzaghi, K. (1936). The shearing resistance of saturated soils and the angle between the planes of shear. In: *The First International Conference on Soil Mechanics and Foundation Engineering, A. Casagrande, P.C. Rutledge, and J.D. Watson, Eds.*, 54–56, *Cambridge,Massachusetts.*

Terzaghi, K. (1950). Mechanisms of landslides. *Geol. Soc. Am., Berkey Volume,* 83-123.

Terzaghi, K., Peck, R. B., and Mesri, G. (1996). Soil mechanics in engineering practice. *John Wiley & Sons*.

Thomas M.A., Mirus B.B., Collins B.D., Lu N., Godt J.W. (2018). Variability in soil-water retention properties and implications for physics-based simulation of landslide early warning criteria. *Landslides*. https://doi.org/10.1007/s10346-018-0950-z

Thota, S.K., and Vahedifard, F. (2021). Stability analysis of unsaturated slopes under elevated temperatures. *Engineering Geology,Volume 293,106317*. ISSN 0013-7952, https://doi.org/10.1016/j.enggeo.2021.106317

Tuller, Markus and Or, Dani (2004). Water retention and characteristic curve. In book*: Encyclopedia of Soils in the Environment. Elsevier Ltd., Oxford, U.K.*

Turkington, T., Remaître, A., Ettema, J., Hussin, H., and van Westen, C. (2016). Assessing debris flow activity in a changing climate. *Climatic Change*, *137*, 293-305. DOI: 10.1007/s10584-016-1657-6

Turner, A.K., and Schuster, R.L. (1996). Landslides: Investigation and Mitigation. *Special Report 247. Transportation Research Board, The National Academies Press, Washington DC.*

Uhlemann S, Chambers J, Wilkinson P, Maurer H, Merritt A, Meldrum P, Kuras O, Gunn D, Smith A, Dijkstra T (2017). Four-dimensional imaging of moisture dynamics during landslide reactivation. *J Geophys Res Earth Surf 122*:*398–418*. https://doi.org/10.1002/2016JF003983

US Army Corps of Engineers (2003). Engineering and Design - Slope Stability. *Washington DC, USA: US Army Corps of Engineers*. Available online: https://www.publications.usace.army.mil/

Valtera, M., and Schaetzl, R. J. (2017). Pit-mound microrelief in forest soils: Review of implications for water retention and hydrologic modelling. *Forest Ecology and Management*, 393. pp. 40–51. https://doi.org/10.1016/j.foreco.2017.02.048

Vanapalli, S., Fredlund, D., and Pufahl, D., (1999). The influence of soil structure and stress history on the soil–water characteristics of a compacted till. *Géotechnique,volum 49*. pp. 143-159.

van Bavel, C.M., and Hillel, D.I. (1976). Calculating potential and actual evaporation from a bare soil surface by simulation of concurrent flow of water and heat. *Agricultural Meteorology, 17*. pp. 453-476.

van Genuchten, M.T. (1980). A Closed-Form Equation for Predicting the Hydraulic Conductivity of Unsaturated Soils. *Soil Science Society of America Journal, 44*. pp. 892-898. Available online: http://soilphysics.okstate.edu/teaching/soil-6583/

Varnes, D.J. (1978). Slope movement Types and Processes. *In special report 176: Landslides: analysis and control (R.L Schuster and R.J. Krizek, eds.), TRB, National Research Council, Washington, D.C*., pp. 11-33.

Varnes D.J., and Savage W. (eds.) (1996). The Slumgullion earth flow: a large-scale natural laboratory. *U.S. Geological Survey Bulletin 2130.*

Walberg, Nils Arne K., and Devoli, Graziella (2014). Regional varsling av jordskerdfare*. Report nr. 44-2014.* Available online: https://publikasjoner.nve.no/

Walker, R.R., and Mortsch, Linda and Vliet, D., and Bellamy, S. (2010). Guide for assessment of hydrologic effects of climate change in Ontario. *Ontario Ministry of Natural Resources and Ontario Ministry of the Environment. EBNFLO Environmental AquaResource Inc.*

Wang W., Wang Y., Sun Q., Zhang M., Qiang Y., Liu M. (2018). Spatial variation of saturated hydraulic conductivity of a loess slope in the South Jingyang Plateau, China. *Eng Geol 236:70–78*. https://doi.org/10. 1016/j.enggeo.2017.08.002

Wang, G., Jiang, Y., Chang, C., Doi, I., and Kamai, T. (2019). Volcaniclastic debris avalanche on Motomachi area of Izu-Oshima, Japan, triggered by severe storm: Phenomenon and mechanisms. *Engineering Geology*, 251(January). pp. 24–36. https://doi.org/10.1016/j.enggeo.2019.02.003

Wienhöfer, J., Lindenmaier, F., Zehe, E. (2011). Challenges in Understanding the Hydrologic Controls on the Mobility of Slow-Moving Landslides. *Vadose Zone J.*, *10*. pp. 496–511. DOI: 10.2136/vzj2009.0182

Wigmore, A. (2019). How we process the NOAA Intergarted Surface Database Historical Weather Data. Available online: https://www.visualcrossing.com/

Wijaya, M., and Leong, E.C. (2018). Discussion of Permeability function for oil sands tailings undergoing volume change during drying. *Canadian Geotechnical Journal: 1-3.* DOI:10.1139/cgj-2018-0136.

Wong, W.K., Haddeland, I., Lawrence, D., and Beldring, S. (2016). Gridded (1x1) hydrological projections for Norway. *NVE Report 59/2016, Norwegian Water Resources and Energy Directorate, Oslo, Norway*. Available online: https://publikasjoner.nve.no/

Wong, J.L., Lee, M.L., Teo, F.Y., Liew, K.W. (2022). A Review of Impacts of Climate Change on Slope Stability. *Climate Change and Water Security. Lecture Notes in Civil Engineering, vol 178. Springer, Singapore*. https://doi.org/10.1007/978-981-16-5501-2_13

Wu, T.H., McKinnell III, W.P., Swanston, D.N. (1979). Strength of tree roots and landslides on Prince of Wales Island, Alaska. *Can. Geotech. J. 16 (1)*. pp. 19–33

Wu, T. H. (2013). Root reinforcement of soil: review of analytical models, test results, and applications to design. *Canadian Geotechnical Journal*, *50*(3), 259-274. https://doi.org/10.1139/cgj-2012-0160

Yeh H.F., Tsai Y.J. (2018). Analyzing the effect of soil hydraulic conductivity anisotropy on slope stability using a coupled hydromechanical framework. *Water 10(7):905.* https://doi.org/10.3390/w10070905

Yong, Shi Jian (2004). Soil mechanics, work team at Hohai Univerity (English version-Chinese Edition). *China Communications Press.* pp.392. ISBN: 978-711-405-0534

Yong-Hong, Y., Jian-Guo, Z., Jian-Hui, Z., Shu-Zhen, L., Cheng-Hua, W., and Qing-Hua, X. (2005). Impacts of soil moisture content and vegetation on shear strength of unsaturated soil. *Wuhan University Journal of Natural Sciences,volum 10,* pp. 682-688.

Yu, H., Salgado, R., Sloan, S., and J. Kim (1998). Limit Analysis versus Limit Equilibrium for Slope Stability. *Journal of Geotechnical and Geoenvironmental Engineering, 124.* pp. 1-11.

Zhao, Yanru,Wen, Tiande, Shao, L.T.,Chen, Rui, Sun, Xiaohui, Huang, Liping, Chen, Xiangsheng (2020). Predicting hysteresis loops of the soil water characteristic curve from initial drying. *Soil Science Society of America Journal. 84.* DOI: 10.1002/saj2.20125.

Zhang, Y., et al. (2015). Rate effects in inter-granular capillary bridges. *Unsaturated Soil Mechanics-from Theory to Practice: Proceedings of the 6th Asia Pacific Conference on Unsaturated Soils. CRC Press*. pp. 463–466.

Zhang, Y. (2015). Stability and Run-out Analysis of Earthquake-induced Landslides. *In A. Moustafa (ed.), Earthquake Engineering - From Engineering Seismology to Optimal Seismic Design of Engineering Structures, IntechOpen, London*. DOI: 10.5772/59439.

Zhu, Y., Ishikawa, T., Yamada, T.J. et al. (2021). Probability assessment of slope instability in seasonally cold regions under climate change. *J Infrastruct Preserv Resil* 2, 20. https://doi.org/10.1186/s43065-021-00034-1

Appendix A

A.I Landslides

Landslides can either be triggered by human activity, natural causes, or a combination of the two. According to Highland and Bobrowsky (2008), hilly terrain, regions with natural patterns of climate and weather, stream and river systems, and human activity involving the clearing of vegetation, modification to slopes, and other urban and rural practices are typical landslide-prone areas. In Norway, weather-induced landslides are often triggered during heavy rainfall, often in combination with intense snowmelt, causing high soil saturation and positive pore pressures (Bondevik and Sorteberg, 2020; Krøgli et al., 2018; Sandersen et al., 1996; Schiliro et al., 2021). The effect of water on slopes depends on factors such as the steepness of the slope, morphology, soil type, underlying geology, and infrastructure (Highland and Bobrowsky, 2008).

Classification of landslides

This chapter is based on theory and terms from -The landslide handbook provided by Highland and Bobrowsky (2008) and Varnes (1996).

Geologists, engineers, and other specialists characterize landslides in various ways. The nomenclature is diverse, reflecting the complexity of the different fields engaged in the study of landslide phenomena. For this study, a landslide is a broad word to describe the downslope movement of soil and rock under gravity.

Landslides have several processes, including falls, toppling, slides (rotational, translational), spreads, and flows. The classification of landslides is presented according to their composition and movement (Table A-1). The different types of movements (Figure A-1) are based on Varnes's (1996) classification system. Failure mechanisms in soil are also described (Ch. 2.3 and Appendix A.III).

Table A-1. *Landslide classification based on Varnes (1996) classification system.*

Type of movement	Rock	Soil
Fall *detachment of soil/rock from a steep slope, with little or no shear displacement along the failure surface. Subsequent free falling, bouncing, and/or rolling*	Rock/ice fall	Boulder/debris/silt fall
Topple *forward rotation out of a slope of a mass of soil or rock around an axis below the centre of gravity of the displaced mass*	Rock block topple Rock flexural topple	Gravel/sand/silt topple
Slide *downslope movement of a soil or rock mass along a surface or rupture. The movement does not occur simultaneously over the full length of the surface of rupture but initiates as a local failure which progressively grows*	Rockslide (rotational, translational, wedge, compound, irregular)	Clay/silt slide (rotational, translational, compound) Gravel/sand/debris slide
Spread *extension of cohesive soil or rock mass combined with subsidence into softer/weaker underlying material*	Rock slope spread	Sand/silt liquefaction spread Sensitive clay spread
Flow *a spatially continues movement of a completely disrupted mass*	Rock/ice avalanche	Sand/silt/debris dry flow Sand/silt/debris/sensitive clay flow slide Debris/mud/earth/peat flow Debris flood Debris avalanche
Slope deformation	Mountain slope deformation Rock slope deformation	Soil slope deformation Soil creep Solifluction

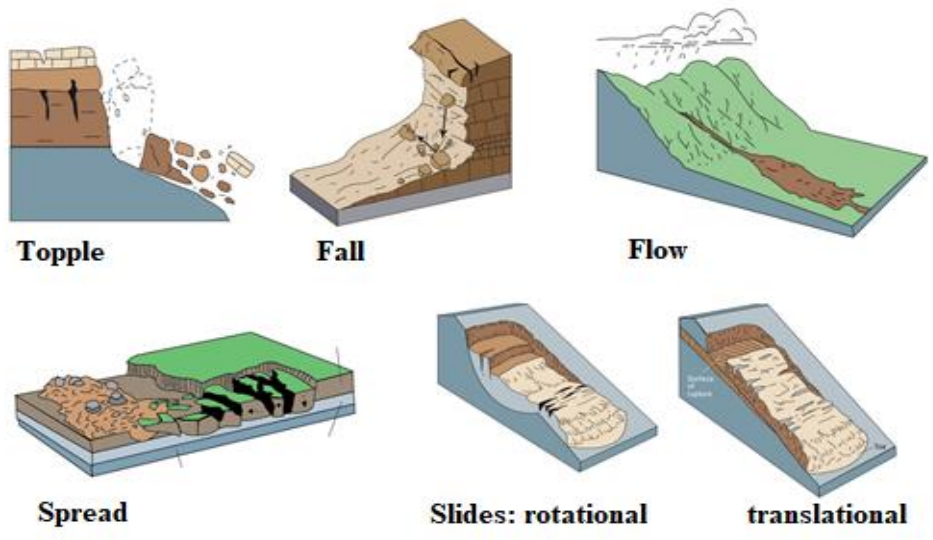

Figure A-1. *Schematics for different types of movements, modified from Highland and Bobrowsky (2008).*

A.II Soil properties and water flow

In soil, continuous voids are enclosed by solid particles. These voids are either fully or partially water saturated. Solid particles and water are considered incompressible, while air is highly compressible. Fully saturated soil is only compressible if the water can flow through the voids, reducing the soil structure's volume and rearranging the soil particles to new positions. As air is compressible, dry, or partially saturated soil will always be able to reduce its volume if the particles can rearrange (Craig, 2004).

Porosity

This chapter's theory is derived from Schwartz and Zhang (2003).

Porosity is determined by grain size, sorting, shape, and packing of the particles. A well-sorted and loosely packed material with rounded grains is essential for porosity. If the grains are poorly sorted, small-scale particles like clay can fill up the voids and block water from flowing. Furthermore, angular grains can block the connection between pores which keep water from flowing through the material. A dense packing will compress the pore volume and limit the connection between the grains. Total porosity refers to all pore space between particles (including non-drainable and non-connected pores) and increases with decreasing grain size (Figure A-2). Effective porosity is a component of total porosity that introduces pore size and connectedness and refers to the pore volume that allows water to flow freely through the pores and drain under gravity (Figure A-2). The total porosity of clay is high; however, due to small grains and dense packing, the surface tension holds the water and limits the flow resulting in low effective porosity (Figure A-2).

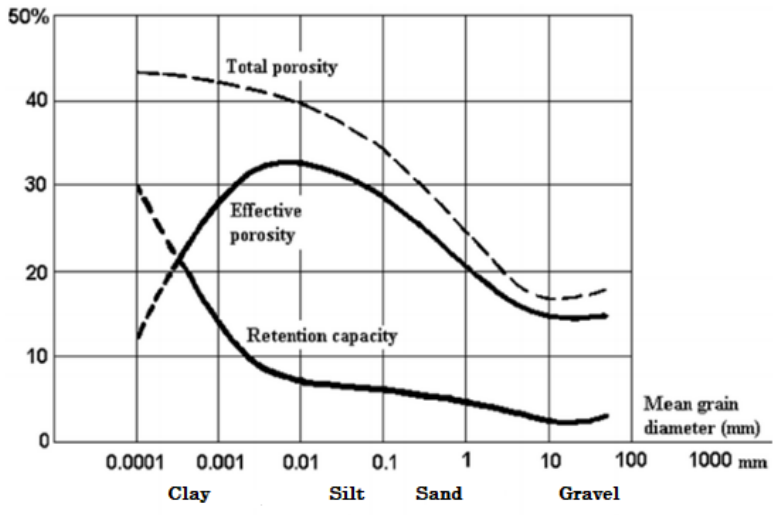

***Figure A-2**. Porosity components as a function of grain size (Huysmans et al., 2005).*

Saturated hydraulic conductivity, k_{sat}

Saturated hydraulic conductivity measures how easily water can flow through a porous material, determined by the effective porosity (Schwartz and Zhang, 2003). The flow rate depends on grain size, degree of sorting, packing, the shape of particles, degree of saturation, and the viscosity of the water, which varies with temperature, homogeneity, and layering of the soil mass (Yong, 2004; Anon, 1999). Fine-grained soils (i.e., clay and silt) have a greater capacity to store water and contribute to increased suction. However, the conductivity is poor due to denser packing and fewer connections between the pores, causing pore pressures to build up (Vanapalli et al., 1999). In contrast to permeability, hydraulic conductivity is a property that assumes constant density and viscosity of the flowing fluid and therefore combines the physical material and the fluid that flows within it. Permeability, on the other hand, is a physical property of the material itself (Schwartz and Zhang, 2003). Freeze and Cherry (1979) classified various soils and their typical ranges of permeability and hydraulic conductivity (Figure A-3).

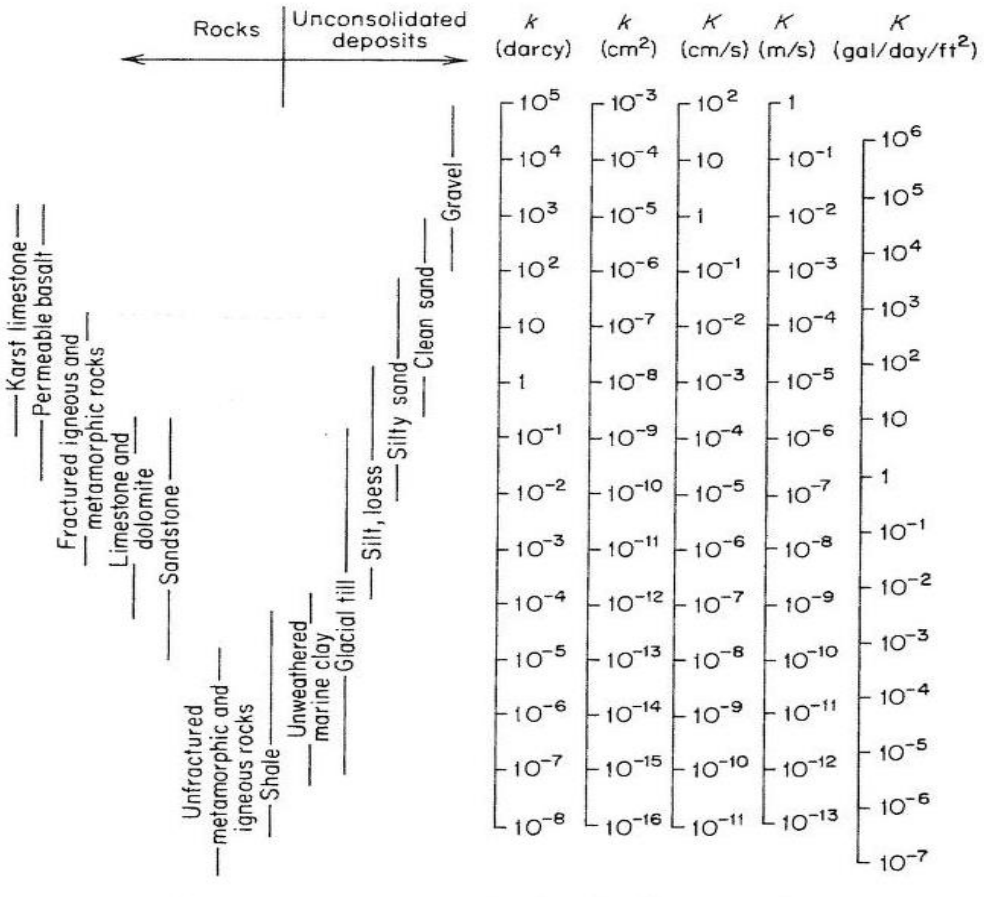

Figure A-3. *Range of values for hydraulic conductivity, K, and permeability, k (after Freeze and Cherry, 1979).*

Spatial variation and directional trends effect on hydraulic conductivity

Isotropy, anisotropy, homogeneity, and heterogeneity are terms used to describe materials' spatial variation and directional trends (Figure A-4). A homogenous material can be considered to have the same properties and hydraulic conductivity throughout the whole medium. Properties and hydraulic conductivity of a heterogeneous material are gradually changing within the medium and have a positional dependence. Isotropic means that hydraulic conductivity has the same value in all directions and has a positional dependence, while anisotropy has a different value for hydraulic conductivity and has directional dependence (Schwartz and Zhang, 2003; Freeze and Cherry, 1979). There are four possible combinations of heterogeneity and anisotropy (Figure A-4):

- Isotropic and homogeneous, which can be found in, for example aeolian deposits
- Anisotropic and homogeneous (glacifluvial layered material)
- Isotropic and heterogeneous (glacial delta)
- Anisotropic and heterogeneous (fractured bedrock)

The material's hydraulic conductivity plays a significant role in regulating water flow. Water flow through a material with varying conductivity impacts the pore water pressure distribution and can cause increased pore pressure locally, thereby increasing the risk of failure (Reid et al., 1988).

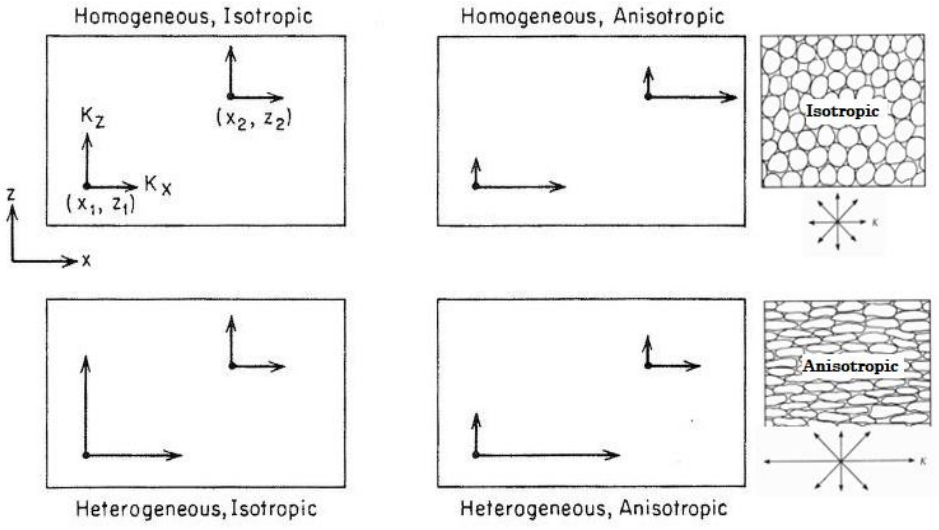

Figure A-4. *Combinations of heterogeneity and anisotropy (after Freeze and Cherry, 1979).*

A.III Types of slope failure in soil

Translational failure

Translational failure (Figure 2-6c; Chapter 2.3.1) occurs in cohesionless granular soils or soils with friction and cohesion above a firm layer parallel to the slope surface. Translational failure is analysed as an infinite slope with no definite boundaries (NGI, 2014), assuming that soil characteristics and porewater pressures are constant at any given depth below the ground surface (Brunsden and Prior, 1984). The form of the potential sliding mass is affected by strata of different strengths (Craig, 2004), where the sliding surface is more likely to pass through the layer of lower shear strength (Huang, 2015). The failure surface will form a parallel slip surface to the slope surface (Abramson et al., 2002) and is usually recognized as a shallow sliding surface compared to the length of the sliding mass (Figure A-5) (NGI, 2014). Translational slides tend to follow discontinuities such as bedding surfaces or contact areas between rock and residual or transported soils. As translational slides continue, the displaced mass may break up, particularly if its velocity or water content increases, and may initiate a flow (Turner and Schuster, 1996). Translational failure is found in natural slopes, often initiated by high groundwater pressures or by toe underloading (Brunsden and Prior, 1984).

***Figure A-5**. A massive translational failure occurred in Taiwan in April 2010 (NBC News, 2010).*

Rotational failure

Rotational slope failure may fail in three ways (Figure A-6) (Yong, 2004);

(1) the failure plane passes through the toe of the slope

(2) the failure plane passes through the face of the slope

(3) the failure surface is deep-seated due to weak soil strata under the toe and passes through the base of the slope

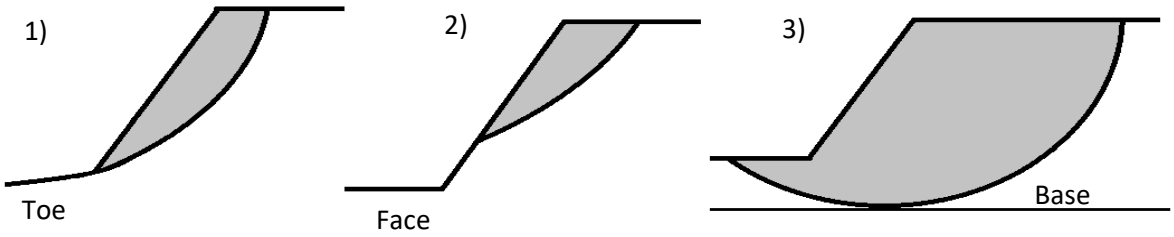

Figure A-6. *Types of rotational failures. Modified (Craig, 2004).*

Rotational failure occurs due to a rotation along a slip surface in cohesive soils, forming a continuous curve, assumed as a non-circular (Figure 2-6b; Chapter 2.3.1) (Figure A-7) or circular slip (Figure 2-6a; Chapter 2.3.1). Non-circular slip occurs when there are existing weak planes and is associated with heterogeneous soil conditions (Craig, 2004).

Figure A-7. *A non-circular rotational failure that occurred in Cusco, Peru in March 2018. Most likely triggered due to high porewater pressures (Prince, 2019).*

In the case of rotational failure in a homogeneous and isotropic material, when the properties of the soil are similar in all directions, a circular shape is assumed, with the failure surface controlled by the strength of the groundmass (Abramson et al., 2002; Craig, 2004). Often the displaced mass may have minor internal deformation (Turner and Schuster, 1996). Here, porewater pressures along the sliding plane vary throughout the slope (NGI, 2014). In slope stability analysis, the circular-shaped failure surface is the most used as it yields satisfactory results (Turner and Schuster, 1996).

Compound failure

Compound failure (Figure 2-6d; Chapter 2.3.1) occurs when an adjacent stratum with considerably varying strength influences the shape of the failure surface, and the adjacent stratum is relatively deep (Craig, 2004; Yong, 2004). Additionally, compound failure may occur in strata where past shear deformations have reduced the shear strength or in ground conditions where the shear strength is distinctly anisotropic (NGI, 2014). Compound failure can be considered a combination of circular and non-circular failure (Abramson et al., 2002), and various failure surfaces may be considered. In 1866, Cullmann (see Yong, 2004) proposed the most straightforward failure surfaces, which entails an infinitely long plane passing through the toe of the slope. The stability analysis searches for potential sliding surfaces that, to the greatest extent possible, follow weak zones in the base profile (NGI, 2014). Although the free body equilibrium analysis in this situation is straightforward, the challenge with composite sliding surfaces is finding the critical surface and reliably calculating the shear strength along that surface. This can produce safety factors that vastly overestimate the actual stability condition (Yong, 2004).

Appendix B

The theory from this chapter is collected from GeoStudio textbook for SEEP/W module (Heat and Mass Transfer Modeling with GeoStudio ref. (Geo-Slope, 2022a)) when other references are not referred to.

B.I The finite element method (FEM)

The finite element method (FEM) is a numerical approach to solving partial differential equations (PDE) for boundary value problems. A conceptual model of a physical system is developed in which PDE is selected, the solution domain is defined (where the material properties must be specified), and boundary conditions are employed to constrain the solution. FEM solves problems by discretizing the domain into smaller, simpler finite elements with well-defined geometry and a predetermined distribution shape for the dependent variable across the element. The PDE across a single element is then described in terms of the dependent variable values at the element nodes. The basic equations that model these finite elements are included in a more extensive system that models the entire problem. The FEM then approximates a solution by minimizing an associated error function using the calculus of variations. The solution provides a spatial and temporal description of the primary variable within the domain (Logan, 2011).

The partial differential equation for groundwater flow is based on the law of conservation of mass and is anchored in the flow and storage processes associated with the porous media. A simplified version of Domenico and Schwartz (1998) theoretical review of groundwater flow is given as follows:

$$\boldsymbol{Q_{w_{in}} - Q_{w_{out}} = V_{st}} \qquad \textbf{(18)}$$

$$Q_{w_{in}}, Q_{w_{out}} = flow\ in/out, V_{st} = change\ in\ water\ storage\ for\ a\ given\ time$$

A steady-state groundwater flow results from an equal flow into and out of the system. Time steps are unnecessary for a steady-state analysis since the water stored in the domain does not change over time.

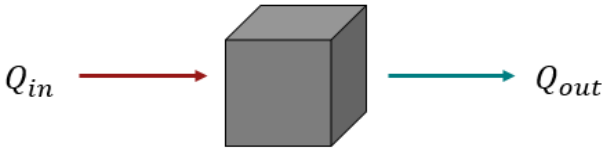

$$\boldsymbol{Q_{w_{in}} - Q_{w_{out}} = V_{st} \quad \rightarrow \quad V_{st} = 0} \tag{19}$$

For transient flow, the water stored in transient systems may fluctuate with time, and flow into the domain is not equal to flow out of the domain.

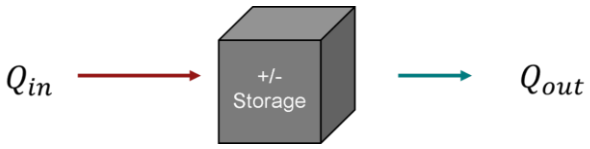

$$\boldsymbol{Q_{w_{in}} - Q_{w_{out}} \neq 0} \tag{20}$$

All flows occur in response to energy gradients, but only the mechanical energy gradients are considered by SEEP/W. The energy state of water, *E*, is represented by three mechanical energies; elastic potential energy (PWP), gravitational potential energy and kinetic energy. To simplify calculations, the kinetic energy can be neglected in groundwater systems. The energy state of water at a given location is then given by

$$\boldsymbol{E = u + \rho g h + \frac{1}{2}\rho v^2 = u + \rho g h} \tag{21}$$

$$u = pore\ water\ pressure, h = elevation, v = flow\ velocity,\ g = gravity, \rho = density\ of\ water$$

When water flow through a porous media, the water will flow from zones of higher head to lower head. Head is energy per unit weight and Bernoulli's Principle of total head, $\boldsymbol{H}$, is

$$\boldsymbol{H = h_z + h_p = \ h_z + \frac{u}{\gamma_w}} \tag{22}$$

$$\boldsymbol{u = h_p \gamma_w}$$

$$h_z = depth\ of\ elevation\ head, h_p = pressure\ head\ due\ to\ pore\ pressure,$$
$$u = pore\ water\ pressure, \gamma_w = unit\ weight\ of\ water$$

Calculating water flow due to mechanical gradients requires knowledge of the pore water pressure and the elevation relative to a datum. According to Darcy's Law, water flows due to mechanical energy gradients and establishes a connection between changes in the energy state and corresponding changes in the water flow. Flowrate is given by

$$\boldsymbol{Q = -KA\frac{\Delta h}{\Delta l} = -KAi} \qquad \textbf{(23)}$$

$$Q{=}flowrate,\ K{=}hydraulic\ conductivity,\ A{=}cross{-}sectional\ area,$$
$$\Delta h{=}change\ in\ water\ total\ head,\ \Delta l{=}change\ in\ distance,\ i{=}hydraulic\ gradient$$

Water flux, $\boldsymbol{q}$, is given by

$$\boldsymbol{q = -K\frac{\Delta h}{\Delta l} = -Ki} \qquad \textbf{(24)}$$

The equations (Eq. 18 - 24) are all simplified concepts of the physical processes included in the partial differential equation solved by SEEP/W. Pressure and gravity-driven flow, as well as storage fluctuations related to water compressibility, soil structure compressibility, and changes in matric suction, are the default settings for physical processes in SEEP/W (see the SEEP/W textbook (Heat and Mass Transfer Modeling) for more detailed reading). However, it is worth mentioning that changes in storage due to soil structure compressibility are due solely to pore-water pressure changes; therefore, the total stresses within the domain are assumed constant.

B.II Material model

Input parameters required by the saturated-unsaturated material model are listed in Table B-1. The volumetric water content (VWC) is a function of matric suction (φ); thus, VWC is equivalent to negative pore-water pressures when air pressure is assumed to be zero. Hydraulic conductivity is a function of the volumetric water content and, therefore, indirectly a function of pore-water pressure.

Table B-1. *Input parameters required by the saturated-unsaturated model in the SEEP/W module (Geo-Slope, 2022a).*

Parameter	Symbol	Unit
Hydraulic Conductivity	$K\ (u_w)$	m/s
Soil Structure Compressibility	β	$m^2/kN\ (1/kPa)$
Volumetric Water Content	$\theta_w\ (u_w)$	-
Anisotropy Ratio	K'_y/K'_x	-
Rotation Angle	α	°

Estimation of volumetric water content as a function of matric suction developed by van Genuchten (1980) can be expressed as:

$$\boldsymbol{\theta_w = \theta_{res} + \frac{\theta_{sat}-\theta_{res}}{[1+\left(\frac{\varphi}{a}\right)^n]^m}} \qquad \textbf{(25)}$$

And the hydraulic conductivity as a function of matric suction can be calculated as follows:

$$\boldsymbol{K_w(\varphi) = K_{sat}\frac{\{1-(a\varphi)^{n-1}[1+(a\varphi)^n]^{-m}\}^2}{[1+(a\varphi)^n]^{\frac{m}{2}}}} \qquad \textbf{(26)}$$

$$a = scale\ parameter\ (kPa), n, m = shape\ parameters,$$
$$\theta_{sat} = saturated\ volumetric\ water\ content, \theta_{res} = residual\ volumetric\ water\ content,$$
$$\varphi = matric\ suction\ (kPa), K_{sat} = saturated\ hydraulic\ conductivity\ (m/s)$$

The method of van Genuchten (1980) can only be employed if the curve fit parameters (*a*, *n*, *m*) are known. These parameters can be obtained in the literature as reference values or by non-linear regression (Eq. 25) on soil water retention curves (SWRC) (Figure B-1). The α parameter is related inversely to the air entry suction for drying or the water entry for wetting, whereas the *n* and *m*(1-1/*n*) parameters describe the slope of the SWRC (Benson et al., 2014).

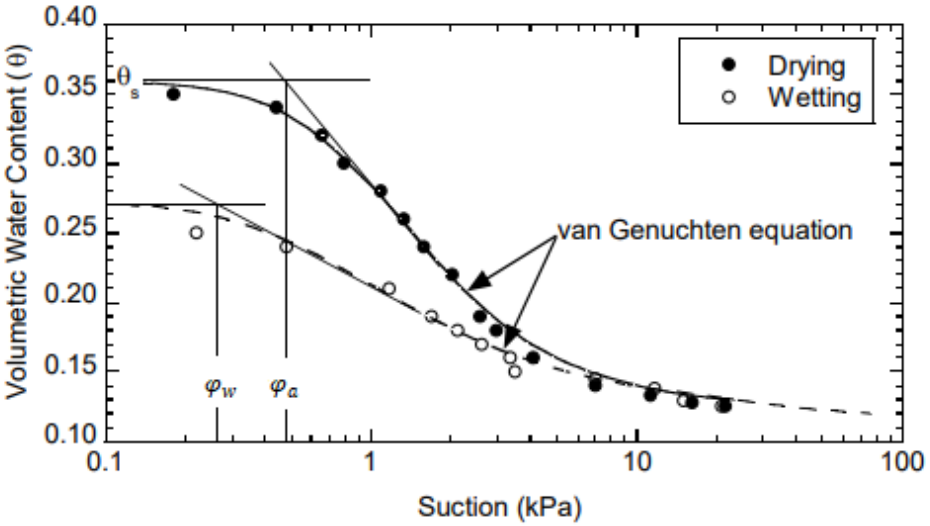

Figure B-1. *Illustration of a Soil Water Retention Curve (SWRC), fitting of the van Genuchten equation and the air entry suction (φ_a), water entry suction (φ_w), and saturated water content (θ_s)(Benson et al., 2014).*

B.III Boundary Conditions for Land-Climate Interactions

In SEEP/W, the Land-Climate Interaction (LCI) boundary condition simulates soil, vegetation, and atmospheric transfers. The ground surface conditions that the LCI boundary condition can reflect, include; bare, snow-covered, and vegetated ground.

By using mass balance equation, the water flux at the ground surface can be calculated:

$$(\boldsymbol{q_P + q_M})\boldsymbol{cos\alpha} + \boldsymbol{q_E} + \boldsymbol{q_R} = \boldsymbol{q_I} \qquad \textbf{(27)}$$

$$q_P = Rainfall, q_M = Snow\ melt, q_E = Evaporation, q_R = Runoff, q_I = Infiltration, \alpha = slope\ angle$$

The Penman-Monteith equation is suggested for vegetated systems where transpiration dominates over evaporation. The SEEP/W module uses, by default, this equation to calculate the evaporation flux (Allen et al., 1998). The Penman-Monteith equation for calculating potential evapotranspiration (PET) is given as:

$$q_{PET} = \frac{1}{h_{fg}} \left[\frac{r_{(q_n - q_g)}}{r + \gamma\left(1 + \frac{r_c}{r_a}\right)} + \frac{\rho_a c_{sa} \frac{p_{v0}{}^a - p_v{}^a}{r_a}}{r + \gamma\left(1 + \frac{r_c}{r_a}\right)} \right] \quad (28)$$

q_{PET}	Potential evaporation flux
h_{fg}	Latent heat of vaporization
q_n	Net radiation
q_g	Ground heat flux
ρ_a	Mean air (atmospheric) density
c_{sa}	Specific heat of moist air
$p_{v0}{}^a - p_v{}^a$	Vapor pressure deficit
$p_{v0}{}^a$	Saturated vapor pressure at the mean air temperature
$p_v{}^a$	Actual vapor pressure of the air at a reference height
r_c	Bulk surface (crop canopy) resistance
r_a	Aerodynamic resistance

Estimation of aerodynamic resistance(r_a) and crop canopy resistance (r_c) is further explained by Allen et al. (1998). To compute evaporation flux under climate boundary conditions, the Penman-Monteith equation requires a variety of meteorological variables (air temperature, relative humidity, wind speed, and solar radiation). Additionally, for the calculation of the evapotranspiration flux, more information on vegetation is needed. A more detailed explanation can be found in "Heat and Mass Transfer Modeling with GeoStudio".

Appendix C

The theory from this chapter is collected from GeoStudio textbook for SLOPE/W module (Stability Modeling with GeoStudio ref. (Geo-Slope, 2022b)) when other references are not referred to.

C.I The limit equilibrium method (LEM)

Most slope stability analysis computer programs are based on the limit equilibrium concept because of their applicability and ability to determine the stability of geotechnical structures (Abramson, 2002). Despite its simplicity (Askari and Farzaneh, 2008), the limit equilibrium method also provides good results compared with other rigorous methods (Yu et al., 1998). The method of slices is the oldest and most popular limit equilibrium technique due to its ability to consider internal forces, pore pressure, and multi-layered slopes (Kalatehjari et al., 2013). This type of analysis is based on the principles of static mechanics. Force and moment for the resistant and driving forces of the material strength, acting within the soil mass, are being compared for each slice and summed to ensure the equilibrium of the entire mass (Geo-Slope, 2022b). The limit equilibrium method does not consider the stress-strain relationship or the corresponding displacement within the soil mass (Fredlund, 1984); assumptions for the shape of the potential failure surface are therefore required. The slip surface is often assumed to be circular or consists of just a few straight lines to simplify computations. The assumed shape depends on the problem geometry and stratigraphy, material properties such as anisotropy, and the capability of the analysis method applied (US Army Corps of Engineers, 2003). Another assumption required to conduct a slope stability analysis is to define the material's shear strength, given by the Mohr-Coulomb equation (Eq. 7; Chapter 2.2.2). Shear strength is expressed as a function of effective normal stress at failure. To account for porewater pressure under unsaturated conditions, the shear strength equation must be modified (Eq. 10; Chapter 2.2.4). Except for the weight of the slice, all forces are unknown and must be calculated to satisfy static equilibrium (Figure C-1) (US Army Corps of Engineers, 2003). The analysis must also include external forces (Craig, 2004).

Many methods of slices have been developed over the years. The methods are all relatively comparable and are often proven to achieve similar results. According to Duncan (1996), the difference between the various methods is less than 6% and depends on the following:

- Which equation of statics are included and satisfied?
- Which interslice forces are included?
- What is the assumed relationship between the interslice shear and normal forces?

The method of slices was initially conceived for the situation where the normal stress along the slip surface is primarily influenced by gravity (weight of the slice). The first method**,** developed by Fellenius in 1936, simplified the assumptions by ignoring all interslice forces, and only moment equilibrium was satisfied, which allowed slope stability calculations by hand (Geo-Slope, 2022b). According to Craig (2004) and Yong (2004), this method underestimates the Factor of Safety and gives an error of 5-20% compared with more accurate methods that include all equations of statics. Craig (2004) concludes that the Fellenius method is no longer recommended in practice. Today, software like GeoStudio (Geo-Slope, 2022b) makes it possible to include all interslice forces through more rigorous mathematical formulations where all equations of statics are satisfied. Morgenstern-Price (1965) and Spencer (1967) are examples of such methods.

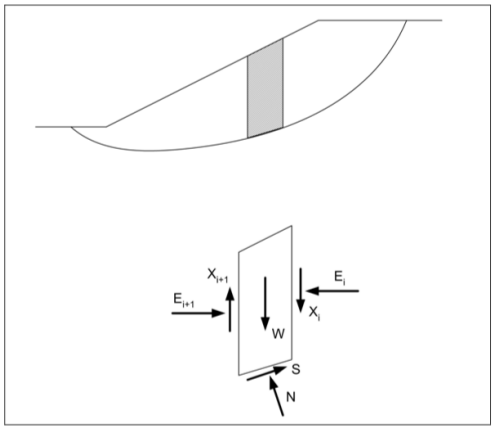

W -weight of the slice,
E - horizontal (normal) forces on the sides of the slice,
X - vertical (shear) forces between slices,
N - normal force on the base,
S – shear force on the base
(US Army Corps of Engineers, 2003).

Figure C-1. *The forces acting on an individual slice (method of slices) (US Army Corps of Engineers, 2003).*

The Morgenstern and Price method include both shear and normal interslice forces where both moments and force equilibrium are satisfied so that the failure surface may be any shape (Morgenstern and Price, 1965; Craig, 2004). Morgenstern and Price (1965) are like the Spencer method but also introduced a user-specified set of interslice force functions in the SLOPE/W module. Examples of available functions include; constant, half-sine, clipped-sine, trapezoidal, and data point-specified functions. Morgenstern and Price method becomes identical to the Spencer method when the constant function is chosen. The interslice force

function depends on the amount of contortion the potential sliding mass must undergo to move and might significantly influence the Factor of Safety for some movements (Appendix C.II). Table C-1 summarizes some available SLOPE/W methods and identifies which statics equations each method satisfies, as well as the interslice forces and the assumed interslice shear and normal force correlations**.** By default, the software SLOPE/W uses the half-sine function for the Morgenstern-Price method. The interslice shear forces typically concentrate in the middle of the sliding mass and are reduced at the crest and toe regions by the half-sine function (Geo-Slope, 2022b).

Table C-1. *Equation of statics satisfied and interslice force characteristics and relationships for some methods available in SLOPE/W module (Geo-Slope,2022b).*

Method	Moment Equilibrium	Force Equilibrium	Interslice Normal (E)	Interslice Shear (X)	Relationship of E-X
Fellenius	Yes	No	No	No	No interslice forces
Bishops's Simplified	Yes	No	Yes	No	Horizontal
Janbu's Simplified	No	Yes	Yes	No	Horizontal
Spencer	Yes	Yes	Yes	Yes	Constant
Morgenstern-Price	Yes	Yes	Yes	Yes	Variable; user function

C.II The influence of interslice forces on failure surfaces

While the force equilibrium is dependent on the interslice shear forces in the case of circular failure surfaces, the moment equilibrium is entirely independent of them. The sliding mass can rotate freely without slipping between the slices; therefore, the shear forces do not affect the moment equilibrium. However, significant interslice slippage is required for the sliding mass to move laterally. Consequently, the horizontal force equilibrium is sensitive to interslice shear. Since the moment equilibrium is entirely independent, interslice shear can be assumed to be zero and still obtain an acceptable Factor of Safety for methods that satisfy moment equilibrium. For a curved slip surface, disregarding the interslice shear when only horizontal force equilibrium is met leads to a Factor of Safety significantly different from what is obtained when both force and moment equilibrium are satisfied. In the case of planar failure, the situation is opposite of the circular slip surface where interslice shear for force equilibrium can be ignored. In contrast, moment equilibrium is sensitive to the interslice

shear as slippage is required for the mass to rotate. A compound failure can be considered a combination of circular and planar failure. In general, the interslice shear forces influence both moment and force equilibrium. Force equilibrium factors of safety increase, while moment equilibrium factors of safety decrease as the interslice shear forces increase. The rigorous formulation suggested by Morgenstern-Price (1965) tends to provide a lower Factor of Safety than other, more simplified methods. However, the opposite situation has been observed depending on the compound failure surface. Moment and force equilibrium both require slippage between the slices; hence the interslice shear is crucial for both types of equilibrium.

C.III General Limit Equilibrium Formulation

The general limit equilibrium formulation is based on two Factor of Safety equations, one with respect to moment equilibrium (F_m) and the other with respect to horizontal force equilibrium (F_f) (Figure C-2). These equations allow a range of interslice shear-normal force conditions (Geo-Slope, 2022b). Morgenstern and Price (1965) assume that the inclination θ, for the interslice forces vary systematically across the slide mass where the relationship is expressed as

$$\boldsymbol{tan\theta = X = E\lambda f(x)} \qquad \textbf{(29)}$$

$f(x)$ =assumed functional relationship with respect to x, λ =percentage of the function used, E =the interslice normal force, X =The interslice shear force

The Factor of Safety equation with respect to moment equilibrium is:

$$\boldsymbol{F_m = \frac{\sum(c'\beta R + (N - u\beta)Rtan\phi')}{\sum Wx - \sum Nf \pm \sum Dd}} \qquad \textbf{(30)}$$

The Factor of Safety equation with respect to horizontal force equilibrium is:

$$\boldsymbol{F_f = \frac{\sum(c'\beta cos\alpha + (N - u\beta)tan\phi' cos\alpha)}{\sum Nsin\alpha - \sum Dcos\omega}} \qquad \textbf{(31)}$$

c' =effective cohesion

ϕ' =effective angle of friction

u =*pore-water pressure*

N =*slice base normal force**

W =*slice weight*

D =*concentrated point load*

$\beta, R, x, f, d, \omega$ =*geometric parameters*

α =*inclination of slice base*

*The slice base normal N is dependent on the interslice shear forces X_R and X_L on either side of a slice

$$N = \frac{W+(X_R-X_L)-\frac{(c'\beta sin\alpha+u\beta tan\phi' sin\alpha)}{F}}{cos\alpha+\frac{sin\alpha\, tan\phi'}{F}} \qquad (32)$$

The formulation is not restricted by the shape of the slip surface and can be applied to any kinematically admissible slip surface shape (Figure C-2). When both moment and force equilibrium are satisfied: $F_m = F_f$ only one Factor of Safety value will be produced for the overall slope, which is also the same for each slice (Geo-Slope, 2022b; Brunsden and Prior, 1984; Yong, 2004).

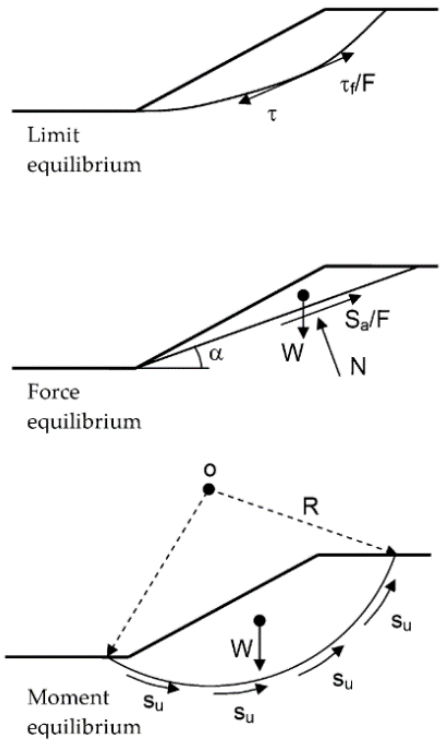

Limit equilibrium:

$$F = \frac{c' + \sigma' \tan\phi'}{\tau} \quad \text{(Effective stress)}$$

Force equilibrium:

$$F = \frac{\text{Sum of resisting forces}}{\text{Sum of driving forces}} \qquad F_f = \frac{\sum(c'\beta cos\alpha + (N-u\beta)tan\phi' cos\alpha)}{\sum N sin\alpha - \sum D cos\omega}$$

Moment equilibrium:

$$F = \frac{\text{Sum of resisting moments}}{\text{Sum of driving moments}} \qquad F_m = \frac{\sum(c'\beta R + (N-u\beta)Rtan\phi')}{\sum Wx - \sum Nf \pm \sum Dd}$$

Figure C-2. *General definitions of limit, force, and moment equilibrium. Modified from (Abramson et al, 2002).*

Appendix D

D.I Climate models

Climate models are based on numerical algorithms and give mathematical representations of the physical processes that govern the climate system. These models can be used to project how the climate system will evolve in the future at a global scale (GCMs) or at a regional scale (RCMs) by employing emission scenarios (Appendix D.II). General circulation models (GCMs) can describe the governing processes in the atmosphere, ocean, land surface, and sea ice but are insufficient for many aspects of regional and local scale estimates due to coarse horizontal, and temporal scales (Wong et al., 2016). In order to represent the local effects of global change, regional circulation models (RCMs) are used to downscale GCM simulations by using GCM output data as lateral boundary conditions (Nilsen et al., 2022; Wong et al., 2016). Various downscaling methods increase the degree of detail (Figure D-1).

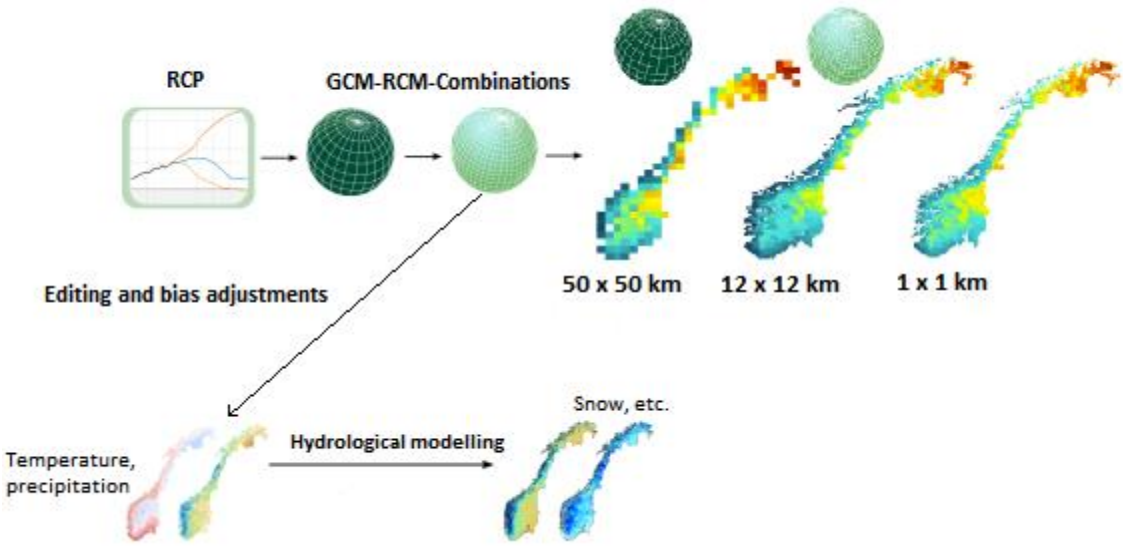

Figure D-1. *Schematic presentation of the modelling chain from global climate models (GCM) and regional climate models (RCM), to climate projections of precipitation/temperature and snow. Modified from (Nilsen et al., 2022).*

Calculations for temperature and precipitation from 12 x 12 km grid data are taken directly from EURO-CORDEX (Jacob et al., 2014). More detailed processes are scaled down by dividing each grid cell from the regional climate model into grid cells of 1 x 1 km and then adjusted against an observation-based data set. The climate projections provide daily resolution until 2100 and cover the Norwegian mainland (Wong et al., 2016). Several

hydrological variables, including the amount of snow, are not estimated by climate models. Instead, they are derived from a hydrological model using precipitation and temperature as input data from downscaled climate models that have been bias-adjusted (Hanssen-Bauer et al., 2015).

D.II Emission scenarios

The most commonly used emission scenarios are RCP 4.5 and RCP 8.5, which describe different scenarios for the future development of global emissions of greenhouse gases and aerosols (Figure 4-16). These emissions are strongly influenced by future population growth, technological and industrial development, energy source selection, energy efficiency, and other socioeconomic factors. For emissions scenario RCP 4.5, greenhouse gas emissions are expected to be relatively stable, with a slight increase until 2040, before they decrease. This scenario requires a significant reduction in climate emissions in an energy-efficient world with an ambitious climate policy in most countries, intending to limit temperature increases to less than 2.5°C by 2100. Emissions scenario RCP 8.5 is referred to as "business as usual". It presumes that there will be continuous growth in climate emissions that follows the same trend as in recent decades. Several greenhouse gases will increase significantly, and it is estimated that the global temperature will rise by more than 4°C by 2100 (Hanssen-Bauer et al., 2015).

Appendix E

Table E-1. *Simulations conducted for the sensitivity analysis. The simulations were carried out varying the saturated horizontal hydraulic conductivity and the anisotropy ratio for layer 1 (6m sandy silt), layer 2 (3m clayey silt) and layer 3 (marine clay).*

ID	***k'_y/k'_x ratio***			***k_{xsat}***			
	Layer 1	**Layer 2**	**Layer 3**	**Layer 1**	**Layer 2**	**Layer 3**	**Layer 3**
40	2	1.5	1	2.40E-06	1.00E-07	5.00E-10	Sat
41	2	1.5	1	5.00E-06	1.00E-07	5.00E-10	Sat
42	2	1.5	1	2.40E-06	5.00E-07	5.00E-10	Sat
43	2	1.5	1	5.00E-06	5.00E-07	5.00E-10	Sat
44	3	1.5	1	2.40E-06	1.00E-07	5.00E-10	Sat
45	3	1.5	1	5.00E-06	1.00E-07	5.00E-10	Sat
46	3	1.5	1	5.00E-06	5.00E-07	5.00E-10	Sat
47	1.5	1.25	1	5.00E-06	5.00E-07	5.00E-10	Sat
47-1	1.5	1.25	1	5.00E-06	5.00E-07	5.00E-09	Sat
47-2	1.5	1.25	1	5.00E-06	5.00E-07	5.00E-11	Sat
47-3	1.5	1.25	0.5	5.00E-06	5.00E-07	5.00E-09	Sat
47-4	1.5	1.25	0.5	5.00E-06	5.00E-07	5.00E-11	Sat
47-5	1.5	1.25	0.25	5.00E-06	5.00E-07	5.00E-09	Sat
47-6	1.5	1.25	0.25	5.00E-06	5.00E-07	5.00E-11	Sat
48	1.5	1.25	1	5.00E-06	3.00E-07	5.00E-10	Sat
49	1.5	1.25	1	5.00E-06	8.00E-07	5.00E-10	Sat
50	1.5	1.25	1	5.00E-06	6.00E-07	5.00E-10	Sat
51	1	1	1	5.00E-06	5.00E-07	5.00E-10	Sat
52	1.5	1.25	1	5.00E-06	6.30E-07	5.00E-10	Sat
52-1	1.5	1.25	1	5.00E-06	6.30E-07	5.00E-08	Sat
52-2	1.5	1.25	1	5.00E-06	6.30E-07	5.00E-09	Sat
52-3	1.5	1.25	1	5.00E-06	6.30E-07	5.00E-11	Sat
52-4	1.5	1.25	1	5.00E-06	6.30E-07	5.00E-12	Sat
52-5	1.5	1.25	1	5.00E-06	6.30E-07	5.00E-13	Sat
52-6	1.5	1.25	0.5	5.00E-06	6.30E-07	5.00E-08	Sat
52-7	1.5	1.25	0.5	5.00E-06	6.30E-07	5.00E-09	Sat
52-8	1.5	1.25	0.5	5.00E-06	6.30E-07	5.00E-11	Sat
52-9	1.5	1.25	0.5	5.00E-06	6.30E-07	5.00E-12	Sat
52-10	1.5	1.25	0.5	5.00E-06	6.30E-07	5.00E-13	Sat
52-11	1.5	1.25	0.25	5.00E-06	6.30E-07	5.00E-08	Sat
52-12	1.5	1.25	0.25	5.00E-06	6.30E-07	5.00E-09	Sat
52-13	1.5	1.25	0.25	5.00E-06	6.30E-07	5.00E-11	Sat
52-14	1.5	1.25	0.25	5.00E-06	6.30E-07	5.00E-12	Sat
52-15	1.5	1.25	0.25	5.00E-06	6.30E-07	5.00E-13	Sat
53	1.5	1.25	1	3.00E-06	6.30E-07	5.00E-10	Sat
54	1.5	1.25	1	7.00E-06	6.30E-07	5.00E-10	Sat
55	1.5	1.25	1	9.00E-06	6.30E-07	5.00E-10	Sat
56	1.75	1.25	1	3.00E-06	6.30E-07	5.00E-10	Sat
57	1.75	1.25	1	7.00E-06	6.30E-07	5.00E-10	Sat
58	1.75	1.25	1	9.00E-06	6.30E-07	5.00E-10	Sat
59	1.75	1.25	1	9.00E-06	5.00E-07	5.00E-10	Sat
60	1.75	1.25	1	5.00E-06	5.00E-07	5.00E-10	Sat
61	2.25	1.5	1	5.00E-06	5.00E-07	5.00E-10	Sat
62	2.25	1.5	1	3.00E-06	5.00E-07	5.00E-10	Sat
63	2.25	1.5	1	1.00E-06	5.00E-07	5.00E-10	Sat
64	2.25	1.5	1	5.00E-06	1.00E-07	5.00E-10	Sat
65	2.25	1.5	1	5.00E-06	6.30E-07	5.00E-10	Sat
66	2.25	1.5	1	5.00E-06	9.00E-07	5.00E-10	Sat
67	1.25	0.75	1	5.00E-06	5.00E-07	5.00E-10	Sat
68	1.25	0.75	1	3.00E-06	5.00E-07	5.00E-10	Sat

69	1.25	0.75	1	1.00E-06	5.00E-07	5.00E-10	Sat
70	1.25	0.75	1	5.00E-06	1.00E-07	5.00E-10	Sat
71	1.25	0.75	1	5.00E-06	6.30E-07	5.00E-10	Sat
72	1.25	0.75	1	5.00E-06	9.00E-07	5.00E-10	Sat
73	1.5	1	0.25	2.40E-05	5.00E-07	5.00E-09	Sat
74	1.5	1	0.25	5.00E-05	5.00E-07	5.00E-09	Sat
75	1.5	1	0.25	2.40E-05	7.00E-07	5.00E-09	Sat
76	1.5	1	0.25	5.00E-05	7.00E-07	5.00E-09	Sat
77	1.5	1	0.25	2.40E-05	1.00E-07	5.00E-09	Sat
78	1.5	1	0.25	5.00E-05	1.00E-07	5.00E-09	Sat
79	1.5	1	0.25	2.40E-06	1.00E-07	5.00E-09	Sat
80	1.5	1	0.25	9.00E-05	1.00E-07	5.00E-09	Sat
81	1.5	1	0.25	1.00E-06	1.00E-07	5.00E-09	Sat
82	1.5	1	0.25	9.30E-05	1.00E-07	5.00E-09	Sat
83	1.5	1	0.25	2.40E-05	1.00E-07	5.00E-11	Sat
84	1.5	1	0.25	5.00E-05	5.00E-07	5.00E-10	Sat
85	1.5	1	0.25	5.00E-06	5.00E-07	5.00E-10	Sat
86	1.5	1	0.25	5.00E-06	5.00E-07	5.00E-09	Sat
87	1.5	1	0.25	7.50E-06	5.00E-07	5.00E-09	Sat
88	1.5	1	0.25	7.00E-06	6.00E-07	5.00E-09	Sat
89	1.5	1	0.25	6.90E-06	6.30E-07	5.00E-09	Sat
90	1.5	1	0.25	7.00E-06	5.80E-07	5.00E-09	Sat
91	1.5	1	0.25	7.70E-06	6.50E-07	5.00E-09	Sat
92	1.5	1	0.25	6.50E-06	5.50E-07	5.00E-09	Sat
93	1.5	1	0.25	6.50E-06	5.50E-07	3.00E-09	Sat
94	1.5	1	0.25	6.50E-06	5.50E-07	7.00E-09	Sat
95	1.5	1	0.25	6.30E-06	5.50E-07	1.00E-09	Sat
96	1.5	1	0.25	5.90E-06	5.50E-07	1.00E-09	Sat
97	1.5	1	0.25	5.30E-06	5.50E-07	1.00E-09	Sat
98	1.5	1	0.25	7.00E-06	6.50E-07	5.00E-09	Sat
99	1.5	1	0.25	7.00E-06	6.50E-07	1.00E-09	Sat
100	1.5	1	0.25	7.00E-06	6.50E-07	9.80E-08	Sat
101	1.5	1	0.15	7.00E-06	6.50E-07	1.00E-09	Sat
102	2	1	0.25	7.00E-06	6.50E-07	1.00E-09	Sat
103	2.0	1	0.25	6.00E-06	6.50E-07	1.00E-09	Sat
104	2	1	0.25	5.00E-06	6.50E-07	1.00E-09	Sat
105	2.5	1	0.25	5.00E-06	6.50E-07	1.00E-09	Sat
106	3	1	0.25	5.00E-06	6.50E-07	1.00E-09	Sat
107	3	1	0.25	3.50E-06	7.00E-07	1.00E-09	Sat
108	3	1	0.25	3.50E-06	4.50E-07	1.00E-09	Sat
109	3	1	0.25	7.00E-06	4.50E-07	1.00E-09	Sat
110	3	1	0.25	7.00E-06	6.00E-07	5.00E-09	Sat
111	2.5	1	0.50	7.00E-06	6.50E-07	1.00E-09	Sat
112	2.5	1	0.50	5.00E-06	5.00E-07	1.00E-09	Sat
113	2.5	1	0.50	5.00E-06	5.00E-07	5.00E-09	Sat
114	2.5	1	0.50	5.00E-06	4.00E-07	5.00E-09	Sat
115	2.5	1	0.50	4.00E-06	7.00E-07	5.00E-09	Sat
116	2.5	1	0.50	4.00E-06	5.00E-07	1.00E-09	Sat
117	3	1	0.10	5.00E-06	6.00E-07	1.00E-09	Sat
118	1.5	1	0.25	7.00E-06	5.80E-07	5.00E-09	Sat
119	1.5	1	0.25	7.70E-06	6.50E-07	5.00E-09	Sat
120	1.5	1	0.25	6.50E-06	5.50E-07	5.00E-09	Sat
121	1.5	1	0.25	6.50E-06	5.50E-07	3.00E-09	Sat
122	1.5	1	0.25	6.50E-06	5.50E-07	7.00E-09	Sat
123	1.5	1	0.25	6.30E-06	5.50E-07	1.00E-09	Sat
124	1.5	1	0.25	5.90E-06	5.50E-07	1.00E-09	Sat
125	1.5	1	0.25	5.30E-06	5.50E-07	1.00E-09	Sat
126	1.5	1	0.25	7.00E-06	6.50E-07	5.00E-09	Sat
127	1.5	1	0.25	7.00E-06	6.50E-07	1.00E-09	Sat
128	1.5	1	0.25	7.00E-06	6.50E-07	9.80E-08	Sat

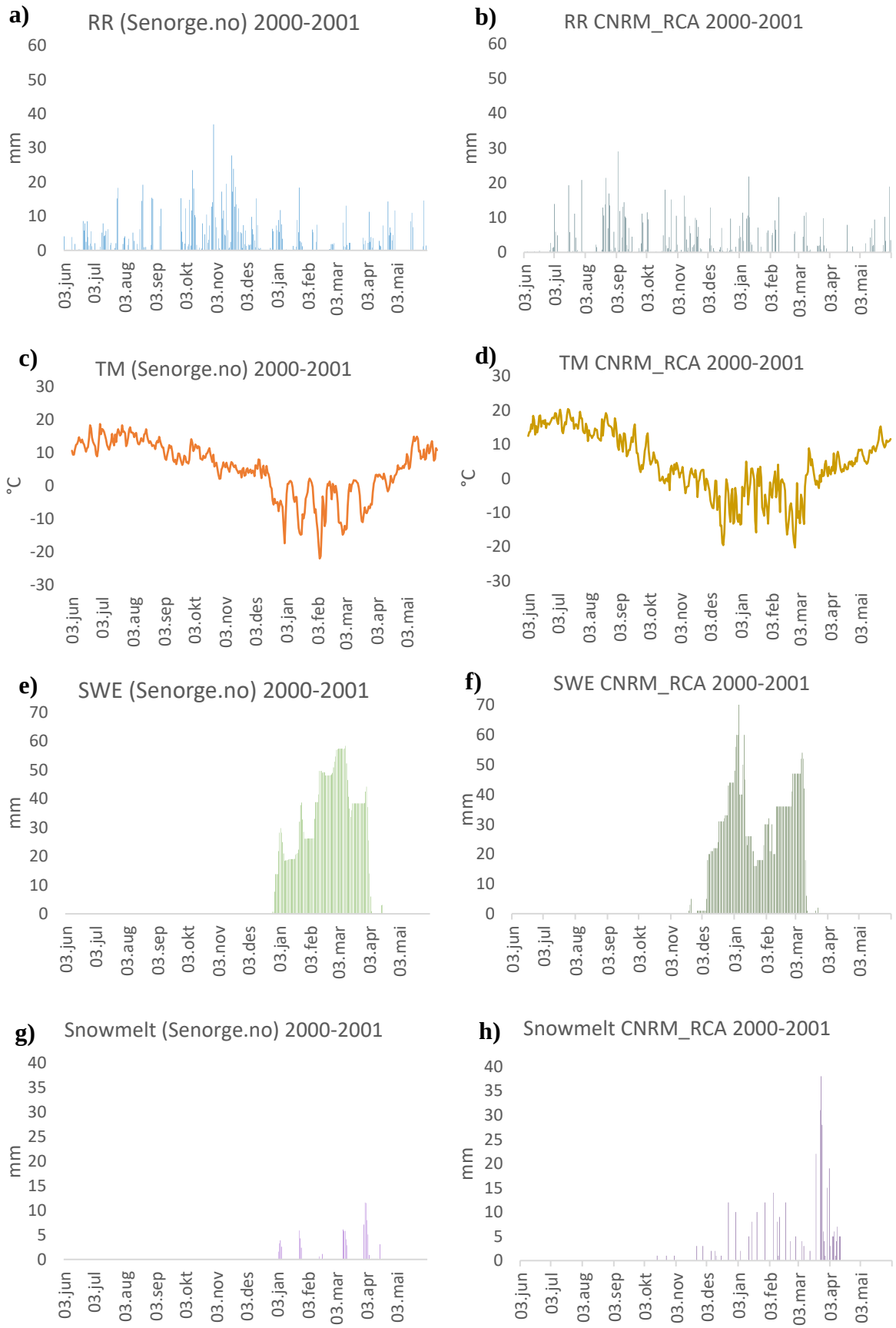

Figure E-1. *Daily values from 3rd June 2000 to 2nd June 2001 for a) measured precipitation, b) predicted precipitation, c) measured temperatures, d) predicted temperatures, e) measured snow water equivalent, f) predicted snow water equivalent, g) measured snowmelt, h) predicted snowmelt.*
Predicted = CNRM_RCA climate model collected from klimaservicecenter.no.
Measured= observation data collected from SeNorge.no.

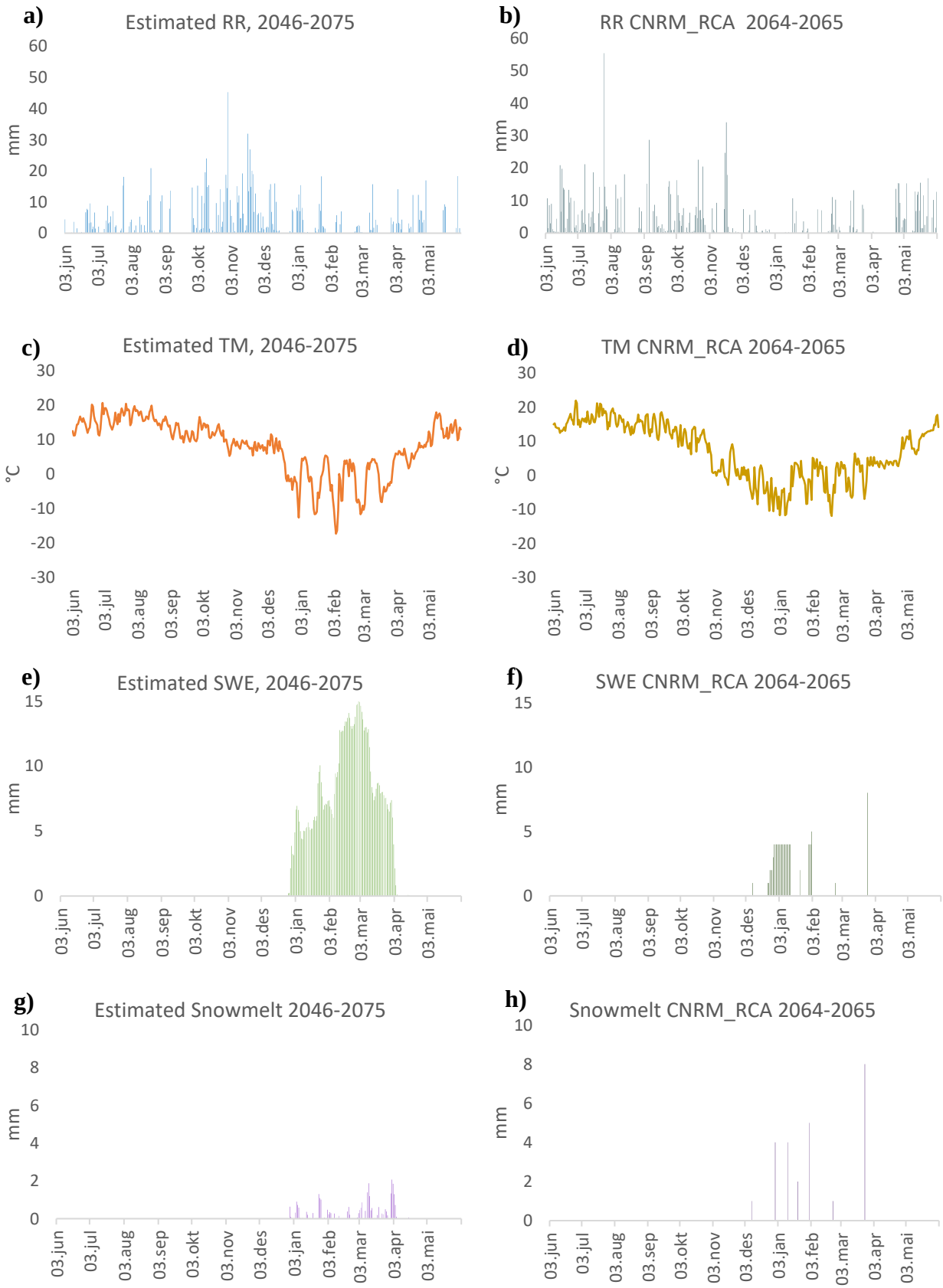

Figure E-2. *Daily values from 3rd June to 2nd June for a) estimated precipitation, b) predicted precipitation, c) estimated temperatures, d) predicted temperatures, e) estimated snow water equivalent, f) predicted snow water equivalent, g) estimated snowmelt, h) predicted snowmelt.*
Predicted = CNRM_RCA climate model collected from klimaservicecenter.no.
Estimated= observation data collected from SeNorge.no with added expected increase (Table 7-4).

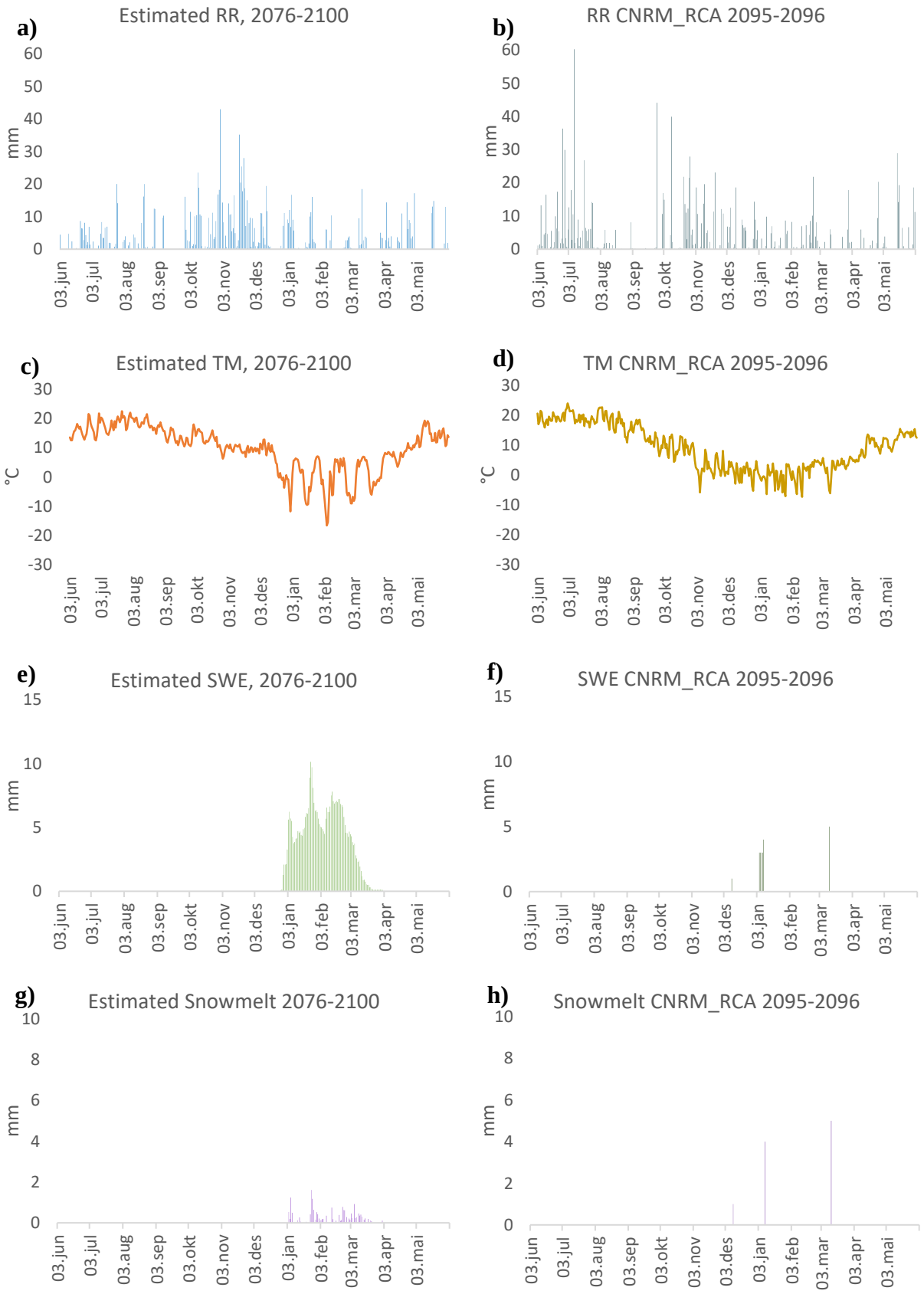

Figure E-3. *Daily values from 3rd June to 2nd June for a) estimated precipitation, b) predicted precipitation, c) estimated temperatures, d) predicted temperatures, e) estimated snow water equivalent, f) predicted snow water equivalent, g) estimated snowmelt, h) predicted snowmelt.*
Predicted = CNRM_RCA climate model collected from klimaservicecenter.no.
Estimated= observation data collected from SeNorge.no with added expected increase (Table 7-5).